
Position-dependent power spectrum: a new observable in the large-scale structure

Chi-Ting Chiang



München 2015

Position-dependent power spectrum: a new observable in the large-scale structure

Chi-Ting Chiang

Dissertation
an der Fakultät für Physik
der Ludwig-Maximilians-Universität
München

vorgelegt von
Chi-Ting Chiang
aus Taipei, Taiwan

München, den Abgabedatum

Erstgutachter: Prof. Dr. Eiichiro Komatsu

Zweitgutachter: Prof. Dr. Jochen Weller

Tag der mündlichen Prüfung: 22 June 2015

Contents

Zusammenfassung	xiii
Abstract	xv
1 Introduction	1
1.1 Why study the position-dependent power spectrum of the large-scale structure?	1
1.2 Observations and measurements of the large-scale structure	5
1.3 Theoretical understanding of the large-scale structure	9
1.3.1 Simulations	9
1.3.2 Theory	12
2 Position-dependent two-point statistics	15
2.1 In Fourier space	15
2.1.1 Position-dependent power spectrum	15
2.1.2 Integrated bispectrum	16
2.1.3 Linear response function	17
2.1.4 Integrated bispectrum of various bispectrum models	19
2.2 In configuration space	21
2.2.1 Position-dependent correlation function	21
2.2.2 Integrated three-point function	22
2.2.3 Connection to the integrated bispectrum	24
2.2.4 Squeezed limit	25
2.2.5 Shot noise	26
3 Separate universe picture	29
3.1 Mapping the overdense universe to the modified cosmology	30
3.2 The modified cosmology in Einstein-de Sitter background	33
3.2.1 Scale factor and Eulerian overdensity	33
3.2.2 Small-scale growth	36
4 Measurement of position-dependent power spectrum	41
4.1 N -body simulations and the estimators	42

4.2	Bispectrum modeling	45
4.2.1	Standard perturbation theory	46
4.2.2	Bispectrum fitting formula	48
4.3	Separate universe approach	49
4.3.1	Linear power spectrum	51
4.3.2	SPT 1-loop power spectrum	52
4.3.3	halofit and Coyote emulator	52
4.3.4	Halo model	55
4.4	Dependence on cosmological parameters	57
4.5	Fisher matrix calculation	58
4.6	Discussion and conclusion	61
5	Measurement of position-dependent correlation function	63
5.1	Measurement of PTHalo mock catalogs	64
5.1.1	Dividing the subvolumes	64
5.1.2	Estimators in the subvolumes	66
5.1.3	Measurements in real space	67
5.1.4	Measurements in redshift space	70
5.2	Measurement of the BOSS DR10 CMASS sample	72
5.3	Interpretation for the measurement of the integrated three-point function .	74
5.4	Discussion and conclusion	76
6	The angle-averaged squeezed limit of nonlinear matter N-point functions and separate universe simulations	79
6.1	Power spectrum response	82
6.1.1	Separate universe picture	82
6.1.2	Linear power spectrum predictions	84
6.1.3	Nonlinear power spectrum predictions	85
6.1.4	Halo model predictions	86
6.2	Separate universe simulations	89
6.3	Results of separate universe simulations	91
6.3.1	Growth-only response functions	92
6.3.2	Full response functions	93
6.3.3	Eulerian response functions	95
6.4	Simulations with rescaled initial amplitudes	96
6.4.1	Comparison to separate universe simulations	96
6.5	Discussion and conclusion	98
7	Summary and outlook	101
A	Tree-level redshift-space bispectrum	103
A.1	Mapping between real and redshift space	103
A.2	Redshift-space kernel	105

A.3	Tree-level redshift-space integrated bispectrum in the squeezed-limit	109
B	Variance of the integrated bispectrum estimator	113
C	Testing the integrated three-point function estimator with Gaussian realizations and the local bias model	119
D	Effects of effective F_2 and G_2 kernels and non-local tidal bias	121
E	Comparison for $i\zeta(r)/\sigma_L^2$ of BOSS DR10 CMASS sample and PTHalo mock catalogs in different redshift bins	123
F	Squeezed-limit N-point functions and power spectrum response	125
F.1	Tree-level result: $n = 1$	127
F.2	Tree-level result: $n = 2$	128
	Bibliography	131
	Acknowledgment	143

List of Figures

1.1	Sketch of the correlation between long and short wavelength modes	3
1.2	SDSS galaxy maps projected on the RA-redshift plane	6
1.3	The first detection of BAOs in 2dFGRS and SDSS	7
1.4	A slice of the Millennium simulation	10
2.1	Normalized integrated bispectrum of the simplest f_{NL} model	20
2.2	Normalized $i\zeta_{L,\text{SPT}}$ and $i\zeta_{L,b_2}$	23
2.3	Normalized $i\zeta_{L,\text{SPT}}$ and $i\zeta_{L,b_2}$ evaluated from Fourier space	25
2.4	Linear response of the correlation function and normalized $i\zeta_{L,\text{SPT}}(r)$	27
3.1	Perturbation in the scale factor in the modified cosmology with Λ CDM background	36
3.2	Linear growth factor in the modified cosmology with Λ CDM background	39
3.3	Logarithmic growth rate in the modified cosmology with Λ CDM background	40
4.1	Position-dependent power spectra measured from 512 subvolumes with $L = 300 h^{-1}$ Mpc in one realization	44
4.2	Normalized integrated bispectrum, averaged over 160 collisionless N -body simulations with Gaussian initial conditions.	45
4.3	Bispectrum modeling for the measured integrated bispectrum in $300 h^{-1}$ Mpc subvolumes	47
4.4	Separate universe approach of the linear and 1-loop response functions for the measured integrated bispectrum in $300 h^{-1}$ Mpc subvolumes	53
4.5	Separate universe approach of the halo fit, the Coyote emulator, and the halo model response functions for the measured integrated bispectrum in $300 h^{-1}$ Mpc subvolumes	54
4.6	Cosmological dependences of the integrated bispectrum	58
4.7	Two-dimensional joint 95% C.L. constraints on galaxy bias and primordial non-Gaussianity for BOSS and HETDEX	60
5.1	Division of random samples into subvolumes in the RA-DEC plane	65
5.2	Measurements of $\xi(r)$ and $i\zeta_L(r)/\sigma_L^2$ of PTHalos mock catalogs in real space	68
5.3	Measurements of $\xi(r)$ and $i\zeta_L(r)/\sigma_L^2$ of PTHalos mock catalogs in redshift space	70

5.4	Correlation matrix estimated from 600 mocks in redshift space	71
5.5	Measurements of $\xi(r)$ and $i\zeta_L(r)/\sigma_L^2$ of BOSS DR10 CMASS sample	73
6.1	Sketch of the squeezed-limit configuration of N -point functions	80
6.2	The first three growth-only response functions	93
6.3	The first three full response functions	94
6.4	The first three Eulerian response functions	95
6.5	Growth-only response functions of separate universe simulations and rescaled-amplitude simulations	100
A.1	Tree-level redshift-space integrated bispectrum	110
B.1	Correlation matrices of the unnormalized and normalized integrated bispectra measured from 160 dark matter N -body simulations	117
B.2	Square root of the variances of the normalized integrated bispectrum	118
C.1	Normalized integrated three-point functions of the mock halo density field	120
E.1	Normalized integrated three-point function of 220 h^{-1} Mpc subvolumes in different redshift bins	124
E.2	Normalized integrated three-point function of 120 h^{-1} Mpc subvolumes in different redshift bins	124

List of Tables

5.1	Fitted amplitudes of $i\zeta_L(r)/\sigma_L^2$, $\xi(r)$, and σ_L^2 of BOSS DR10 CMASS sample	74
5.2	Best-fitting b_2 and their uncertainties for BOSS DR10 CMASS sample for the extended models	75
D.1	Best-fitting values of b_1 and b_2 of the mock catalogs for various bispectrum models	122

Zusammenfassung

In dieser Dissertation führe ich eine neue Observable der grossräumigen Struktur des Universums ein, das ortsabhängige Leistungsspektrum. Diese Größe bietet ein Mass für den “gequetschten” Limes der Dreipunktfunktion (Bispektrum), das heisst, eine Wellenzahl ist wesentlich kleiner als die beiden übrigen. Physikalisch beschreibt dieser Limes der Dreipunktfunktion die Modulation des Leistungsspektrums auf kleinen Skalen durch grossräumige Moden. Diese Modulation wird sowohl durch die Schwerkraft bewirkt als auch (möglicherweise) durch die kosmologische Inflation im frühen Universum.

Für die Messung teilen wir das Gesamtvolumen der Himmelsdurchmusterung, oder kosmologischen Simulation, in Teilvolumina ein. In jedem Teilvolumen messen wir die Überdichte relativ zur mittleren Dichte der Materie (oder Anzahldichte der Galaxien) und das lokale Leistungsspektrum. Anschliessend messen wir die Korrelation zwischen Überdichte und Leistungsspektrum. Ich zeige, dass diese Korrelation einem Integral über die Dreipunktfunktion entspricht. Wenn die Skala, an der das Leistungsspektrum ausgewertet wird (inverse Wellenzahl, um genau zu sein), viel kleiner als die Größe des Teilvolumens ist, dann ist das Integral über die Dreipunktfunktion vom gequetschten Limes dominiert.

Um physikalisch zu verstehen, wie eine grossräumige Dichtefluktuation das lokale Leistungsspektrum beeinflusst, wenden wir das Bild vom “unabhängigen Universum” (“separate universe”) an. Im Kontext der allgemeinen Relativitätstheorie kann eine langwellige Dichtefluktuation exakt durch eine Friedmann-Robertson-Walker-(FRW-)Raumzeit beschrieben werden, deren Parameter sich von der “wahren” FRW-Raumzeit unterscheiden und eindeutig von der Dichtefluktuation bestimmt werden. Die Modulation des lokalen Leistungsspektrums kann dann durch die Strukturbildung innerhalb der modifizierten FRW-Raumzeit beschrieben werden. Insbesondere zeige ich, dass die Dreipunktfunktion im gequetschten Limes durch diesen Ansatz einfacher und besser beschrieben wird als durch die herkömmliche Herangehensweise mittels Störungstheorie.

Diese neue Observable ist nicht nur einfach zu interpretieren (sie stellt die Antwort des lokalen Leistungsspektrums auf eine großskalige Dichtestörung dar), sie ermöglicht zudem die komplexe Berechnung der vollen Dreipunktsfunktion zu umgehen, weil das Leistungsspektrum genauso wie die mittlere Dichte wesentlich leichter als die Dreipunktsfunktion zu bestimmen sind.

Anschließend wende ich die gleiche Methodik auf die Daten der Himmelsdurchmusterung SDSS-III Baryon Oscillation Spectroscopic Survey (BOSS) an, insbesondere den

Data Release 10 CMASS Galaxienkatalog. Wie ich zeige, stimmt das in den wirklichen Daten gemessene ortsabhängige Leistungsspektrum mit den sogenannten “mock” (also simulierten) Galaxienkatalogen überein, die auf dem PTHalo-Algorithmus basieren und die räumliche Verteilung der wirklichen Galaxien im statistischen Sinne möglichst genau beschreiben wollen. Genauer gesagt, liegen die Daten innerhalb der Streuung, die das ortsabhängige Leistungsspektrum zwischen den verschiedenen Realisierungen von “mock” Katalogen aufweist. Diese Streuung beträgt ca. 10% des Mittelwerts. In Kombination mit dem (anisotropen) globalen Leistungsspektrum der Galaxien sowie dem Signal im schwachen Gravitationslinseneffekt, benutze ich diese 10%-Messung des ortsabhängigen Leistungsspektrums, um den quadratischen Bias-Parameter der von BOSS gemessenen Galaxien zu bestimmen, mit dem Ergebnis $b_2 = 0.41 \pm 0.41$ (68% Vertrauensintervall).

Schließlich verallgemeinern wir die Analyse der Antwort des lokalen Leistungsspektrums auf eine Häufung von m großräumigen Wellenlängenmoden, wobei $m \leq 3$. In Analogie zum vorherigen Fall, kann die resultierende Modulation des Leistungsspektrums mit der $m + 2$ -Punktskorrelationsfunktion im Limes gequetschter Konfigurationen (so dass immer zwei Wellenlängen wesentlich länger sind als die anderen), gemittelt über die auftretenden Winkel, in Verbindung gebracht werden. Mit Hilfe von Simulationen “unabhängiger Universen”, das heißt N -body-Simulationen in Anwesenheit von Dichtestörungen unendlicher Länge, vergleichen wir unsere semianalytischen Modelle, die auf dem Bild der unabhängigen Universen basieren, mit den vollständig nichtlinearen Simulationen bei bisher unerreichter Genauigkeit. Zudem testen wir die Annahme der gewöhnlichen Störungstheorie, dass die nichtlineare N -Punktskorrelationsfunktion vollständig durch das lineare Leistungsspektrum bestimmt ist. Wir finden bereits Abweichungen von 10% bei Wellenzahlen von $k \simeq 0.2 - 0.5 h \text{ Mpc}^{-1}$ für die Drei- bis Fünf-Punktskorrelationsfunktion bei Rotverschiebung $z = 0$. Dieses Ergebnis deutet darauf hin, dass die gewöhnliche Störungstheorie nicht ausreicht um die Dynamik kollisionsloser Teilchen für Wellenzahlen größer als diese korrekt vorherzusagen, selbst wenn alle höheren Ordnungen in die Berechnung mit einbezogen werden.

Abstract

We present a new observable, position-dependent power spectrum, to measure the large-scale structure bispectrum in the so-called squeezed configuration, where one wavenumber, say k_3 , is much smaller than the other two, i.e. $k_3 \ll k_1 \approx k_2$. The squeezed-limit bispectrum measures how the small-scale power spectrum is modulated by a long-wavelength scalar density fluctuation, and this modulation is due to gravitational evolution and also possibly due to the inflationary physics.

We divide a survey volume into smaller subvolumes. We compute the local power spectrum and the mean overdensity in each smaller subvolume, and then measure the correlation between these two quantities. We show that this correlation measures the integral of the bispectrum, which is dominated by the squeezed configurations if the wavenumber of the local power spectrum is much larger than the corresponding wavenumber of the size of the subvolumes. This integrated bispectrum measures how small-scale power spectrum responds to a long-wavelength mode.

To understand theoretically how the small-scale power spectrum is affected by a long-wavelength overdensity gravitationally, we use the “separate universe picture.” A long-wavelength overdensity compared to the scale of interest can be absorbed into the change of the background cosmology, and then the small-scale structure formation evolves in this modified cosmology. We show that this approach models nonlinearity in the bispectrum better than the traditional approach based on the perturbation theory.

Not only this new observable is straightforward to interpret (the response of the small-scale power spectrum to a long-wavelength overdensity), but it also sidesteps the complexity of the full bispectrum estimation because both power spectrum and mean overdensity are significantly easier to estimate than the full bispectrum.

We report on the first measurement of the bispectrum with the position-dependent correlation function from the SDSS-III Baryon Oscillation Spectroscopic Survey (BOSS) Data Release 10 CMASS sample. We detect the amplitude of the bispectrum of the BOSS CMASS galaxies at 7.4σ , and constrain their nonlinear bias to be $b_2 = 0.41 \pm 0.41$ (68% C.L.) combining our bispectrum measurement with the anisotropic clustering and the weak lensing signal.

We finally generalize the study to the response of the small-scale power spectrum to m long-wavelength overdensities for $m \leq 3$. Similarly, this response can be connected to the angle-average $(m+2)$ -point function in the squeezed configurations where two wavenumbers are much larger than the other ones. Using separate universe simulations, i.e. N -body sim-

ulations performed in the presence of an infinitely long-wavelength overdensity, we compare our semi-analytical models based on the separate universe approach to the fully nonlinear simulations to unprecedented accuracy. We also test the standard perturbation theory hypothesis that the nonlinear n -point function is completely predicted by the linear power spectrum at the same time. We find discrepancies of 10% at $k \simeq 0.2 - 0.5 h \text{ Mpc}^{-1}$ for three- to five-point functions at $z = 0$. This result suggests that the standard perturbation theory fails to describe the correct dynamics of collisionless particles beyond these wavenumbers, even if it is calculated to all orders in perturbations.

Chapter 1

Introduction

1.1 Why study the position-dependent power spectrum of the large-scale structure?

The standard cosmological paradigm has been well developed and tested by the observations of the cosmic microwave background (CMB) and the large-scale structure. The inhomogeneities seen in the universe originate from quantum fluctuations in the early universe, and these quantum fluctuations were stretched to macroscopic scales larger than the horizon during the cosmic inflation [69, 132, 5, 99], which is the early phase with exponential growth of the scale factor. After the cosmic inflation, the hot Big-Bang universe expanded and cooled down, and the macroscopic inhomogeneities entered into horizon and seeded all the structures we observe today.

With the success of connecting the quantum fluctuations in the early universe to the structures we see today, the big questions yet remain: What is the physics behind inflation? Also, what is nature of dark energy, which causes the accelerated expansion in the late-time universe (see [57] for a review)? As the standard cosmological paradigm passes almost all the tests from the current observables, especially the two-point statistics of CMB and galaxy surveys, it is necessary to go to higher order statistics to obtain more information and critically test the current model. In particular, the mode coupling between a long-wavelength scalar density fluctuation and the small-scale structure formation receives much attention in the past few years. This coupling is due to the nonlinear gravitational evolution (see [17] for a review), and possibly the inflationary physics. Therefore, this provides a wonderful opportunity to test our understanding of gravity, as well as to probe the properties of inflation.

Traditionally, the n -point function with $n > 2$ is used to characterize the mode coupling. Specifically, if one is interested in the coupling between one long-wavelength mode and two short-wavelength modes, we measure the three-point correlation function or its Fourier counterpart, the bispectrum, in the so-called “squeezed configurations,” in which one wavenumber, say k_3 , is much smaller than the other two, i.e. $k_3 \ll k_1 \approx k_2$.

In the simplest model for the primordial non-Gaussianity (see [27] for a review on the

general primordial non-Gaussianities from various inflation models), the primordial scalar potential is given by

$$\Phi(\mathbf{r}) = \phi(\mathbf{r}) + f_{\text{NL}} [\phi^2(\mathbf{r}) - \langle \phi^2(\mathbf{r}) \rangle] , \quad (1.1)$$

where $\phi(\mathbf{r})$ is a Gaussian field and f_{NL} is a constant characterizing the amplitude of the non-Gaussianity, which encodes the properties of inflation. Note that $\langle \phi^2(\mathbf{r}) \rangle$ assures $\langle \Phi(\mathbf{r}) \rangle = 0$. This simple model is known as the local-type primordial non-Gaussianity because $\Phi(\mathbf{r})$ depends locally on $\phi(\mathbf{r})$. The bispectrum of this local model is

$$B_{\Phi}(\mathbf{k}_1, \mathbf{k}_2, \mathbf{k}_3) = 2f_{\text{NL}} [P_{\Phi}(k_1)P_{\Phi}(k_2) + 2 \text{ cyclic}] , \quad (1.2)$$

where $P_{\Phi}(k) \propto k^{n_s-4}$ is the power spectrum of the primordial scalar potential and $n_s \simeq 0.96$ is its spectral index [88]. We can rewrite B_{Φ} of this local model by fixing one wavenumber, say k_1 , as

$$\begin{aligned} B_{\Phi}(\mathbf{k}_1, \mathbf{k}_2, \mathbf{k}_3) &\propto k_1^{2(n_s-4)} \left[\left(\frac{k_2}{k_1}\right)^{n_s-4} + \left(\frac{k_3}{k_1}\right)^{n_s-4} + \left(\frac{k_2}{k_1}\right)^{n_s-4} \left(\frac{k_3}{k_1}\right)^{n_s-4} \right] \\ &\propto k_1^{2(n_s-4)} \left[\left(\frac{k_2}{k_1}\right)^{n_s-4} + \left(\frac{|\mathbf{k}_1 + \mathbf{k}_2|}{k_1}\right)^{n_s-4} + \left(\frac{k_2}{k_1}\right)^{n_s-4} \left(\frac{|\mathbf{k}_1 + \mathbf{k}_2|}{k_1}\right)^{n_s-4} \right] , \end{aligned} \quad (1.3)$$

where $\mathbf{k}_3 = -\mathbf{k}_1 - \mathbf{k}_2$ because of the assumption of homogeneity. B_{Φ} apparently peaks at $k_1 \approx k_2 \gg k_3 \approx 0$, so the local-type primordial non-Gaussianity is the most prominent in the squeezed-limit bispectrum.

Constraining the physics of inflation using the squeezed-limit bispectrum of CMB is a solved problem [87]. With the Planck satellite, the current constraint on the local-type primordial non-Gaussianity is $f_{\text{NL}} = 2.5 \pm 5.7$ (68% C.L.) using the temperature data alone and $f_{\text{NL}} = 0.8 \pm 5.0$ using the temperature and polarization data [128]. These are close to the best limits obtainable from CMB. To improve upon them, we must go beyond CMB to the large-scale structure, where observations are done in three-dimensional space (unlike CMB embedded on a two-dimensional sphere). Thus, in principle, the large-scale structure contains more information to improve the constraint on the physics of inflation.

Measuring the three-point function from the large-scale structure (e.g. distribution of galaxies), however, is considerably more challenging compared to CMB. From the measurement side, the three-point function measurements are computationally expensive. In configuration space, the measurements rely on finding particle triplets with the naive algorithm scaling as N_{par}^3 where N_{par} is the number of particles. Current galaxy redshift surveys contain roughly a million galaxies, and we need 50 times as many random samples as the galaxies for characterizing the survey window function accurately. Similarly, in Fourier space, the bispectrum measurements require counting all possible triangle configurations formed by different Fourier modes, which is also computationally expensive. From the modeling side, galaxy surveys have more complicated survey selection function, which can bias the estimation (see e.g. [30]). Additionally, the nonlinear gravitational evolution

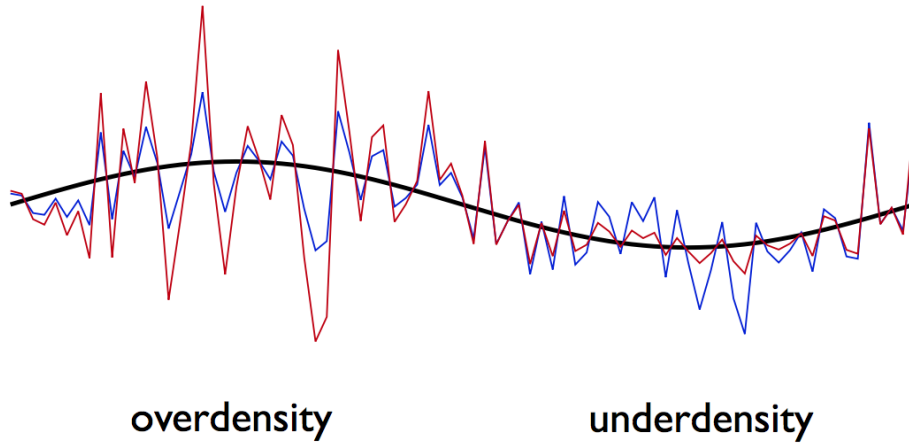


Figure 1.1: In the absence of the correlation between long and short wavelength modes, the blue fluctuation have the same statistical property in the overdense and underdense regions. On the other hand, in the presence of the positive correlation between long and short wavelength modes, the red fluctuation has larger (smaller) variance in the overdense (undersense) region.

of matter density field and the complexity of galaxy formation make it challenging to extract the primordial signal. The above difficulties explain why only few measurements of the three-point function of the large-scale structure have been reported in the literature [142, 55, 167, 82, 119, 109, 110, 105, 62, 67].

Since our main interest is to measure the three-point function of the squeezed configurations, there is a simpler way to sidestep all the above complexities of the three-point function estimation. As we stated, in the presence of the mode coupling between long- and short-wavelength modes, a long-wavelength density fluctuation modifies the small-scale structure formation, and so the observables become *position-dependent*. Figure 1.1 sketches the short-wavelength modes with (red) and without (blue) correlation with the long-wavelength mode. As a consequence, for example, the n -point statistics and the halo mass function would depend on the local long-wavelength overdensity, or equivalently the position in space. Measurements of spatially-varying observables capture the effect of mode coupling, and can be used to test our understanding of gravity and the physics of inflation. A similar idea of measuring the shift of the peak position of the baryonic acoustic oscillation in different environments has been studied in [129].

In this dissertation, we focus on the position-dependent two-point statistics (see [32, 115] for the mass function). Consider a galaxy redshift survey or simulation. Instead of measuring the power spectrum within the entire volume, we divide the volume into many subvolumes, within which we measure the power spectrum. These power spectra of subvolumes vary spatially, and the variation is correlated with the mean overdensities of the subvolumes with respect to the entire volume. This correlation measures an integral of the bispectrum (or the three-point function in configuration space), which represents the

response of the small-scale clustering of galaxies (as measured by the position-dependent power spectrum) to the long-wavelength density perturbation (as measured by the mean overdensity of the subvolumes).

Not only is this new observable, *position-dependent power spectrum*, of the large-scale structure conceptually straightforward to interpret, but it is also simpler to measure than the full bispectrum, as the machineries for the two-point statistics estimation are well developed (see [56] for power spectrum and [91] for two-point function) and the measurement of the overdensity is simple. In particular, the computational requirement is largely alleviated because we explore a subset of the three-point function corresponding to the squeezed configurations. More precisely, in Fourier space we only need to measure the power spectrum, and in configuration space the algorithm of measuring the two-point function by finding particle pairs scales as $N_s(N_{\text{par}}/N_s)^2 = N_{\text{par}}^2/N_s$ for the entire volume with N_s being the number of subvolumes. In addition, for a fixed size of the subvolume, the measurement depends on only one wavenumber or one separation, so estimating the covariance matrix is easier than that of the full bispectrum from a realistic number of mock catalogs. The position-dependent power spectrum can thus be regarded as a useful compression of information of the squeezed-limit bispectrum.

As this new observable uses basically the existing and routinely applied machineries to measure the two-point statistics, one can easily gain extra information of the three-point function, which is sensitive to the nonlinear bias of the observed tracers, from the current spectroscopic galaxy surveys. Especially, since the position-dependent power spectrum picks up the signal of the squeezed-limit bispectrum, it is sensitive to the primordial non-Gaussianity of the local type.

This dissertation is organized as follows. In the rest of this chapter, we review the status of the observations of the large-scale structure, and the current theoretical understanding.

In chapter 2, we introduce the main topic of this dissertation: position-dependent power spectrum and correlation function. We show how the correlation between the position-dependent two-point statistics and the long-wavelength overdensity is related to the three-point statistics. We also make theoretical template for this correlation using various bispectrum models.

In chapter 3, we introduce the “separate universe approach,” in which a long-wavelength overdensity is absorbed into the background, and the small-scale structure formation evolves in the corresponding modified cosmology. This is the basis for modeling the response of the small-scale structure formation to the long-wavelength overdensity. We consider the fiducial cosmology to be flat Λ CDM, and show that the overdensity acts as the curvature in the separate universe.

In chapter 4, we measure the position-dependent power spectrum from cosmological N -body simulations. We compare various theoretical approaches to modeling the measurements from simulations, particularly the separate universe approach when the scales of the position-dependent power spectrum are much smaller than that of the long-wavelength overdensity. We also study the dependences of the position-dependent power spectrum on the cosmological parameters, as well as using the Fisher matrix to predict the expected constraints on biases and local-type primordial non-Gaussianity for current and future

galaxy surveys.

In chapter 5, we report on the first measurement of the three-point function with the position-dependent correlation function from the SDSS-III Baryon Oscillation Spectroscopic Survey Data Release 10 (BOSS DR10) CMASS sample. We detect the amplitude of the three-point function of the BOSS CMASS galaxies at 7.4σ . Combining the constraints from position-dependent correlation function, global two-point function, and the weak lensing signal, we determine the quadratic (nonlinear) bias of BOSS CMASS galaxies.

In chapter 6, we generalize the study to the response of the small-scale power spectrum in the presence of m long-wavelength modes for $m \leq 3$. This response can be linked to the angular-averaged squeezed limit of $(m + 2)$ -point functions. We shall also introduce the separate universe simulations, in which N -body simulations are performed in the presence of a long-wavelength overdensity by modifying the cosmological parameters. The separate universe simulations allow unprecedented measurements for the squeezed-limit n -point function. Finally, we test the standard perturbation theory hypothesis that the nonlinear n -point function is completely predicted by the linear power spectrum at the same time. We find discrepancies of 10% at $k \simeq 0.2 - 0.5 h \text{ Mpc}^{-1}$ for five- to three-point functions at $z = 0$. This suggests the breakdown of the standard perturbation theory, and quantifies the scales that the corrections of the effective fluid become important for the higher order statistics.

In chapter 7, we summarize this dissertation, and present the outlook.

1.2 Observations and measurements of the large-scale structure

In the 1960s, before the invention of the automatic plate measuring machine and the densitometer, the galaxy catalogs such as Zwicky [174] and Lick [146] relied on visual inspection of poorly calibrated photographic plates. These surveys consisted of different neighboring photographic plates, so the uniformity of the calibration, which might cause large-scale gradients in the observed area, was a serious issue. Because of the lack of the redshifts (depths) of galaxies, only the angular clustering studies were possible. In addition, the sizes of the surveys were much smaller than the ones today, thus only the clustering on small scales, where the nonlinear effect is strong, can be studied. Nevertheless, in the 1970s Peebles and his collaborators did the first systematic study on galaxy clustering using the catalogs at that time. The series of studies, starting with [125], considered galaxies as the tracers of the large-scale structure for the first time, which was a ground-breaking idea. These measurements confirmed the power-law behavior of the angular two-point function, and the interpretation was done in the framework of Einstein-de Sitter universe, i.e. matter-dominated flat Friedmann-Lemaître-Robertson-Walker universe.

In the 1980s, the invention of the automatic scanning machines as well as CCDs revolutionized the large-scale structure surveys, and resulted in a generation of wide-field surveys with better calibration and a three-dimensional view of the universe. Photographic plates

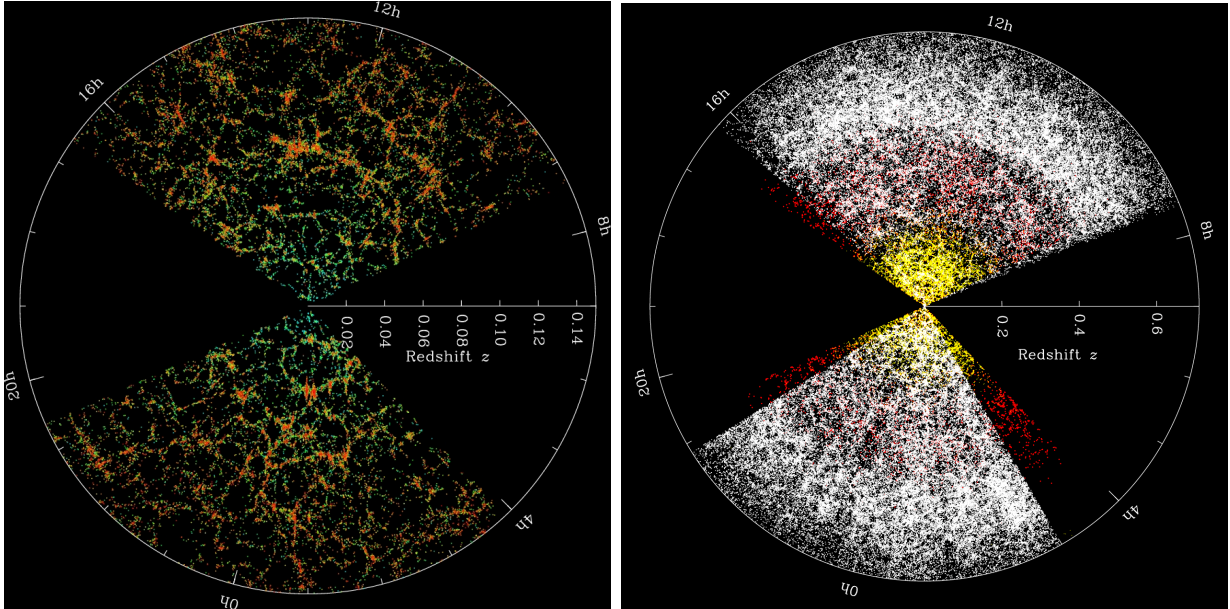


Figure 1.2: (Credit: Michael Blanton and SDSS collaboration) SDSS galaxy maps projected on the RA-redshift plane. (Left) The SDSS main galaxy sample out to $z \sim 0.15$. (Right) Yellow, red, and white dots are the SDSS main galaxy sample, luminous red galaxies, and CMASS sample, respectively, out to $z \sim 0.7$.

became obsolete for the large-scale structure studies, and nowadays photometric surveys use large CCD cameras with millions of pixels. The galaxy redshift surveys, which generally require target selections with photometric detection and then spectroscopic follow-up, thus open a novel avenue to study the universe. It was shown that the redshift-space two-point correlation function in the CfA survey [74] agreed well with the previous studies on angular clustering, if the redshift direction is integrated over [46]. In the 1990s, the number of galaxies in surveys was $\sim 10^3 - 10^4$, but with these data it was already shown that the large-scale power spectrum was inconsistent with the CDM model [52, 135, 168], in agreement with the study done in the angular clustering [101].

Another quantum leap of the sizes of the galaxy surveys happened in the 2000s, when the technology of the massive multi-fiber or multi-slit spectroscopy became feasible. Surveys such as Two-degree-Field Galaxy Redshift Survey (2dFGRS) [34] and Sloan Digital Sky Survey (SDSS) [172] targeted at obtaining spectra of $\sim 10^5 - 10^6$ galaxies. The left panel of figure 1.2 shows the SDSS main galaxy sample out to $z \sim 0.15$, which corresponds to roughly $440 h^{-1}$ Mpc. It is clear even visually that the distribution of galaxies follows filamentary structures, with voids in between the filaments. These data contain precious information of the properties of the universe. For example, in 2005, the baryonic acoustic oscillations (BAO) in the two-point statistics were detected for the first time by 2dFGRS [33] in the power spectrum and SDSS [54] in the two-point correlation function, as shown

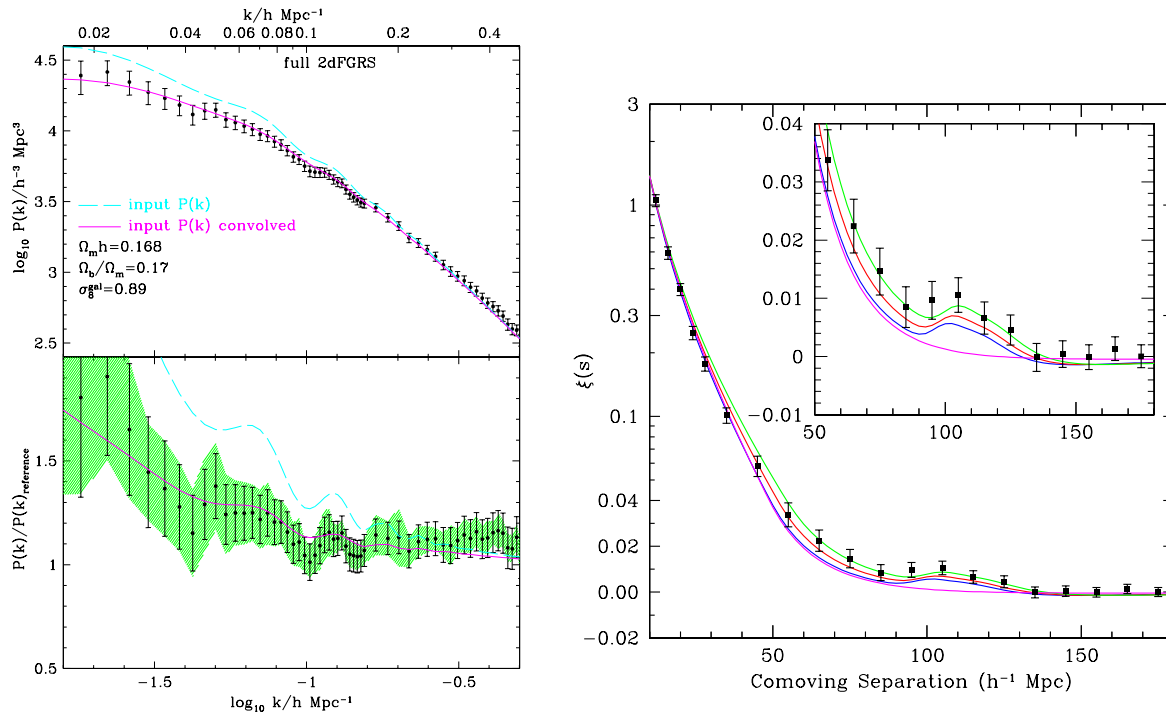


Figure 1.3: (Credit: 2dFGRS and SDSS collaborations) The first detection of BAOs in 2dFGRS (left) and SDSS (right). The analysis of 2dFGRS was done in Fourier space, and the BAOs are the wiggles in the power spectrum at $0.05 h \text{Mpc}^{-1} \lesssim k \lesssim 0.2 h \text{Mpc}^{-1}$; the analysis of SDSS was done in configuration space, and the BAOs are the bump in the two-point correlation function at $r \sim 100 h^{-1} \text{Mpc}$.

in figure 1.3. The detection is phenomenal given the fact that the BAOs are of order a few percent features on the smooth functions. Galaxy surveys in this era started probing the weakly nonlinear regime, where the theoretical understanding is better, so we can extract cosmological information.

With the success of the first BAO detection, more galaxy redshift surveys, such as WiggleZ [22, 23] and SDSS-III Baryon Oscillation Spectroscopic Survey (BOSS) [7, 6], followed and extended to higher redshifts. The right panel of figure 1.2 shows the galaxy map of SDSS out to $z \sim 0.7$, which corresponds to roughly $1800 h^{-1} \text{Mpc}$. The BAO feature can be used as a standard ruler to measure the angular diameter distance and Hubble expansion rate. This is particularly useful for studying the time-dependence of dark energy, which began to dominate the universe at $z \sim 0.4$ where the galaxy clustering is measured. The BAOs in the galaxy clustering thus becomes a powerful probe of dark energy.

Thus far, most of the studies have focused on the two-point statistics. However, there is much more information in the higher-order statistics. Especially, ongoing galaxy surveys such as Dark Energy Survey [162] and the extended BOSS, as well as upcoming galaxy

surveys such as Hobby Eberly Telescope Dark Energy eXperiment (HETDEX) [71] and Subaru Prime Focus Spectrograph [156] will measure the galaxies at even higher redshift. For instance, HETDEX will use Lyman-alpha emitters as tracers to probe the matter distribution at $1.9 \lesssim z \lesssim 3.5$. At such high redshift, the gravitational evolution is relatively weak and can still be predicted analytically, hence this is an ideal regime to critically test our understanding of gravity, as well as the physics of inflation via the primordial non-Gaussianity.

Currently, most of the constraint on the local-type primordial non-Gaussianity from the large-scale structure is through the scale-dependent bias [45, 106, 151]. That is, dark matter halos (or galaxies) are biased tracers of the underlying matter distribution forming at density peaks, so the formation of halos would be modulated by the additional correlation between the long and short wavelength modes due to the primordial non-Gaussianity. As a result, the halo bias contains a k^{-2} scale-dependent correction, and this correction is prominent on large scale. Measurements of the large-scale galaxy power spectrum, which is proportional to bias squared, can thus be used to constrain the primordial non-Gaussianity of the local type.

This distinct feature appears in the galaxy power spectrum at very large scales, hence it is crucial to have a huge survey volume to beat down the cosmic variance. Moreover, if the galaxies are highly biased, then the signal-to-noise ratio would also increase. Thus, many studies have used quasars at $0.5 \lesssim z \lesssim 3.5$ from SDSS to constrain the primordial non-Gaussianity [72, 2, 92]. Similar methods, such as combining the abundances and clustering of the galaxy clusters [102] as well as the correlation between CMB lensing and large-scale structure [61, 60], have also been proposed to study the primordial non-Gaussianity from large-scale structure. It is predicted in [92] that for Large Synoptic Survey Telescope [100] the constraint on f_{NL} , parametrization of the local-type primordial non-Gaussianity, using the scale-dependent bias can reach $\sigma(f_{\text{NL}}) \sim 5$ (95% C.L.).

The error bar on f_{NL} from the scale-dependent bias is limited by the number of Fourier modes on large scales. On the other hand, for the bispectrum analysis, we are looking for triangles formed by different Fourier modes, so the bispectrum contains more information and will have a tighter constraint on f_{NL} . The difficulty for using the large-scale structure bispectrum to constrain f_{NL} is that gravity produces non-zero squeezed-limit bispectrum even without primordial non-Gaussianity, and the signal from gravity dominates for the current limit on f_{NL} . This is why recent measurements of the large-scale structure bispectrum have focused on constraining the growth and galaxy biases [105, 62].

The difficulty in modeling nonlinear effects can be alleviated if the observations are done in the high-redshift universe, where the gravitational evolution on quasi-linear scales can still be described by the perturbation theory approach. While theoretically we are reaching the stage for studying the higher-order statistics, e.g. the three-point correlation function or the bispectrum, if the data are obtained at high redshift, in practice the measurements and analyses are still computational challenging. It is thus extremely useful to find a way to compress the information, such that studying the three-point correlation function of the galaxy clustering is feasible.

Another complexity of the bispectrum measurement from galaxy surveys is the window

function effect. Namely, galaxy surveys almost always have non-ideal survey geometry, e.g. masking around the close and bright objects or the irregular boundaries, as well as the spatial changes in the extinction, transparency, and seeing. These effects would bias the measurement, and extracting the true bispectrum signal becomes difficult. While the observational systematics would enter into the estimation of both power spectrum and bispectrum, the technique of deconvolving the window function effects, e.g. [134, 133], has been relatively well developed for the two-point statistics.

The subject of this dissertation is to find a method to more easily extract the bispectrum in the squeezed configurations, where one wavenumber, say k_3 , is much smaller than the other two, i.e. $k_3 \ll k_1 \approx k_2$. The squeezed-limit bispectrum measures the correlation between one long-wavelength mode (k_3) and two short-wavelength modes (k_1, k_2), which is particularly sensitive to the local-type primordial non-Gaussianity. Specifically, we divide a survey into subvolumes, and measure the correlation between the position-dependent two-point statistics and the long-wavelength overdensity. This correlation measures an integral on the bispectrum, and is dominated by the squeezed-limit signal if the wavenumber of the position-dependent two-point statistics is much larger than the wavenumber corresponding to the size of the subvolumes. Therefore, without employing the three-point function estimator, we can extract the squeezed-limit bispectrum by the position-dependent two-point statistics technique. Furthermore, nonlinearity of the correlation between the position-dependent two-point statistics and a long-wavelength mode can be well modeled by the separate universe approach, in which the long-wavelength overdensity is absorbed into the background cosmology; the window function effect can also be well taken care of because this technique measures essentially the two-point function and the mean overdensity, for which the procedures for removing the window function effects are relatively well developed. With the above advantages, the position-dependent two-point statistics is thus a novel and promising method to study the squeezed-limit bispectrum of the large-scale structure.

Galaxy redshift surveys has entered a completely new era at which the sizes (e.g. survey volume and number of observed galaxies) are huge, and redshifts are high. As the signal-to-noise ratio of the higher-order statistics, especially for the primordial non-Gaussianity, will be much higher in the upcoming galaxy surveys than the previous ones, we should do our best to extract the precious signal for improving our understanding of the universe. The new observable, position-dependent power spectrum, proposed in the dissertation would help us achieve this goal.

1.3 Theoretical understanding of the large-scale structure

1.3.1 Simulations

How do we understand the gravitational evolution of the large-scale structure? Because of the process is nonlinear, the gold standard is the cosmological N -body simulations of

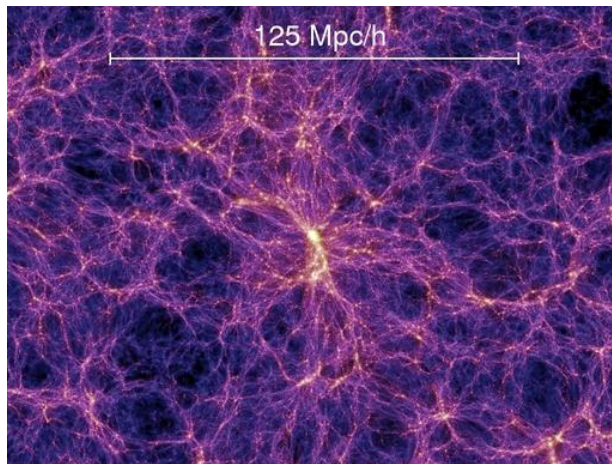


Figure 1.4: (Credit: Volker Springel) A slice of the Millennium simulation shows the cosmic web of the large-scale structure.

collisionless particles.

Using N -body simulations to solve for gravitational dynamics has a long history (see e.g. [48] for a review). The first computer calculation was done back in 1963 by [1] with $N = 16$. Later, N has roughly doubled every two years following Moore’s law, and nowadays state-of-the-art simulations for collisionless particles have $N = 10^9 - 5 \times 10^{10}$, e.g. [154, 161, 155, 86]. The N -body codes, such as GADGET-2 [153], solve dynamics of dark matter particles, and dark matter particles are grouped into dark matter halos by algorithms such as friends-of-friends or spherical overdensity. We can thus study the properties of these halos, such as the clustering and the mass function. Figure 1.4 shows a slice of the Millennium simulation [154]. The cosmic web of the large-scale structure is obvious, and we also find the similarity between the simulation and the observation, i.e. figure 1.2.

Direct observations, however, can only be done for luminous objects, e.g. galaxies, so we must relate galaxies to the halos. As baryonic physics is more complicated than gravity-only dynamics, simulations of galaxy formation can only be done with the usage of sub-grid physics models. That is, the empirical relations of the feedback from baryonic physics such as supernovae and active galactic nuclei are used in the galaxy formation simulations. State-of-the-art hydrodynamic simulations for the galaxy formation are Illustris [169] and EAGLE [136]. Since these simulations are extremely computationally intensive, the simulation box size cannot be too large (e.g. $\sim 100 h^{-1}$ Mpc for both Illustris and EAGLE). On the other hand, galaxy redshift surveys at present day have sizes of order $1 - 10 h^{-3}$ Gpc³.

Alternatively, we can link the simulated dark matter halos to galaxies using techniques such as semi-analytic models [81], which use the merging histories of dark matter halos, or halo occupation distribution [16, 90], which uses the statistical relation between halos and galaxies. As both methods contain free parameters in the models, these parameters can be

tuned such that multiple properties (e.g. clustering and environmental dependence) of the “simulated” galaxies match the observed ones (see [68] for the recent comparison between semi-analytic models and the observations). These thus provide a practically feasible way to populate galaxies in dark matter halos in the simulations.

The remaining task, especially for the clustering analysis of galaxy redshift surveys, is to generate a large suite of simulations with halos, so they can be used to estimate the covariance matrices of the correlation function or the power spectrum, which are the necessary ingredient for the statistical interpretation of the cosmological information. In particular, the present-day galaxy redshift surveys contain a huge volume, and if high enough mass resolution for halos (which depend on the properties of the observed galaxies) is required, N -body simulation are not practical. Thus, most analyses for the two-point statistics of galaxy surveys use algorithms such that the scheme of solving dynamics is simplified to generate “mock” halos. For example, COLA [159] solves the long-wavelength modes analytically and short-wavelength modes by N -body simulations, and PTHalos [143, 104, 103] is based on the second-order Lagrangian perturbation theory.

As the full N -body simulations are regarded as the standard, we can input identical initial conditions to various codes for generating mock catalogs (halos) and compare the performances. Currently most of the observations now have been focused on the two-point statistics and the mass function, so these algorithms are designed to recover these two quantities. On the other hand, for the three-point function, which is more sensitive to nonlinear effects, more careful and systematic studies are necessary. One recent comparison between major methodologies for generating mock catalogs shows that the differences between N -body simulations and mock generating codes are much larger for the three-point function than for the two-point function [31]. This suggests that at this moment the full N -body simulations are still required to understand the three-point function, or the bispectrum in Fourier space.

The full bispectrum contains triangles formed by different Fourier modes. While the configurations of the bispectrum can be simulated easily if three wavenumbers are similar, the squeezed triangles are more difficult because a large volume is needed to simulate the coupling between long-wavelength modes and small-scale structure formation. In particular, if high enough mass resolution is required, the simulations become computationally demanding. In this dissertation, we provide a solution to this problem. Specifically, we absorb the long-wavelength overdensity into the modified background cosmology (which is the subject in chapter 3) and perform the N -body simulations in the separate universe (which is the subject in section 6.2). This setting simulates how the small-scale structure is affected by a long-wavelength mode. As the box size of the separate universe simulations can be small ($\sim 500 h^{-1}$ Mpc), increasing the mass resolution becomes feasible. This technique is therefore useful for understanding the nonlinear coupling between long and short wavelength modes.

Another computational challenge to the bispectrum analysis is the number of Fourier bins. Specifically, the bispectrum contains all kinds of triangles, so the number of bins is much larger than that of the power spectrum. If the mock catalogs are used to estimate the covariance matrix, many more realizations are required to characterize the bispectrum than

the power spectrum. The lack of realizations of mock catalogs would result in errors in the covariance matrix estimation, and the parameter estimation would be affected accordingly [51]. Therefore, even if there is an algorithm to generate mock catalogs with accurate two- and three-point statistics, we still need a huge amount of them for data analysis, which can be computational challenging. The advantage of the position-dependent power spectrum is that it depends only on one wavenumber, so the number of bins is similar to that of the power spectrum. This means that we only need a reasonable number of realizations (~ 1000) for analyzing the power spectrum and position-dependent power spectrum jointly.

1.3.2 Theory

While N -body simulations are the gold standard for understanding nonlinearity of the large-scale structure, it is impractical to run various simulations with different cosmological parameters or models. It is therefore equally important to develop analytical models so they are easier to compute. We can then use them in the cosmological inferences, e.g. the Markov chain Monte Carlo methods.

The most commonly used technique is the perturbation theory approach, in which the fluctuations are assumed to be small so they can be solved recursively (see [17] for a review). For example, in the standard perturbation theory (SPT), the density fluctuations and peculiar velocity fields are assumed to be small. Using this assumption, we can expand the continuity, Euler, and Poisson equations at different orders, and solve the coupled differential equations order by order (see appendix A and [77] for a brief overview on SPT). The SPT power spectrum at the first order contains the product of two first order fluctuations (P_{11}); the next-to-leading order SPT power spectrum contains the products of first and third order fluctuations (P_{13}) as well as two second order fluctuations (P_{22}). A similar approach can be done in Lagrangian space, in which the displacement field mapping the initial (Lagrangian) position to the final (Eulerian) position of fluid element is solved perturbatively [108, 107].

Generally, the perturbation theory approach works well on large scales and at high redshift, where nonlinearity is small. On small scale and at low redshift, the nonlinear effect becomes more prominent, including higher order corrections is thus necessary. However, the nonlinear effect can be so large that even including more corrections does not help. The renormalized perturbation theory (RPT) was introduced to alleviate the problem [41, 18]. Specifically, RPT categorizes the corrections into two kinds: the mode-coupling effects and the renormalization of the propagator (of the gravitational dynamics). Thus, in RPT the corrections for nonlinearity become better defined, and so the agreement with the nonlinear power spectrum extends to smaller scales compared to SPT. Another approach is the effective field theory (EFT) [25]: on large-scale the matter fluid is characterized by parameters such as sound speed and viscosity, and these parameters are determined by the small-scale physics that is described by the Boltzmann equation. In practice, these parameters are measured from N -body simulations with a chosen smoothing radius. As for RPT, EFT also gives better agreement with the nonlinear power spectrum on smaller scales compared to SPT.

A different kind of approach to compute the clustering properties of the large-scale structure is to use some phenomenological models. The well known phenomenological model is the halo model (see [35] for a review), where all matter is assumed to be contained inside halos, which are characterized by the density profile (e.g. NFW profile [118]) and the mass function (e.g. Sheth-Tormen mass function [149]). The matter n -point functions is then the sum of one-halo term (all n positions are in one halo), two-halo term ($(n - 1)$ positions are in one halo and the other one is in a different halo), to n -halo term (n positions are in n different halos). The small-scale nonlinear matter power spectrum should thereby be described by the halo properties, i.e. the one-halo term. Some recent work attempted to extend the halo model to better describe the nonlinear matter power spectrum. For example, in [116], the Zeldovich approximation [173] is added in the two-halo term, and a polynomial function ($A_0 + A_2k^2 + A_4k^4 + \dots$) is added to model the baryonic effects; in [145], the two-halo term with the Zeldovich approximation is connected to the SPT one-loop power spectrum ($P_{11} + P_{13} + P_{22}$), but a more more complicated function is used for the one-halo term.

One can also construct fitting functions based on results of N -body simulations. The most famous fitting functions of the nonlinear matter power spectrum are the halofit prescription [152] and the Coyote emulator [70]. More specifically, the Coyote emulator was constructed with a suite of N -body simulations with a chosen range of cosmological parameters (e.g. Ω_b, Ω_m). Then, the power spectrum is computed based on the interpolation of the input cosmological parameters. Thus, the apparent limitation of these simulation-calibrated fitting formulae is that they are only reliable within limited range of cosmological parameters and restricted cosmological models.

Similar to that of simulations, most of the theory work has been focused on precise description of nonlinearity of the matter power spectrum, while relatively few work has been devoted to investigate nonlinearity of the bispectrum. Therefore, the matter bispectrum is normally computed at the SPT tree-level, i.e. the product of two first order fluctuations and a second order fluctuation. Some studies [140, 64, 63] considered nonlinearity of the bispectrum by replacing the SPT kernel with fitting formulae containing some parameters, which are then obtained by fitting to N -body simulations. These models, however, lack the theoretical foundation, and it is unclear how the fitting parameters would depend on the cosmological parameters.

In this dissertation, we provide a semi-analytical model for describing the bispectrum in the squeezed configurations. Specifically, we show that the real-space angle-average squeezed-limit bispectrum is the response of the power spectrum to an isotropically infinitely long-wavelength overdensity. Due to the presence of this overdensity, the background cosmology is modified, and the small-scale power spectrum evolves as if matter is in the separate universe. In chapter 4, we show it is straightforward to combine the separate universe approach and the power spectrum computed from perturbation theory approach, phenomenological models, or simulation-calibrated fitting formulae. More importantly, the results of the separate universe approach agree better with the N -body simulation measurements in the squeezed limit than that of the real-space bispectrum fitting formula. In chapter 6, we generalize the separate universe approach to the response of the small-scale

power spectrum to m infinitely long-wavelength overdensities for $m \leq 3$. As expected, this response is related to the squeezed-limit $(m+2)$ -point function with a specific configuration shown in figure 6.1. The separate universe approach is thus extremely useful for modeling the squeezed-limit n -point functions, and its analytical form can be added to the fitting formulae.

As future galaxy surveys contain data with unprecedented amount and quality which can be used to test our understanding of gravity and the physics of inflation, accurate theoretical model, especially for the bispectrum, is required to achieve the goal. While the full bispectrum contains various triangles formed by different Fourier modes, in this dissertation we present the theoretical model specifically for the squeezed triangles, so more work needs to be done for the other configurations.

Chapter 2

Position-dependent two-point statistics

2.1 In Fourier space

2.1.1 Position-dependent power spectrum

Consider a density fluctuation field, $\delta(\mathbf{r})$, in a survey (or simulation) of volume V_r . The mean overdensity of this volume vanishes by construction, i.e.

$$\bar{\delta} = \frac{1}{V_r} \int_{V_r} d^3r \delta(\mathbf{r}) = 0 . \quad (2.1)$$

The global power spectrum of this volume can be estimated as

$$\hat{P}(\mathbf{k}) = \frac{1}{V_r} |\delta(\mathbf{k})|^2 , \quad (2.2)$$

where $\delta(\mathbf{k})$ is the Fourier transform of $\delta(\mathbf{r})$.

We now identify a subvolume V_L centered at \mathbf{r}_L . The mean overdensity of this subvolume is

$$\bar{\delta}(\mathbf{r}_L) = \frac{1}{V_L} \int_{V_L} d^3r \delta(\mathbf{r}) = \frac{1}{V_L} \int d^3r \delta(\mathbf{r}) W(\mathbf{r} - \mathbf{r}_L) , \quad (2.3)$$

where $W(\mathbf{r})$ is the window function. For simplicity and a straightforward application to the N -body simulation box, throughout this dissertation we use a cubic window function given by

$$W(\mathbf{r}) = W_L(\mathbf{r}) = \prod_{i=1}^3 \theta(r_i), \quad \theta(r_i) = \begin{cases} 1, & |r_i| \leq L/2, \\ 0, & \text{otherwise} . \end{cases} \quad (2.4)$$

where L is the side length of V_L . The results are not sensitive to the exact choice of the window function, provided that the scale of interest is much smaller than L . While $\bar{\delta} = 0$, $\bar{\delta}(\mathbf{r}_L)$ is non-zero in general. In other words, if $\bar{\delta}(\mathbf{r}_L)$ is positive (negative), then this subvolume is overdense (underdense) with respect to the mean density in V_r .

Similar to the definition of the global power spectrum in V_r , we define the position-dependent power spectrum in V_L as

$$\hat{P}(\mathbf{k}, \mathbf{r}_L) \equiv \frac{1}{V_L} |\delta(\mathbf{k}, \mathbf{r}_L)|^2, \quad (2.5)$$

where

$$\delta(\mathbf{k}, \mathbf{r}_L) \equiv \int_{V_L} d^3r \delta(\mathbf{r}) e^{-i\mathbf{r}\cdot\mathbf{k}} \quad (2.6)$$

is the *local* Fourier transform of the density fluctuation field. The integral ranges over the subvolume centered at \mathbf{r}_L . With this quantity, the mean density perturbation in the subvolume centered at \mathbf{r}_L is given by

$$\bar{\delta}(\mathbf{r}_L) = \frac{1}{V_L} \delta(\mathbf{k} = 0, \mathbf{r}_L). \quad (2.7)$$

One can use the window function W_L to extend the integration boundaries to infinity as

$$\delta(\mathbf{k}, \mathbf{r}_L) = \int d^3r \delta(\mathbf{r}) W_L(\mathbf{r} - \mathbf{r}_L) e^{-i\mathbf{r}\cdot\mathbf{k}} = \int \frac{d^3q}{(2\pi)^3} \delta(\mathbf{k} - \mathbf{q}) W_L(\mathbf{q}) e^{-i\mathbf{r}_L\cdot\mathbf{q}}, \quad (2.8)$$

where $W_L(\mathbf{q}) = L^3 \prod_{i=1}^3 \text{sinc}(q_i L/2)$ is the Fourier transform of the window function and $\text{sinc}(x) = \sin(x)/x$. Therefore, the position-dependent power spectrum of the subvolume V_L centered at \mathbf{r}_L is

$$\hat{P}(\mathbf{k}, \mathbf{r}_L) = \frac{1}{V_L} \int \frac{d^3q_1}{(2\pi)^3} \int \frac{d^3q_2}{(2\pi)^3} \delta(\mathbf{k} - \mathbf{q}_1) \delta(-\mathbf{k} - \mathbf{q}_2) W_L(\mathbf{q}_1) W_L(\mathbf{q}_2) e^{-i\mathbf{r}_L\cdot(\mathbf{q}_1 + \mathbf{q}_2)}. \quad (2.9)$$

2.1.2 Integrated bispectrum

The correlation between $\hat{P}(\mathbf{k}, \mathbf{r}_L)$ and $\bar{\delta}(\mathbf{r}_L)$ is given by

$$\begin{aligned} \langle \hat{P}(\mathbf{k}, \mathbf{r}_L) \bar{\delta}(\mathbf{r}_L) \rangle &= \frac{1}{V_L^2} \int \frac{d^3q_1}{(2\pi)^3} \int \frac{d^3q_2}{(2\pi)^3} \int \frac{d^3q_3}{(2\pi)^3} \langle \delta(\mathbf{k} - \mathbf{q}_1) \delta(-\mathbf{k} - \mathbf{q}_2) \delta(-\mathbf{q}_3) \rangle \\ &\quad \times W_L(\mathbf{q}_1) W_L(\mathbf{q}_2) W_L(\mathbf{q}_3) e^{-i\mathbf{r}_L\cdot(\mathbf{q}_1 + \mathbf{q}_2 + \mathbf{q}_3)}, \end{aligned} \quad (2.10)$$

where $\langle \rangle$ denotes the ensemble average over many universes. In the case of a simulation or an actual survey, the average is taken instead over all the subvolumes in the simulation or the survey volume. Through the definition of the bispectrum, $\langle \delta(\mathbf{q}_1) \delta(\mathbf{q}_2) \delta(\mathbf{q}_3) \rangle = B(\mathbf{q}_1, \mathbf{q}_2, \mathbf{q}_3) (2\pi)^3 \delta_D(\mathbf{q}_1 + \mathbf{q}_2 + \mathbf{q}_3)$ where δ_D is the Dirac delta function, eq. (2.10) can be rewritten as

$$\begin{aligned} \langle \hat{P}(\mathbf{k}, \mathbf{r}_L) \bar{\delta}(\mathbf{r}_L) \rangle &= \frac{1}{V_L^2} \int \frac{d^3q_1}{(2\pi)^3} \int \frac{d^3q_3}{(2\pi)^3} B(\mathbf{k} - \mathbf{q}_1, -\mathbf{k} + \mathbf{q}_1 + \mathbf{q}_3, -\mathbf{q}_3) \\ &\quad \times W_L(\mathbf{q}_1) W_L(-\mathbf{q}_1 - \mathbf{q}_3) W_L(\mathbf{q}_3) \\ &\equiv iB_L(\mathbf{k}). \end{aligned} \quad (2.11)$$

As anticipated, the correlation of the position-dependent power spectrum and the local mean density perturbation is given by an integral of the bispectrum, and we will therefore refer to this quantity as the *integrated bispectrum*, $iB_L(\mathbf{k})$.

As expected from homogeneity, the integrated bispectrum is independent of the location (\mathbf{r}_L) of the subvolumes. Moreover, for an isotropic window function and bispectrum, the result is also independent of the direction of \mathbf{k} . The cubic window function eq. (2.4) is of course not entirely spherically symmetric,¹ and there is a residual dependence on \hat{k} in eq. (2.11). In the following, we will focus on the angle average of eq. (2.11),

$$\begin{aligned} iB_L(k) &\equiv \int \frac{d^2\hat{k}}{4\pi} iB(\mathbf{k}) = \left\langle \left(\int \frac{d^2\hat{k}}{4\pi} \hat{P}(\mathbf{k}, \mathbf{r}_L) \right) \bar{\delta}(\mathbf{r}_L) \right\rangle \\ &= \frac{1}{V_L^2} \int \frac{d^2\hat{k}}{4\pi} \int \frac{d^3q_1}{(2\pi)^3} \int \frac{d^3q_3}{(2\pi)^3} B(\mathbf{k} - \mathbf{q}_1, -\mathbf{k} + \mathbf{q}_1 + \mathbf{q}_3, -\mathbf{q}_3) \\ &\quad \times W_L(\mathbf{q}_1)W_L(-\mathbf{q}_1 - \mathbf{q}_3)W_L(\mathbf{q}_3) . \end{aligned} \quad (2.12)$$

The integrated bispectrum contains integrals of three sinc functions, $\text{sinc}(x)$, which are damped oscillating functions and peak at $|x| \lesssim \pi$. Most of the contribution to the integrated bispectrum thus comes from values of q_1 and q_3 at approximately $1/L$. If the wavenumber \mathbf{k} we are interested in is much larger than $1/L$ (e.g., $L = 300 h^{-1} \text{ Mpc}$ and $k \gtrsim 0.3 h \text{ Mpc}^{-1}$), then the dominant contribution to the integrated bispectrum comes from the bispectrum in squeezed configurations, i.e., $B(\mathbf{k} - \mathbf{q}_1, -\mathbf{k} + \mathbf{q}_1 + \mathbf{q}_3, -\mathbf{q}_3) \rightarrow B(\mathbf{k}, -\mathbf{k}, -\mathbf{q}_3)$ with $q_1 \ll k$ and $q_3 \ll k$.

2.1.3 Linear response function

Consider the following general separable bispectrum,

$$B(\mathbf{k}_1, \mathbf{k}_2, \mathbf{k}_3) = f(\mathbf{k}_1, \mathbf{k}_2)P(k_1)P(k_2) + 2 \text{ cyclic}, \quad (2.13)$$

where $f(\mathbf{k}_1, \mathbf{k}_2) = f(k_1, k_2, \hat{k}_1 \cdot \hat{k}_2)$ is a dimensionless symmetric function of two \mathbf{k} vectors and the angle between them. If f is non-singular as one of the k vectors goes to zero, we can write, to lowest order in q_1/k and q_3/k ,

$$\begin{aligned} B(\mathbf{k} - \mathbf{q}_1, -\mathbf{k} + \mathbf{q}_1 + \mathbf{q}_3, -\mathbf{q}_3) &= f(\mathbf{k} - \mathbf{q}_1, -\mathbf{q}_3)P(|\mathbf{k} - \mathbf{q}_1|)P(q_3) \\ &\quad + f(-\mathbf{k} + \mathbf{q}_1 + \mathbf{q}_3, -\mathbf{q}_3)P(|-\mathbf{k} + \mathbf{q}_1 + \mathbf{q}_3|)P(q_3) \\ &\quad + f(\mathbf{k} - \mathbf{q}_1, -\mathbf{k} + \mathbf{q}_1 + \mathbf{q}_3)P(|\mathbf{k} - \mathbf{q}_1|)P(|-\mathbf{k} + \mathbf{q}_1 + \mathbf{q}_3|) \\ &= 2f(\mathbf{k}, 0)P(k)P(q_3) + f(\mathbf{k}, -\mathbf{k})[P(k)]^2 + \mathcal{O}\left(\frac{q_{1,3}}{k}\right) . \end{aligned} \quad (2.14)$$

¹We choose the cubic subvolumes merely for simplicity. In general one can use any shapes. For example, one may prefer to divide the subvolumes into spheres, which naturally lead to an isotropic integrated bispectrum $iB_L(k)$.

For matter, momentum conservation requires that $f(\mathbf{k}, -\mathbf{k}) = 0$ [126], as can explicitly be verified for the F_2 kernel of perturbation theory. We then obtain

$$\int \frac{d^2 \hat{k}}{4\pi} B(\mathbf{k} - \mathbf{q}_1, -\mathbf{k} + \mathbf{q}_1 + \mathbf{q}_3, -\mathbf{q}_3) = \check{f}(k)P(k)P(q_3) + \mathcal{O}\left(\frac{q_{1,3}}{k}\right)^2, \quad (2.15)$$

where $\check{f}(k) \equiv 2f(0, k)$. Note that the terms linear in $q_{1,3}$ cancel after angular average. Since the window function in real space satisfies $W_L^2(\mathbf{r}) = W_L(\mathbf{r})$, we have

$$\int \frac{d^3 q_1}{(2\pi)^3} W_L(\mathbf{q}_1)W_L(-\mathbf{q}_1 - \mathbf{q}_3) = W_L(\mathbf{q}_3). \quad (2.16)$$

Performing the \mathbf{q}_1 integral in eq. (2.12) then yields

$$iB_L(k) \stackrel{kL \rightarrow \infty}{=} \frac{1}{V_L^2} \int \frac{d^3 q_3}{(2\pi)^3} W_L^2(\mathbf{q}_3)P(q_3)\check{f}(k)P(k) = \sigma_L^2 \check{f}(k)P(k), \quad (2.17)$$

where σ_L^2 is the variance of the density field on the subvolume scale,

$$\sigma_L^2 \equiv \frac{1}{V_L^2} \int \frac{d^3 q_3}{(2\pi)^3} W_L^2(\mathbf{q}_3)P(q_3). \quad (2.18)$$

Eq. (2.17) shows that the integrated bispectrum measures how the small-scale power spectrum, $P(k)$, responds to a large-scale density fluctuation with variance σ_L^2 , with a response function given by $\check{f}(k)$.

An intuitive way to arrive at the same expression is to write the response of the small-scale power spectrum to a large-scale density fluctuation as

$$\hat{P}(\mathbf{k}, \mathbf{r}_L) = P(\mathbf{k})|_{\bar{\delta}=0} + \left. \frac{dP(\mathbf{k})}{d\bar{\delta}} \right|_{\bar{\delta}=0} \bar{\delta}(\mathbf{r}_L) + \dots, \quad (2.19)$$

where we have neglected gradients and higher derivatives of $\bar{\delta}(\mathbf{r}_L)$. We then obtain, to leading order,

$$iB_L(k) = \sigma_L^2 \left. \frac{d \ln P(k)}{d\bar{\delta}} \right|_{\bar{\delta}=0} P(k). \quad (2.20)$$

Comparing this result with eq. (2.17), we find that $\check{f}(k)$ indeed corresponds to the *linear response* of the small-scale power to the large-scale density fluctuation, $d \ln P(k)/d\bar{\delta}$. Inspired by eq. (2.20), we define another quantity, the *normalized integrated bispectrum*,

$$\frac{iB_L(k)}{\sigma_L^2 \hat{P}(k)}. \quad (2.21)$$

This quantity is equal to $\check{f}(k)$ and the linear response function in the limit of $kL \rightarrow \infty$.

For the standard perturbation theory kernel

$$f(\mathbf{k}_1, \mathbf{k}_2) = F_2(\mathbf{k}_1, \mathbf{k}_2) = \frac{5}{7} + \frac{1}{2} \frac{\mathbf{k}_1 \cdot \mathbf{k}_2}{k_1 k_2} \left(\frac{k_1}{k_2} + \frac{k_2}{k_1} \right) + \frac{2}{7} \left(\frac{\mathbf{k}_1 \cdot \mathbf{k}_2}{k_1 k_2} \right)^2, \quad (2.22)$$

in the squeezed limit the integrated bispectrum becomes (see appendix A.2 for the detailed derivation)

$$iB_L(k) \stackrel{kL \rightarrow \infty}{\equiv} \left[\frac{47}{21} - \frac{1}{3} \frac{d \ln P_l(k)}{d \ln k} \right] P_l(k) \sigma_L^2, \quad (2.23)$$

and the response function is

$$\check{f}(k) = \frac{47}{21} - \frac{1}{3} \frac{d \ln P_l(k)}{d \ln k}. \quad (2.24)$$

We shall discuss more details in section 4.2.1.

2.1.4 Integrated bispectrum of various bispectrum models

To evaluate the integrated bispectrum, we insert the bispectrum models into eq. (2.12) and perform the eight-dimensional integral. Because of the high dimensionality of the integral, we use the Monte Carlo integration routine in GNU Scientific Library to numerically evaluate $iB_L(k)$. Let us consider the simplest model of galaxy bispectrum with local-type primordial non-Gaussianity

$$B_g(\mathbf{k}_1, \mathbf{k}_2, \mathbf{k}_3) = b_1^3 B_{\text{SPT}}(\mathbf{k}_1, \mathbf{k}_2, \mathbf{k}_3) + b_1^2 b_2 B_{b_2}(\mathbf{k}_1, \mathbf{k}_2, \mathbf{k}_3) + b_1^3 f_{\text{NL}} B_{f_{\text{NL}}}(\mathbf{k}_1, \mathbf{k}_2, \mathbf{k}_3), \quad (2.25)$$

where b_1 is the linear bias, b_2 is the quadratic nonlinear bias, and f_{NL} is the parametrization for the local-type primordial non-Gaussianity. Note that the scale-dependent bias due to the local type non-Gaussianity [45, 106, 151] is neglected in eq. (2.25), and the latest bispectrum model with primordial non-Gaussianity can be found in [10, 158].

The first two terms of eq. (2.25) are due to the nonlinear gravitational evolution. Specifically, the standard perturbation theory (SPT) with local bias model predicts (see appendix A.2 for detailed derivation)

$$\begin{aligned} B_{\text{SPT}}(\mathbf{k}_1, \mathbf{k}_2, \mathbf{k}_3) &= 2F_2(\mathbf{k}_1, \mathbf{k}_2) P_l(k_1, a) P_l(k_2, a) + 2 \text{cyclic} \\ B_{b_2}(\mathbf{k}_1, \mathbf{k}_2, \mathbf{k}_3) &= P_l(k_1, a) P_l(k_2, a) + 2 \text{cyclic}, \end{aligned} \quad (2.26)$$

where $P_l(k)$ is the linear bispectrum. For the bispectrum of local-type primordial non-Gaussianity, we consider the local ansatz for the primordial scalar potential as [89]

$$\Phi(\mathbf{r}) = \phi(\mathbf{r}) + f_{\text{NL}} [\phi^2(\mathbf{r}) - \langle \phi^2(\mathbf{r}) \rangle], \quad (2.27)$$

where $\phi(\mathbf{r})$ is a Gaussian field, and f_{NL} is a constant characterizing the amplitude of the primordial non-Gaussianity. As the density fluctuations are linked to the scalar potential through the Poisson equation

$$\delta(\mathbf{k}, a) = M(k, a) \Phi(\mathbf{k}), \quad M(k, a) = \frac{2}{3} \frac{D(a)}{H_0^2 \Omega_m} k^2 T(k), \quad (2.28)$$

with $D(a)$ and $T(k)$ being the linear growth factor and the transfer function respectively, in the leading order the primordial non-Gaussianity appears in matter bispectrum as

$$f_{\text{NL}} B_{f_{\text{NL}}}(\mathbf{k}_1, \mathbf{k}_2, \mathbf{k}_3) = 2f_{\text{NL}} M(k_1, a) M(k_2, a) M(k_3, a) [P_\Phi(k_1) P_\Phi(k_2) + 2 \text{cyclic}], \quad (2.29)$$

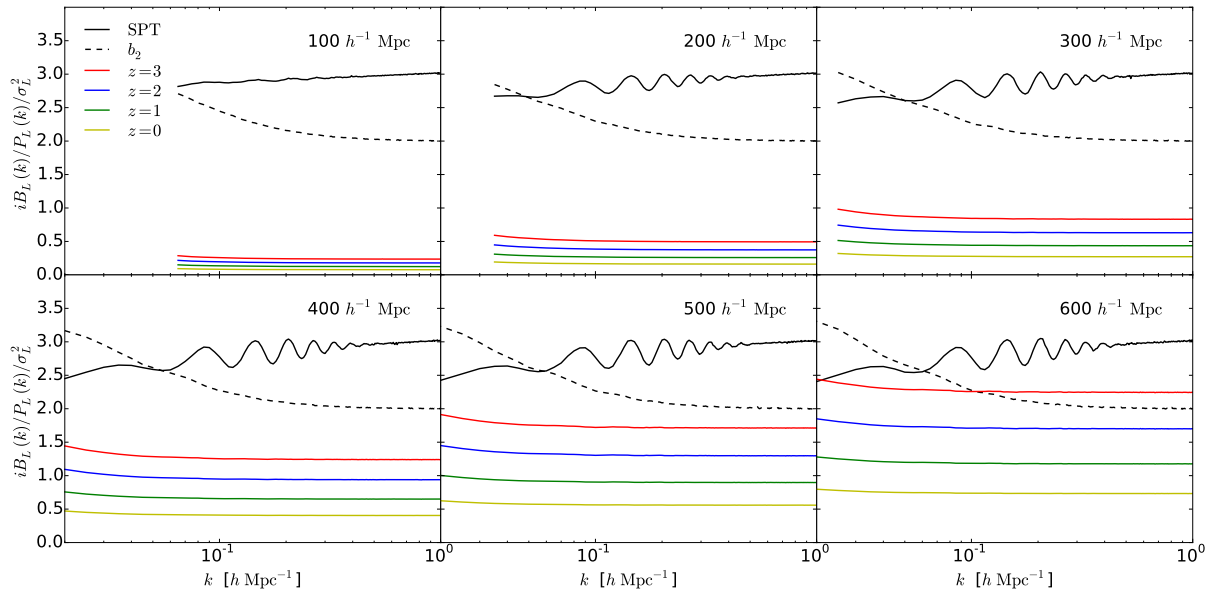


Figure 2.1: Normalized integrated bispectrum in different sizes of subvolumes. The colored lines show non-Gaussian components at different redshifts assuming $f_{\text{NL}} = 50$, while the solid and dashed lines show linear and nonlinear bias components assuming $b_1 = b_2 = 1$. The cut-off at low- k corresponds to the fundamental frequencies of the subvolumes, $2\pi/L$.

where $P_\Phi(k)$ is the power spectrum of the scalar potential.

Figure 2.1 shows the normalized integrated bispectrum, for which we shall denote as ib_L in this section, in different sizes of subvolumes. For the parameters we assume $b_1 = b_2 = 1$ and $f_{\text{NL}} = 50$. We find that contributions from late-time evolution (black solid and dashed lines for $ib_{L,\text{SPT}}(k)$ and $ib_{L,b_2}(k)$, respectively) are redshift-independent, but the ones from primordial non-Gaussianity (colored lines at different redshifts) increase with increasing redshift. This is due to the redshift-dependence in $M(k, a)$. Namely, while $ib_{L,\text{SPT}}(k)$ and $ib_{L,b_2}(k)$ are independent of $D(a)$, $ib_{L,f_{\text{NL}}}(k)$ is proportional to $1/D(a)$. This means that it is more promising to hunt for primordial non-Gaussianity in high-redshift galaxy surveys. We also find that for a given subvolume size $ib_{L,f_{\text{NL}}}(k)$ is fairly scale-independent, as $ib_{L,\text{SPT}}(k)$ and $ib_{L,b_2}(k)$. This is somewhat surprising because when k (the scale of the position-dependent power spectrum) is large we reach the squeezed limit, and this should be the ideal region to search for primordial non-Gaussianity. However, it turns out that what really determines the amplitude of $ib_{L,f_{\text{NL}}}(k)$ is the subvolumes size, as we can see from different panels in figure 2.1. One can understand this by considering the long-wavelength mode, k_l , and the short-wavelength modes, k_s ($k_s \gg k_l$). In the squeezed limit,

$$\begin{aligned}
 B_{f_{\text{NL}}}(k_l, k_s, k_s) &\propto M(k_l)M^2(k_s)[2P_\Phi(k_l)P_\Phi(k_s) + P_\Phi^2(k_s)] \\
 &\propto M(k_l)M^2(k_s)P_\Phi(k_l)P_\Phi(k_s) ,
 \end{aligned}
 \tag{2.30}$$

as $P_\Phi(k) \propto k^{n_s-4}$ with $n_s = 0.95$. Also $M(k) \propto k^2$ and k^0 on large and small scales respectively, hence

$$ib_{L,f_{\text{NL}}}(k) \propto \frac{k_l^{n_s-2} k_s^{n_s-4}}{\sigma_{L,l}^2 M^2(k_s) P_\Phi(k_s)} \propto \frac{k_l^{n_s-2}}{\sigma_{L,l}^2}, \quad (2.31)$$

which is k_s -independent and the amplitude of $ib_{L,f_{\text{NL}}}(k)$ is solely determined by k_l , the subvolume size. This means that to hunt for primordial non-Gaussianity, it is necessary to use different sizes of subvolumes to break the degeneracy between $ib_{L,f_{\text{NL}}}(k)$ and the late-time contributions.

2.2 In configuration space

2.2.1 Position-dependent correlation function

We now turn to the position-dependent two-point statistics in configuration space, i.e. position-dependent correlation function. Consider a density fluctuation field, $\delta(\mathbf{r})$, in a survey (or simulation) volume V_r . The global two-point function can be estimated as

$$\hat{\xi}(\mathbf{r}) = \frac{1}{V_r} \int_{V_r} d^3x \delta(\mathbf{r} + \mathbf{x}) \delta(\mathbf{x}). \quad (2.32)$$

Similarly, we define the position-dependent correlation function of a cubic subvolume V_L centered at \mathbf{r}_L to be

$$\begin{aligned} \hat{\xi}(\mathbf{r}, \mathbf{r}_L) &= \frac{1}{V_L} \int_{\mathbf{x}, \mathbf{r} + \mathbf{x} \in V_L} d^3x \delta(\mathbf{r} + \mathbf{x}) \delta(\mathbf{x}) \\ &= \frac{1}{V_L} \int d^3x \delta(\mathbf{r} + \mathbf{x}) \delta(\mathbf{x}) W_L(\mathbf{r} + \mathbf{x} - \mathbf{r}_L) W_L(\mathbf{x} - \mathbf{r}_L), \end{aligned} \quad (2.33)$$

where $W_L(\mathbf{r})$ is the window function given in eq. (2.4). In this dissertation, we consider only the angle-averaged position-dependent correlation function (i.e. monopole) defined by

$$\hat{\xi}(r, \mathbf{r}_L) = \int \frac{d^2\hat{r}}{4\pi} \hat{\xi}(\mathbf{r}, \mathbf{r}_L) = \frac{1}{V_L} \int \frac{d^2\hat{r}}{4\pi} \int d^3x \delta(\mathbf{r} + \mathbf{x}) \delta(\mathbf{x}) W_L(\mathbf{r} + \mathbf{x} - \mathbf{r}_L) W_L(\mathbf{x} - \mathbf{r}_L). \quad (2.34)$$

Again, while the overdensity in the entire volume $\bar{\delta} = \int_{V_r} d^3r \delta(\mathbf{r})$ is zero by construction, the overdensity in the subvolume $\bar{\delta}(\mathbf{r}_L) = \int_{V_L} d^3r \delta(\mathbf{r}) = \int_{V_r} d^3r \delta(\mathbf{r}) W_L(\mathbf{r} - \mathbf{r}_L)$ is in general non-zero.

The ensemble average of eq. (2.34) is not equal to $\xi(r)$. Specifically,

$$\begin{aligned} \langle \hat{\xi}(r, \mathbf{r}_L) \rangle &= \frac{1}{V_L} \int \frac{d^2\hat{r}}{4\pi} \int d^3x \langle \delta(\mathbf{r} + \mathbf{x}) \delta(\mathbf{x}) \rangle W_L(\mathbf{r} + \mathbf{x} - \mathbf{r}_L) W_L(\mathbf{x} - \mathbf{r}_L) \\ &= \xi(r) \frac{1}{V_L} \int \frac{d^2\hat{r}}{4\pi} \int d^3x' W_L(\mathbf{r} + \mathbf{x}') W_L(\mathbf{x}') \equiv \xi(r) f_{L,\text{bndry}}(r), \end{aligned} \quad (2.35)$$

where $f_{L,\text{bdry}}(r)$ is the boundary effect due to the finite size of the subvolume. While $f_{L,\text{bdry}}(r) = 1$ for $r = 0$, the boundary effect becomes larger for larger separations. The boundary effect can be computed by the five-dimensional integral in eq. (2.35). Alternatively, it can be evaluated by the ratio of the number of the random particle pairs of a given separation in a finite volume to that in an infinite volume. We have evaluated $f_{L,\text{bdry}}(r)$ in both ways, and the results are in an excellent agreement.

As the usual two-point function estimators based on pair counting (such as Landy-Szalay estimator which will be discussed in section 5.1.2) or grid counting (which will be discussed in appendix C) do not contain the boundary effect, when we compare the measurements to the model which is calculated based on eq. (2.34), we shall divide the model by $f_{L,\text{bdry}}(r)$ to correct for the boundary effect.

2.2.2 Integrated three-point function

The correlation between $\hat{\xi}(r, \mathbf{r}_L)$ and $\bar{\delta}(\mathbf{r}_L)$ is given by

$$\begin{aligned} \langle \hat{\xi}(r, \mathbf{r}_L) \bar{\delta}(\mathbf{r}_L) \rangle &= \frac{1}{V_L^2} \int \frac{d^2 \hat{r}}{4\pi} \int d^3 x_1 \int d^3 x_2 \langle \delta(\mathbf{r} + \mathbf{x}_1) \delta(\mathbf{x}_1) \delta(\mathbf{x}_2) \rangle \\ &\quad \times W_L(\mathbf{r} + \mathbf{x}_1 - \mathbf{r}_L) W_L(\mathbf{x}_1 - \mathbf{r}_L) W_L(\mathbf{x}_2 - \mathbf{r}_L) \\ &= \frac{1}{V_L^2} \int \frac{d^2 \hat{r}}{4\pi} \int d^3 x_1 \int d^3 x_2 \zeta(\mathbf{r} + \mathbf{x}_1 + \mathbf{r}_L, \mathbf{x}_1 + \mathbf{r}_L, \mathbf{x}_2 + \mathbf{r}_L) \\ &\quad \times W_L(\mathbf{r} + \mathbf{x}_1) W_L(\mathbf{x}_1) W_L(\mathbf{x}_2), \end{aligned} \quad (2.36)$$

where $\zeta(\mathbf{r}_1, \mathbf{r}_2, \mathbf{r}_3) \equiv \langle \delta(\mathbf{r}_1) \delta(\mathbf{r}_2) \delta(\mathbf{r}_3) \rangle$ is the three-point correlation function. Because of the assumption of homogeneity and isotropy, the three-point function depends only on the separations $|\mathbf{r}_i - \mathbf{r}_j|$ for $i \neq j$, and so $\langle \hat{\xi}(r, \mathbf{r}_L) \bar{\delta}(\mathbf{r}_L) \rangle$ is independent of \mathbf{r}_L . Furthermore, as the right-hand-side of eq. (2.36) is an integral of the three-point function, we will refer to this quantity as the ‘‘integrated three-point function,’’ $i\zeta_L(r) \equiv \langle \hat{\xi}(r, \mathbf{r}_L) \bar{\delta}(\mathbf{r}_L) \rangle$.

$i\zeta_L(r)$ can be computed if $\zeta(\mathbf{r}_1, \mathbf{r}_2, \mathbf{r}_3)$ is known. For example, SPT with the local bias model at the tree level in real space gives

$$\zeta(r) = b_1^3 \zeta_{\text{SPT}}(r) + b_1^2 b_2 \zeta_{b_2}(r), \quad (2.37)$$

where ζ_{SPT} and ζ_{b_2} are given below. Here, b_1 and b_2 are the linear and quadratic (nonlinear) bias parameters, respectively. Because of the high dimensionality of the integral, we use the Monte Carlo integration routine in the GNU Scientific Library to numerically evaluate the eight-dimensional integral for $i\zeta_L(r)$.

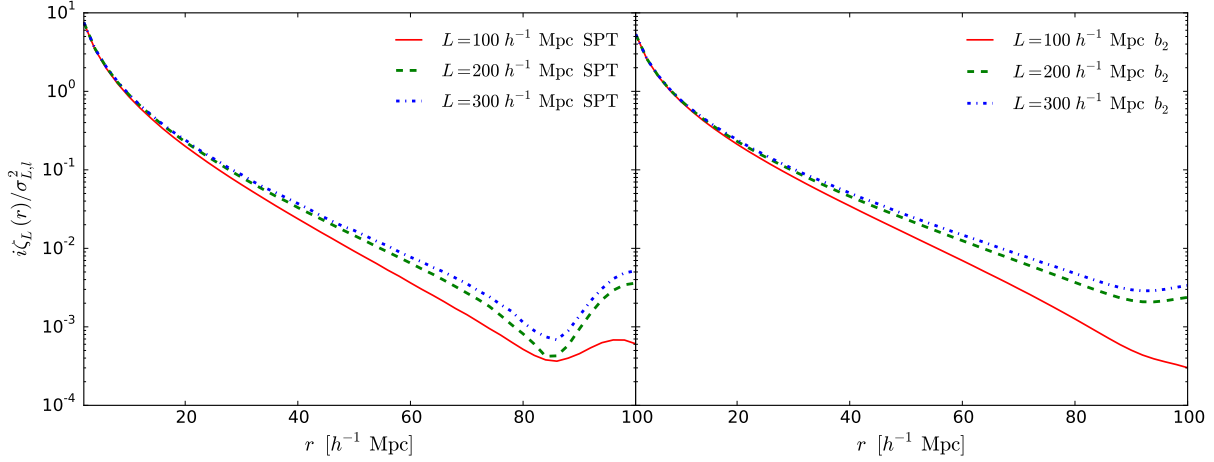


Figure 2.2: Normalized $i\zeta_{L,\text{SPT}}$ (left) and $i\zeta_{L,b_2}$ (right) for $L = 100 h^{-1}$ Mpc (red solid), $200 h^{-1}$ Mpc (green dashed), and $300 h^{-1}$ Mpc (blue dotted) at $z = 0$.

The first term, ζ_{SPT} , is given by [79, 12]

$$\begin{aligned} \zeta_{\text{SPT}}(\mathbf{r}_1, \mathbf{r}_2, \mathbf{r}_3) &= \frac{10}{7} \xi_l(r_{12}) \xi_l(r_{23}) + \mu_{12,23} [\xi'_l(r_{12}) \phi'_l(r_{23}) + \xi'_l(r_{23}) \phi'_l(r_{12})] \\ &+ \frac{4}{7} \left\{ -3 \frac{\phi'_l(r_{12}) \phi'_l(r_{23})}{r_{12} r_{13}} - \frac{\xi_l(r_{12}) \phi'_l(r_{23})}{r_{23}} - \frac{\xi_l(r_{23}) \phi'_l(r_{12})}{r_{12}} \right. \\ &\quad \left. + \mu_{12,23}^2 \left[\xi_l(r_{12}) + \frac{3\phi'_l(r_{12})}{r_{12}} \right] \left[\xi_l(r_{23}) + \frac{3\phi'_l(r_{23})}{r_{23}} \right] \right\} \\ &+ 2 \text{ cyclic} , \end{aligned} \quad (2.38)$$

where $r_{12} = |\mathbf{r}_1 - \mathbf{r}_2|$, $\mu_{12,23}$ is the cosine between \mathbf{r}_{12} and \mathbf{r}_{23} , ' refers to the spatial derivative, and

$$\xi_l(r) \equiv \int \frac{dk}{2\pi^2} k^2 P_l(k) \text{sinc}(kr), \quad \phi_l(r) \equiv \int \frac{dk}{2\pi^2} P_l(k) \text{sinc}(kr), \quad (2.39)$$

with $P_l(k)$ being the linear matter power spectrum. The subscript l denotes the quantities in the linear regime. The second term, ζ_{b_2} , is the nonlinear local bias three-point function. The nonlinear bias three-point function is then

$$\zeta_{b_2}(\mathbf{r}_1, \mathbf{r}_2, \mathbf{r}_3) = \xi_l(r_{12}) \xi_l(r_{23}) + 2 \text{ cyclic} . \quad (2.40)$$

Note that ζ_{SPT} and ζ_{b_2} are simply Fourier transform of B_{SPT} and B_{b_2} respectively, as shown in eq. (2.26).

Figure 2.2 shows the scale-dependencies of $i\zeta_{L,\text{SPT}}$ and $i\zeta_{L,b_2}$ at $z = 0$ with $P_l(k)$ computed by CLASS [94]. We normalize $i\zeta_L(r)$ by $\sigma_{L,l}^2$, where

$$\sigma_{L,l}^2 \equiv \langle \bar{\delta}_l(\mathbf{r}_L)^2 \rangle = \frac{1}{V_L^2} \int \frac{d^3k}{(2\pi)^3} P_l(k) |W_L(\mathbf{k})|^2 , \quad (2.41)$$

is the variance of the linear density field in the subvolume V_L . The choice of this normalization is similar to that of the integrated bispectrum as discussed in section 2.1.2, and we shall discuss more details in section 2.2.4. We find that the scale-dependencies of $i\zeta_{L,\text{SPT}}(r)$ and $i\zeta_{L,b_2}(r)$ are similar especially on small scales. This is because the scale-dependence of the bispectrum in the squeezed limit is (see appendix of appendix A.3)

$$B_{\text{SPT}} \rightarrow \left[\frac{68}{21} - \frac{1}{3} \frac{d \ln k^3 P_l(k)}{d \ln k} \right] P_l(k) P_l(q) , \quad B_{b_2} \rightarrow 2P_l(k) P_l(q) , \quad (2.42)$$

where k and q are the short- and long-wavelength modes, respectively. For a power-law power spectrum without features, the squeezed-limit B_{SPT} and B_{b_2} have exactly the same scale dependence and cannot be distinguished. This results in a significant residual degeneracy between b_1 and b_2 , and will be discussed in chapter 5 where we measure the integrated three-point function of real data and fit to the models. When r is small, $i\zeta_L(r)/\sigma_{L,l}^2$ becomes independent of the subvolume size. We derive this feature when we discuss the squeezed limit, where $r \ll L$, in section 2.2.4.

2.2.3 Connection to the integrated bispectrum

Fourier transforming the density fields, the integrated three-point function can be written as

$$\begin{aligned} i\zeta_L(\mathbf{r}) &= \frac{1}{V_L^2} \int \frac{d^3 q_1}{(2\pi)^3} \cdots \int \frac{d^3 q_6}{(2\pi)^3} (2\pi)^9 \delta_D(\mathbf{q}_1 + \mathbf{q}_2 + \mathbf{q}_3) \delta_D(\mathbf{q}_1 + \mathbf{q}_2 + \mathbf{q}_4 + \mathbf{q}_5) \delta_D(\mathbf{q}_3 + \mathbf{q}_6) \\ &\quad \times B(\mathbf{q}_1, \mathbf{q}_2, \mathbf{q}_3) W_L(\mathbf{q}_4) W_L(\mathbf{q}_5) W_L(\mathbf{q}_6) e^{i[\mathbf{r} \cdot (\mathbf{q}_1 + \mathbf{q}_4) - \mathbf{r}_L \cdot (\mathbf{q}_4 + \mathbf{q}_5 + \mathbf{q}_6)]} \\ &= \int \frac{d^3 k}{(2\pi)^3} iB_L(\mathbf{k}) e^{i\mathbf{r} \cdot \mathbf{k}} , \end{aligned} \quad (2.43)$$

and it is simply the Fourier transform of the integrated bispectrum. Similarly, the angle-averaged integrated three-point function is related to the angle-averaged integrated bispectrum (eq. (2.12)) as

$$i\zeta_L(r) = \int \frac{k^2 dk}{2\pi^2} iB_L(k) \text{sinc}(kr) . \quad (2.44)$$

In chapter 5, we measure the integrated three-point function of real data, and thus we need the model for $i\zeta_L(r)$ in redshift space. Unlike the three-point function in real space (eq. (2.38) and eq. (2.40)), we do not have the analytical expression for redshift-space three-point function in configuration space. Since the integrated three-point function is the Fourier transform of the integrated bispectrum, we compute the redshift-space integrated three-point function by first evaluating the redshift-space angle-averaged integrated bispectrum with eq. (2.12)², and then performing the one-dimensional integral eq. (2.44). This operation thus requires a nine-dimensional integral.

²The explicit expression of the SPT redshift-space bispectrum is in appendix A.2.

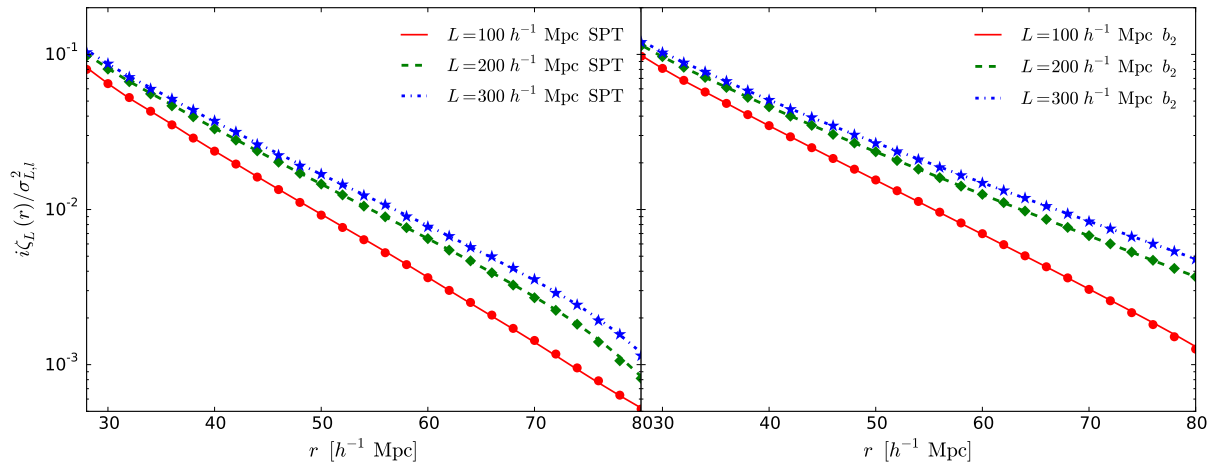


Figure 2.3: Normalized $i\zeta_{L,\text{SPT}}$ (left) and $i\zeta_{L,b_2}$ (right) for $L = 100 h^{-1}$ Mpc (red solid), $200 h^{-1}$ Mpc (green dashed), and $300 h^{-1}$ Mpc (blue dotted) at $z = 0$ evaluated from Fourier space of a nine-dimensional integral (eq. (2.12) and eq. (2.44)). The same quantities evaluated from configuration space of an eight-dimensional integral (eq. (2.36)) are shown with symbols.

To check the precision of numerical integration, we compare the results from the eight-dimensional integral in eq. (2.36) with the nine-dimensional integral eq. (2.12) and eq. (2.44) for both $i\zeta_{L,\text{SPT}}$ and $i\zeta_{L,b_2}$. As the latter gives a noisy result, we apply a Savitzky-Golay filter (with window size 9 and polynomial order 4) six times, and the results are shown in figure 2.3. We find that, on the scales of interest ($30 h^{-1}$ Mpc $\leq r \leq 78 h^{-1}$ Mpc, which we will justify in section 5.1.3), both results are in agreement to within 2%. As the current uncertainty on the measured integrated correlation function presented in this dissertation is of order 10% (see section 5.2 for more details), the numerical integration yields sufficiently precise results.

2.2.4 Squeezed limit

In the squeezed limit, where the separation of the position-dependent correlation function is much smaller than the size of the subvolume ($r \ll L$), the integrated three-point function has a straightforward physical interpretation, as for the integrated bispectrum. In this case, the mean density in the subvolume acts effectively as a constant “background” density (see chapter 3 for more details). Consider the position-dependent correlation function, $\hat{\xi}(\mathbf{r}, \mathbf{r}_L)$, is measured in a subvolume with overdensity $\bar{\delta}(\mathbf{r}_L)$. If the overdensity is small, we may Taylor expand $\hat{\xi}(\mathbf{r}, \mathbf{r}_L)$ in orders of $\bar{\delta}$ as

$$\hat{\xi}(\mathbf{r}, \mathbf{r}_L) = \xi(\mathbf{r})|_{\bar{\delta}=0} + \left. \frac{d\xi(\mathbf{r})}{d\bar{\delta}} \right|_{\bar{\delta}=0} \bar{\delta} + \mathcal{O}(\bar{\delta}^2). \quad (2.45)$$

The integrated three-point function in the squeezed limit is then, at leading order in the variance $\langle \bar{\delta}^2 \rangle$, given by

$$i\zeta_L(\mathbf{r}) = \langle \hat{\xi}(\mathbf{r}, \mathbf{r}_L) \bar{\delta}(\mathbf{r}_L) \rangle = \left. \frac{d\xi(\mathbf{r})}{d\bar{\delta}} \right|_{\bar{\delta}=0} \langle \bar{\delta}^2 \rangle + \mathcal{O}(\bar{\delta}^3). \quad (2.46)$$

As $\langle \bar{\delta}^2 \rangle = \sigma_L^2$, $i\zeta_L(\mathbf{r})$ normalized by σ_L^2 is $d\xi(\mathbf{r})/d\bar{\delta}$ at leading order, which is the linear response of the correlation function to the overdensity. Note that in eq. (2.46) there is no dependence on the subvolume size apart from σ_L^2 , as shown also by the asymptotic behavior of the solid lines in figure 2.2 for $r \rightarrow 0$.

As $i\zeta_L(r)$ is the Fourier transform of $iB_L(k)$, the response of the correlation function, $d\xi(r)/d\bar{\delta}$, is also the Fourier transform of the response of the power spectrum, $dP(k)/d\bar{\delta}$. For example, we can calculate the response of the linear matter correlation function, $d\xi_l(r)/d\bar{\delta}$, by Fourier transforming the response of the linear power spectrum, which is given in eqs. (2.23)–(2.24). In figure 2.4, we compare the normalized $i\zeta_{L,\text{SPT}}(r)$ with $d\xi_l(r)/d\bar{\delta}$. Due to the large dynamic range of the correlation function, we divide all the predictions by $\xi(r)$. As expected, the smaller the subvolume size, the smaller the r for $i\zeta_{L,\text{SPT}}(r)$ to be close to $[1/\xi_l(r)][d\xi_l(r)/d\bar{\delta}]$, i.e., reaching the squeezed limit. Specifically, for $100 h^{-1}$ Mpc, $200 h^{-1}$ Mpc, and $300 h^{-1}$ Mpc subvolumes, the squeezed limit is reached to 10% level at $r \sim 10 h^{-1}$ Mpc, $18 h^{-1}$ Mpc, and $25 h^{-1}$ Mpc, respectively.

2.2.5 Shot noise

If the density field is traced by discrete particles, $\delta_d(\mathbf{r})$, then the three-point function contains a shot noise contribution given by

$$\begin{aligned} \langle \delta_d(\mathbf{r}_1) \delta_d(\mathbf{r}_2) \delta_d(\mathbf{r}_3) \rangle &= \langle \delta(\mathbf{r}_1) \delta(\mathbf{r}_2) \delta(\mathbf{r}_3) \rangle \\ &+ \left[\frac{\langle \delta(\mathbf{r}_1) \delta(\mathbf{r}_2) \rangle}{\bar{n}(\mathbf{r}_3)} \delta_D(\mathbf{r}_1 - \mathbf{r}_3) + 2 \text{ cyclic} \right] + \frac{\delta_D(\mathbf{r}_1 - \mathbf{r}_2) \delta_D(\mathbf{r}_1 - \mathbf{r}_3)}{\bar{n}(\mathbf{r}_2) \bar{n}(\mathbf{r}_3)}, \end{aligned} \quad (2.47)$$

where $\bar{n}(r)$ is the mean number density of the discrete particles. The shot noise can be safely neglected for the three-point function because it only contributes when $\mathbf{r}_1 = \mathbf{r}_2$, $\mathbf{r}_1 = \mathbf{r}_3$, or $\mathbf{r}_2 = \mathbf{r}_3$. On the other hand, the shot noise of the integrated three-point function can be computed by inserting eq. (2.47) into eq. (2.36), which yields

$$i\zeta_{\text{shot}}(r) = \xi(r) \frac{1}{V_L^2} \int \frac{d^2 \hat{r}}{4\pi} \int d^3 x \left[\frac{1}{\bar{n}(\mathbf{x} + \mathbf{r} + \mathbf{r}_L)} + \frac{1}{\bar{n}(\mathbf{x} + \mathbf{r}_L)} \right] W_L(\mathbf{x} + \mathbf{r}) W_L(\mathbf{x}), \quad (2.48)$$

where we have assumed $r > 0$. If we further assume that the mean number density is constant, then the shot noise of the integrated three-point function can be simplified as

$$i\zeta_{\text{shot}}(r) = 2\xi(r) \frac{1}{V_L \bar{n}} f_{L,\text{bndry}}(r). \quad (2.49)$$

³If $\bar{\delta} = \bar{\delta}_l$ then $\sigma_L^2 = \sigma_{L,l}^2$. But $\bar{\delta}$ can in principle be nonlinear or the mean overdensity of the biased tracers, so here we denote the variance to be σ_L^2 .

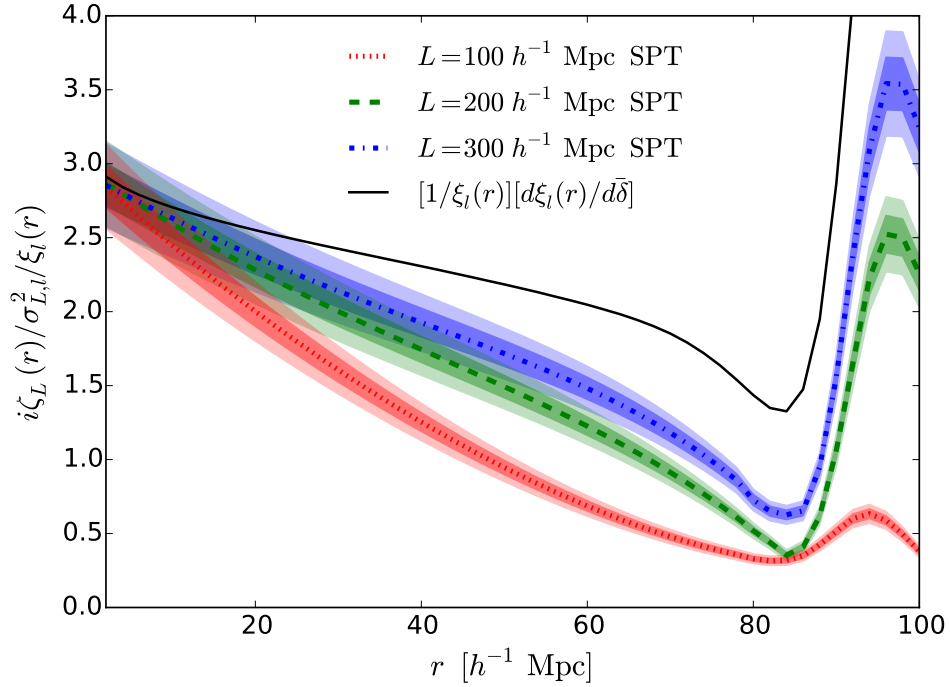


Figure 2.4: The linear response function $[1/\xi_L(r)][d\xi_L(r)/d\bar{\delta}]$ (black solid) and the normalized $i\zeta_{L,\text{SPT}}(r)$ for $L = 100 h^{-1}$ Mpc (red dotted), $200 h^{-1}$ Mpc (green dashed), and $300 h^{-1}$ Mpc (blue dot-dashed). The light and dark bands correspond to $\pm 5\%$ and $\pm 10\%$ of the predictions, respectively.

For the measurements of PTHalos mock catalogs and the BOSS DR10 CMASS sample, the shot noise is subdominant (less than 7% of the total signal on the scales of interest).

Chapter 3

Separate universe picture

Mode coupling plays a fundamental role in cosmology. Even if the initial density fluctuations generated by inflation are perfectly Gaussian, the subsequent nonlinear gravitational evolution couples long and short wavelength modes as well as generates non-zero bispectrum. A precise understanding of how a long-wavelength density affects the small-scale structure formation gravitationally is necessary, especially for extracting the signal of bispectrum due to primordial non-Gaussianity.

A useful way to describe the behavior of the small-scale structure formation in an overdense (underdense) environment is the separate universe picture [13, 112, 150, 11, 147, 97, 98, 43, 44]. Imagine a local observer who can only access to the comoving distance of the short-wavelength modes $\sim 1/k_S$. If there exists a long-wavelength mode such that $1/k_L \gg 1/k_S$, then the local small-scale physics would be interpreted with a Friedmann-Lemaître-Robertson-Walker (FLRW) background [93]. That is, in the separate universe picture, the overdensity is absorbed into the modified background cosmology, and the small-scale structure formation evolves in this modified cosmology.

The separate universe picture can be proven from the general relativistic approach: one locally constructs a frame, Conformal Fermi Coordinates, such that it is valid across the scale of a coarse-grained universe Λ^{-1} ($k_L < \Lambda < k_S$) at all times [123, 43, 44]. In Conformal Fermi Coordinates, the small-scale structure around an observer is interpreted as evolving in FLRW universe modified by the long-wavelength overdensity. The separate universe picture is restricted to scales larger than the sound horizons of all fluid components, where all fluid components are comoving.

In the presence of $\bar{\delta}$, the background cosmology changes, and the position-dependent power spectrum is affected accordingly. Since the response of the position-dependent power spectrum to the long-wavelength overdensity, $[dP(k)/d\bar{\delta}]_{\bar{\delta}=0}$, can be related to the bispectrum in the squeezed configurations, the separate universe picture is useful for modeling the squeezed-limit bispectrum generated by nonlinear gravitational evolution. Not only this is conceptually straightforward to interpret, but it also captures more nonlinear effects than the direct bispectrum modeling, as we will show in chapter 4.

In this chapter, which serves as the basis for the later separate universe approach modeling, we derive the mapping between the overdense universe in a spatially flat background

cosmology (but with cosmological constant) to the modified cosmology in section 3.1. In section 3.2, we show that if the background cosmology is Einstein-de Sitter, i.e. matter dominated, then the changes in the scale factor and the linear growth factor can be solved analytically.

3.1 Mapping the overdense universe to the modified cosmology

Consider the universe with mean density $\bar{\rho}(t)$ and a region with overdensity $\delta_\rho(t)$, then the mean density $\tilde{\rho}(t)$ in this region is

$$\tilde{\rho}(t) = \bar{\rho}(t)[1 + \delta_\rho(t)] . \quad (3.1)$$

In this section, we shall derive the mapping of the cosmological parameters between the fiducial (overdense) and modified cosmologies as a function of the linearly extrapolated (Lagrangian) present-day overdensity

$$\delta_{L0} = \delta_\rho(t_i) \frac{D(t_0)}{D(t_i)} , \quad (3.2)$$

where D is the linear growth function of the fiducial cosmology, t_0 is the present time, and t_i is some initial time at which $\delta_\rho(t_i)$ is still small. However, we shall not assume δ_{L0} to be small.

The mean overdensity of the overdense region can be expressed in terms of the standard cosmological parameters, i.e. $\bar{\rho}(t_0) = \Omega_m \frac{3H_0^2}{8\pi G}$ and $H_0 = 100 h \text{ km s}^{-1} \text{ Mpc}^{-1}$, as

$$\frac{\Omega_m h^2}{a^3(t)} [1 + \delta_\rho(t)] = \frac{\tilde{\Omega}_m \tilde{h}^2}{\tilde{a}^3(t)} \quad (3.3)$$

where the parameters in the modified cosmology are denoted with tilde. For the fiducial cosmology, we adopt the standard convention for the scale factor such that $a(t_0) = 1$. In contrast, for the modified cosmology, it is convenient to choose $\tilde{a}(t \rightarrow 0) = a$ and $\delta_\rho(a \rightarrow 0) = 0$, which then leads to

$$\Omega_m h^2 = \tilde{\Omega}_m \tilde{h}^2 . \quad (3.4)$$

We also introduce

$$\tilde{a}(t) = a(t)[1 + \delta_a(t)] , \quad (3.5)$$

so that

$$1 + \delta_\rho(t) = [1 + \delta_a(t)]^{-3} . \quad (3.6)$$

Using eq. (3.5), the first and second time derivatives, represented with dots, of the scale factor are

$$\begin{aligned}\frac{\dot{\tilde{a}}}{\tilde{a}} &= \tilde{H} = \frac{\dot{a}[1 + \delta_a] + a\dot{\delta}_a}{a[1 + \delta_a]} = H + \frac{\dot{\delta}_a}{1 + \delta_a}, \\ \frac{\ddot{\tilde{a}}}{\tilde{a}} &= \frac{\ddot{a}[1 + \delta_a] + 2\dot{a}\dot{\delta}_a + a\ddot{\delta}_a}{a[1 + \delta_a]} = \frac{\ddot{a}}{a} + \frac{\ddot{\delta}_a + 2H\dot{\delta}_a}{1 + \delta_a}.\end{aligned}\quad (3.7)$$

The two Friedmann equations in the flat fiducial cosmology are

$$\begin{aligned}\left(\frac{\dot{a}}{a}\right)^2 &= H^2(t) = \frac{8\pi G}{3}[\bar{\rho}(t) + \rho_X(t)], \\ \frac{\ddot{a}}{a} &= -\frac{4\pi G}{3}[\bar{\rho}(t) + \rho_X(t) + 3p_x(t)],\end{aligned}\quad (3.8)$$

where ρ_X and p_x are the energy density and pressure for dark energy, respectively. For the modified cosmology, the Friedmann equations hold, but with non-zero curvature \tilde{K} and modified densities and scale factor as

$$\begin{aligned}\left(\frac{\dot{\tilde{a}}}{\tilde{a}}\right)^2 &= \tilde{H}^2(t) = \frac{8\pi G}{3}[\tilde{\rho}(t) + \tilde{\rho}_X(t)] - \frac{\tilde{K}}{\tilde{a}^2(t)}, \\ \frac{\ddot{\tilde{a}}}{\tilde{a}} &= -\frac{4\pi G}{3}[\tilde{\rho}(t) + \tilde{\rho}_X(t) + 3\tilde{p}_x(t)].\end{aligned}\quad (3.9)$$

Before we derive the relation for the curvature \tilde{K} , let us first discuss the dark energy component.

If dark energy is not a cosmological constant, then there are also perturbations in dark energy fluid, i.e. $\delta\rho_X = \tilde{\rho}_X - \rho_X$ and $\delta p_X = \tilde{p}_X - p_X$. In order for the separate universe approach to work, matter and dark energy have to be comoving and follow geodesics of the FLRW metric. Since this requires negligible pressure gradients, the separate universe approach is only applicable to density perturbations with wavelength $2\pi/k$ that are much larger than the dark energy sound horizon, $k \ll H_0/|c_s|$, where the sound speed is defined as $c_s^2 = \delta p_X/\delta\rho_X$ [36]. This means that the region with the overdensity that we consider here has to be much larger than the dark energy sound horizon. For simplicity, in the following we shall assume that dark energy is just a cosmological constant Λ , thereby $\tilde{\rho}_\Lambda = \rho_\Lambda$ and $\tilde{p}_\Lambda = p_\Lambda = -\rho_\Lambda$.

In order to be a valid Friedmann model, the curvature has to be conserved, i.e. $\dot{\tilde{K}} = 0$. To show this, we express the curvature using the first Friedmann equation and take the time derivative:

$$\begin{aligned}\dot{\tilde{K}} &= \frac{16\pi G}{3}\tilde{a}\dot{\tilde{a}}[\tilde{\rho} + \tilde{\rho}_\Lambda] + \frac{8\pi G}{3}\tilde{a}^2\dot{\tilde{\rho}} - 2\tilde{a}\dot{\tilde{a}}\ddot{\tilde{a}} = \frac{16\pi G}{3}\tilde{a}\dot{\tilde{a}}[\tilde{\rho} + \tilde{\rho}_\Lambda] - \frac{24\pi G}{3}\tilde{a}\dot{\tilde{a}}\dot{\tilde{\rho}} - 2\tilde{a}\dot{\tilde{a}}\ddot{\tilde{a}} \\ &= \frac{8\pi G}{3}\tilde{a}\dot{\tilde{a}}[-\dot{\tilde{\rho}} + 2\dot{\tilde{\rho}}_\Lambda] - 2\tilde{a}\dot{\tilde{a}}\ddot{\tilde{a}} = 2\tilde{a}\dot{\tilde{a}}\frac{\ddot{\tilde{a}}}{\tilde{a}} - 2\tilde{a}\dot{\tilde{a}}\ddot{\tilde{a}} = 0,\end{aligned}\quad (3.10)$$

where we use $\dot{\tilde{\rho}}_\Lambda = 0$ and the continuity equation $\dot{\tilde{\rho}} = -3\tilde{\rho}\tilde{H}$.

To solve the curvature of the modified cosmology in terms of the fiducial cosmological parameters and δ_{L0} , we express \tilde{K} by the difference of the first Friedmann equation between the modified and fiducial cosmologies as

$$\begin{aligned} \frac{\tilde{K}}{a^2} &= \frac{8\pi G}{3} \tilde{\rho} \delta_\rho (1 + \delta_a)^2 - 2H \dot{\delta}_a (1 + \delta_a) - \dot{\delta}_a^2 \\ &= \frac{8\pi G}{3} \tilde{\rho} [(1 + \delta_a)^{-1} - (1 + \delta_a)^2] - 2H \dot{\delta}_a (1 + \delta_a) - \dot{\delta}_a^2, \end{aligned} \quad (3.11)$$

where we use eq. (3.6) and eq. (3.7) to represent δ_ρ and \tilde{H} , respectively. Since the curvature is conserved (eq. (3.10)), eq. (3.11) can be evaluated at an early time t_i at which the perturbations $\delta_a(t_i)$ and $\delta_\rho(t_i)$ are infinitesimal as well as the universe is in matter domination. In this regime, we have

$$H^2 = H_0^2 \Omega_m a^{-3}, \quad \delta_a = -\delta_\rho/3, \quad \dot{\delta}_a = H \delta_a, \quad (3.12)$$

with which we can derive

$$\frac{\tilde{K}}{a^2(t_i)} = \frac{8\pi G}{3} \tilde{\rho}(t_i) [-3\delta_a(t_i)] - 2H^2(t_i) \delta_a(t_i) = \frac{5\Omega_m H_0^2 \delta_\rho(t_i)}{3a^3(t_i)}. \quad (3.13)$$

This then to express \tilde{K} in terms of the fiducial cosmological parameters and δ_{L0} as

$$\frac{\tilde{K}}{H_0^2} = \frac{5}{3} \frac{\Omega_m}{a(t_i)} \delta_\rho(t_i) = \frac{5}{3} \frac{\Omega_m}{D(t_0)} \delta_{L0}, \quad (3.14)$$

where we use the fact that in the matter dominated regime $D(t_i) = a(t_i)$.

We now derive the cosmological parameters, $\tilde{\Omega}_m$, $\tilde{\Omega}_\Lambda$, and $\tilde{\Omega}_K$ of the modified cosmology. Note that by convention these parameters are defined through the first Friedmann equation at \tilde{t}_0 where $\tilde{a}(\tilde{t}_0) = 1$ and $\tilde{H}(\tilde{t}_0) = \tilde{H}_0$, therefore

$$\tilde{\Omega}_K = -\frac{\tilde{K}}{\tilde{H}_0^2}; \quad \tilde{\Omega}_m = \frac{8\pi G}{3\tilde{H}_0^2} \tilde{\rho}(\tilde{t}_0); \quad \tilde{\Omega}_\Lambda = \frac{8\pi G}{3\tilde{H}_0^2} \rho_\Lambda. \quad (3.15)$$

The cosmological parameters in the modified cosmology can be related to the ones in the fiducial cosmology through $\tilde{H}_0 = H_0(1 + \delta_H)$, which become

$$\tilde{\Omega}_m = \Omega_m(1 + \delta_H)^{-2}, \quad \tilde{\Omega}_\Lambda = \Omega_\Lambda(1 + \delta_H)^{-2}, \quad \tilde{\Omega}_K = 1 - \tilde{\Omega}_m - \tilde{\Omega}_\Lambda = 1 - (1 + \delta_H)^{-2}, \quad (3.16)$$

where we use $\Omega_m + \Omega_\Lambda = 1$ because the fiducial cosmology is flat.

Alternatively, δ_H can be expressed in terms of \tilde{K} as

$$\delta_H = \left(1 - \frac{\tilde{K}}{H_0^2}\right)^{1/2} - 1. \quad (3.17)$$

There is no solution for δ_H if $\tilde{K}/H_0^2 > 1$, or equivalently $\delta_{L0} > (\frac{5}{3} \frac{\Omega_m}{D(t_0)})^{-1}$. This is because for such a large positive curvature, the universe reaches turn around before $\tilde{a} = 1$, at which the modified cosmological parameters are defined. In other words, this is not a physical problem, but merely a parameterization issue under the standard convention.

Finally, we shall derive the equation for $\delta_a(t)$, so that the observables of different cosmologies can be compared at the same physical time t . Inserting the second Friedmann equation of the fiducial and modified cosmologies into eq. (3.7) yields an ordinary differential equation for the perturbation to the scale factor

$$\ddot{\delta}_a + 2H\dot{\delta}_a + \frac{4\pi G}{3}\bar{\rho} [(1 + \delta_a)^{-2} - (1 + \delta_a)] = 0, \quad (3.18)$$

or equivalently

$$\ddot{\delta}_\rho + 2H\dot{\delta}_\rho - \frac{4}{3} \frac{\dot{\delta}_\rho^2}{1 + \delta_\rho} - 4\pi G\rho\delta_\rho(1 + \delta_\rho) = 0. \quad (3.19)$$

When linearizing ($\delta_\rho \ll 1$) eq. (3.19), one obtains the equation for the linear growth factor. More generally, eq. (3.19) is exactly the equation for the interior density of a spherical top-hat perturbation in a Λ CDM universe [138]. For a certain t_{out} , one can numerically calculate $\delta_a(t_{\text{out}})$ through eq. (3.18) to get $\tilde{a}(t_{\text{out}}) = a(t_{\text{out}})[1 + \delta_a(t_{\text{out}})]$. Alternatively, one can numerically evaluate $\tilde{a}(t_{\text{out}})$ by

$$t_{\text{out}} = \int_0^{a(t_{\text{out}})} \frac{da}{aH(a)} = \int_0^{\tilde{a}(t_{\text{out}})} \frac{d\tilde{a}}{\tilde{a}\tilde{H}(\tilde{a})} = \int_0^{a(t_{\text{out}})[1+\delta_a(t_{\text{out}})]} \frac{d\tilde{a}}{\tilde{a}\tilde{H}(\tilde{a})}. \quad (3.20)$$

3.2 The modified cosmology in Einstein-de Sitter background

In the Einstein-de Sitter (EdS) universe we have

$$\Omega_m = 1; \quad \rho_\Lambda = 0; \quad H(a) = H_0 a^{-3/2}; \quad a(t) = \left(\frac{3}{2}H_0 t\right)^{2/3}; \quad D(t) = a(t). \quad (3.21)$$

In this section, we shall show that if the background cosmology is EdS, then the scale factor $\delta_a(t)$ and the Eulerian overdensity $\delta_\rho(t)$, as well as the linear growth factor $\tilde{D}(t)$ and the logarithmic growth rate $\tilde{f}(t)$ in the modified cosmology (overdense region) can be expressed in series of δ_{L0} .

3.2.1 Scale factor and Eulerian overdensity

In order to solve $\delta_a(t)$, we consider the spherical collapse model for a overdense region [66, 126, 122]. Since the scale of this region is much smaller than the horizon size, we can use the Newtonian dynamics and write the equation of motion of a shell of particles at radius \tilde{r} as

$$\ddot{\tilde{r}} = -\frac{G\tilde{M}}{\tilde{r}^2}, \quad \tilde{M} = \frac{4\pi}{3}\tilde{\rho}(t_i)\tilde{r}^3(t_i) = \text{constant}, \quad (3.22)$$

where t_i is some initial time. Note that in eq. (3.22) we neglect the shell crossing, i.e. if $\tilde{r}_1(t_i) > \tilde{r}_2(t_i)$ then $\tilde{r}_1(t) > \tilde{r}_2(t)$ for all t .

Eq. (3.22) is known as the ‘‘cycloid’’ and the parametric solution is

$$\tilde{a}(\theta) = \frac{\tilde{r}(\theta)}{\tilde{x}} = A(1 - \cos \theta) , \quad t(\theta) = B(\theta - \sin \theta) , \quad (3.23)$$

where \tilde{x} is some comoving distance for the normalization. Using the Leibniz rule, one finds that

$$\dot{\tilde{r}} = \frac{d\tilde{r}}{d\theta} \frac{d\theta}{dt} = \frac{A\tilde{x}}{B} \frac{\sin \theta}{(1 - \cos \theta)} , \quad \ddot{\tilde{r}} = -\frac{A\tilde{x}}{B^2} \frac{1}{(1 - \cos \theta)^2} , \quad (3.24)$$

and the equation of motion thus requires

$$\frac{A^3 \tilde{x}^3}{B^2} = G\tilde{M} = \frac{4\pi G}{3} \tilde{\rho}(t_i) \tilde{a}^3(t_i) \tilde{x}^3 \Leftrightarrow \frac{A^3}{B^2} = \frac{\tilde{H}_0^2 \tilde{\Omega}_m}{2} . \quad (3.25)$$

Note that since this region is overdense, $\tilde{\Omega}_m - 1 = -\tilde{\Omega}_K > 0$ and it is positively curved. For an underdense (negatively curved) region, the similar parameterization works with \cos and \sin in eq. (3.24) replaced by \cosh and \sinh .

To determine the constants A and B , we can write the first Friedmann equation using the parametric solution as

$$\begin{aligned} \tilde{H}^2 &= \left(\frac{\dot{\tilde{a}}}{\tilde{a}} \right)^2 = \frac{1}{B^2} \frac{(1 - \cos^2 \theta)}{(1 - \cos \theta)^4} = \tilde{H}_0^2 \left\{ \tilde{\Omega}_m [A(1 - \cos \theta)]^{-3} + (1 - \tilde{\Omega}_m) [A(1 - \cos \theta)]^{-2} \right\} \\ \frac{(1 - \cos^2 \theta)}{B^2} &= \frac{\tilde{H}_0^2}{A^2} \left\{ \left[\frac{\tilde{\Omega}_m}{A} - (\tilde{\Omega}_m - 1) \right] - \cos \theta \left[\frac{\tilde{\Omega}_m}{A} - 2(\tilde{\Omega}_m - 1) \right] - \cos^2 \theta (\tilde{\Omega}_m - 1) \right\} . \end{aligned} \quad (3.26)$$

Since eq. (3.26) is valid for all θ , the coefficient multiplied by $\cos \theta$ must be zero, which then allows us to solve

$$A = \frac{1}{2} \frac{\tilde{\Omega}_m}{(\tilde{\Omega}_m - 1)} , \quad B = \frac{1}{2} \frac{\tilde{\Omega}_m}{\tilde{H}_0 (\tilde{\Omega}_m - 1)^{3/2}} . \quad (3.27)$$

One finds that eq. (3.27) indeed yields $A^3/B^2 = \tilde{H}_0^2 \tilde{\Omega}_m/2$.

For simplicity, we define

$$\epsilon = \frac{\tilde{\Omega}_m - 1}{\tilde{\Omega}_m} = 1 - (1 + \delta_H)^2 = \frac{\tilde{K}}{\tilde{H}_0^2} = \frac{5}{3} \delta_{L0} , \quad (3.28)$$

so that

$$\tilde{a}(\theta) = \frac{1}{2} \epsilon^{-1} (1 - \cos \theta) ; \quad t(\theta) = \frac{3}{4} t_0 \epsilon^{-3/2} (\theta - \sin \theta) . \quad (3.29)$$

The goal is to obtain

$$\tilde{a}(t) = a(t) [1 + \delta_a(t)] = a(t) \left[1 + \sum_{n=1}^{\infty} e_n [a(t) \delta_{L0}]^n \right] , \quad \tilde{a}(t_0) = 1 + \sum_{n=1}^{\infty} e_n \delta_{L0}^n , \quad (3.30)$$

we thus need to solve θ_0 such that

$$t(\theta_0) = t_0 = \frac{3}{4}t_0\epsilon^{-3/2}(\theta_0 - \sin \theta_0) \Leftrightarrow \theta_0 - \sin \theta_0 = \frac{3}{4}\epsilon^{-3/2}. \quad (3.31)$$

We perform a series expansion,

$$\theta_0 - \sin \theta_0 = \frac{1}{6}\theta_0^3 - \frac{1}{120}\theta_0^5 + \dots = \sum_{n=1}^{\infty} b_n \theta_0^{2n+1}, \quad (3.32)$$

and solve θ_0 order by order. That is, for the n^{th} order solution, we solve

$$\frac{4}{3}\epsilon^{3/2} = \sum_{k=1}^n b_k \left[\theta_0^{(n-k+1)} \right]^{2k+1}, \quad (3.33)$$

and $\theta_0 = \lim_{n \rightarrow \infty} \theta_0^{(n)}$. Note that in order to trust the final solution at order δ_{L0}^m , the series solution needs to be expanded to $n = m + 1$. In the following we choose $m = 5$, which yields

$$\theta_0 = 2\epsilon^{1/2} \left[1 + \frac{1}{15}\epsilon + \frac{2}{175}\epsilon^2 + \frac{4}{1575}\epsilon^3 + \frac{43}{67375}\epsilon^4 + \dots \right]. \quad (3.34)$$

Finally, we insert eq. (3.34) into $\tilde{a}(\theta)$, expand in ϵ , replace ϵ with $\frac{5}{3}\delta_{L0}$, and match with eq. (3.30) for the coefficients e_n . For the first five coefficients, we get

$$e_1 = -\frac{1}{3}; \quad e_2 = -\frac{1}{21}; \quad e_3 = -\frac{23}{1701}; \quad e_4 = -\frac{1894}{392931}; \quad e_5 = -\frac{3293}{1702701}. \quad (3.35)$$

Once $\delta_a(t)$ is known, we can use eq. (3.6) to solve the Eulerian overdensity $\delta_\rho(t) = \sum_{n=1}^{\infty} f_n [\delta_{L0} a(t)]^n$, and the first five coefficients are

$$f_1 = 1; \quad f_2 = \frac{17}{21}; \quad f_3 = \frac{341}{567}; \quad f_4 = \frac{55805}{130997}; \quad f_5 = \frac{213662}{729729}. \quad (3.36)$$

While eqs. (3.35)–(3.36) are strictly valid only if the background is EdS, we find that they are also accurate in Λ CDM background if $a(t)$ is replaced with $D(t)/D(t_0)$, where $D(t)$ is the growth factor in the fiducial cosmology. In other words,

$$\delta_a(t) = \sum_{n=1}^{\infty} e_n \left[\delta_{L0} \frac{D(t)}{D(t_0)} \right]^n; \quad \delta_\rho(t) = \sum_{n=1}^{\infty} f_n \left[\delta_{L0} \frac{D(t)}{D(t_0)} \right]^n. \quad (3.37)$$

Figure 3.1 quantifies the performance of the EdS expansion with $a(t)$ being replaced by $D(t)/D(t_0)$ for $\delta_a(t)$, i.e. eq. (3.37). For a large range of δ_{L0} , the results of EdS expansion agree very well with the numerical solution of the differential equation eq. (3.18). Specifically, at the third (fifth) order expansion, the fractional difference is at the sub-percent level for $|\delta_{L0}| \sim 1$.

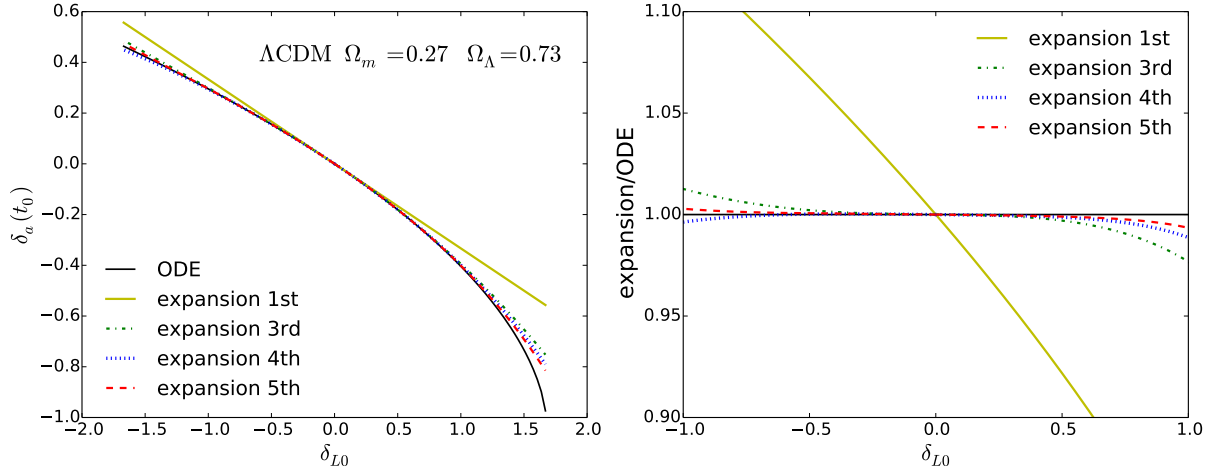


Figure 3.1: (Left) Perturbation in the scale factor in the modified cosmology, $\delta_a(t_0)$, as a function of δ_{L0} . The present-day scale factor is $a(t_0) = 1$ in the background Λ CDM universe, with $\Omega_m = 0.27$ and $\Omega_\Lambda = 0.73$. The black solid line shows the numerical solution to the ordinary differential equation, eq. (3.18); the yellow solid, green dot-dashed, blue dotted, and red dashed lines show the series solutions in EdS, eq. (3.37), at the first, third, fourth, and fifth order, respectively. (Right) Same as the left panel, but for the ratios of the series solutions expansion to the solution of the ordinary differential equation.

3.2.2 Small-scale growth

In this subsection, we shall iteratively solve the linear growth factor $\tilde{D}(t)$ and logarithmic growth rate $\tilde{f}(t)$ in series of δ_{L0} , as eqs. (3.35)–(3.36), in the modified cosmology with the EdS background. We consider a small-scale (short-wavelength) density perturbation in the overdense region such that $\tilde{\delta}_s = \tilde{\rho}/\tilde{\bar{\rho}} - 1$. Note that $\tilde{\delta}_s$ should not be confused with the long-wavelength density perturbation δ_ρ of this entirely overdense region with respect to the EdS background. Moreover, $\tilde{\delta}_s$ is defined with respect to the background density of the overdense universe $\tilde{\bar{\rho}}$ instead of the EdS background $\bar{\rho}$.

The small-scale growth equation for $\tilde{\delta}_s$ in the modified cosmology is given by

$$\ddot{\tilde{\delta}}_s + 2\tilde{H}\dot{\tilde{\delta}}_s - 4\pi G\tilde{\rho}\tilde{\delta}_s = 0. \quad (3.38)$$

Using

$$\begin{aligned} \tilde{H}^2 &= \tilde{H}_0^2 \left[\tilde{\Omega}_m \tilde{a}^{-3} + (1 - \tilde{\Omega}_m) \tilde{a}^{-2} \right] = H_0^2 \left(\tilde{a}^{-3} - \frac{5}{3} \delta_{L0} \tilde{a}^{-2} \right), \\ 4\pi G\tilde{\rho} &= \frac{3}{2} \tilde{\Omega}_m \tilde{H}_0^2 \tilde{a}^{-3} = \frac{3}{2} H_0^2 \tilde{a}^{-3}, \end{aligned} \quad (3.39)$$

the growth equation can be rewritten as

$$\ddot{\tilde{\delta}}_s + 2H_0 \left(\tilde{a}^{-3} - \frac{5}{3} \delta_{L0} \tilde{a}^{-2} \right)^{1/2} \dot{\tilde{\delta}}_s - \frac{3}{2} H_0^2 \tilde{a}^{-3} \tilde{\delta}_s = 0 . \quad (3.40)$$

Note that although we map the overdense universe to a positively curved universe, the curvature contribution to the Poisson equation is neglected. If $\tilde{K}/H_0^2 \sim 1$, the correction in the Poisson equation becomes relevant for the small-scale modes $\tilde{\delta}_s$ that are around the horizon size. Since we are studying the subhorizon evolution of the small-scale modes, and moreover we are mostly interested in the overdensity such that $\tilde{K}/H_0^2 \sim \delta_{L0} \ll 1$, the correction is entirely negligible. Thus, the curvature contributes to the growth only through the expansion rate \tilde{H} .

Replacing the time coordinate t with $y = \ln a(t)$ where $a(t)$ is the scale factor in the EdS background, we rewrite the growth equation as

$$\frac{d^2}{dy^2} \tilde{\delta}_s + \left[2(1 + \delta_a)^{-3/2} \left(1 - \frac{5}{3} \delta_{L0} [1 + \delta_a] \right)^{1/2} - \frac{3}{2} \right] \frac{d}{dy} \tilde{\delta}_s - \frac{3}{2} (1 + \delta_a)^{-3} \tilde{\delta}_s = 0 , \quad (3.41)$$

Thus far, all the derivations are exact. To see that eq. (3.41) makes sense, we consider the zeroth order approximation, i.e. $\delta_{L0} \rightarrow 0$. In this regime, $\delta_a \rightarrow 0$ and the growth equation becomes

$$\frac{d^2}{dy^2} \tilde{\delta}_s^{(0)} + \frac{1}{2} \frac{d}{dy} \tilde{\delta}_s^{(0)} - \frac{3}{2} \tilde{\delta}_s^{(0)} = 0 , \quad (3.42)$$

where the subscript (0) denotes that it is the zeroth order solution. There are two solutions to $\tilde{\delta}_s^{(0)}$, the growing mode proportional to a and the decaying mode proportional to $a^{-3/2}$. As expected, because $\delta_{L0} \rightarrow 0$, the result is identical to the growth in the background EdS cosmology. In the following, we shall drop the decaying mode following the standard practice. Furthermore, we shall normalize $\tilde{\delta}_s^{(0)}$ to $a(t)$ at early times, and replace it with $\tilde{D}(t)$ to denote the small-scale growth factor. This means $\tilde{D}^{(0)}(t) = a(t)$.

To solve higher order solutions, we insert the expansion of δ_a in terms of $a(t)\delta_{L0} = e^y \delta_{L0}$ (eq. (3.30) and eq. (3.35)) into the growth equation and obtain

$$\frac{d^2}{dy^2} \tilde{D}(y) + \left[\sum_{m=0}^{\infty} c_m \delta_{L0}^m e^{my} \right] \frac{d}{dy} \tilde{D}(y) - \left[\sum_{m=0}^{\infty} d_m \delta_{L0}^m e^{my} \right] \tilde{D}(y) = 0 , \quad (3.43)$$

with coefficients c_m and d_m given by

$$2(1 + \delta_a)^{-3/2} \left(1 - \frac{5}{3} \delta_{L0} [1 + \delta_a] \right)^{1/2} - \frac{3}{2} = \sum_{m=0}^{\infty} c_m [a(t)\delta_{L0}]^m$$

$$\frac{3}{2} (1 + \delta_a)^{-3} = \sum_{m=0}^{\infty} d_m [a(t)\delta_{L0}]^m . \quad (3.44)$$

Correspondingly, we write the pure growing-mode solution in series of δ_{L0} as

$$\tilde{D} = \sum_{n=0}^{\infty} g_n \delta_{L0}^n e^{(n+1)y} = D(t) \sum_{n=0}^{\infty} g_n [a(t) \delta_{L0}]^n \quad (3.45)$$

with coefficients g_n . Given our normalization, i.e. $\tilde{D}^{(0)} = a(t)$, $g_0 = 1$. Thus,

$$\frac{d}{dy} \tilde{D}(y) = \sum_{n=0}^{\infty} (n+1) g_n \delta_{L0}^n e^{(n+1)y} ; \quad \frac{d^2}{dy^2} \tilde{D}(y) = \sum_{n=0}^{\infty} (n+1)^2 g_n \delta_{L0}^n e^{(n+1)y} . \quad (3.46)$$

Supposed that we have solutions of $\tilde{D}(y)$ to the $(n-1)^{\text{th}}$ order, then the solution at the n^{th} order has to satisfy

$$(n+1)^2 g_n \delta_{L0}^n e^{(n+1)y} + \sum_{m=0}^n g_{n-m} \delta_{L0}^{n-m} e^{(n-m+1)y} [(n-m+1)c_m - d_m] e^{my} \delta_{L0}^m = 0 . \quad (3.47)$$

The term $\delta_{L0}^n e^{(n+1)y}$ factors out, and we obtain a simple algebraic relation for g_n in terms of c_m and d_m for $0 \leq m \leq n$, and g_m for $0 \leq m \leq n-1$ as

$$(n+1)^2 g_n + \sum_{m=0}^n g_{n-m} [(n-m+1)c_m - d_m] = 0 . \quad (3.48)$$

Using e_n in eq. (3.35) to get c_m and d_m through eq. (3.44), we obtain the first five g_n to be

$$g_1 = \frac{13}{21} ; g_2 = \frac{71}{189} ; g_3 = \frac{29609}{130977} ; g_4 = \frac{691858}{5108103} ; g_5 = \frac{8682241}{107270163} . \quad (3.49)$$

Similar to the previous subsection, the expansion of \tilde{D} in terms of δ_{L0} with the coefficients (eq. (3.49)) is strictly valid in the EdS background cosmology. In order to generalize from EdS to other cosmologies, we replace $a(t)$ with $D(t)/D(t_0)$, so that

$$\tilde{D}(t) = D(t) \left\{ 1 + \sum_{n=1}^{\infty} g_n \left[\delta_{L0} \frac{D(t)}{D(t_0)} \right]^n \right\} . \quad (3.50)$$

Figure 3.2 quantifies the performance of the expansion with $a(t)$ being replaced by $D(t)/D(t_0)$ for $\tilde{D}(t)$, i.e. eq. (3.50). The agreement is not as good as for $\delta_a(t)$, nevertheless the fifth order expansion gives 5% fractional differences at $|\delta_{L0}| \sim 1$. Note also that while for positive δ_{L0} the EdS expansion is always smaller than (but converging to) the numerical solution in Λ CDM, for negative δ_{L0} the fourth order expansion has a different trend compared to the other orders. This is because at the n^{th} order δ_{L0}^n dominates when $|\delta_{L0}| > 1$, and at the negative δ_{L0} end the result would thus depend on the parity of the expansion order. It is clear though the higher the expansion order, the better the agreement.

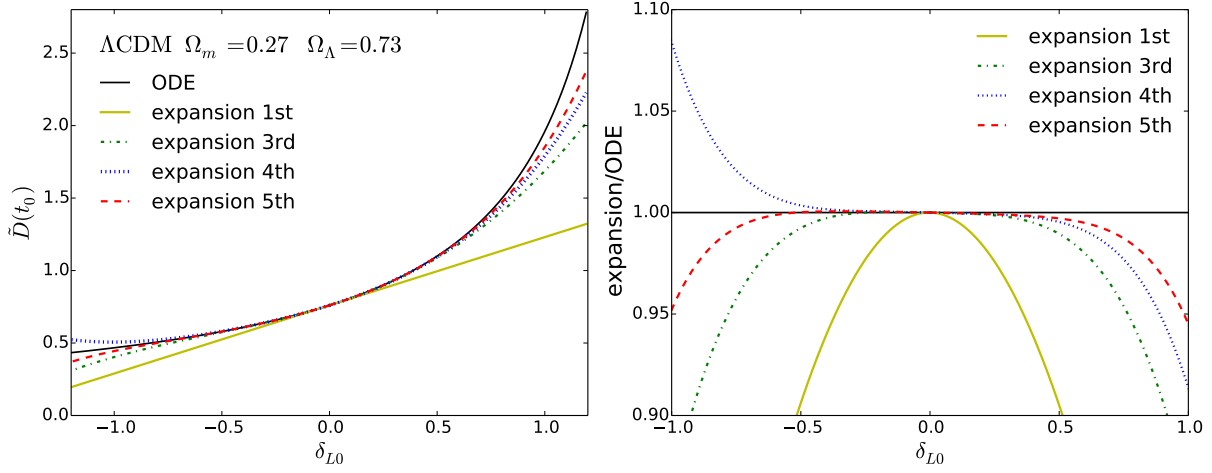


Figure 3.2: (Left) The linear growth factor in the modified cosmology, $\tilde{D}(t_0)$ with $a(t_0) = 1$, in the background Λ CDM universe with $\Omega_m = 0.27$ and $\Omega_\Lambda = 0.73$. The black solid line shows the numerical solution to eq. (3.40); the yellow solid, green dot-dashed, blue dotted, and red dashed lines show the series solutions, eq. (3.50), at the first, third, fourth, and fifth order, respectively. (Right) Same as the left panel, but for the ratios of the series solutions to the solution of the differential equation of the small-scale growth.

With the expansions of $\delta_a(t)$ (eq. (3.37)) and $\tilde{D}(t)$ (eq. (3.50)), we can finally derive the series expansion for the logarithmic growth rate,

$$f(t) = \frac{d \ln D(t)}{d \ln a(t)} = \frac{\dot{D}(t) a(t)}{D(t) \dot{a}(t)}. \quad (3.51)$$

In the modified cosmology, we have (defining $e_0 = 1$ as for g_0)

$$\begin{aligned} \tilde{f}(t) &= \frac{\dot{\tilde{D}}}{\tilde{D}} \frac{\tilde{a}}{\dot{\tilde{a}}} = \frac{\dot{D} \sum_{n=0}^{\infty} (n+1) g_n \delta_L^n(t)}{D \sum_{n=0}^{\infty} g_n \delta_L^n(t)} \frac{a \sum_{n=0}^{\infty} e_n \delta_L^n(t)}{\dot{a} \sum_{n=0}^{\infty} e_n \delta_L^n(t) + a \frac{\dot{D}}{D} \sum_{n=0}^{\infty} n e_n \delta_L^n(t)} \\ &= f \frac{\sum_{n=0}^{\infty} (n+1) g_n \delta_L^n(t)}{\sum_{n=0}^{\infty} g_n \delta_L^n(t)} \frac{\sum_{n=0}^{\infty} e_n \delta_L^n(t)}{\sum_{n=0}^{\infty} e_n \delta_L^n(t) + f \sum_{n=0}^{\infty} n e_n \delta_L^n(t)}, \end{aligned} \quad (3.52)$$

where $\delta_L(t) = \delta_{L0} \frac{D(t)}{D(t_0)}$. Note that in the EdS background $f = 1$, and so eq. (3.52) can be simplified as

$$\tilde{f}(t) = \frac{\sum_{n=0}^{\infty} (n+1) g_n \delta_L^n(t)}{\sum_{n=0}^{\infty} g_n \delta_L^n(t)} \frac{\sum_{n=0}^{\infty} e_n \delta_L^n(t)}{\sum_{n=0}^{\infty} (n+1) e_n \delta_L^n(t)}. \quad (3.53)$$

Figure 3.3 shows the performance of the expansion of \tilde{f} in the Λ CDM background. It is not as good as for \tilde{D} , but for $|\delta_{L0}| \sim 0.8$ the fifth order expansion gives approximately 5% fractional difference with respect to the numerical solution of the differential equation. One also notes the parity-feature at the negative δ_{L0} , as for \tilde{D} .

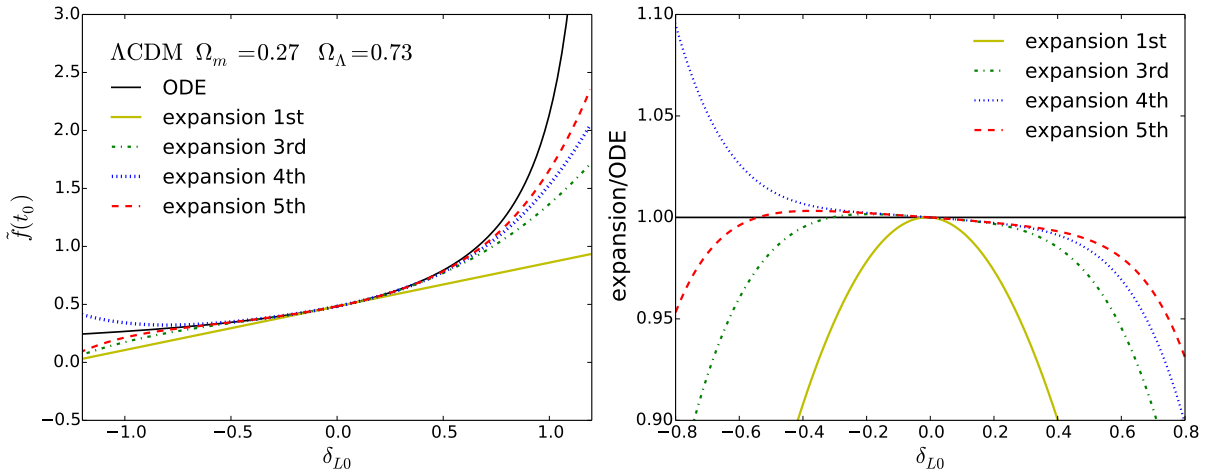


Figure 3.3: (Left) The logarithmic growth rate in the modified cosmology, $\tilde{f}(t_0)$ with $a(t_0) = 1$, in the background Λ CDM universe with $\Omega_m = 0.27$ and $\Omega_\Lambda = 0.73$. The black solid line shows the numerical solution to eq. (3.40); the yellow solid, green dot-dashed, blue dotted, and red dashed lines show the series solutions, eq. (3.52), at the first, third, fourth, and fifth order, respectively. (Right) Same as the left panel, but for the ratios of the series solutions to the solution of the differential equation of the small-scale growth.

Chapter 4

Measurement of position-dependent power spectrum

As introduced in section 2.1, the correlation between the position-dependent power spectrum,

$$\hat{P}(\mathbf{k}, \mathbf{r}_L) = \frac{1}{V_L} \int \frac{d^3 q_1}{(2\pi)^3} \int \frac{d^3 q_2}{(2\pi)^3} \delta(\mathbf{k} - \mathbf{q}_1) \delta(-\mathbf{k} - \mathbf{q}_2) W_L(\mathbf{q}_1) W_L(\mathbf{q}_2) e^{-i\mathbf{r}_L \cdot (\mathbf{q}_1 + \mathbf{q}_2)} , \quad (4.1)$$

and the mean overdensity,

$$\bar{\delta}(\mathbf{r}_L) = \frac{1}{V_L} \int \frac{d^3 q}{(2\pi)^3} \delta(-\mathbf{q}) W_L(\mathbf{q}) e^{-i\mathbf{r}_L \cdot \mathbf{q}} , \quad (4.2)$$

is the integrated bispectrum,

$$\begin{aligned} iB_L(k) &= \langle \hat{P}(k, \mathbf{r}_L) \bar{\delta}(\mathbf{r}_L) \rangle \\ &= \frac{1}{V_L^2} \int \frac{d^2 \hat{k}}{4\pi} \int \frac{d^3 q_1}{(2\pi)^3} \int \frac{d^3 q_3}{(2\pi)^3} B(\mathbf{k} - \mathbf{q}_1, -\mathbf{k} + \mathbf{q}_1 + \mathbf{q}_3, -\mathbf{q}_3) \\ &\quad \times W_L(\mathbf{q}_1) W_L(-\mathbf{q}_1 - \mathbf{q}_3) W_L(\mathbf{q}_3) , \end{aligned} \quad (4.3)$$

with V_L being the size of the subvolume.

In the squeezed limit where the scale of the position-dependent power spectrum is much smaller than the subvolume size, i.e. $k \gg 1/L$, the integrated bispectrum can be simplified as

$$iB_L(k) \stackrel{kL \rightarrow \infty}{=} \frac{1}{V_L^2} \int \frac{d^3 q}{(2\pi)^3} W_L^2(\mathbf{q}) P(q) \check{f}(k) P(k) = \sigma_L^2 \check{f}(k) P(k) , \quad (4.4)$$

where $\check{f}(k) = 2f(0, k)$ with $f(\mathbf{k}_1, \mathbf{k}_2)$ being a dimensionless symmetric function for the separable bispectrum, and σ_L^2 is the variance of the density fluctuation in V_L ,

$$\sigma_L^2 = \frac{1}{V_L^2} \int \frac{d^3 q}{(2\pi)^3} P(q) W_L^2(\mathbf{q}) . \quad (4.5)$$

An intuitive way to arrive at eq. (4.4) is to consider the expansion of the position-dependent power spectrum in the presence of a long-wavelength density fluctuation $\bar{\delta}$ as

$$\hat{P}(k, \mathbf{r}_L) = P(k)|_{\bar{\delta}=0} + \left. \frac{dP(k)}{d\bar{\delta}} \right|_{\bar{\delta}=0} \bar{\delta} + \dots, \quad (4.6)$$

and the leading-order correlation between $P(k, \mathbf{r}_L)$ and $\bar{\delta}$ is

$$iB_L(k) = \sigma_L^2 \left. \frac{d \ln P(k)}{d\bar{\delta}} \right|_{\bar{\delta}=0} P(k). \quad (4.7)$$

Inspired by eq. (4.4) and eq. (4.7), we define the normalized integrated bispectrum to be

$$\frac{iB_L(k)}{\hat{P}(k)\sigma_L^2}, \quad (4.8)$$

and it is equal to the linear response function, $\check{f}(k)$ or $d \ln P(k)/d\bar{\delta}$, in the limit of $kL \rightarrow \infty$.

In this chapter, we measure the position-dependent power spectrum and the integrated bispectrum from N -body simulations in section 4.1, and compare with the theoretical modeling of the measurements in section 4.2 and section 4.3. At the end of this chapter, we shall discuss the dependence of the integrated bispectrum on the cosmological parameters in section 4.4, and the expected constraint on the primordial non-Gaussianity using the Fisher matrix calculation in section 4.5. We conclude in section 4.6.

4.1 N -body simulations and the estimators

We now present measurements of the position-dependent power spectrum from 160 collisionless N -body simulations of a $2400 h^{-1}$ Mpc box with 768^3 particles (which corresponds to $2.29 \times 10^{12} M_\odot$). The same simulations are used in [47], and we refer to section 3 of [47] for more details. In short, the initial conditions are set up using different realizations of Gaussian random fields with the linear power spectrum computed by CAMB [96, 95]. We adopt a flat Λ CDM cosmology, and the cosmological parameters are $\Omega_m = 0.27$, $\Omega_b h^2 = 0.023$, $h = 0.7$, $n_s = 0.95$, and $\sigma_8 = 0.7913$. The particles are displaced from the initial grid points using the second-order Lagrangian perturbation theory [40] at the initial redshift $z_i = 19$. The simulations are carried out using the Tree-PM code Gadget-2 [153], taking only the gravitational force into account.

To construct the density fluctuation field on grid points, we first distribute all the particles in the $2400 h^{-1}$ Mpc box onto a 1000^3 grid by the cloud-in-cell (CIC) density assignment scheme. Then the density fluctuation field at the grid point \mathbf{r}_g is

$$\hat{\delta}(\mathbf{r}_g) = \frac{N(\mathbf{r}_g)}{\bar{N}} - 1, \quad (4.9)$$

where hat denotes the estimated quantities, $N(\mathbf{r}_g)$ is the fractional number of particles after the CIC assignment at \mathbf{r}_g , and $\bar{N} = 768^3/1000^3$ is the mean number of particles in each grid cell.

We then divide the $2400 h^{-1}$ Mpc box in each dimension by $N_{\text{cut}} = 4, 8,$ and 20 , so that there are $64, 512,$ and 8000 subvolumes with a side length of $600, 300,$ and $120 h^{-1}$ Mpc, respectively. The mean density perturbation in a subvolume centered at \mathbf{r}_L is

$$\hat{\delta}(\mathbf{r}_L) = \frac{1}{N_{\text{grid}}^3} \sum_{\mathbf{r}_g \in V_L} \hat{\delta}(\mathbf{r}_g), \quad (4.10)$$

where $(N_{\text{grid}})^3 = (1000/N_{\text{cut}})^3$ is the number of grid points within the subvolume. To compute the position-dependent power spectrum, we use FFTW¹ to Fourier transform $\hat{\delta}(\mathbf{r}_g)$ in each subvolume with the grid size $(N_{\text{grid}})^3$. While the fundamental frequency of the subvolume, $k_F = 2\pi/L$, decreases with the subvolume size L , the Nyquist frequency of the FFT grid, $k_{Ny} = k_F N_{\text{grid}}/2 \approx 1.3 h \text{ Mpc}^{-1}$, is the same in all cases.

The position-dependent power spectrum is then computed as

$$\hat{P}(k, \mathbf{r}_L) = \frac{1}{V_L N_{\text{mode}}} \sum_{k - \Delta k/2 \leq |\mathbf{k}_i| \leq k + \Delta k/2} |\hat{\delta}(\mathbf{k}_i, \mathbf{r}_L)|^2, \quad (4.11)$$

where N_{mode} is the number of Fourier modes in the bin $[k - \Delta k/2, k + \Delta k/2]$, and we set $\Delta k \approx 0.01 h \text{ Mpc}^{-1}$ in all cases. We choose this Δk for all N_{cut} to sample well the baryon acoustic oscillations (BAO) and thereby are able to show how the window function of the different subvolumes damps the BAO (see figure 4.2). We follow the procedures in [78] to correct for the smoothing due to the CIC density assignment and also for the aliasing effect in the power spectrum. Note, however, that this correction is only important for wavenumbers near the Nyquist frequency $1.31 h \text{ Mpc}^{-1}$, and we are interested in scales $k \lesssim 0.4 h \text{ Mpc}^{-1}$.

Figure 4.1 shows the position-dependent power spectrum measured from 512 subvolumes with $L = 300 h^{-1}$ Mpc in one realization at $z = 0$. The color represents $\hat{\delta}(\mathbf{r}_L)$ of each subvolume. The positive correlation between the subvolume power spectra and $\hat{\delta}(\mathbf{r}_L)$ is obvious. The response of the position-dependent power spectrum to the long-wavelength density fluctuation is clearly measurable at high significance in the simulations.

We measure the integrated bispectrum through

$$i\hat{B}_L(k) = \frac{1}{N_{\text{cut}}^3} \sum_{i=1}^{N_{\text{cut}}^3} \hat{P}(k, \mathbf{r}_{L,i}) \hat{\delta}(\mathbf{r}_{L,i}), \quad (4.12)$$

where $\hat{P}(k, \mathbf{r}_{L,i})$ and $\hat{\delta}(\mathbf{r}_{L,i})$ are measured in the i^{th} subvolume. Further, motivated by eq. (4.4), we normalize the integrated bispectrum by the mean power spectrum in the subvolumes,

$$\bar{\hat{P}}_L(k) = \frac{1}{N_{\text{cut}}^3} \sum_{i=1}^{N_{\text{cut}}^3} \hat{P}(k, \mathbf{r}_{L,i}), \quad (4.13)$$

¹Fast Fourier Transformation library: www.fftw.org

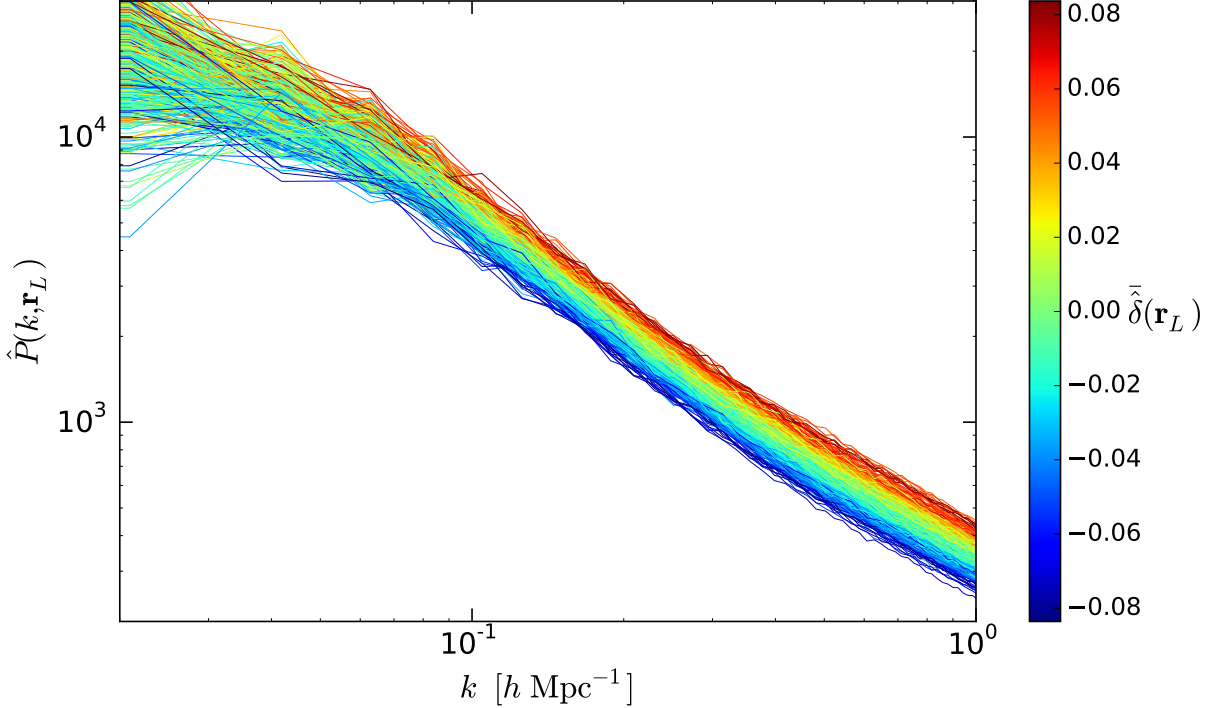


Figure 4.1: Position-dependent power spectra measured from 512 subvolumes with $L = 300 h^{-1} \text{ Mpc}$ in one realization at $z = 0$. The color represents $\bar{\delta}(\mathbf{r}_L)$ of each subvolume.

and the variance of the mean density fluctuation in the subvolumes,

$$\hat{\sigma}_L^2 = \frac{1}{N_{\text{cut}}^3} \sum_{i=1}^{N_{\text{cut}}^3} \hat{\delta}^2(\mathbf{r}_{L,i}) . \quad (4.14)$$

Note that by construction

$$\bar{\delta}_L = \frac{1}{N_{\text{cut}}^3} \sum_{i=1}^{N_{\text{cut}}^3} \hat{\delta}(\mathbf{r}_{L,i}) = 0 . \quad (4.15)$$

This quantity

$$\frac{i\hat{B}_L(k)}{\bar{\hat{P}}_L(k)\hat{\sigma}_L^2} , \quad (4.16)$$

is the estimator of the normalized integrated bispectrum (eq. (4.8)), and is equal to the linear response function, $d \ln P(k)/d\bar{\delta}$, given in eq. (4.7) in the limit of $kL \rightarrow \infty$.

Figure 4.2 shows the normalized integrated bispectrum, averaged over 160 collisionless N -body simulations at different redshifts. For clarity, no error bars are shown in this figure. We have compared the results with a higher-resolution simulation with 1536^3 particles and

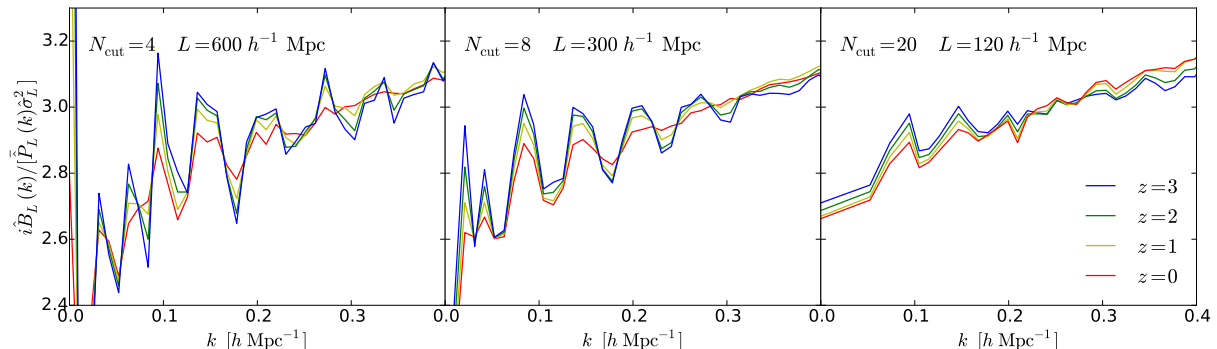


Figure 4.2: Normalized integrated bispectrum averaged over 160 collisionless N -body simulations with Gaussian initial conditions. From left to right are $N_{\text{cut}} = 4$ ($L = 600 h^{-1}$ Mpc), 8 ($300 h^{-1}$ Mpc), and 20 ($120 h^{-1}$ Mpc); the blue, green, yellow, and red lines are $z = 3$, 2, 1, and 0, respectively. For clarity, we do not show the error bars.

starting at higher redshift ($z_i = 49$ compared to $z_i = 19$ for our 160 simulations). For the scales and redshifts shown in figure 4.2, the differences are less than 1%. However, we expect an up to 5% uncertainty in the integrated bispectrum at $z = 3$ (less at lower z) due to transients which affect the bispectrum more strongly than the power spectrum [40, 111], as well as other systematics such as mass resolution.

Since the initial conditions are Gaussian, the bispectrum is generated entirely by non-linear gravitational evolution. We thus measure the effect of a long-wavelength density perturbation on the evolution of small-scale structures. The wiggles visible in each panel of figure 4.2 are due to the BAOs. The BAOs in the right panel are strongly damped because the box size ($120 h^{-1}$ Mpc) approaches the BAO scale, and the window function smears the BAO feature [30]. Further, BAO amplitudes are larger at higher redshifts as they are less damped by nonlinear evolution [53]. The broad-band shape of the normalized integrated bispectrum evolves on small scales due to nonlinear evolution, leading to an effective steepening of its slope. We now turn to the theoretical modeling of the results shown in figure 4.2.

4.2 Bispectrum modeling

We use two different approaches to model the integrated bispectrum. In the first approach, we model the bispectrum and compute the integral to obtain the integrated bispectrum. In the second approach, we model the response of the small-scale power spectrum to a long wavelength perturbation directly using the “separate universe” picture. For clarity, we will show the comparison between model prediction and simulations only for the $L = 300 h^{-1}$ Mpc subvolumes ($N_{\text{cut}} = 8$). The agreement with simulations is independent of subvolume size as long as the subvolume size is large enough for $\bar{\delta}$ to be in the linear regime,

and the window function is taken into account.

We first compute the integrated bispectrum by using a model for the bispectrum in eq. (4.3) and perform the eight-dimensional integral. Because of the high dimensionality, we use the Monte Carlo integration routine in GNU Scientific Library to evaluate the angular-averaged integrated bispectrum. In the following, we consider two different models for the matter bispectrum.

4.2.1 Standard perturbation theory

The standard perturbation theory (SPT) [17] gives the tree-level matter bispectrum as

$$B_{\text{SPT}}(\mathbf{k}_1, \mathbf{k}_2, \mathbf{k}_3) = 2[P_l(k_1)P_l(k_2)F_2(\mathbf{k}_1, \mathbf{k}_2) + 2 \text{cyclic}], \quad (4.17)$$

where $P_l(k)$ is the linear matter power spectrum, and

$$F_2(\mathbf{k}_1, \mathbf{k}_2) = \frac{5}{7} + \frac{1}{2} \frac{\mathbf{k}_1 \cdot \mathbf{k}_2}{k_1 k_2} \left(\frac{k_1}{k_2} + \frac{k_2}{k_1} \right) + \frac{2}{7} \left(\frac{\mathbf{k}_1 \cdot \mathbf{k}_2}{k_1 k_2} \right)^2. \quad (4.18)$$

In order to normalize the integrated bispectrum, we need an expression for the mean subvolume power spectrum $\tilde{P}_L(k)$. For this we use the linear power spectrum convolved with the window function,

$$P_{l,L}(k) = \frac{1}{V_L} \int \frac{d^3q}{(2\pi)^3} P_l(|\mathbf{k} - \mathbf{q}|) |W_L(\mathbf{q})|^2, \quad (4.19)$$

while the variance of the mean density fluctuation in the subvolumes is given by eq. (4.5). Both quantities are calculated through Monte Carlo integration.

We compare the normalized integrated bispectrum measured from the simulations with the SPT prediction in figure 4.3 (red lines). The SPT prediction is independent of redshift. This is because the linear power spectra at various redshifts are only different by the wavenumber-independent linear growth factor, $D^2(z)$. Therefore, the linear growth factor cancels out in the normalized integrated bispectrum. The SPT predictions agree with the simulations relatively well at $z \geq 1$ and $k \lesssim 0.2 h \text{ Mpc}^{-1}$, whereas they fail at lower redshifts as well as on smaller scales, where nonlinearities become too strong to be described by SPT. Especially, the BAO amplitudes at $k \gtrsim 0.2 h \text{ Mpc}^{-1}$ are affected: while the SPT predictions are redshift-independent, the simulations show smaller BAO amplitudes at lower redshifts.

The eight-dimensional integral in eq. (4.3) simplifies greatly if we focus on the squeezed-limit bispectrum. In appendix A, we show (note that $B_{\text{SPT}} \equiv B_{\text{SQ1,1}}$)

$$\begin{aligned} & \int \frac{d^2\Omega_{\hat{\mathbf{k}}}}{4\pi} B_{\text{SPT}}(\mathbf{k} - \mathbf{q}_1, -\mathbf{k} + \mathbf{q}_1 + \mathbf{q}_3, -\mathbf{q}_3) \\ &= \left[\frac{68}{21} - \frac{1}{3} \frac{d \ln k^3 P_l(k)}{d \ln k} \right] P_l(k) P_l(q_3) + \mathcal{O} \left[\left(\frac{q_{1,3}}{k} \right)^2 \right], \end{aligned} \quad (4.20)$$

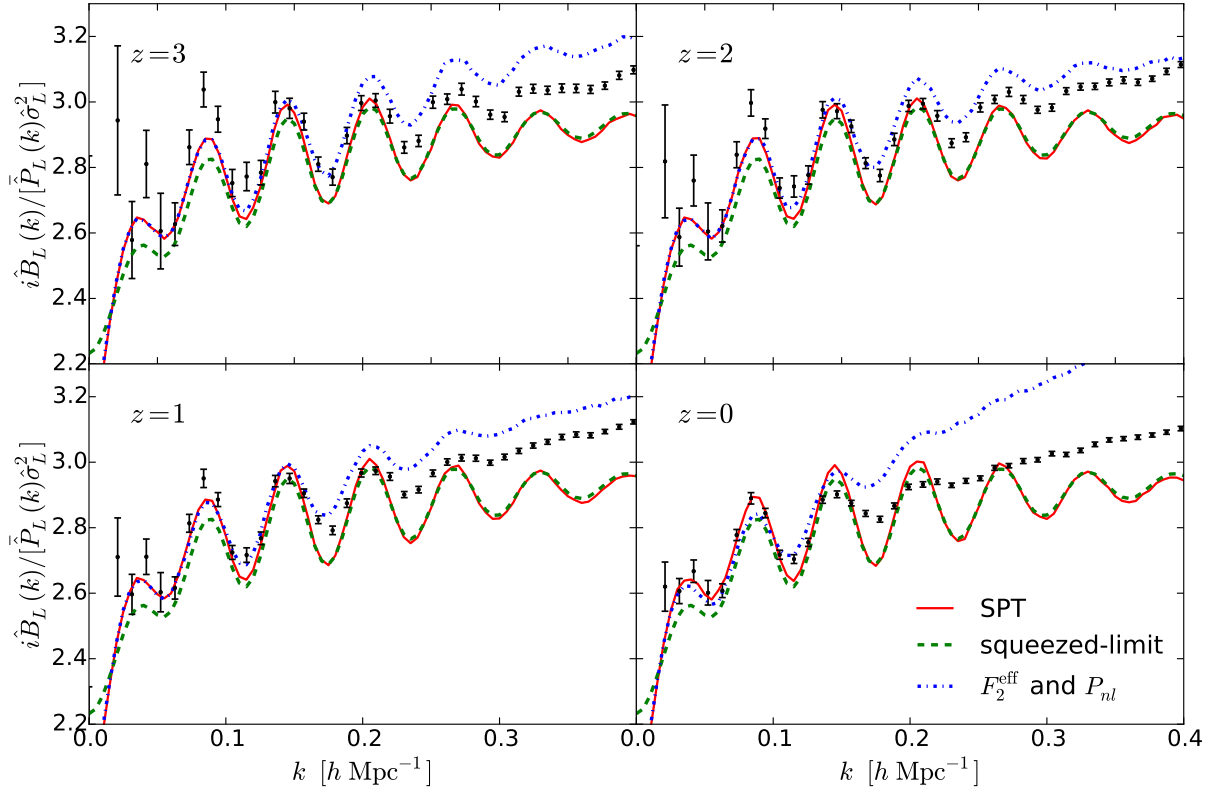


Figure 4.3: The SPT and the $F_2^{\text{eff}}(\mathbf{k}_1, \mathbf{k}_2)$ predictions for the normalized integrated bispectrum at different redshifts. The red solid and blue dot-dashed lines are computed by the direct integration of the eight-dimensional integral (eq. (4.3)) with the standard $F_2(\mathbf{k}_1, \mathbf{k}_2)$ kernel and the linear power spectrum, and $F_2^{\text{eff}}(\mathbf{k}_1, \mathbf{k}_2)$ and the nonlinear power spectrum, respectively. The green dashed lines show the squeezed-limit approximation (eq. (4.21)) to the SPT results. The N -body simulation results are shown by the black data points with the error bars showing the standard deviation on the mean measured from 160 simulations.

for $k \gg q_1, q_3$. We can then apply eq. (4.4) and perform all the integrals analytically in the limit of $kL \rightarrow \infty$ to obtain

$$\begin{aligned}
 iB_{L,\text{SPT}}(k) &= \frac{1}{V_L^2} \int \frac{d^2\Omega_{\hat{\mathbf{k}}}}{4\pi} \int \frac{d^3q_1}{(2\pi)^3} \int \frac{d^3q_3}{(2\pi)^3} B_{\text{SPT}}(\mathbf{k} - \mathbf{q}_1, -\mathbf{k} + \mathbf{q}_1 + \mathbf{q}_3, -\mathbf{q}_3) \\
 &\quad \times W_L(\mathbf{q}_1)W_L(-\mathbf{q}_1 - \mathbf{q}_3)W_L(\mathbf{q}_3) \\
 &\stackrel{kL \rightarrow \infty}{=} \left[\frac{68}{21} - \frac{1}{3} \frac{d \ln k^3 P_l(k)}{d \ln k} \right] P_l(k) \sigma_L^2. \tag{4.21}
 \end{aligned}$$

Comparing this result with eq. (4.7), we find that the linear response of the power spectrum

in SPT is given by

$$\left. \frac{d \ln P_l(k)}{d\bar{\delta}} \right|_{\text{SPT}} = \frac{68}{21} - \frac{1}{3} \frac{d \ln k^3 P_l(k)}{d \ln k}. \quad (4.22)$$

The green dashed lines in figure 4.3 show the squeezed-limit approximation given in eq. (4.21). While they are different from the full integration (red solid lines) at $k \lesssim 0.2 h \text{ Mpc}^{-1}$, for which the squeezed-limit approximation fails and the direct integration is required, they agree well, with the fractional difference being less than 1.5% (1% for $L = 600 h^{-1} \text{ Mpc}$), at $k \gtrsim 0.2 h \text{ Mpc}^{-1}$, corresponding to a value of $1/(kL) \lesssim 0.02$. Thus, the squeezed-limit is reached already with good precision for $kL \gtrsim 50$.

Eq. (4.21) does not contain any window function effect apart from that in the variance σ_L^2 . While this is a good approximation for the slowly-varying part of the integrated bispectrum, it does not capture the smearing of the BAO features due to the window function. We incorporate this effect by replacing $d \ln P_l(k)/d \ln k$ with appropriately convolved forms, $\text{conv}[dP_l(k)/d \ln k] / \text{conv}[P_l(k)]$, in eq. (4.21). This form is motivated by the separate universe approach discussed in section 4.3, and provides an accurate result as shown in figure 4.3.

4.2.2 Bispectrum fitting formula

The SPT predictions fail on smaller scales as well as at lower redshifts where nonlinearity becomes too strong to be described by SPT. An empirical fitting formula for nonlinear evolution of the matter bispectrum was proposed in [140] and further improved in [64]. In short, the form is the same as the tree-level matter bispectrum, but $F_2(\mathbf{k}_1, \mathbf{k}_2)$ is replaced by an effective kernel, $F_2^{\text{eff}}(\mathbf{k}_1, \mathbf{k}_2)$, which contains nine fitting parameters, $\{a_1, \dots, a_9\}$, to account for nonlinearity (see eqs. 2.6 and 2.12 in [64] for details). Therefore, we use $F_2^{\text{eff}}(\mathbf{k}_1, \mathbf{k}_2)$ and compute the integrated bispectrum by performing the eight-dimensional integral numerically with Monte Carlo integration. We use the same values of the best-fit parameters provided in table 2 of [64], which were calibrated by fitting to simulation results between $z = 0$ and $z = 1.5$. In contrast to the SPT formalism that uses the linear power spectrum in eq. (4.17), the fitting formula uses the nonlinear power spectrum, for which we use the mean power spectrum measured from the 160 simulation boxes. For the normalization of the integrated bispectrum, we convolve the nonlinear power spectrum with the subvolume window function as in eq. (4.19). Note that the F_2^{eff} fitting formula is not specifically designed for the squeezed configuration, but instead was calibrated to a wide range of triangle configurations of the matter bispectrum.

The blue dot-dashed lines in figure 4.3 show the normalized integrated bispectrum computed with F_2^{eff} , which clearly depends on redshift. At $z \gtrsim 1$, the F_2^{eff} modeling and the simulations are in good agreement at $k \lesssim 0.2 h \text{ Mpc}^{-1}$. At $k > 0.2 h \text{ Mpc}^{-1}$, although the F_2^{eff} modeling predicts larger broad-band power of the normalized integrated bispectrum, the BAO amplitudes still agree well with the simulations. This is most obvious for the two BAO peaks at $0.25 h \text{ Mpc}^{-1} \leq k \leq 0.35 h \text{ Mpc}^{-1}$. On the other hand, at $z = 0$, the F_2^{eff} modeling predicts much larger normalized integrated bispectrum on small

scales than measured in the simulations, so that the fitting formula does not perform much better than tree-level perturbation theory at $z = 0$.

4.3 Separate universe approach

In the second approach, we compute the effects of a long-wavelength density fluctuation on the small-scale power spectrum by treating each over- and under dense region as a separate universe with a different background density. This approach thus neglects the finite size of the subvolumes and is valid for wavenumbers which satisfy $kL \gg 1$ (specifically, $kL \gtrsim 50$ for percent-level accuracy).

The power spectrum in a separate universe with an infinite-wavelength density perturbation, $\bar{\delta}$, with respect to the global flat Λ CDM cosmology can be expanded as in eq. (4.6). Through eqs. (4.7)–(4.8), the normalized integrated bispectrum is equal to the linear response of the nonlinear matter power spectrum at wavenumber k to $\bar{\delta}$:

$$\frac{iB_L(k)}{P(k)\sigma_L^2} = \frac{d \ln P(k)}{d\bar{\delta}} . \quad (4.23)$$

This is not exactly true if the subvolumes for which $iB_L(k)$ is measured are not spherical. For example, since the cubic window function is anisotropic, the integrated bispectrum might pick up contributions from the tidal field. However, we have verified that the anisotropy of the cubic window function has a negligible effect, by computing the dipole and quadrupole of the integrated bispectrum through eq. (4.3). The ratios to the monopole are less than 10^{-5} on the scales of interest.

A universe with an infinite-wavelength density perturbation with respect to a flat fiducial cosmology is equivalent to a universe with non-zero curvature. This alters the scale factor, Hubble rate, and linear growth as shown in chapter 3, and thus affects the power spectrum. Say this long-wavelength overdensity is

$$\bar{\delta}(t) = \frac{\tilde{\bar{\rho}}(t)}{\bar{\rho}(t)} - 1 = \frac{D(t)}{D(t_0)} \bar{\delta}(t_0) , \quad (4.24)$$

where $\bar{\rho}(t)$ is the background matter density in the fiducial cosmology, $D(t)$ is the linear growth factor in the same cosmology, $\tilde{\bar{\rho}}$ is the background matter density in a slightly curved universe, t_0 is a reference time such that $a(t_0) = 1$, and $\bar{\delta}_0$ is the density perturbation at t_0 . Note that as in chapter 3, we denote the quantities in the modified (curved) cosmology with a tilde.

In eq. (4.24) and in the following of this section, we assume that $\bar{\delta}(t)$ is small and evolves linearly. This is justified because here we consider the subvolume to be $300 h^{-1}$ Mpc, and so $\sigma_L^2(z=0) \sim 9 \times 10^{-4}$. One can also see this in figure 4.1: $|\hat{\bar{\delta}}(\mathbf{r}_L)| \lesssim 0.08$ in 512 subvolumes with $L = 300 h^{-1}$ Mpc of one realization at $z = 0$. Therefore, we shall consider the effect on the power spectrum only to the linear order in $\bar{\delta}(t)$, and drop $\bar{\delta}^n(t)$ for $n \geq 2$.

With this assumption, the scale factor in the modified cosmology is given by

$$\tilde{a}(t) = a(t) \left[1 - \frac{1}{3} \bar{\delta}(t) \right] . \quad (4.25)$$

Since the physical coordinates are the same in two cosmologies, this implies that the comoving coordinates of the two cosmologies are related by

$$\tilde{\mathbf{x}} = \frac{a(t)}{\tilde{a}(t)} \mathbf{x} = \left[1 + \frac{1}{3} \bar{\delta}(t) \right] \mathbf{x} . \quad (4.26)$$

What we want is to compare the observables between the fiducial and modified cosmologies, so the quantities computed in the comoving coordinates of the modified cosmology have to be mapped to that with respect to the comoving coordinates of the fiducial cosmology. Specifically, in order to match to the comoving coordinates of the fiducial cosmology, we transform the comoving coordinates in the modified cosmology as

$$\check{\mathbf{x}} = \left[1 - \frac{1}{3} \bar{\delta}(t) \right] \tilde{\mathbf{x}} = c \tilde{\mathbf{x}} \quad (4.27)$$

where c is a constant at a given time. This assures $\check{\mathbf{x}} = \mathbf{x}$.

Let us now consider how the transform in the coordinates affects the two-point statistics. Since the correlation function is a dimensionless scalar quantity, in the new coordinates $\check{\mathbf{x}}$ with the transformation of $\check{x}_i = c_i x_i$ (for $i = 0, 1$, and 2) the correlation function $\check{\xi}(\check{\mathbf{x}})$ must be

$$\check{\xi}(\check{x}_0, \check{x}_1, \check{x}_2) = \xi(x_0, x_1, x_2) . \quad (4.28)$$

The power spectrum is then transformed as

$$\begin{aligned} \check{P}(\check{k}_0, \check{k}_1, \check{k}_2) &= \int d^3 \check{x} \check{\xi}(\check{x}_0, \check{x}_1, \check{x}_2) e^{-i(\check{x}_0 \check{k}_0 + \check{x}_1 \check{k}_1 + \check{x}_2 \check{k}_2)} \\ &= c_0 c_1 c_2 \int d^3 x \xi(x_0, x_1, x_2) e^{-i(c_0 x_0 \check{k}_0 + c_1 x_1 \check{k}_1 + c_2 x_2 \check{k}_2)} \\ &= c_0 c_1 c_2 \int d^3 x \xi(x_0, x_1, x_2) e^{-i(x_0 k_0 + x_1 k_1 + x_2 k_2)} \\ &= c_0 c_1 c_2 P(k_0, k_1, k_2) = c_0 c_1 c_2 P(c_0 \check{k}_0, c_1 \check{k}_1, c_2 \check{k}_2) , \end{aligned} \quad (4.29)$$

where we define $\check{k}_i = c_i^{-1} k_i$. This makes sense because $k \sim x^{-1}$ and so $\check{k}_i \sim \check{x}_i^{-1} = c_i^{-1} x_i^{-1} \sim c_i^{-1} k_i$ (see also appendix A of [123]).

Inserting c through eq. (4.27), we have the change in power spectrum up to the linear order of $\bar{\delta}(t)$ as

$$\begin{aligned} \tilde{P}(k, t) &\rightarrow \left[1 - \frac{1}{3} \bar{\delta}(t) \right]^3 P \left(k \left[1 - \frac{1}{3} \bar{\delta}(t) \right], t \right) \\ &= [1 - \bar{\delta}(t)] P(k, t) \left[1 - \frac{1}{3} \frac{d \ln P(k, t)}{d \ln k} \bar{\delta}(t) \right] \\ &= P(k, t) \left[1 - \frac{1}{3} \frac{d \ln k^3 P(k, t)}{d \ln k} \bar{\delta}(t) \right] . \end{aligned} \quad (4.30)$$

Eq. (4.30) is also known as the “dilation” effect in [97, 98], which is the consequence that the presence of the long-wavelength overdensity perturbation slows down the local expansion rate.

Another effect arises due to the change in the “reference density”. That is, the background density in two cosmologies are related by $\tilde{\rho}(t) = \rho(t) [1 + \bar{\delta}(t)]$, and since power spectrum is proportional to density squared, in the overdense universe the power spectrum at the linear order of $\bar{\delta}(t)$ becomes

$$\tilde{P}(\tilde{k}, t) \rightarrow [1 + \bar{\delta}(t)]^2 \tilde{P}(\tilde{k}, t) = [1 + 2\bar{\delta}(t)] \tilde{P}(\tilde{k}, t). \quad (4.31)$$

Combining the effects of dilation and the reference density, and using the scale factor instead of time, the power spectrum in the presence of $\bar{\delta}$ is given by

$$\begin{aligned} P(k, a|\bar{\delta}) &= [1 + 2\bar{\delta}(t)] \tilde{P}(k, \tilde{a}) \left[1 - \frac{1}{3} \frac{d \ln k^3 P(k, t)}{d \ln k} \bar{\delta}(t) \right] \\ &= \tilde{P} \left(k, a \left[1 - \frac{1}{3} \bar{\delta}(a) \right] \right) \left[1 + \left(2 - \frac{1}{3} \frac{d \ln k^3 P(k, a)}{d \ln k} \right) \bar{\delta}(a) \right]. \end{aligned} \quad (4.32)$$

Note that this expression is only valid to linear order in $\bar{\delta}$.

Both $P(k)$ and $\bar{\delta}$ are measured in a finite volume, described by the window function W_L . In order to take this into account, eq. (4.32) is convolved by the window function. Note that we take the convolution *after* applying the derivative $d \ln k^3 P(k)/d \ln k$, rather than taking the derivative of the convolved power spectrum. This is because the window function is fixed in terms of observed coordinates (in the fiducial cosmology), i.e., it is not subject to the rescaling of eq. (4.26). Taking the slope of the convolved power spectrum would correspond to a window function defined in the “local” curved cosmology.

4.3.1 Linear power spectrum

For the linear power spectrum, P_l , we have

$$\tilde{P}_l \left(k, a \left[1 - \frac{1}{3} \bar{\delta}(a) \right] \right) = \left(\frac{\tilde{D} \left(a \left[1 - \frac{1}{3} \bar{\delta}(a) \right] \right)}{D(a)} \right)^2 P_l(k, a). \quad (4.33)$$

As shown in section 3.2.2 (see also appendix D of [11]), the linear growth factor is changed following

$$\tilde{D} \left(a \left[1 - \frac{1}{3} \bar{\delta}(a) \right] \right) = D(a) \left[1 + \frac{13}{21} \bar{\delta}(a) \right], \quad (4.34)$$

where $D(a)$ is the growth factor in the fiducial cosmology. The prefactor 13/21 is only strictly valid for an Einstein-de Sitter cosmology; however, the cosmology dependence is very mild. The fractional difference of $d \ln D(a)/d \bar{\delta}$ between Λ CDM cosmology and Einstein-de Sitter universe at $z = 0$ is at the 0.1% level.

Putting everything together, eq. (4.32) yields for the linear response function of the linear power spectrum

$$\frac{d \ln P_l(k, a)}{d\bar{\delta}(a)} = \frac{68}{21} - \frac{1}{3} \frac{d \ln k^3 P_l(k, a)}{d \ln k}. \quad (4.35)$$

This result (which again is only exact for Einstein-de Sitter) matches the expression derived from the F_2 kernel given in eq. (4.22).

4.3.2 SPT 1-loop power spectrum

Expanding matter density fluctuations to third order, one obtains the so-called ‘‘SPT 1-loop power spectrum’’ given by $P(k, a) = P_l(k, a) + P_{22}(k, a) + 2P_{13}(k, a)$, where [17]

$$\begin{aligned} P_{22}(k, a) &= 2 \int \frac{d^3 q}{(2\pi)^3} P_l(q, a) P_l(|\mathbf{k} - \mathbf{q}|, a) [F_2(\mathbf{q}, \mathbf{k} - \mathbf{q})]^2, \\ 2P_{13}(k, a) &= \frac{2\pi k^2}{252} P_l(k, a) \int_0^\infty \frac{dq}{(2\pi)^3} P_l(q, a) \\ &\quad \times \left[100 \frac{q^2}{k^2} - 158 + 12 \frac{k^2}{q^2} - 42 \frac{q^4}{k^4} + \frac{3}{k^5 q^3} (q^2 - k^2)^3 (2k^2 + 7q^2) \ln \left(\frac{k+q}{|k-q|} \right) \right]. \end{aligned} \quad (4.36)$$

Both P_{22} and P_{13} are proportional to $D^4(a)$. Modifying the growth factor as described in section 4.3.1, we obtain the linear response function of the SPT 1-loop power spectrum as

$$\frac{d \ln P(k, a)}{d\bar{\delta}(a)} = \frac{68}{21} - \frac{1}{3} \frac{d \ln k^3 P(k, a)}{d \ln k} + \frac{26}{21} \frac{P_{22}(k, a) + 2P_{13}(k, a)}{P(k, a)}. \quad (4.37)$$

Note that this can easily be generalized to n loops in perturbation theory by using that $d \ln P_{(n\text{-loop})}(k, a) / d \ln D(a) = 2n + 2$. We include the window function effect by computing $\text{conv}[dP(k)/d\bar{\delta}]/\text{conv}[P(k)]$.

Figure 4.4 compares the linear theory and the SPT 1-loop predictions with the N -body simulation results. The SPT 1-loop prediction captures the damping of BAOs due to nonlinear evolution, and agrees well with the simulation results at $z = 1, 2$, and 3 . This is expected from the excellent performance of the 1-loop matter power spectrum at high redshifts as demonstrated by [77]. The agreement degrades rapidly at $z = 0$, also as expected. Note that comparing $z = 2$ and 3 , the 1-loop prediction seems to agree better with the measurements at $z = 2$. However, as mentioned in section 4.1, transients and other systematics might have an impact of up to 5% on the measurements at $z = 3$, which is larger than the difference shown in the top left panel of figure 4.4.

4.3.3 halofit and Coyote emulator

We now apply the separate universe approach to simulation-calibrated fitting formulae for the nonlinear matter power spectrum, specifically the halofit prescription [152] and the

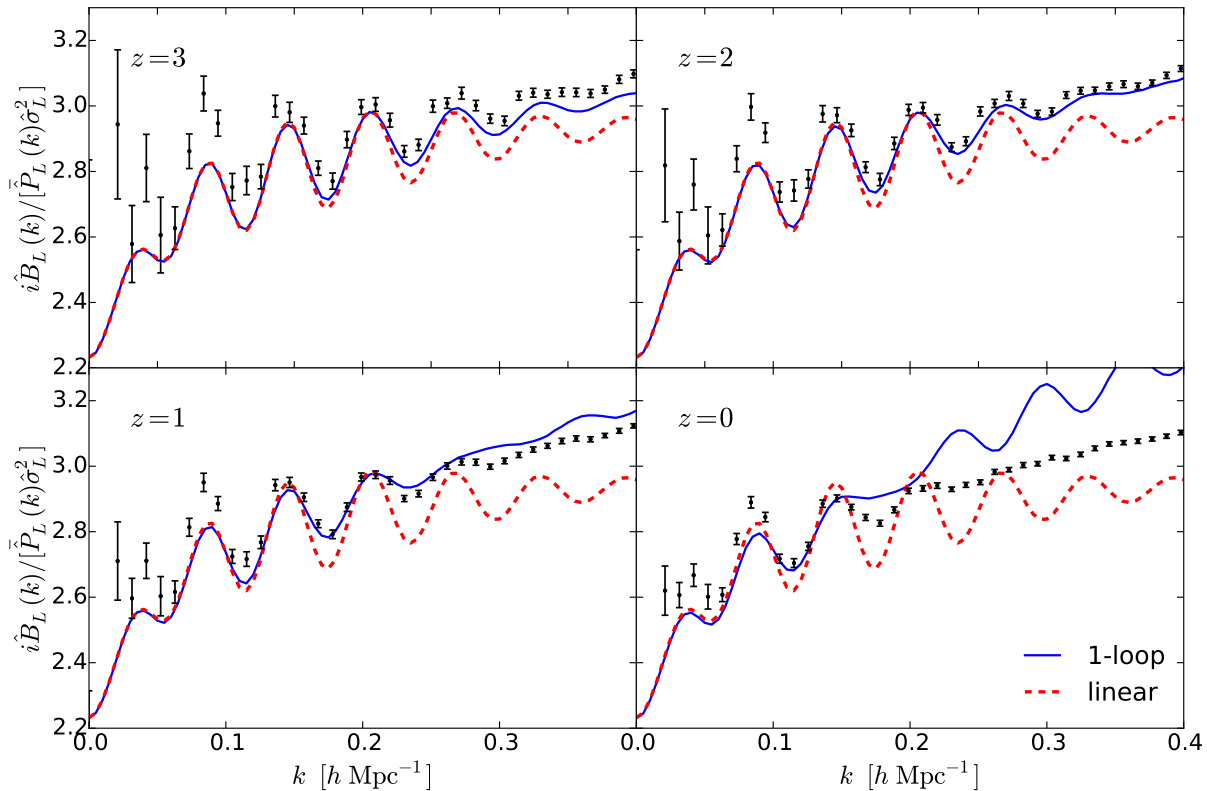


Figure 4.4: Normalized integrated bispectrum from the N -body simulations (points with error bars) and the linear response functions, $d \ln \tilde{P}(k, a) / d \delta(a)$, computed from the separate universe approach combined with perturbation theory. The red dashed lines show the linear theory results (eq. (4.35)), while the blue solid lines show the SPT 1-loop results (eq. (4.37)). The agreement between the 1-loop predictions and the simulation results is very good at $z \geq 1$. Note that the difference between the normalized integrated bispectrum and the linear response function at $k \lesssim 0.2 \text{ h Mpc}^{-1}$ is due to the squeezed limit not being reached yet (see the text below eq. (4.22)).

Coyote emulator [70]. These prescriptions yield $\tilde{P}(k, a)$ for a given set of cosmological parameters, so that eq. (4.32) can be immediately applied. However, the Coyote emulator does not provide predictions for curved cosmologies, and we hence adopt a simpler approach here.

In case of the linear power spectrum, the effect of the modified cosmology enters only through the modified growth factor given in eq. (4.34). Correspondingly, we can approximate the effect on the nonlinear power spectrum by a change in the value of the power spectrum normalization σ_8 at redshift zero,

$$\sigma_8 \rightarrow \left[1 + \frac{13}{21} \bar{\delta}_0 \right] \sigma_8, \quad (4.38)$$

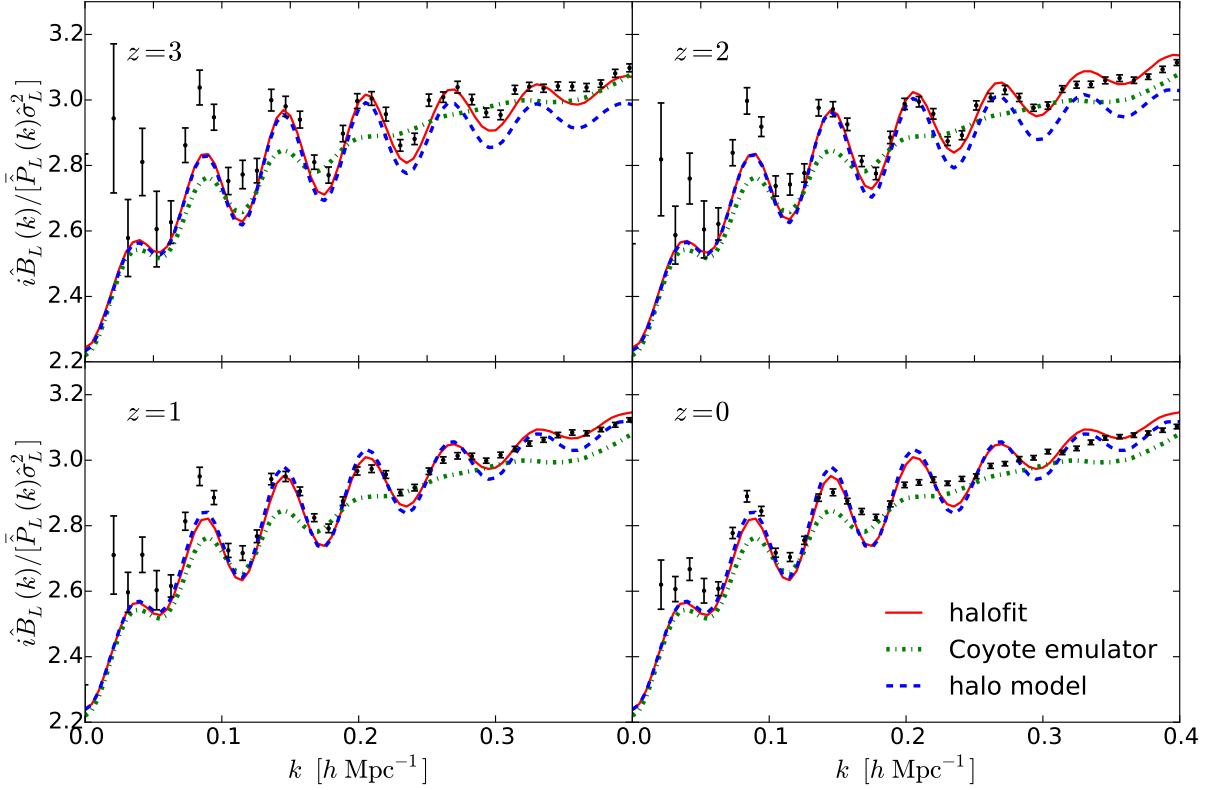


Figure 4.5: Same as figure 4.4, but for the linear response functions computed from halofit (red solid), the Coyote emulator (green dot-dashed), and the halo model (blue dashed).

where we have used the Einstein-de Sitter prediction. Therefore, the nonlinear power spectrum response becomes

$$\frac{d \ln P_{nl}(k, a)}{d \bar{\delta}(a)} = \frac{13}{21} \frac{d \ln P_{nl}(k, a)}{d \ln \sigma_8} + 2 - \frac{1}{3} \frac{d \ln k^3 P_{nl}(k, a)}{d \ln k}. \quad (4.39)$$

The results of applying eq. (4.39) to halofit (red solid) and the Coyote emulator (green dot-dashed) are shown in figure 4.5. In terms of broad-band power, the halofit prediction provides a good match. However, the predicted BAO amplitude are larger than the measurement, especially at low redshift at $k \gtrsim 0.3 h \text{ Mpc}^{-1}$. Also, while the BAO phases of halofit follow the SPT prediction, there are some differences with respect to the measurement of the N -body simulations due to the nonlinear evolution. The Coyote emulator performs to better than $\sim 2\%$ over the entire range of scales and redshifts. It slightly underpredicts the small-scale power at $k > 0.3 h \text{ Mpc}^{-1}$ for $z \geq 1$. For redshifts $z \geq 2$ and on the scales considered, the 1-loop predictions are of comparable accuracy to the Coyote emulator, while the latter provides a better fit at lower redshifts. Finally, note also our previous caveat regarding transients at the end of section 4.3.2.

4.3.4 Halo model

In the halo model (see [35] for a review), all matter is assumed to be contained within halos with a certain distribution of mass given by the mass function, and a certain density profile. Along with the clustering properties of the halos, these quantities then determine the statistics of the matter density field on all scales including the nonlinear regime. N -point functions can be conveniently decomposed into one- through N -halo pieces. In the following, we will follow the most common halo model approach and assume a linear local bias of the halos.

Adopting the notation of [157], the halo model power spectrum, $P^{\text{HM}}(k)$, is given by

$$P^{\text{HM}}(k) = P^{2\text{h}}(k) + P^{1\text{h}}(k) , \quad P^{2\text{h}}(k) = [I_1^1(k)]^2 P_l(k) , \quad P^{1\text{h}}(k) = I_2^0(k, k) , \quad (4.40)$$

where

$$I_m^n(k_1, \dots, k_m) \equiv \int d \ln M \, n(\ln M) \left(\frac{M}{\bar{\rho}} \right)^m b_n(M) u(M|k_1) \cdots u(M|k_m) , \quad (4.41)$$

and $n(\ln M)$ is the mass function (comoving number density per interval in log mass), M is the halo mass, $b_n(M)$ is the n -th order local bias parameter, and $u(M|k)$ is the dimensionless Fourier transform of the halo density profile, for which we use the NFW profile [118]. We normalize u so that $u(M|k \rightarrow 0) = 1$. The notation given in eq. (4.41) assumes $b_0 \equiv 1$. $u(M|k)$ depends on M through the scale radius r_s , which in turn is given through the mass-concentration relation. All functions of M in eq. (4.41) are also functions of z although we have not shown this for clarity. In the following, we adopt the Sheth-Tormen mass function [149] with the corresponding peak-background split bias, and the mass-concentration relation of [24]. The exact choice of the latter has negligible impact on the mildly nonlinear scales, but does not affect the conclusion.

We now derive how the power spectrum given in eq. (4.40) responds to an infinitely long-wavelength density perturbation $\bar{\delta}$, as was done for the halofit and Coyote emulator approaches. For this, we consider the one-halo and two-halo terms separately. The key physical assumption we make is that halo profiles in *physical* coordinates are unchanged by the long-wavelength density perturbation. That is, halos at a given mass M in the presence of $\bar{\delta}$ have the same scale radius r_s and scale density $\rho(r_s)$ as in the fiducial cosmology. This assumption, which is related to the stable clustering hypothesis, can be tested independently with simulations, but we shall leave it for future work. Given this assumption, the density perturbation $\bar{\delta}$ then mainly affects the linear power spectrum, which determines the halo-halo clustering (two-halo term), and the abundance of halos at a given mass.

We begin with the two-halo term. The response of the linear power spectrum is given by eq. (4.35). The expression for the two-halo term in eq. (4.40) is simply the convolution (in configuration space) of the halo correlation function in the linear bias model with the halo density profiles. By assumption, the density profiles do not change, hence I_1^1 only changes through the bias $b_1(M)$ and the mass function $n(\ln M)$. The bias $b_N(M)$

quantifies the N -th order response of the mass function $n(\ln M)$ to an infinite-wavelength density perturbation [115, 137]:

$$b_N(M) = \frac{1}{n(\ln M)} \left. \frac{\partial^N n(\ln M)}{\partial \bar{\delta}^N} \right|_{\bar{\delta}=0}. \quad (4.42)$$

We then have

$$\begin{aligned} \left. \frac{\partial n(\ln M)}{\partial \bar{\delta}} \right|_{\bar{\delta}=0} &= b_1(M) n(\ln M), \\ \left. \frac{\partial b_1(M)}{\partial \bar{\delta}} \right|_{\bar{\delta}=0} &= -[b_1(M)]^2 + b_2(M). \end{aligned} \quad (4.43)$$

Thus,

$$\begin{aligned} \frac{\partial}{\partial \bar{\delta}} I_1^1(k) &= \int d \ln M n(\ln M) \left(\frac{M}{\bar{\rho}} \right) \{ [b_1(M)]^2 - [b_1(M)]^2 + b_2(M) \} u(M|k) \\ &= \int d \ln M n(\ln M) \left(\frac{M}{\bar{\rho}} \right) b_2(M) u(M|k) \\ &= I_1^2(k). \end{aligned} \quad (4.44)$$

In the large-scale limit, $k \rightarrow 0$, this vanishes by way of the halo model consistency relation

$$\int d \ln M n(\ln M) \left(\frac{M}{\bar{\rho}} \right) b_N(M) = \begin{cases} 1, & N = 1, \\ 0, & N \geq 1. \end{cases} \quad (4.45)$$

For finite k however, eq. (4.44) does not vanish. Thus, the linear response function of the two-halo term becomes

$$\left. \frac{dP^{2h}(k)}{d\bar{\delta}} \right|_{\bar{\delta}=0} = \left[\frac{68}{21} - \frac{1}{3} \frac{d \ln k^3 P_l(k)}{d \ln k} \right] P^{2h}(k) + 2I_1^2(k) I_1^1(k) P_l(k). \quad (4.46)$$

Note that we recover the tree-level result given in eq. (4.35) in the large-scale limit. Strictly speaking, this expression is not consistent, since the term I_1^2 implies a non-zero b_2 while in eq. (4.40) we have assumed a pure linear bias. Of course, if we allowed for b_2 in eq. (4.40), we would obtain a contribution from b_3 in eq. (4.46), and so on. This reflects the fact that the halo model itself cannot be made entirely self-consistent. Note that in eq. (4.46) the slope is taken from the *linear*, not two-halo power spectrum. This is a consequence of our assumption that halo profiles do not change due to $\bar{\delta}$; in other words, having $d \ln k^3 P^{2h} / d \ln k$ would imply that the profiles do change (in the sense that they are fixed in comoving, rather than physical coordinates).

We now turn to the one-halo term. Given our assumption about density profiles, this term is much simpler. The only effect is the change in the mass function, which through eq. (4.42) (for $N = 1$) yields

$$\frac{\partial}{\partial \bar{\delta}} I_2^0(k, k) = I_2^1(k, k). \quad (4.47)$$

We thus obtain

$$\left. \frac{dP^{1h}(k)}{d\bar{\delta}} \right|_{\bar{\delta}=0} = I_2^1(k, k). \quad (4.48)$$

Putting everything together, we obtain

$$\left. \frac{d \ln P^{\text{HM}}(k)}{d\bar{\delta}} \right|_{\bar{\delta}=0} = [P^{\text{HM}}(k)]^{-1} \left[\left(\frac{68}{21} - \frac{1}{3} \frac{d \ln k^3 P_l(k)}{d \ln k} \right) P^{2h}(k) + 2I_1^2(k) I_1^1(k) P_l(k) + I_2^1(k, k) \right]. \quad (4.49)$$

The prediction of eq. (4.49) is shown as the blue dashed lines in figure 4.5. The amplitude and broad-band shape agree with the simulations well. The main discrepancy in the halo model prediction is the insufficient damping of the BAO wiggles.

An alternative approach to derive the halo model prediction for $iB_L(k)$ is to use higher N -point functions [84, 97], which are decomposed into one-, \dots , N -halo terms. We now compare eq. (4.49) with the results of [97], which were derived from the halo model four-point function in the collapsed limit. Note that the squeezed limit is assumed in both approaches. Their eq. (27) is

$$\left. \frac{d \ln P^{\text{HM}}(k)}{d\bar{\delta}} \right|_{\bar{\delta}=0} = [P^{\text{HM}}(k)]^{-1} \left[\left(\frac{68}{21} - \frac{1}{3} \frac{d \ln k^3 P^{2h}(k)}{d \ln k} \right) P^{2h}(k) + I_2^1(k, k) \right]. \quad (4.50)$$

There are two differences to eq. (4.49): the term $\propto I_1^2$ is absent, and the slope is taken from P^{2h} rather than P_l . The I_1^2 term is absent in eq. (4.50) as by assumption b_2 was taken to be zero in the four-point function of [97]; as discussed above, its inclusion is somewhat ambiguous given the lack of self-consistency of the halo model approach. The different power spectrum slopes are due to the different sources of this term in the two derivations. In our case, the assumption of unchanged halo profiles dictates the form of eq. (4.49). In the derivation of eq. (4.50), the slope originates from the integral over the F_2 kernel in the three-halo term, which proceeds as described in appendix A but involves P^{2h} instead of P_l . Note however that the numerical difference between eq. (4.50) and eq. (4.49) is only at the percent level.

4.4 Dependence on cosmological parameters

Both the matter power spectrum and (integrated) bispectrum depend on the cosmological parameters such as Ω_m , σ_8 , n_s . However, the normalized integrated bispectrum is much less sensitive to cosmology as the leading cosmology dependence is taken out by the normalizing denominator.

Eq. (4.37) is useful for understanding the dependence of the response function of the power spectrum (and thus the normalized integrated bispectrum) on cosmological parameters. The second term depends on the local spectral index of the matter power spectrum, $d \ln k^3 P(k) / d \ln k$, which depends on the initial power spectrum tilt, n_s , and the matter and radiation densities which change the redshift of matter-radiation equality as well as

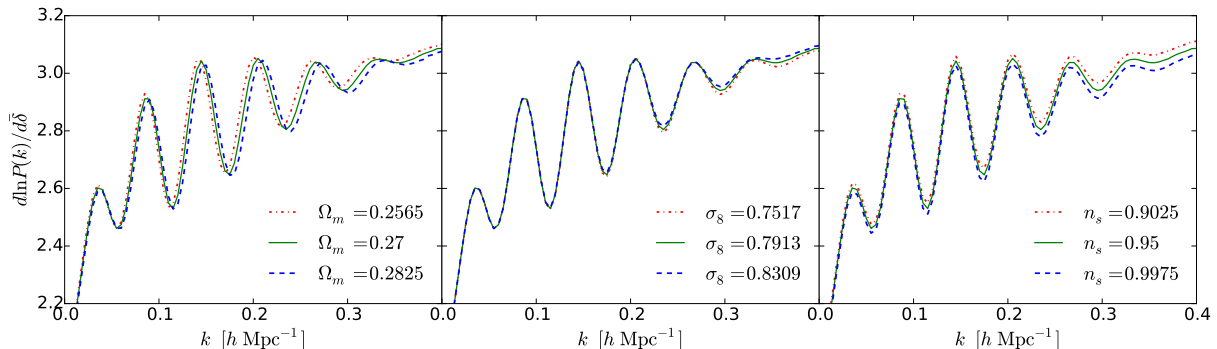


Figure 4.6: The linear response functions computed from the SPT 1-loop power spectrum with various cosmological parameters at $z = 2$. The fiducial cosmology ($\Omega_m = 0.27$, $\sigma_8 = 0.7913$, and $n_s = 0.95$) is shown in green solid lines. The red dot-dashed (blue dashed) lines represent the cosmologies with -5% ($+5\%$) of the fiducial parameters, Ω_m (left), σ_8 (middle), and n_s (right).

the BAO scale. It also depends on the shape of BAO wiggles, and increasing the amplitude of the matter power spectrum (σ_8) leads to a stronger damping of the BAO feature. Increasing σ_8 further increases the last term, which is proportional to σ_8^2 .

Figure 4.6 shows the linear response functions, $d \ln P(k, a)/d\bar{\delta}(a)$ computed from the SPT 1-loop power spectrum (eq. (4.37)) at $z = 2$ when varying cosmological parameters by $\pm 5\%$. The effects on the response functions are at the percent level or less, illustrating the weak cosmology dependence of this observable. On the scales considered, the shift in the BAO scale when varying Ω_m leads to the relatively largest effect. We expect that the sensitivity to changes in σ_8 will be higher on smaller, more nonlinear scales.

4.5 Fisher matrix calculation

Now that we understand the behavior of the integrated bispectrum, how does it compare with the full bispectrum in terms of measuring the cosmological parameters, particularly the primordial non-Gaussianity? In this section, we perform the Fisher matrix calculation (see e.g. [160] for a review) for both the full bispectrum analysis and the integrated bispectrum technique, and compare the performances between the two methods. We shall use the simplest primordial non-Gaussianity model as discussed in section 2.1.4, i.e.

$$\begin{aligned}
 B_g(\mathbf{k}_1, \mathbf{k}_2, \mathbf{k}_3) &= b_1^3 B_{\text{SPT}}(\mathbf{k}_1, \mathbf{k}_2, \mathbf{k}_3) + b_1^2 b_2 B_{b_2}(\mathbf{k}_1, \mathbf{k}_2, \mathbf{k}_3) + b_1^3 f_{\text{NL}} B_{f_{\text{NL}}}(\mathbf{k}_1, \mathbf{k}_2, \mathbf{k}_3) \\
 iB_{L,g}(k) &= b_1^3 iB_{L,\text{SPT}}(k) + b_1^2 b_2 iB_{L,b_2}(k) + b_1^3 f_{\text{NL}} iB_{L,f_{\text{NL}}}(k) .
 \end{aligned}
 \tag{4.51}$$

The Fisher matrix of the reduced bispectrum $Q(k_1, k_2, k_3) \equiv B(k_1, k_2, k_3)/[P(k_1)P(k_2) +$

2 cyclic] is given by

$$F_{Q,\alpha\beta} = \sum_{k_1, k_2, k_3 \leq k_{\max}} \frac{\partial Q(k_1, k_2, k_3)}{\partial p_\alpha} \frac{\partial Q(k_1, k_2, k_3)}{\partial p_\beta} \frac{1}{\Delta Q^2(k_1, k_2, k_3)}, \quad (4.52)$$

where (k_1, k_2, k_3) have to form a triangle, $p_\alpha \in [b_1, b_2, f_{\text{NL}}]$ are the parameters we want to constrain, and $\Delta Q^2(k_1, k_2, k_3)$ is the variance of the reduced bispectrum estimator. Similarly, the Fisher matrix of the integrated bispectrum can be written as

$$F_{ib_L, \alpha\beta} = \sum_L \sum_{k \leq k_{\max}} \frac{\partial ib_L(k)}{\partial p_\alpha} \frac{\partial ib_L(k)}{\partial p_\beta} \frac{1}{\Delta ib_L^2(k)}. \quad (4.53)$$

Here, we ignore off-diagonal elements of the covariance matrix of Q or ib_L . In general, nonlinear evolution generates non-vanishing covariances. This is, however, justified at high redshift ($z \geq 2$) as we show in the right panel of figure B.1.

The variance of the estimator for the integrated bispectrum is computed in appendix B. The variance of the estimator for the bispectrum is computed [144]

$$\Delta B^2(k_1, k_2, k_3) = \frac{\pi s_{123}}{k_1 k_2 k_3} P(k_1) P(k_2) P(k_3), \quad (4.54)$$

where $s_{123} = 6, 2, 1$ for equilateral, isosceles, and general triangles, respectively (we set Δk to be the fundamental frequency). Similar to the integrated bispectrum, we assume that the variance of the reduced bispectrum is dominated by the numerators, so

$$\Delta Q^2(k_1, k_2, k_3) \approx \frac{\Delta B^2(k_1, k_2, k_3)}{[P(k_1)P(k_2) + 2 \text{ cyclic}]^2}. \quad (4.55)$$

Since galaxies are observed in redshift space, we model the redshift-space distortions by the simple Kaiser factor, $P_z = K_p P_r$ and $B_z = K_b B_r$, where the subscripts r and z denote the real- and redshift-space quantities, and

$$K_p = 1 + \frac{2f}{3b_1} + \frac{1}{5} \left(\frac{f}{b_1} \right)^2, \quad K_b = 1 + \frac{2f}{3b_1} + \frac{1}{9} \left(\frac{f}{b_1} \right)^2 \quad (4.56)$$

with $f = d \ln D / d \ln a$ being the growth rate. The derivatives of Q and ib_L with respect to b_1 thus contain the contributions from dK_p/db_1 and dK_b/db_1 . The variances of the redshift-space reduced bispectrum and the normalized integrated bispectrum with the Poisson shot noise are then given by

$$\begin{aligned} \Delta Q^2(k_1, k_2, k_3) &\approx \frac{\pi s_{123}}{k_1 k_2 k_3} \frac{[P_z(k_1) + P_{\text{shot}}][P_z(k_2) + P_{\text{shot}}][P_z(k_3) + P_{\text{shot}}]}{[P_z(k_1)P_z(k_2) + 2 \text{ cyclic}]^2} \\ \Delta ib_L^2(k) &\approx \frac{V_L}{V_r N_{kL}} \frac{[\sigma_{L,z}^2 + P_{\text{shot}}/V_L][P_{L,z}(k) + P_{\text{shot}}]^2}{\sigma_{L,z}^4 P_{L,z}^2(k)}, \end{aligned} \quad (4.57)$$

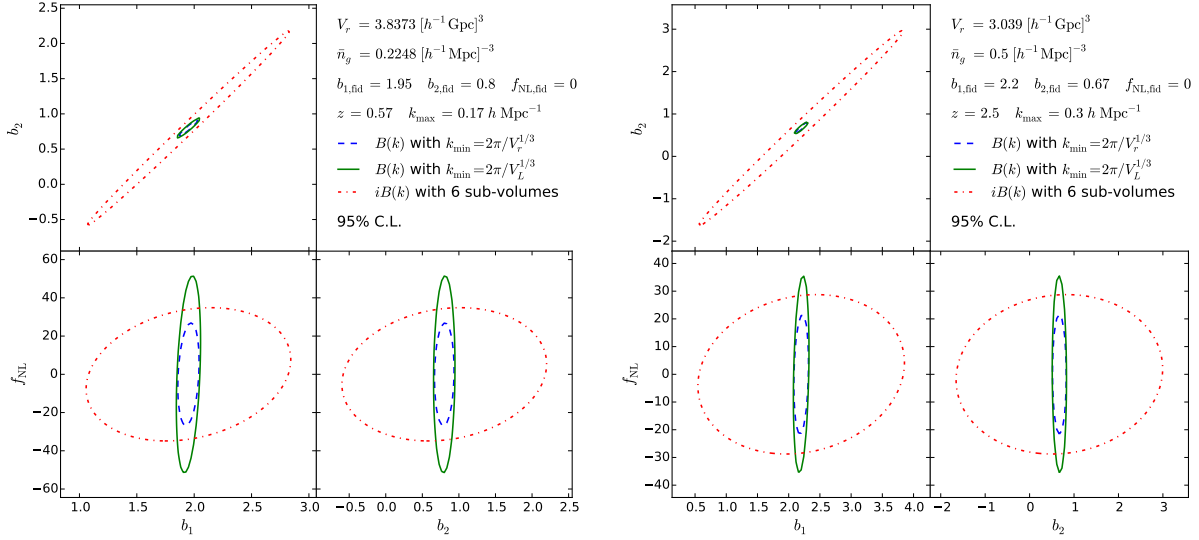


Figure 4.7: Two-dimensional joint 95% C.L. constraints on galaxy bias and primordial non-Gaussianity for BOSS (left) and HETDEX (right). The survey parameters are in the top right panel. The top left, bottom left, and bottom right panels show the joint constraints on (b_1, b_2) , (b_1, f_{NL}) , and (b_2, f_{NL}) marginalized over f_{NL} , b_2 , and b_1 , respectively. The blue dashed, green solid, and red dot-dashed lines are for full bispectrum with $k_{\text{min}} = k_F = 2\pi/V_r^{1/3}$, full bispectrum with $k_{\text{min}} = k_{F,L} = 2\pi/L$ where L is the largest subvolume size ($600 h^{-1}$ Mpc), and integrated bispectrum for six sizes of subvolumes ($100 h^{-1}$ Mpc to $600 h^{-1}$ Mpc with an increment of $100 h^{-1}$ Mpc), respectively.

where $P_z(k) = b_1^2 K_p P_L(k)$, $\sigma_{L,z}^2 = b_1^2 K_p \sigma_L^2$, and $P_{L,z}(k) = b_1^2 K_p P_L(k)$.

Figure 4.7 shows the two-dimensional joint 95% C.L. constraints on galaxy bias and primordial non-Gaussianity for BOSS [4] (left) and HETDEX [71] (right). The survey parameters and the fiducial cosmological parameters are shown in the top-right of each panel. The blue dashed line is the full bispectrum analysis with $k_{\text{min}} = 2\pi/V_r^{1/3}$ being the fundamental frequency of the entire survey V_r ; the green solid line is the full bispectrum analysis with $k_{\text{min}} = 2\pi/V_L^{1/3}$ being the fundamental frequency of the largest subvolume for the integrated bispectrum ($V_L = [600 h^{-1} \text{ Mpc}]^3$); the red dot-dashed line is the integrated bispectrum with six sizes of subvolumes from $100 h^{-1}$ Mpc to $600 h^{-1}$ Mpc (with an increment of $100 h^{-1}$ Mpc) with $k_{\text{min}} = 2\pi/V_L^{1/3}$ being the fundamental frequency of the corresponding subvolumes.

One finds that as long as k_{min} is set to be the fundamental frequency of the largest subvolume, the integrated bispectrum technique gives the similar constraint on f_{NL} compared to the full bispectrum analysis.² On the other hand, the integrated bispectrum has

²Note that the numerical results are sensitive to the choices of k_{min} and k_{max} because we count the Fourier modes in this range. For different lines, although k_{max} is set to be the same, in practice we stop

poor constraints on b_1 and b_2 compared to the full bispectrum analysis. In particular, in the top-left panel the signal of integrated bispectrum has a strong degeneracy between b_1 and b_2 . This is somewhat expected because in figure 2.1 one finds that not only the black solid and black dashed lines have similar scale dependences in a given subvolume, but in different subvolumes they all have similar contribution, unlike the bispectrum of the primordial non-Gaussianity. This thus makes it difficult to break the degeneracy between b_1 and b_2 using the integrated bispectrum.

We also find that while the full bispectrum analysis and the integrated bispectrum technique give similar constraints on f_{NL} , the number of counted Fourier modes differ dramatically. For example, for the BOSS parameter, the full bispectrum analysis with $k_{\text{min}} = 2\pi/V_r^{1/3}$ counts 7113 configurations of triangles, whereas the integrated bispectrum technique counts only 54 Fourier modes. Even if k_{min} is set to be $2\pi/V_L^{1/3}$ for the full bispectrum analysis, there are still 6730 configurations of triangles. This is a big advantage for the integrated bispectrum technique because estimating the covariance matrix from mock catalogs would require a large number of realizations, which will be difficult (but not impossible) to obtain for the full bispectrum. This difference in the number of counted Fourier modes also explains why the full bispectrum analysis has much better constraints on b_1 and b_2 . However, many of the triangles do not contain much more information on f_{NL} , so if one is interested in measuring f_{NL} , the integrated bispectrum technique provides an easier approach and captures most of the information.

4.6 Discussion and conclusion

In this chapter, we have demonstrated a novel method to measure the squeezed-limit bispectrum. By measuring the correlation between the mean density fluctuation and the position-dependent power spectrum, we obtain a measurement of an integral of the bispectrum (integrated bispectrum) without having to actually measure three-point correlations in the data. The integrated bispectrum is dominated by the squeezed-limit bispectrum, which is much easier to model than the full bispectrum for all configurations. This is evidenced by figure 4.4 and figure 4.5, where we show model predictions accurate to a few percent using existing techniques and without tuning any parameters.

A further, key advantage of this new observable is that both the mean density fluctuation and the power spectrum are significantly easier to measure in actual surveys than the bispectrum in terms of survey selection functions. In particular, the procedures developed for power spectrum estimation can be directly applied to the measurement of the position-dependent power spectrum. Additionally, the position-dependent power spectrum depends on only one wavenumber (at fixed size of the subvolume) rather than the three wavenumbers of the bispectrum. Consequently, the covariance matrix also becomes easier

counting Fourier modes if $k > k_{\text{max}}$. Therefore they have different “true” k_{max} , and the contour area would be affected, especially the green solid lines seem to have slightly worse constraints on f_{NL} compared to the red dot-dashed lines. Here, however, what we are interested in is the general properties between different methods, so we should neglect the effect due to different k_{max} .

to model.

We have measured the position-dependent power spectrum in 160 collisionless N -body simulations with Gaussian initial conditions, and have used two different approaches, bispectrum modeling and the separate universe approach, to model the measurements. All of the approaches work well on large scales, $k \lesssim 0.2 h \text{ Mpc}^{-1}$, and at high redshift. On small scales, where nonlinearities become important, the separate universe approach (section 4.3) applied through the Coyote emulator prescription performs best at redshifts $z < 2$, while the SPT 1-loop predictions perform equally well at $z \geq 2$. Both show agreement to within a few percent up to $k = 0.4 h \text{ Mpc}^{-1}$. Accurate predictions for the position-dependent power spectrum on these and even smaller scales can be obtained by applying the separate universe approach to dedicated small-box N -body simulations of curved cosmologies, as described in section 6.2.

The normalized integrated bispectrum is relatively insensitive to changes in cosmological parameters (section 4.4), and we do not expect that it will allow for competitive cosmology constraints. On the other hand, this property can also be an advantage: since this observable can be predicted accurately without requiring a precise knowledge of the cosmology, it can serve as a useful systematics test for example in weak lensing surveys. As an example, consider eq. (4.4) applied to shear measurements. A constant multiplicative bias $1 + m$ in the shear estimation contributes a factor $(1 + m)^3$ on the left hand side of the equation, and a factor $(1 + m)^4$ on the right hand side. Thus, by comparing the measured normalized integrated bispectrum with the (essentially cosmology-independent) expectation, one can constrain the multiplicative shear bias.

The position-dependent power spectrum can also naturally be applied to the case of spectroscopic galaxy surveys, in which case the nonlinear bias of the observed tracers also contributes to the bispectrum and position-dependent power spectrum. Thus, when applied to halos or galaxies, this observable can serve as an independent probe of the bias parameters and break degeneracies between bias and growth which are present when only considering the halo or galaxy power spectrum. We shall exploit this to measure the nonlinear bias of the BOSS CMASS galaxies in chapter 5.

We finally use the Fisher matrix to show that if multiple sizes of subvolumes are used, the position-dependent power spectrum captures most of the information of the local-type non-Gaussianity contained in the full bispectrum analysis, but for much less Fourier modes. This is a huge advantage for this novel technique as the computational requirement for estimating the covariance matrix is largely alleviated. Consequently, the position-dependent power spectrum provides an easier approach for hunting the primordial non-Gaussianity for future galaxy surveys.

Chapter 5

Measurement of position-dependent correlation function

In this chapter, we measure the position-dependent correlation function and the integrated three-point function from real data, the SDSS-III Baryon Oscillation Spectroscopic Survey Data Release 10 (BOSS DR10) CMASS sample [3, 6].

As introduced in section 2.2, the correlation between the position-dependent correlation function,

$$\hat{\xi}(r, \mathbf{r}_L) = \int \frac{d^2 \hat{r}}{4\pi} \hat{\xi}(\mathbf{r}, \mathbf{r}_L) = \frac{1}{V_L} \int \frac{d^2 \hat{r}}{4\pi} \int d^3 x \delta(\mathbf{r} + \mathbf{x}) \delta(\mathbf{x}) W_L(\mathbf{r} + \mathbf{x} - \mathbf{r}_L) W_L(\mathbf{x} - \mathbf{r}_L), \quad (5.1)$$

and the mean overdensity,

$$\bar{\delta}(\mathbf{r}_L) = \frac{1}{V_L} \int \frac{d^3 q}{(2\pi)^3} \delta(-\mathbf{q}) W_L(\mathbf{q}) e^{-i\mathbf{r}_L \cdot \mathbf{q}}, \quad (5.2)$$

is the integrated three-point function

$$\begin{aligned} i\zeta_L(r) &= \langle \hat{\xi}(r, \mathbf{r}_L) \bar{\delta}(\mathbf{r}_L) \rangle \\ &= \frac{1}{V_L^2} \int \frac{d^2 \hat{r}}{4\pi} \int d^3 x_1 \int d^3 x_2 \zeta(\mathbf{r} + \mathbf{x}_1 + \mathbf{r}_L, \mathbf{x}_1 + \mathbf{r}_L, \mathbf{x}_2 + \mathbf{r}_L) \\ &\quad \times W_L(\mathbf{r} + \mathbf{x}_1) W_L(\mathbf{x}_1) W_L(\mathbf{x}_2), \end{aligned} \quad (5.3)$$

where V_L is the size of the subvolume. Inspired by the behavior in the squeezed-limit where $r \ll L$, we define the normalized integrated three-point function as $i\zeta_L(r)/\sigma_L^2$ with σ_L^2 being the variance of the fluctuations in V_L . Note that when comparing the model to the measurements, we shall divide the model by $f_{L,\text{bdry}}(r)$, which is given in eq. (2.35), to correct for the boundary effect.

The integrated three-point function is simply the Fourier transform of the integrated bispectrum

$$i\zeta_L(r) = \int \frac{k^2 dk}{2\pi^2} iB_L(k) \text{sinc}(kr). \quad (5.4)$$

Therefore, if we do not have the analytical expression for the three-point function, we can first compute the integrated bispectrum and Fourier transform it to obtain the integrated three-point function. One example is the redshift-space integrated three-point function, for which we first evaluate the redshift-space integrated bispectrum with the explicit expression of the SPT redshift-space bispectrum given in appendix A.2, and then apply eq. (5.4). We also show that the precision of this operation (nine-dimensional integral in total) is within 2% on the scales of interest ($30 h^{-1} \text{ Mpc} \leq r \leq 78 h^{-1} \text{ Mpc}$, which we will justify in section 5.1.3).

This chapter is organized as follows. In section 5.1 and section 5.2, we measure the position-dependent correlation function from PTHalos mock catalogs [143, 104, 103] and the BOSS DR10 CMASS sample, respectively. The cosmological interpretation of the measurement is in section 5.3. We conclude in section 5.4.

5.1 Measurement of PTHalo mock catalogs

We first apply the position-dependent correlation function technique to the 600 PTHalo mock galaxy catalogs of the BOSS DR10 CMASS sample in the North Galactic Cap (NGC). From now on, we refer to the real and mock BOSS DR10 CMASS samples as the “observations” and “mocks”, respectively.

We use the redshift range of $0.43 < z < 0.7$, and each realization of mocks contains roughly 400,000 galaxies. We convert the positions of galaxies in RA, DEC, and redshift to comoving distances using the cosmological parameters of the mocks. The mocks have the same observational conditions as the observations, and we correct the observational systematics by weighting each galaxy differently. Specifically, we upweight a galaxy if its nearest neighbor has a redshift failure (w_{zf}) or a missing redshift due to a close pair (w_{cp}). We further apply weights to correct for the correlation between the number density of the observed galaxies and stellar density (w_{star}) and seeing (w_{see}). We apply the same weights as done in the analyses of the BOSS collaboration, namely FKP weighting, $w_{\text{FKP}} = [1 + P_w \bar{n}(z) \text{comp}]^{-1}$ [56], where $P_w = 20000 h^{-3} \text{ Mpc}^3$, and $\bar{n}(z)$ and “comp” are the expected galaxy number density and the survey completeness, respectively, provided in the catalogs. Therefore, each galaxy is weighted by $w_{\text{BOSS}} = (w_{cp} + w_{zf} - 1)w_{\text{star}}w_{\text{see}}w_{\text{FKP}}$.

In this section, we present measurements from mocks in real space in section 5.1.3 and redshift space in section 5.1.4. The application to the CMASS DR10 sample is the subject of section 5.2.

5.1.1 Dividing the subvolumes

We use SDSSPix¹ to pixelize the DR10 survey area. In short, at the lowest resolution (res=1) SDSSPix divides the sphere equally into $n_x = 36$ longitudinal slices across the hemisphere (at equator each slice is 10 degrees wide), and each slice is divided into $n_y = 13$ pieces along constant latitudes with equal area. Thus, for res=1 there are $n_x \times n_y = 468$

¹SDSSPix: <http://dls.physics.ucdavis.edu/~scranton/SDSSPix>

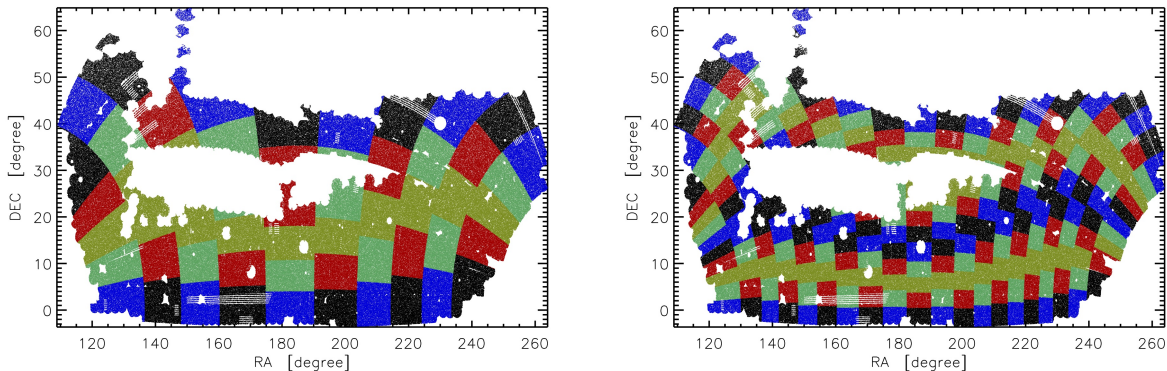


Figure 5.1: Division of random samples into subvolumes with two resolutions in the RA-DEC plane. Each colored pattern extends over the redshift direction.

pixels. In general the total number of pixels is $n'_x \times n'_y = (\text{res } n_x) \times (\text{res } n_y) = (\text{res})^2 \times 468$, and in this chapter we shall set $\text{res}=1024$. After the pixelization, the i^{th} object (a galaxy or a random sample) has the pixel number (i_x, i_y) .

We use two different subvolume sizes. To cut the irregular survey volume into subvolumes with roughly the same size, we first divide the random samples at all redshifts into 10 and 20 slices across longitudes with similar numbers of random samples; we then divide the random samples in each slice into 5 and 10 segments across latitudes with similar numbers of random samples. Figure 5.1 shows the two resolutions of our subvolumes before the redshift cuts. (Note that this resolution is different from the resolution of SDSSPix, which we always set to $\text{res}=1024$.) Each colored pattern extends over the redshift direction. Finally, we divide the two resolutions into three ($z_{\text{cut}} = 0.5108, 0.5717$) and five ($z_{\text{cut}} = 0.48710, 0.52235, 0.55825, 0.60435$) redshift bins.

As a result, there are 150 and 1000 subvolumes for the low and high resolution configurations, respectively. The sizes of the subvolumes are approximately $V_L^{1/3} = 220 h^{-1}$ Mpc and $120 h^{-1}$ Mpc, respectively². The fractional differences between the numbers of the random samples in subvolumes for the low and high resolutions are within $\begin{smallmatrix} +0.68\% \\ -0.58\% \end{smallmatrix}$ and $\begin{smallmatrix} +1.89\% \\ -1.83\% \end{smallmatrix}$, respectively. Since the number of random samples represents the effective volume, all subvolumes at a given resolution have similar effective volumes. We assign galaxies into subvolumes following the division of random samples.

²The shapes of the subvolumes are not exactly cubes. For example, for the high resolution, the ratios of square root of the area to the depth, $\sqrt{L_x L_y}/L_z$, are roughly 0.78, 1.42, 1.51, 1.28, and 0.71, from the lowest to the highest redshift bins. The results are not sensitive to the exact shape of the subvolumes, as long as the separation of the position-dependent correlation function that we are interested in is sufficiently smaller than L_x , L_y , and L_z .

5.1.2 Estimators in the subvolumes

In the i^{th} subvolume, we measure the mean overdensity with respect to the entire NGC, $\bar{\delta}_i$, and the position-dependent correlation function, $\hat{\xi}_i(r)$. The mean overdensity is estimated by comparing the total weighted galaxies to the expected number density given by the random samples, i.e.,

$$\bar{\delta}_i = \frac{1}{\alpha} \frac{w_{g,i}}{w_{r,i}} - 1, \quad \alpha \equiv \frac{\sum_{i=1}^{N_s} w_{g,i}}{\sum_{i=1}^{N_s} w_{r,i}} = \frac{w_{g,\text{tot}}}{w_{r,\text{tot}}}, \quad (5.5)$$

where $w_{g,i}$ and $w_{r,i}$ are the total weights (w_{BOSS}) of galaxies and random samples in the i^{th} subvolume, respectively, and N_s is the number of subvolumes.

We use the Landy-Szalay estimator [91] to estimate the position-dependent correlation function as

$$\hat{\xi}_{\text{LS},i}(r, \mu) = \frac{DD_i(r, \mu)}{RR_i(r, \mu)} \left(\frac{[\sum_r w_{r,i}]^2 - \sum_r w_{r,i}^2}{[\sum_g w_{g,i}]^2 - \sum_g w_{g,i}^2} \right) - \frac{DR_i(r, \mu)}{RR_i(r, \mu)} \frac{([\sum_r w_{r,i}]^2 - \sum_r w_{r,i}^2)}{\sum_g w_{g,i} \sum_r w_{r,i}} + 1, \quad (5.6)$$

where $DD_i(r, \mu)$, $DR_i(r, \mu)$, and $RR_i(r, \mu)$ are the weighted numbers of galaxy-galaxy, galaxy-random, and random-random pairs within the i^{th} subvolume, respectively, and μ is the cosine between the line-of-sight vector and the vector connecting galaxy pairs ($\mathbf{r}_1 - \mathbf{r}_2$). The summations such as $\sum_r w_{r,i}$ and $\sum_g w_{g,i}$ denote the sum over all the random samples and galaxies within the i^{th} subvolume, respectively. The angular average correlation function is then $\hat{\xi}_{\text{LS},i}(r) = \int_0^1 d\mu \hat{\xi}_{\text{LS},i}(r, \mu)$.

Eq. (5.6) estimates the correlation function assuming that the density fluctuation is measured relative to the *local* mean. However, the position-dependent correlation function defined in eq. (5.1) uses the density fluctuation relative to the *global* mean. These two fluctuations can be related by $\delta_{\text{global}} = (1 + \bar{\delta})\delta_{\text{local}} + \bar{\delta}$ with $\bar{\delta} = \bar{n}_{\text{local}}/\bar{n}_{\text{global}} - 1$. Thus, the position-dependent correlation function, $\hat{\xi}_i(r)$, is related to the Landy-Szalay estimator as

$$\hat{\xi}_i(r) = (1 + \bar{\delta}_i)^2 \hat{\xi}_{\text{LS},i}(r) + \bar{\delta}_i^2. \quad (5.7)$$

To compute the average quantities over all subvolumes, we weight by $w_{r,i}$ in the corresponding subvolume. For example, for a given variable g_i in the i^{th} subvolume, the average over all subvolumes, \bar{g} , is defined by

$$\bar{g} = \frac{1}{w_{r,\text{tot}}} \sum_{i=1}^{N_s} g_i w_{r,i}. \quad (5.8)$$

Since the number of random samples in each subvolume represents the effective volume, the average quantities are effective-volume weighted. Eq. (5.8) assures that the mean of the individual subvolume overdensities is zero,

$$\bar{\delta} = \frac{1}{w_{r,\text{tot}}} \sum_{i=1}^{N_s} \bar{\delta}_i w_{r,i} = \frac{1}{w_{r,\text{tot}}} \sum_{i=1}^{N_s} \left[\frac{1}{\alpha} w_{g,i} - w_{r,i} \right] = \frac{\alpha}{\alpha} - 1 = 0. \quad (5.9)$$

We also confirm that $\bar{\xi}(r)$ from eq. (5.7) agrees with the two-point function of all galaxies in the entire survey, on scales smaller than the subvolume size. With $\hat{\xi}_i(r)$ and $\bar{\delta}_i$, we estimate the shot-noise-corrected integrated three-point function in the subvolume of size L as

$$i\zeta(r) = \frac{1}{w_{r,\text{tot}}} \sum_{i=1}^{N_s} \left[\hat{\xi}_i(r) \bar{\delta}_i - 2\bar{\xi}(r) \frac{(1+\alpha)}{\alpha} \frac{\sum_r w_{r,i}^2}{\sum_r \bar{n}_{r,i} \text{comp}_{r,i} w_{r,i}^2} \left(\sum_r \frac{1}{\bar{n}_{r,i} \text{comp}_{r,i}} \right)^{-1} \right] w_{r,i}, \quad (5.10)$$

where the second term in the parentheses is the shot noise contribution, and $\bar{n}_{r,i}$ and $\text{comp}_{r,i}$ are the expected galaxy number density and the survey completeness, respectively, of the random samples. Similarly, we estimate the shot-noise-corrected variance of the fluctuations in the subvolumes of size L as

$$\sigma_L^2 = \frac{1}{w_{r,\text{tot}}} \sum_{i=1}^{N_s} \left[\bar{\delta}_i^2 - \frac{(1+\alpha)}{\alpha} \frac{\sum_r w_{r,i}^2}{\sum_r \bar{n}_{r,i} \text{comp}_{r,i} w_{r,i}^2} \left(\sum_r \frac{1}{\bar{n}_{r,i} \text{comp}_{r,i}} \right)^{-1} \right] w_{r,i}, \quad (5.11)$$

where the second term in the parentheses is the shot noise contribution. We find that the shot noise is subdominant (less than 10%) in both $i\zeta(r)$ and σ_L^2 .

5.1.3 Measurements in real space

Figure 5.2 shows the measurements of the two-point function $\xi(r)$ from the entire survey (top left) and the normalized integrated three-point functions (bottom panels),

$$\frac{i\zeta_L(r)}{\sigma_L^2} = \left(\frac{1}{w_{r,\text{tot}}} \sum_{i=1}^{N_s} \left[\hat{\xi}_i(r) \bar{\delta}_i w_{r,i} \right] \right) \frac{1}{\sigma_L^2}, \quad (5.12)$$

for the subvolumes of two sizes ($220 h^{-1}$ Mpc in the bottom-left and $120 h^{-1}$ Mpc in the bottom-right panels). The gray lines show individual realizations, while the dashed lines show the mean.

We now fit models of $\xi(r)$ and $i\zeta_L(r)/\sigma_L^2$ to the measurements in $30 h^{-1} \text{ Mpc} \leq r \leq 78 h^{-1} \text{ Mpc}$. We choose this fitting range because there are less galaxy pairs at larger separations due to the subvolume size, and the nonlinear effect becomes too large for our SPT predictions to be applicable at smaller separations. For the two-point function, we take the Fourier transform of [42]

$$P_g(k) = b_1^2 [P_l(k) e^{-k^2 \sigma_v^2} + A_{\text{MC}} P_{\text{MC}}(k)], \quad (5.13)$$

where b_1 is the linear bias, $P_l(k)$ is the linear power spectrum, A_{MC} is the mode coupling constant, and

$$P_{\text{MC}}(k) = 2 \int \frac{d^3 q}{(2\pi)^3} P_l(q) P_l(|\mathbf{k} - \mathbf{q}|) [F_2(\mathbf{q}, \mathbf{k} - \mathbf{q})]^2. \quad (5.14)$$

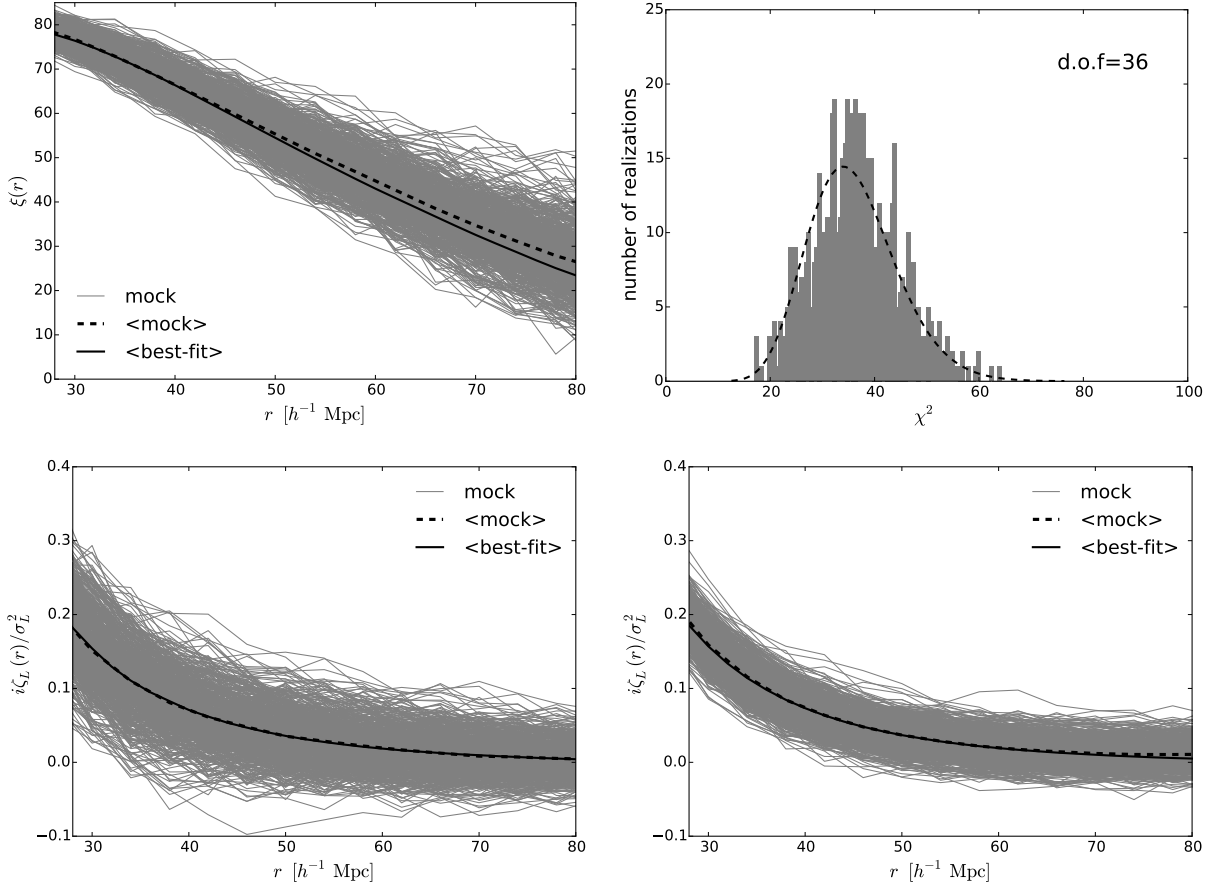


Figure 5.2: (Top left) $\xi(r)$ of the mocks in real space. The gray lines show individual realizations, while the dashed line shows the mean. The black solid line shows the best-fitting model. (Top right) χ^2 -histogram of the 600 mocks jointly fitting the models to $\xi(r)$ and $i\zeta_L(r)/\sigma_L^2$ in real space. The dashed line shows the χ^2 -distribution with d.o.f.=36. (Bottom left) $i\zeta_L(r)/\sigma_L^2$ of the mocks in real space for 220 h^{-1} Mpc subvolumes. (Bottom right) Same as the bottom left panel, but for 120 h^{-1} Mpc subvolumes.

Hence, $\xi_g(r) = b_1^2[\xi_{l,\sigma_v}(r) + A_{\text{MC}}\xi_{\text{MC}}(r)]$ with

$$\xi_{l,\sigma_v}(r) = \int \frac{d^3k}{(2\pi)^3} P_l(k) e^{-k^2\sigma_v^2} e^{i\mathbf{k}\cdot\mathbf{r}}, \quad \xi_{\text{MC}}(r) = \int \frac{d^3k}{(2\pi)^3} P_{\text{MC}}(k) e^{i\mathbf{k}\cdot\mathbf{r}}. \quad (5.15)$$

We use a fixed value of $\sigma_v^2 = 20.644$. Varying it has only small effect on the other fitted parameters. For the integrated three-point function, we use the SPT calculation with the boundary effect correction, which is given by

$$\frac{i\zeta_{L,g}(r)}{\sigma_L^2} = \frac{b_1 i\zeta_{L,\text{SPT}}(r) + b_2 i\zeta_{L,b_2}(r)}{\sigma_{L,l}^2} + \frac{1}{f_{L,\text{bndry}}(r)}, \quad (5.16)$$

where $i\zeta_{L,\text{SPT}}(r)$ and $i\zeta_{L,b_2}(r)$ are computed from eq. (5.3) with eq. (2.38) and eq. (2.40), respectively, and $\sigma_{L,l}^2$ is the variance of the linear power spectrum computed from eq. (2.41), using the subvolume sizes of $L = 220$ and $120 h^{-1}$ Mpc and the redshift of $z = 0.57$. Note that the size of the subvolumes affects the values of $\sigma_{L,l}^2$. We determine L by first measuring b_1^2 using the real-space two-point function of the entire survey, and then find L such that $b_1^2 \sigma_{L,l}^2 = \sigma_L^2$ assuming the cubic top-hat window function³. We find that these values ($L = 220$ and $120 h^{-1}$ Mpc) agree well with the cubic root of the total survey volume divided by the number of subvolumes, to within a few percent.

We fit the models to $\xi(r)$ and $i\zeta_L(r)/\sigma_L^2$ of both subvolumes simultaneously by minimizing

$$\chi^2 = \sum_{ij} C_{ij}^{-1} (D_i - M_i)(D_j - M_j), \quad (5.17)$$

where C^{-1} is the inverse covariance matrix computed from the 600 mocks, D_i and M_i are the data and the model in the i^{th} bin, respectively. The models contain three fitting parameters b_1 , b_2 , and A_{MC} .

The models computed with the mean of the best-fitting parameters of 600 mocks are shown as the black solid lines in figure 5.2. The best-fitting parameters are $b_1 = 1.971 \pm 0.076$, $b_2 = 0.58 \pm 0.31$, and $A_{\text{MC}} = 1.44 \pm 0.93$, where the error bars are 1- σ standard deviations. The agreement between the models and the mocks is good, with a difference much smaller than the scatter among 600 mocks. Upon scrutinizing, the difference in $\xi(r)$ is larger for larger separations because the fit is dominated by the small separations with smaller error bars. On the other hand, for $i\zeta(r)/\sigma_L^2$ the agreement is good for two sizes of subvolumes at all scales of interest. This indicates that the SPT calculation is sufficient to capture the three-point function of the mocks in real space.

The data points in figure 5.2 are highly correlated. To quantify the quality of the fit, we compute the χ^2 -histogram from 600 mocks, and compare it with the χ^2 -distribution with the corresponding degrees of freedom (d.o.f.). There are 13 fitting points for each measurement ($\xi(r)$ and two sizes of subvolumes for $i\zeta_L(r)/\sigma_L^2$) and three fitting parameters, so d.o.f.=36. The top right panel of figure 5.2 shows the χ^2 -histogram. The dashed line shows the χ^2 -distribution with d.o.f.=36. The agreement is good, and we conclude that our models well describe both $\xi(r)$ and $i\zeta_L(r)/\sigma_L^2$ of the mocks in real space.

Our b_1 is in good agreement with the results presented in figure 16 of [62], whereas our b_2 is smaller than theirs, which is $\simeq 0.95$, by 1.2σ . This may be due to the difference in the bispectrum models. While we restrict to the local bias model and the tree-level bispectrum, [62] includes a non-local tidal bias [113, 9, 148] and uses more sophisticated bispectrum modeling using the effective F_2 kernel [64, 63]. In appendix D, we show that using the effective F_2 kernel and the non-local tidal bias in the model increases the value of b_2 , but the changes are well within the 1- σ uncertainties. Also, the differences of the goodness of fit for various models are negligible.

The fitting range as well as the shapes of the bispectrum may also affect the results: the integrated correlation function is sensitive only to the squeezed configurations, whereas

³In principle, the shape of the window function also affects $\sigma_{L,l}^2$, but we ignore this small effect.

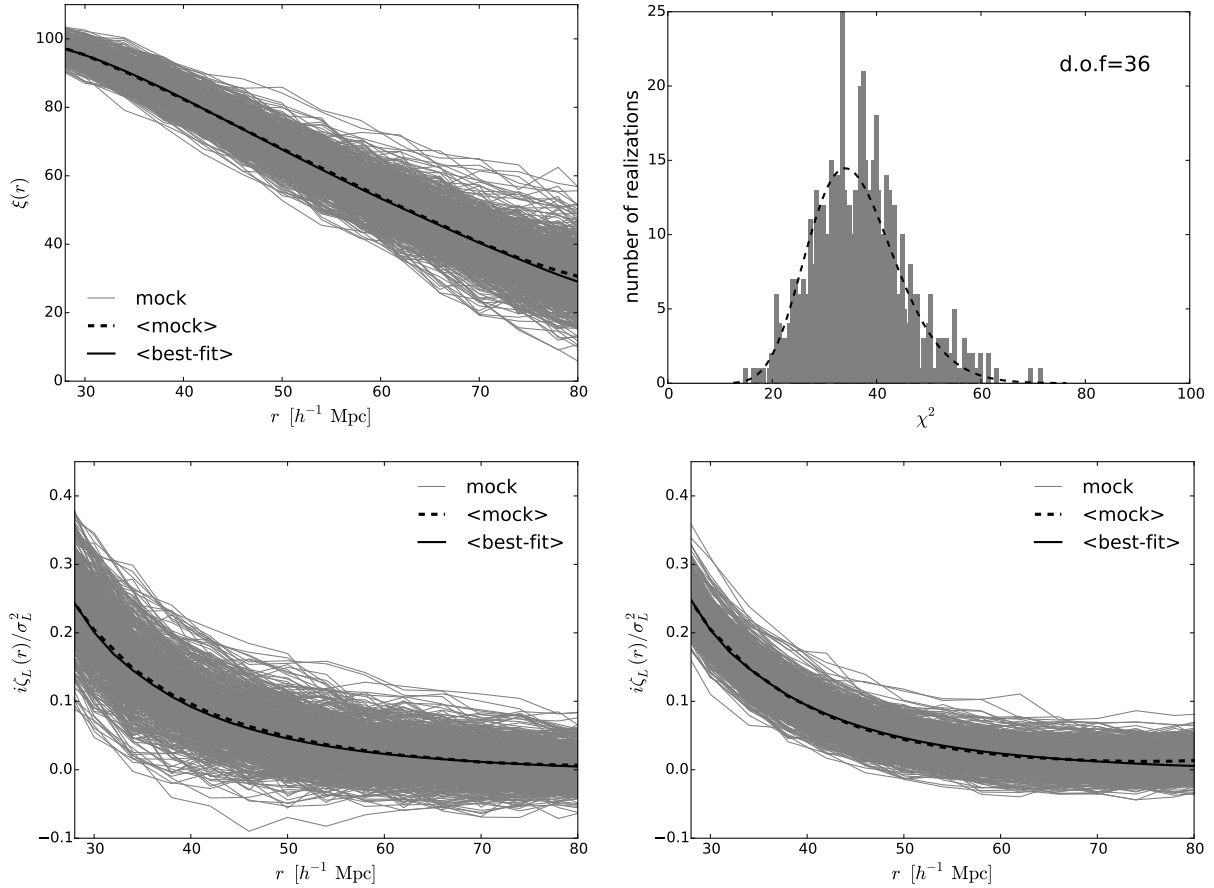


Figure 5.3: Same as figure 5.2 but in redshift space.

[62] includes more equilateral and collapsed triangle configurations. Understanding this difference merits further investigations.

5.1.4 Measurements in redshift space

Figure 5.3 shows the measurements of $\xi(r)$ (top left) and $i\zeta_L(r)/\sigma_L^2$ ($220 h^{-1}$ Mpc in the bottom-left and $120 h^{-1}$ Mpc in the bottom-right panels) of the mocks in redshift space. The gray lines show individual realizations, while the dashed lines show the mean. Similar to the analysis in section 5.1.3, we fit the models in redshift space to the measurements in $30 h^{-1} \text{ Mpc} \leq r \leq 78 h^{-1} \text{ Mpc}$. In this section, we use General Relativity to compute the growth rate, $f(z) \approx \Omega_m(z)^{0.55}$, which yields $f(z = 0.57) = 0.751$. We shall allow f to vary when interpreting the measurements in the actual data.

Since there is no baryonic acoustic oscillation feature on the scales we are interested in,

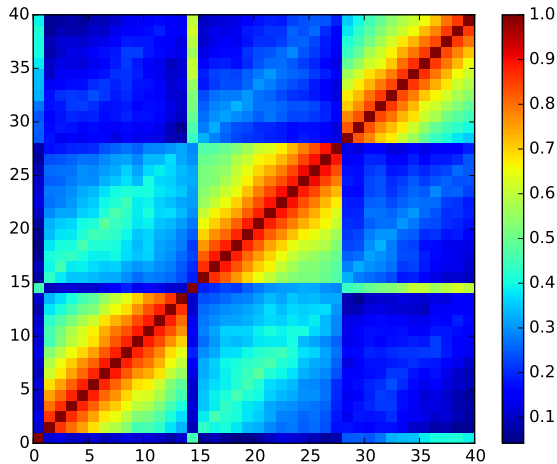


Figure 5.4: Correlation matrix estimated from 600 mocks in redshift space. The figure shows σ_L^2 and $i\zeta_L(r)/\sigma_L^2$ of $220 h^{-1}$ Mpc subvolumes from bin 0 to 13, σ_L^2 and $i\zeta_L(r)/\sigma_L^2$ of $120 h^{-1}$ Mpc subvolumes from bin 14 to 27, and $\xi(r)$ from bin 28 to 40.

we model the redshift-space two-point correlation function as

$$\xi_{g,z}(r) = b_1^2 [\xi_{l,\sigma_v}(r) + A_{\text{MC}}\xi_{\text{MC}}(r)] K, \quad (5.18)$$

where $\xi_{l,\sigma_v}(r)$ and $\xi_{\text{MC}}(r)$ are given in eq. (5.15) and

$$K \equiv 1 + \frac{2}{3}\beta + \frac{1}{5}\beta^2, \quad (5.19)$$

is the Kaiser factor with $\beta \equiv f/b_1$ [80]. As we do not include the subdominant term proportional to b_2 in the two-point function, it only gives constraint on b_1 , which we can then use to break the degeneracy with b_2 in the integrated three-point function. We find that this simple modeling yields unbiased b_1 and fulfills the demand. We calculate the redshift-space integrated three-point function by first evaluating the integrated bispectrum using SPT at the tree level (the explicit expression of the redshift-space bispectrum is given in appendix A.2), compute its one-dimensional Fourier transform, as eq. (5.4), and then correct for the boundary effect. The σ_L^2 of the mocks in redshift space agrees with $b_1^2 K \sigma_{L,l}^2$ to percent level. The redshift-space models thus contain, as before in real space, the three fitting parameters, b_1 , b_2 , and A_{MC} . We then simultaneously fit $\xi(r)$ and $i\zeta_L(r)/\sigma_L^2$ of both subvolumes by minimizing eq. (5.17). Figure 5.4 shows the correlation matrix (C_{ij} in χ^2 , normalized by $\sqrt{C_{ii}C_{jj}}$) estimated from the 600 mocks in redshift space. Because we normalize the integrated three-point function by σ_L^2 , the covariance between $i\zeta_L(r)/\sigma_L^2$ and σ_L^2 is negligible. On the other hand, the covariances between $i\zeta_L(r)/\sigma_L^2$ and $\xi(r)$, between $\xi(r)$, and between $i\zeta_L(r)/\sigma_L^2$ for two sizes of subvolumes are significant.

The models computed with the mean of the best-fitting parameters of 600 mocks are shown as the thick solid lines in figure 5.3. The best-fitting parameters are $b_1 = 1.931 \pm$

0.077, $b_2 = 0.54 \pm 0.35$, and $A_{\text{MC}} = 1.37 \pm 0.82$. The agreement between the models and the measurements in redshift space is as good as in real space.

Again, our b_1 is in good agreement with the results presented in figure 16 of [62], whereas our b_2 is smaller than theirs, which is $\simeq 0.75$, but still well within the $1\text{-}\sigma$ uncertainty. As noted in section 5.1.3, the adopted models of the bispectrum are different. In appendix D, we show that using the effective F_2 and G_2 kernels and the non-local tidal bias in the model increases the value of b_2 . However, the changes are within the uncertainties, and the goodness of the fit is similar for different models. Thus, in this paper we shall primarily use the SPT at the tree level with local bias for simpler interpretation of the three-point function, but also report the results for the extended models.

5.2 Measurement of the BOSS DR10 CMASS sample

We now present measurements of the position-dependent correlation function from the BOSS DR10 CMASS sample⁴ in NGC. The detailed description of the observations can be found in [3, 6]. Briefly, the sample contains 392,372 galaxies over 4,892 deg² in the redshift range of $0.43 < z < 0.7$, which corresponds to the comoving volume of approximately $2 h^{-3} \text{ Gpc}^3$. We also weight the galaxies by w_{BOSS} to correct for the observational systematics. We follow section 5.1.1 to divide the observations into subvolumes. However, the observations have their own set of random samples, which are different from the ones of the mocks (the random samples of the mocks have slightly higher \bar{n} and different $\bar{n}(z)$), so we adjust the redshift cuts to be $z_{\text{cut}} = 0.5108, 0.5717$ and $z_{\text{cut}} = 0.48710, 0.52235, 0.55825, 0.60435$ for the two resolutions, respectively. The resulting properties of subvolumes of the observations and mocks are similar.

The mocks are constructed to match the two-point function of the observed galaxies, but not for the three-point function. Hence there is no guarantee that the three-point function of mocks agrees with the observations. We can test this using our measurements.

The measurements of $\xi(r)$ and $i\zeta_L(r)/\sigma_L^2$ from the observations are shown as the solid lines in figure 5.5. The measurements are consistent visually with the mocks within the scatter of the mocks⁵; and we shall quantify the goodness of the fit using χ^2 statistics later.

To quantify statistical significance of the detection of $i\zeta_L(r)/\sigma_L^2$ and the goodness of fit, we use the mean of the mocks as the model (instead of the model based on perturbation theory used in section 5.1.4), and fit only the amplitudes of $i\zeta_L(r)/\sigma_L^2$, $\xi(r)$, and σ_L^2 to the observations and the 600 mocks by minimizing eq. (5.17). Specifically, we use $O_i(r) = A_i O_i^{\text{mock}}(r)$ as the model, where $O_1(r) = i\zeta_L(r)/\sigma_L^2$, $O_2(r) = \xi(r)$, and $O_3 = \sigma_L^2$, with the amplitudes A_1, A_2, A_3 .

Table 5.1 summarizes the fitted amplitudes. The $1\text{-}\sigma$ uncertainties and the correlations are estimated from the 600 mocks. Since we normalize $i\zeta_L(r)$ by σ_L^2 , the correlation between

⁴Catalogs of galaxies and the random samples can be found in <http://www.sdss3.org>.

⁵These measurements of $i\zeta_L(r)/\sigma_L^2$ are done for one effective redshift. We compare $i\zeta_L(r)/\sigma_L^2$ of the observations and mocks in different redshift bins in appendix E, finding that the observations and mocks are consistent at all redshift bins to within the scatter of the mocks.

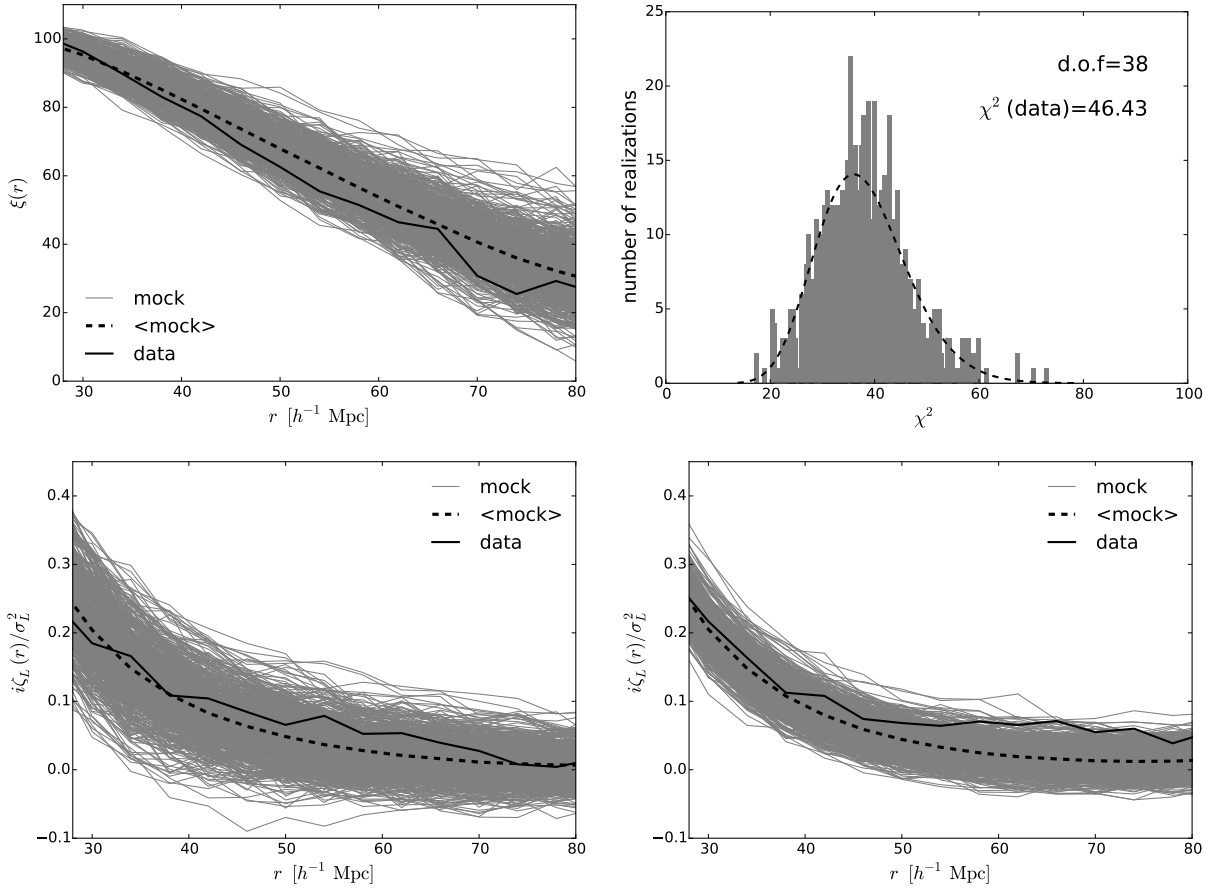


Figure 5.5: Measurements of the BOSS DR10 CMASS sample (black solid lines). The gray lines show individual mocks in redshift space and the dashed line shows the mean of mocks. (Top left) $\xi(r)$, (Bottom left) $i\zeta_L(r)/\sigma_L^2$ for 220 h^{-1} Mpc subvolumes, and (Bottom right) $i\zeta_L(r)/\sigma_L^2$ for 120 h^{-1} Mpc subvolumes. (Top right) χ^2 -histogram of the 600 mocks jointly fitting the three amplitudes to $\xi(r)$ and $i\zeta_L(r)/\sigma_L^2$ in redshift space. The dashed line shows the χ^2 -distribution with d.o.f.=38. The χ^2 value measured from the BOSS DR10 CMASS sample is 49.3.

A_1 and A_3 is small. On the other hand, A_2 and A_3 are correlated significantly because σ_L^2 is an integral of the two-point function [eq. (2.41)].

Comparing the BOSS DR10 CMASS sample to the mean of the mocks, we find that $i\zeta(r)/\sigma_L^2$ is 1- σ lower, $\xi(r)$ is unbiased (by construction of the mocks), and σ_L^2 is 2- σ higher. It is intriguing that σ_L^2 of the observations is larger than the mean of the mocks because it measures an integral over the two-point function. Presumably, this happens because σ_L^2 also includes contributions from very small separations (including stochasticity at zero separations), for which the mocks were not optimized. We find $A_1 = 0.89 \pm 0.12$, i.e., a 7.4σ detection of the integrated three-point function of the BOSS DR10 CMASS sample.

	A_1	A_2	A_3		(A_1, A_2)	(A_1, A_3)	(A_2, A_3)
1- σ error	0.12	0.03	0.04	corr	0.34	0.09	0.36
best-fit (DR10)	0.89	1.02	1.08				

Table 5.1: Results of fitting the amplitudes: A_1 is $i\zeta_L(r)/\sigma_L^2$, A_2 is $\xi(r)$, and A_3 is σ_L^2 . (Left) The 1- σ uncertainties of the amplitudes estimated from the mocks, and the best-fitting amplitudes of BOSS DR10 CMASS sample with respect to the mean of the mocks. (Right) The correlation coefficients of the amplitudes.

In order to assess the goodness of fit, we use the distribution of χ^2 , a histogram of which is shown in the top right panel of figure 5.5. In total there are 41 fitting points (13 fitting points for $\xi(r)$ and two sizes of subvolumes for $i\zeta_L(r)/\sigma_L^2$, and two fitting points for σ_L^2) with three fitting parameters, so d.o.f.=38. The χ^2 value of the observations is 49.3, and the probability to exceed this χ^2 value is more than 10%. Given the fact that the mocks are constructed to match only the two-point function of the observations, this level of agreement for both the two-point and integrated three-point correlation functions is satisfactory.

5.3 Interpretation for the measurement of the integrated three-point function

What can we learn from the measured $i\zeta_L(r)/\sigma_L^2$? In section 5.1.4, we show that the prediction for $i\zeta_L(r)/\sigma_L^2$ based on SPT at the tree-level in redshift space provides an adequate fit to the mocks to within the scatter of the mocks; thus, we can use this prediction to infer cosmology from $i\zeta_L(r)/\sigma_L^2$. Note that any unmodeled effects in the integrated three-point function such as nonlinearities of the matter density, nonlocal bias parameters, and redshift-space distortions beyond the Kaiser factor, will tend to bias our measurement of cosmological parameters based on $i\zeta_L(r)$. We will discuss caveats at the end of this section.

Since the linear two-point and the tree-level three-point functions are proportional to σ_8^2 and σ_8^4 , respectively, and σ_L^2 is proportional to σ_8^2 , the scaling of the redshift-space correlation functions is

$$\begin{aligned} \xi_{g,z}(r) &= b_1^2 K \left[\xi_{l,\sigma_v}^{\text{fid}}(r) \left(\frac{\sigma_8}{\sigma_{8,\text{fid}}} \right)^2 + A_{\text{MC}} \xi_{\text{MC}}^{\text{fid}}(r) \left(\frac{\sigma_8}{\sigma_{8,\text{fid}}} \right)^4 \right], \\ \frac{i\zeta_{L,g,z}(r)}{\sigma_L^2} &= \frac{i\zeta_{L,g,z}^{\text{fid}}(r)}{b_1^2 \sigma_{L,l}^2 K} \left(\frac{\sigma_8}{\sigma_{8,\text{fid}}} \right)^2 \frac{1}{f_{L,\text{bdry}}(r)}, \end{aligned} \quad (5.20)$$

where “fid” denotes the quantities computed with the fiducial value of σ_8 . Note that $\xi_{\text{MC}}(r)$ is proportional to σ_8^4 because it is an integral of two linear power spectra (see eq. (5.14)). Since $\xi_{l,\sigma_v}(r)$ dominates the signal, the parameter combinations $b_1\sigma_8$ and $K = 1 + 2\beta/3 + \beta^2/5$ are degenerate in the two-point function. That is, the amplitude of

5.3 Interpretation for the measurement of the integrated three-point function

	baseline	eff kernel	tidal bias	both
b_2	0.41 ± 0.41	0.51 ± 0.41	0.48 ± 0.41	0.60 ± 0.41

Table 5.2: Best-fitting b_2 and their uncertainties for BOSS DR10 CMASS sample for the extended models. The detailed description of the extended models is in appendix D.

the two-point function measures only $(b_1\sigma_8)^2 + \frac{2}{3}(b_1\sigma_8)(f\sigma_8) + \frac{1}{5}(f\sigma_8)^2$. This degeneracy can be lifted by including the quadrupole of the two-point function in redshift space. See [130, 164, 131, 19] for the latest measurements using the BOSS DR11 sample.

As for the three-point function, figure 2.2 shows that the b_1^3 and $b_1^2b_2$ terms are comparable for $b_1 \approx b_2$. This means that, at the three-point function level, the nonlinear bias appears in the leading order, so the amplitude of the three-point function measures a linear combination of b_1 and b_2 . This provides a wonderful opportunity to determine b_2 . The challenge is to break the degeneracy between b_2 , b_1 , f , and σ_8 . For this purpose, we combine our results with the two-point function in redshift space and the weak lensing measurements of BOSS galaxies. We take the constraints on $b_1\sigma_8(z = 0.57) = 1.29 \pm 0.03$ and $f(z = 0.57)\sigma_8(z = 0.57) = 0.441 \pm 0.043$ from table 2 of [130]. To further break the degeneracy between b_1 , f , and σ_8 , we take the constraint on $\sigma_8 = 0.785 \pm 0.044$ from [114, 117], where they jointly analyze the clustering and the galaxy-galaxy lensing using the BOSS DR11 CMASS sample and the shape catalog from Canada France Hawaii Telescope Legacy Survey.

We assume Gaussian priors on $b_1\sigma_8$, $f\sigma_8$, and σ_8 with the known covariance between $b_1\sigma_8$ and $f\sigma_8$. The cross-correlation coefficient between $b_1\sigma_8$ and $f\sigma_8$ is -0.59 , as shown in figure 6 of [130]. We then run the Markov Chain Monte Carlo with the Metropolis-Hastings algorithm to fit the model eq. (5.20) to the observed $i\zeta(r)/\sigma_L^2$. We find $b_2 = 0.41 \pm 0.41$, and the results for the extended models are summarized in table 5.2.

The value of b_2 we find is lower than the mean of the mocks, $b_2^{\text{mock}} = 0.54 \pm 0.35$. The difference is mainly due to two reasons. First, the amplitude of the integrated three-point function of the observations is lower than that of the mocks by 10% ($A_1 = 0.89 \pm 0.12$). Second, the priors from the correlation function and lensing constraint b_1 to be close to 2.18, which is larger than that of the mocks, $b_1^{\text{mock}} = 1.93$. Thus, it requires a smaller b_2 to fit the three-point function. The argument is similar for the extended models. Note, however, that the nonlinear bias of the data is still statistically consistent with the mocks.

Let us conclude this section by listing three caveats regarding our cosmological interpretation of the measured integrated three-point function.

1. The models we use, eq. (5.20), are based on tree-level perturbation theory, the lowest order redshift-space distortion treatment, as well as on the local bias parametrization. While this simple model describes the mocks well, as shown in section 5.1.3 and 5.1.4, we discuss in appendix D that using the effective F_2 and G_2 and the non-local tidal bias brings b_2 closer to that of [62]. We, however, find similar goodness of fit for various models, and thus we cannot distinguish between these models.
2. Covariances between the integrated three-point function, monopole and quadrupole

two-point function, and weak lensing signals are ignored. This can and should be improved by performing a joint fit to all the observables.

3. The cosmology is fixed throughout the analysis, except for f and σ_8 . In principle, marginalizing over the cosmological parameters is necessary to obtain self-consistent results, although the normalized integrated three-point function is not sensitive to cosmological parameters such as Ω_m as shown in figure 4.6.

These caveats need to be addressed in the future work.

5.4 Discussion and conclusion

In this chapter, we have reported on the first measurement of the three-point function with the position-dependent correlation function from the SDSS-III BOSS DR10 CMASS sample. The correlation between the position-dependent correlation function measured within subvolumes and the mean overdensities of those subvolumes is robustly detected at 7.4σ .

Both the position-dependent correlation function and the mean overdensity are easier to measure than the three-point function. The computational expense for the two-point function is much cheaper than the three-point function estimator using the triplet-counting method. In addition, for a fixed size of the subvolume, the integrated three-point function depends only on one variable (i.e., separation), unlike the full three-point function which depends on three separations. This property allows for a useful compression of information in the three-point function in the squeezed configurations, and makes physical sense because the integrated three-point function measures how the small-scale two-point function, which depends only on the separation, responds to a long-wavelength fluctuation, as introduced in chapter 4. As there are only a small number of measurement bins, the covariance matrix of the integrated three-point function is easier to estimate than that of the full three-point function from a realistic number of mocks. We have demonstrated this advantage in this chapter.

Of course, since this technique measures the three-point function with one long-wavelength mode (mean overdensity in the subvolumes) and two relatively small-wavelength modes (position-dependent correlation function), it is not very sensitive to the three-point function of other configurations, which were explored in [62].

We have used the mock galaxy catalogs, which are constructed to match the two-point function of the SDSS-III BOSS DR10 CMASS sample in redshift space, to validate our method and theoretical model. We show that in both real and redshift space, the integrated three-point function of the mocks can be well described by the tree-level SPT model. However, the nonlinear bias which we obtain from the mocks is higher than that reported in [62]. This is possibly due to the differences in the scales and configurations of the three-point function used for the analyses. As discussed in section 5.3, any unmodeled nonlinear effects in the redshift-space integrated three-point function of CMASS galaxies will tend to bias b_2 , and will bias this parameter differently than the measurement of [62].

Taking the mean of the mocks as the model, and treating the amplitudes of two- and three-point functions as free parameters, we find the best-fit amplitudes of $i\zeta(r)/\sigma_L^2$, $\xi(r)$, and σ_L^2 of the CMASS sample. With respect to the mean of the mocks, the observations show a somewhat smaller $i\zeta(r)/\sigma_L^2$ ($A_1 = 0.89 \pm 0.12$) and larger σ_L^2 , while the ensemble two-point function $\xi(r)$ matches the mocks. Given that the mocks are generated to match specifically the two-point function of the BOSS DR10 CMASS sample within a certain range of separations, the level of agreement between the observations and mocks is satisfactory.

Finally, by combining the integrated three-point function and the constraints from the anisotropic clustering ($b_1\sigma_8$ and $f\sigma_8$ in [130]) and from the weak lensing measurements (σ_8 in [117]), we break the degeneracy between b_1 , b_2 , f , and σ_8 . We find $b_2 = 0.41 \pm 0.41$ for the BOSS DR10 CMASS sample. The caveat of this result is that our model, eq. (5.20), relies on a rather simple model in redshift space as well as on the local bias parametrization. We leave the extension of the model to improved bias and redshift-space distortion modeling (especially in light of the comparison with the results in [62]) for future work.

In summary, we have demonstrated that the integrated three-point function is a new observable which can be measured straightforwardly from galaxy surveys using basically the existing and routinely applied machinery to compute the two-point function, and has the potential to yield a useful constraint on the quadratic nonlinear bias parameter. Moreover, since the integrated three-point function is most sensitive to the bispectrum in the squeezed configurations, it is sensitive to primordial non-Gaussianity of the local type (see section 2.1.4 and section 4.5 for more details), thereby offering a probe of the physics of inflation. We plan to extend this work to search for the signature of primordial non-Gaussianity in the full BOSS galaxy sample.

Chapter 6

The angle-averaged squeezed limit of nonlinear matter N -point functions and separate universe simulations

In the previous chapters, we have introduced the position-dependent two-point statistics and shown the measurements from N -body simulations and observations. In this chapter, we shall generalize the study to the angle-averaged squeezed limit of nonlinear matter N -point functions, and demonstrate how to use the “separate universe simulations” to address this issue. Specifically, we consider the case of the squeezed limit such that there is a hierarchy between two large wavenumbers \mathbf{k} and \mathbf{k}' , and $N - 2$ small wavenumbers $\mathbf{k}_1, \dots, \mathbf{k}_n$. The configuration is sketched in figure 6.1.

The squeezed limit of matter N -point functions has been the subject of a large body of work in the context of the so-called “consistency relations” for the large-scale structure [85, 127, 39, 83, 166, 165, 84, 38, 37, 120, 15, 73, 121]. The contributions to N -point functions in the squeezed limit are ordered by the ratio of wavenumbers k_i/k , which is assumed to be much less than one. The lowest order contributions, $\propto (k_i/k)^{-1}$ when the N -point function is written in terms of the overdensity δ , are fixed by the requirement that a uniform potential perturbation as well as a uniform velocity (boost) do not lead to any locally observable effect on the density field, as demanded by the equivalence principle [85, 127, 166, 44]. They are also referred to as “kinematic contributions”.

The next order contribution, $\propto (k_i/k)^0$, is the lowest order at which a *physical* coupling of long- and short-wavelength modes happens. More precisely, the contributions at this order correspond to the impact of a uniform long-wavelength density or tidal perturbation. When considering equal-time N -point functions and subhorizon perturbations $k_i \gg aH$, the kinematic contributions disappear, and the physical $(k_i/k)^0$ contributions are the leading contribution to the N -point function in the squeezed limit.

In this chapter, we disregard tidal fields, which leads us to first angle-average over the $N - 2$ small momenta (wavenumbers) in the N -point function. Specifically, we consider

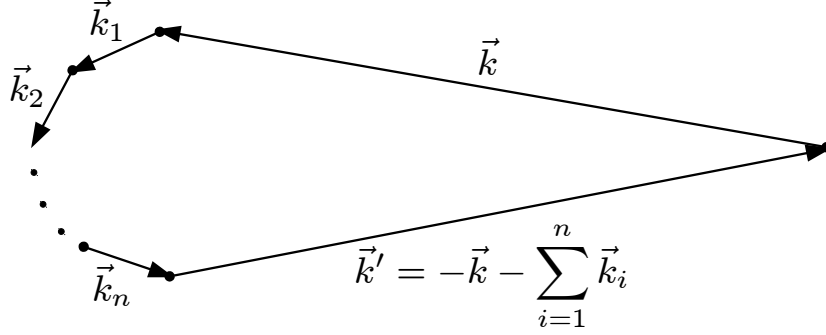


Figure 6.1: Sketch of the squeezed-limit configuration of N -point functions considered in this chapter. $\mathbf{k}_1, \dots, \mathbf{k}_n$ denote the long-wavelength modes which are spherically averaged in eq. (6.1), while \mathbf{k} and \mathbf{k}' denote the small-scale modes which are allowed to be fully nonlinear.

\mathcal{S}_{N-2} defined through

$$\mathcal{S}_{N-2}(k, k'; k_1, \dots, k_{N-2}) \equiv \int \frac{d^2 \hat{k}_1}{4\pi} \dots \int \frac{d^2 \hat{k}_{N-2}}{4\pi} \langle \delta(\mathbf{k}) \delta(\mathbf{k}') \delta(\mathbf{k}_1) \dots \delta(\mathbf{k}_{N-2}) \rangle'_c \quad (6.1)$$

where \hat{k}_i are unit vectors and $\langle \delta(\mathbf{k}_1) \dots \delta(\mathbf{k}_N) \rangle'_c$ denotes the nonlinear connected matter N -point function with the momentum constraint $(2\pi)^3 \delta_D(\mathbf{k}_1 + \dots + \mathbf{k}_N)$ dropped. Note that the momentum constraint fixes \mathbf{k}' in terms of \mathbf{k} and $\mathbf{k}_1, \dots, \mathbf{k}_{N-2}$. We now let k_1, \dots, k_{N-2} go to zero, and normalize the result by the nonlinear power spectrum $P(k)$ and the linear power spectra $P_l(k_1) \dots P_l(k_{N-2})$ to obtain a dimensionless quantity:

$$R_{N-2}(k) = \lim_{k_i \rightarrow 0} \frac{\mathcal{S}_{N-2}(k, k'; k_1, \dots, k_{N-2})}{P(k) P_l(k_1) \dots P_l(k_{N-2})}. \quad (6.2)$$

Note that in this limit, spatial homogeneity enforces $\mathbf{k}' = -\mathbf{k} + \mathcal{O}(k_i/k)$, so that (for statistically isotropic initial conditions) the right-hand-side of eq. (6.2) depends only on k .

In appendix F (see also [165]), we show that $R_n(k)$ correspond exactly to the power spectrum response functions, which quantify the change in the nonlinear matter power spectrum to an infinite-wavelength density perturbation. These response functions are defined as the coefficients of the expansion of the power spectrum in the *linearly extrapolated initial overdensity* δ_{L0} :

$$P(k, t | \delta_{L0}) = \sum_{n=0}^{\infty} \frac{1}{n!} R_n(k, t) \left[\delta_{L0} \hat{D}(t) \right]^n P(k, t), \quad (6.3)$$

where $P(k, t | \delta_{L0})$ is the nonlinear matter power spectrum at time t in the presence of a homogeneous (infinite-wavelength) density perturbation, and $\hat{D}(t)$ is the linear growth

factor normalized to unity today. We have set $R_0(k, t) = 1$ by definition. Thus, by measuring R_n , we measure the angle-averaged squeezed limit (eq. (6.2)) of the nonlinear matter $(n + 2)$ -point function. For $n = 1$, the response R_1 describes the angle-averaged squeezed-limit bispectrum, as discussed in chapter 2 and chapter 4.

Independently of the derivation of eqs. (6.2)–(6.3), we also present accurate measurements of R_n for $n = 1, 2, 3$ using N -body simulations which do not rely on approximations in section 6.2. Specifically, we resort to N -body simulations with an external homogeneous overdensity imposed via the *separate universe* approach described in chapter 3. A flat FLRW universe with a homogeneous overdensity is exactly equivalent to a different, curved FLRW universe, so that N -body simulations in this modified cosmology provide, in principle, the exact result for the response functions $R_n(k)$. This in turn corresponds to the exact (in the limit of infinite volume and resolution) measurement of the squeezed-limit N -point function (eq. (6.2)). The measurements of $R_1(k)$ are presented in [97]. We shall extend to $n = 2$ and 3.

Many semi-analytical approaches to nonlinear large-scale structure assume that nonlinear matter statistics can be described as a unique function of the linear matter power spectrum, i.e. the power spectrum of initial fluctuations linearly extrapolated to a given time. In the context of consistency relations, this approximation has been studied in e.g. [165, 84]. This ansatz is motivated by the fact that in Einstein-de Sitter (flat matter-dominated universe), and to a very good approximation in Λ CDM, the perturbation theory predictions factorize into powers of the linear growth factor and convolutions of products of the initial matter power spectra and time-independent functions. Another way to phrase this ansatz is that nonlinear large-scale structure only depends on the normalization of the fluctuations at a given time, and not on the growth *history*.

In the context of squeezed-limit N -point functions, this ansatz can be tested quantitatively by comparing the outputs of separate universe simulations at a given time with simulations in which the initial amplitude of fluctuations is rescaled to match the *linear* power spectrum at the same time. The difference between these “rescaled initial amplitude” simulations and the separate universe simulations corresponds to the error made in the ansatz of assuming that the linear power spectrum at a given time uniquely describes nonlinear large-scale structure at the same time. For $n = 1$, it is studied in [98] and found that the two simulations differ in the nonlinear regime. A closely related test using the matter bispectrum is shown in [120]. We shall study this comparison in more detail and for $n = 1, 2$ and 3 in section 6.4.

This chapter is organized as follows. In section 6.1, we develop semi-analytic predictions for the power spectrum response. In section 6.2, we describe the methodology of performing the separate universe simulations. In section 6.3, we compare the measurements from N -body simulations to the semi-analytic predictions. In section 6.4, we compare the rescaled simulations to the separate universe simulations. We conclude in section 6.5.

6.1 Power spectrum response

We define the n -th order response function $R_n(k)$ of the power spectrum as the n -th derivative of the power spectrum with respect to the linearly extrapolated (or Lagrangian) overdensity δ_L , normalized by the power spectrum. The definition, consistent with eq. (6.3), is

$$R_n(k, t) = \frac{1}{P(k)} \frac{d^n P(k, t | \delta_L)}{d[\delta_L(t)]^n} \Bigg|_{\delta_L=0}, \quad (6.4)$$

where $\delta_L(t) \equiv \delta_{L0} \hat{D}(t)$. In the following, we will frequently suppress the time argument for clarity. Analogously, one can define the power spectrum response functions with respect to the fully evolved (or Eulerian) nonlinear overdensity δ_ρ . Since we can expand the nonlinear overdensity in powers of δ_L with known coefficients via the spherical collapse (see chapter 3), the n -th order Eulerian response function is given by a sum of R_m with $m \leq n$. Motivated by the relation eq. (6.2), we mainly consider the Lagrangian response functions. In the remainder of this section, we develop semi-analytic models for the response functions based on the separate universe picture.

6.1.1 Separate universe picture

The idea of absorbing an infinitely-wavelength overdensity perturbation δ_ρ into the background modified (curved) cosmology is extensively discussed in chapter 3, and the response of the power spectrum to the overdensity is also discussed in chapter 4 (but restricted to the linear order). In this section, we shall first summarize results, and generalize the study to higher order response, i.e. $n > 1$.

Because of the overdensity, the expansion slows down, and the overdense region behaves as a universe with positive curvature. The scale factor in the modified cosmology can be written as

$$\tilde{a}(t) = a(t) [1 + \delta_a(t)] , \quad (6.5)$$

where the quantities in the modified cosmology are denoted with a tilde. Since the *physical* distance is the same in both cosmologies, eq. (6.5) implies the change of the *comoving* distance to be

$$\tilde{\mathbf{x}} = \frac{a(t)}{\tilde{a}(t)} \mathbf{x} = [1 + \delta_a(t)]^{-1} . \quad (6.6)$$

Furthermore, due to mass conservation, the fractional difference in the scale factor is related to the overdensity δ_ρ by

$$1 + \delta_\rho(t) = [1 + \delta_a(t)]^{-3} . \quad (6.7)$$

Using the separate universe picture, we consider the matter power spectrum in this patch just as that of a region with no homogeneous overdensity but properly modified cosmology. The modification of the cosmology is such that the shape of the linear power spectrum is unchanged, since the ratio of photon, baryon, and cold dark matter densities

is unmodified; moreover, the transfer function parameters are unchanged: $\tilde{\Omega}_m \tilde{h}^2 = \Omega_m h^2$ and $\tilde{\Omega}_b \tilde{h}^2 = \Omega_b h^2$. Thus, only the growth of structure is affected.

The power spectrum that enters in the response given by eq. (6.4) is defined with respect to the background density and comoving coordinates of the fiducial cosmology. Hence, the power spectrum calculated for the modified cosmology has to be mapped to that with respect to the background density and comoving coordinates of the fiducial cosmology. As discussed in chapter 4, this mapping yields the “reference density” and “dilation” contributions to the response. These can be calculated exactly at any scale k to any given order given the nonlinear matter power spectrum in the *fiducial* cosmology. That is, we do not need to run N -body simulations to calculate these effects. They are thus merely “projection effects”, unlike the effect of the modified cosmology on the growth of structure, which requires simulations in order to provide an accurate estimate.

Let us denote the power spectrum for the modified cosmology as $\tilde{P}(\tilde{k})$. Then, the reference density effect simply rescales the power spectrum as,

$$P(k) \stackrel{\text{ref. density}}{=} (1 + \delta_\rho)^2 \tilde{P}(k) , \quad (6.8)$$

where the argument of $\tilde{P}(k)$ is not modified. The dilation effect due to the change in the coordinates given by eq. (6.6) implies $k \rightarrow \tilde{k} = (1 + \delta_a)k$ and changes the power spectrum by (see chapter 4 for detailed derivation)

$$P(k) \stackrel{\text{dilation}}{=} (1 + \delta_a)^3 \tilde{P}([1 + \delta_a]k) . \quad (6.9)$$

Putting the two together and using eq. (6.7) yields

$$P(k) = (1 + \delta_\rho) \tilde{P}([1 + \delta_a]k) , \quad (6.10)$$

where all quantities are evaluated at some fixed time t . Note that one prefactor of $(1 + \delta_\rho)$ cancels, since the effect of the increased density is partially canceled by the corresponding decrease in physical volume. As derived in chapter 3, for an Einstein de-Sitter fiducial universe (and to high accuracy in Λ CDM) $\delta_a(t)$ and $\delta_\rho(t)$ have series solutions of the form

$$\delta_a(t) = \sum_{n=1}^{\infty} e_n \left[\delta_{L0} \hat{D}(t) \right]^n , \quad \delta_\rho(t) = \sum_{n=1}^{\infty} f_n \left[\delta_{L0} \hat{D}(t) \right]^n , \quad (6.11)$$

where $\hat{D}(t) = D(t)/D(t_0)$ is the fiducial growth factor normalized to one at the epoch t_0 to which we extrapolate $\delta_{L0} = \delta_L(t_0)$. Note that the values of e_n and f_n are given in eq. (3.35) and eq. (3.36), respectively.

The third contribution to R_n comes from the effect of the modified cosmology on the growth of structure, which as mentioned above is the physical contribution which requires N -body simulations for an accurate measurement. We thus define a set of *growth-only response functions* $G_n(k)$ which isolate the nontrivial effect of the long-wavelength perturbation on the growth of small-scale structure,

$$G_n(k) \equiv \left. \frac{1}{P(k)} \frac{d^n \tilde{P}(k)}{d\delta_L^n} \right|_{\delta_L=0} . \quad (6.12)$$

That is, G_n are defined as R_n without the contributions from the reference density and dilation given by eq. (6.10). This definition is an extension of the similar decomposition for $n = 1$ shown in [147, 84, 15, 98]. Thus, the formula for the power spectrum (with respect to global coordinates) in the presence of a long-wavelength overdensity is given by

$$P(k|\delta_L) = (1 + \delta_\rho) \left[\left(1 + \sum_{n=1}^{\infty} \frac{1}{n!} G_n(\tilde{k}) \delta_L^n \right) P(\tilde{k}) \right]_{\tilde{k}=(1+\delta_a)k} . \quad (6.13)$$

Clearly, by the Leibniz rule, at any given order n the total or “full” response $R_n(k)$, eq. (6.4), is composed of the functions $G_m(k)$ and the numbers e_m, f_m with $1 \leq m \leq n$, where the e_m multiply derivatives of $G_l(k)$ and $P(k)$ with respect to k (up to the n^{th} derivative). Specifically, the first three full response functions are given by

$$R_1(k) = f_1 + e_1 \frac{kP'(k)}{P(k)} + G_1(k) , \quad (6.14)$$

$$\begin{aligned} \frac{R_2(k)}{2} &= f_2 + e_2 \frac{kP'(k)}{P(k)} + e_1^2 \frac{k^2 P''(k)}{2P(k)} + \frac{G_2(k)}{2} + f_1 e_1 \frac{kP'(k)}{P(k)} \\ &\quad + f_1 G_1(k) + e_1 \frac{kP'(k)}{P(k)} G_1(k) + e_1 k G_1'(k) , \end{aligned} \quad (6.15)$$

$$\begin{aligned} \frac{R_3(k)}{6} &= f_1 G_1(k) e_1 \frac{kP'(k)}{P(k)} + f_3 + \frac{G_3(k)}{6} + e_3 \frac{kP'(k)}{P(k)} + f_1 \frac{G_2(k)}{2} + f_1 e_2 \frac{kP'(k)}{P(k)} \\ &\quad + f_1 e_1^2 \frac{k^2 P''(k)}{2P(k)} + f_2 G_1(k) + f_2 e_1 \frac{kP'(k)}{P(k)} + (f_1 e_1 + e_2) k G_1'(k) + e_1^2 \frac{k^2 G_1''(k)}{2} \\ &\quad + e_1 k \frac{G_2'(k)}{2} + e_1^2 \frac{kP'(k)}{P(k)} k G_1'(k) + e_1^3 \frac{k^3 P'''(k)}{6P(k)} + 2e_1 e_2 \frac{k^2 P''(k)}{2P(k)} \\ &\quad + e_1 \frac{kP'(k)}{P(k)} \frac{G_2(k)}{2} + G_1(k) \left(e_2 \frac{kP'(k)}{P(k)} + e_1^2 \frac{k^2 P''(k)}{2P(k)} \right) , \end{aligned} \quad (6.16)$$

where the primes denote derivatives with respect to k .

6.1.2 Linear power spectrum predictions

We now evaluate eq. (6.13) for the simplest case, i.e., the response of the linear matter power spectrum. In linear theory, the growth is scale-independent and given by the linear growth factor. Thus, the growth-only response functions are scale-independent and just described by the linear growth factor in the modified cosmology $\tilde{D}(t)$,

$$G_n^{\text{linear}} = \frac{1}{D^2} \frac{d^n (\tilde{D}^2)}{d\delta_L^n} \Big|_{\delta_L=0} . \quad (6.17)$$

As for $\delta_a(t)$ and $\delta_\rho(t)$, \tilde{D} also has the perturbative expansion in powers of δ_L as

$$\tilde{D}(t) = D(t) \left\{ 1 + \sum_{n=1}^{\infty} g_n \left[\delta_{L0} \hat{D}(t) \right]^n \right\} . \quad (6.18)$$

Thus, for an Einstein-de Sitter fiducial universe (and to high accuracy in Λ CDM), the linear response functions are simply constants. Inserting the values of g_n from eq. (3.49), we obtain

$$\{G_n^{\text{linear}}\}_{n=1,\dots,4} = \left\{ \frac{26}{21}, \frac{3002}{1323}, \frac{240272}{43659}, \frac{197919160}{11918907} \right\}. \quad (6.19)$$

eq. (6.13) evaluated for the linear matter power spectrum $P_l(k, t)$ then becomes

$$P_l(k, t|\delta_L) = [1 + \delta_\rho(t)] \left(\frac{\tilde{D}(t)}{D(t)} \right)^2 P_{l,\text{fid}}([1 + \delta_a(t)]k, t). \quad (6.20)$$

Inserting the series expansions, we obtain

$$\begin{aligned} P_l(k, t|\delta_{L0}) &= \left(1 + \sum_{n=1}^{\infty} f_n [\delta_{L0} \hat{D}(t)]^n \right) \left(1 + \sum_{n=1}^{\infty} g_n [\delta_{L0} \hat{D}(t)]^n \right)^2 \\ &\times P_{l,\text{fid}} \left(\left[1 + \sum_{n=1}^{\infty} e_n [\delta_{L0} \hat{D}(t)]^n \right] k, t \right). \end{aligned} \quad (6.21)$$

Eq. (6.21) allows for a consistent expansion in δ_{L0} . Specifically, $d^n P_l(k)/d\delta_{L0}^n$ is given by the n -th order coefficient in this expansion, multiplied by $n!$.

6.1.3 Nonlinear power spectrum predictions

Beyond the linear matter power spectrum, the growth coefficients G_n will become scale-dependent functions $G_n(k)$. Consider now what standard perturbation theory (SPT) predicts. The power spectrum prediction is given by a series

$$P^{\text{SPT}}(k) = P_l(k) + P^{1\text{-loop}}(k) + P^{2\text{-loop}}(k) + \dots, \quad (6.22)$$

where $P^{n\text{-loop}}$ scales as $[P_l]^n$. In an Einstein-de Sitter universe, one can show (e.g., [17]) that the time- and scale-dependence of each order in perturbation theory factorizes, so that one can write

$$P^{\text{SPT}}(k, t) = \hat{D}^2(t) P_l(k, t_0) + \hat{D}^4(t) P^{1\text{-loop}}(k, t_0) + \hat{D}^6(t) P^{2\text{-loop}}(k, t_0) + \dots, \quad (6.23)$$

where $P^{n\text{-loop}}(k, t_0)$ is a convolution of n factors of $P_l(k, t_0)$ with *time-independent* coefficients. While eq. (6.23) is only strictly correct in Einstein-de Sitter, it is used very commonly for Λ CDM as well, since departures from the exact result are typically of order 1% or less, and since it simplifies the calculation significantly. Various variants of SPT, such as the renormalized perturbation theory (RPT) [41], share the same property.

Eq. (6.23) allows for a very simple evaluation of the growth-only response: as discussed above, the shape of the linear power spectrum in the modified cosmology is unchanged, and hence $\tilde{P}^{\text{SPT}}(\tilde{k})$ can be simply evaluated by replacing the fiducial $\hat{D}(t)$ in eq. (6.23) with the modified one, eq. (6.18). This is equivalent to assuming that the entire late-time

cosmology dependence of the nonlinear matter power spectrum enters through the linear growth factor [165, 84, 15]. In section 6.4, we shall test this prescription to all orders in SPT calculations by performing simulations with a rescaled initial power spectrum.

Apart from the SPT calculation, we can also apply this approximation to any prescription that maps a given linear power spectrum to a nonlinear one. In particular, we will show results for halofit [152]. In this case, where the dependence on the linear growth factor is not explicit, we instead compute the derivative with respect to the normalization of the linear power spectrum,

$$\frac{d}{d\tilde{D}} \rightarrow \frac{d\tilde{\sigma}_8}{d\tilde{D}} \frac{d}{d\tilde{\sigma}_8}, \quad (6.24)$$

which at the redshift considered yields the equivalent change of the linear matter power spectrum. This leads to

$$D^n \frac{d^n P(k)}{d\tilde{D}^n} \rightarrow \sigma_8^n \frac{d^n P(k)}{d\tilde{\sigma}_8^n}. \quad (6.25)$$

We use a five-point stencil with a step size of 0.75% in σ_8 to compute numerically the derivatives with respect to σ_8 . In conjunction with the change of the linear growth factor eq. (6.18), this allows us to compute the growth-only response $G_n(k)$ for perturbation theory as well as fitting formulae of the nonlinear matter power spectrum.

6.1.4 Halo model predictions

In section 4.3.4, we have derived the linear response of the power spectrum under the halo model framework, in which all matter is assumed to be contained within halos with a certain distribution of mass (given by the mass function) and density profile. In this section, we shall focus on generalizing the derivation to higher order responses for the halo model approach.

Adopting the notation in section 4.3.4, the halo model power spectrum, P^{HM} , is given by

$$P^{\text{HM}}(k) = P^{2\text{h}}(k) + P^{1\text{h}}(k), \quad P^{2\text{h}}(k) = [I_1^1(k)]^2 P_l(k), \quad P^{1\text{h}}(k) = I_2^0(k, k), \quad (6.26)$$

where

$$I_m^n(k_1, \dots, k_m) \equiv \int d \ln M \, n(\ln M) \left(\frac{M}{\bar{\rho}} \right)^m b_n(M) u(M|k_1) \cdots u(M|k_m), \quad (6.27)$$

and $n(\ln M)$ is the mass function (comoving number density per interval in log mass), M is the halo mass, $b_n(M)$ is the n -th order local bias parameter, and $u(M|k)$ is the dimensionless Fourier transform of the halo density profile, for which we use the NFW profile. One can find more details in section 4.3.4.

To derive how the power spectrum given in eq. (6.26) responds to a homogeneous (infinitely long-wavelength) density perturbation δ_L , we consider the one-halo ($P^{1\text{h}}$) and two-halo ($P^{2\text{h}}$) terms separately. The key physical assumption we make is that halo profiles in *physical* coordinates are unchanged by δ_L . That is, halos at a given mass M in the

presence of δ_L have the same scale radius r_s and scale density $\rho(r_s)$ as in the fiducial cosmology. We will discuss this assumption later in this section. Given this assumption, the density perturbation δ_L then mainly affects the linear power spectrum, which determines the halo-halo clustering (two-halo term), and the abundance of halos at a given mass.

For the two-halo term, as the response of the linear power spectrum is derived in eq. (6.21), the remaining task is to consider the effect on I_1^1 . By the assumption that the density profile does not change in the presence of δ_L , I_1^1 only changes through the bias $b_1(M)$ and the mass function $n(\ln M)$. The bias $b_N(M)$ quantifies the N -th order response of the mass function $n(\ln M)$ to δ_L :

$$b_N(M) = \frac{1}{n(\ln M)} \left. \frac{\partial^N n(\ln M)}{\partial \delta_L^N} \right|_0, \quad \text{or} \quad \left. \frac{\partial^N n(\ln M)}{\partial \delta_L^N} \right|_0 = b_N(M) n(\ln M). \quad (6.28)$$

Thus,

$$\left. \frac{\partial^N}{\partial \delta_L^N} I_1^1(k) \right|_{\delta_L=0} = \int d \ln M \left(\frac{M}{\bar{\rho}} \right) \left. \frac{\partial^N}{\partial \delta_L^N} [b_1(M) n(\ln M)] \right|_{\delta_L=0} u(M|k) = I_1^{N+1}(k). \quad (6.29)$$

Note that in the large-scale limit, $k \rightarrow 0$, this vanishes for $N \geq 1$ by way of the halo model consistency relation

$$I_1^N(k) = \int d \ln M n(\ln M) \left(\frac{M}{\bar{\rho}} \right) b_N(M) = \begin{cases} 1, & N = 1, \\ 0, & N > 1. \end{cases} \quad (6.30)$$

For finite k eq. (6.29) does not vanish, we thus have

$$I_1^1(k, t | \delta_{L0}) = \sum_{n=0}^{\infty} \frac{1}{n!} I_1^{n+1}(k, t) [\hat{D}(t) \delta_{L0}]^n. \quad (6.31)$$

Thus, the two-halo term in the presence of δ_{L0} becomes

$$\begin{aligned} P^{2h}(k, t | \delta_{L0}) &= \left(1 + \sum_{n=1}^{\infty} f_n [\delta_{L0} \hat{D}(t)]^n \right) \left(1 + \sum_{n=1}^{\infty} g_n [\delta_{L0} \hat{D}(t)]^n \right)^2 \\ &\times \left(\sum_{n=0}^{\infty} \frac{1}{n!} I_1^{n+1}(k, t) [\hat{D}(t) \delta_{L0}]^n \right)^2 P_{l,\text{fid}} \left(\left[1 + \sum_{n=1}^{\infty} e_n [\delta_{L0} \hat{D}(t)]^n \right] k, t \right). \end{aligned} \quad (6.32)$$

Note that we recover the tree-level result given in eq. (6.21) in the large-scale limit, where only $n = 0$ of the third term in eq. (6.32) survives. Note also that in eq. (6.32) the dilation effect only enters in the *linear*, not 2-halo, power spectrum. This is a consequence of our assumption that halo profiles do not change due to the long-wavelength density perturbation.

For the one-halo term, due to our assumption about density profiles, the only effect is the change in the mass function, which through eq. (6.28) becomes

$$\frac{\partial^N}{\partial \delta_L^N} I_2^0(k, k) = I_2^N(k, k), \quad (6.33)$$

and thus

$$P^{\text{1h}}(k, t|\delta_{L0}) = \sum_{n=0}^{\infty} \frac{1}{n!} I_2^n(k, k, t) [\hat{D}(t)\delta_{L0}]^n. \quad (6.34)$$

Putting one-halo and two-halo terms together, we obtain

$$\begin{aligned} P^{\text{HM}}(k, t|\delta_{L0}) &= \left(1 + \sum_{n=1}^{\infty} f_n [\delta_{L0}\hat{D}(t)]^n\right) \left(1 + \sum_{n=1}^{\infty} g_n [\delta_{L0}\hat{D}(t)]^n\right)^2 \\ &\times \left(\sum_{n=0}^{\infty} \frac{1}{n!} I_1^{n+1}(k, t) [\hat{D}(t)\delta_{L0}]^n\right)^2 P_{l,\text{fid}} \left(\left[1 + \sum_{n=1}^{\infty} e_n [\delta_{L0}\hat{D}(t)]^n\right] k, t\right) \\ &+ \sum_{n=0}^{\infty} \frac{1}{n!} I_2^n(k, k, t) [\hat{D}(t)\delta_{L0}]^n. \end{aligned} \quad (6.35)$$

The contribution $\propto I_1^{n+1}$ (for $n > 0$) is numerically much smaller than the other terms (see also the discussion in section 4.3.4). Since it is much smaller than the overall accuracy of the halo model description, we will neglect it in the following. This yields

$$\begin{aligned} P^{\text{HM}}(k, t|\delta_{L0}) &= \left(1 + \sum_{n=1}^{\infty} f_n [\delta_{L0}\hat{D}(t)]^n\right) \left(1 + \sum_{n=1}^{\infty} g_n [\delta_{L0}\hat{D}(t)]^n\right)^2 \\ &\times (I_1^1(k, t))^2 P_{l,\text{fid}} \left(\left[1 + \sum_{n=1}^{\infty} e_n [\delta_{L0}\hat{D}(t)]^n\right] k, t\right) \\ &+ \sum_{n=0}^{\infty} \frac{1}{n!} I_2^n(k, k, t) [\hat{D}(t)\delta_{L0}]^n. \end{aligned} \quad (6.36)$$

Explicitly, the first and second order full response functions are given by

$$\begin{aligned} R_1^{\text{HM}}(k) &= \left[f_1 + 2g_1 + e_1 \frac{d \ln P_l(k, t)}{d \ln k}\right] P^{\text{2h}}(k, t) + I_2^1(k, k, t) \\ R_2^{\text{HM}}(k) &= \left[2f_2 + 2f_1g_1 + (f_1 + 2g_1)e_1 \frac{d \ln P_l(k, t)}{d \ln k} + 2g_1^2 + 4g_2\right. \\ &\quad \left.+ 2e_2 \frac{d \ln P_l(k, t)}{d \ln k} + e_1^2 \frac{1}{P} \frac{d^2 P_l(k, t)}{d(\ln k)^2}\right] P^{\text{2h}}(k, t) + I_2^2(k, k, t). \end{aligned} \quad (6.37)$$

We also derive the growth-only response functions in the halo model approach. Since the halo profiles are assumed fixed in physical coordinates, this means that we need to rescale the halo model terms, I_m^n , accordingly. Following our discussion in section 6.1.1, we have $\tilde{k} = (1 + \delta_a)k$, where \tilde{k} is the comoving wavenumber with respect to the modified cosmology. We then obtain

$$I_m^n \Big|_{\text{growth only}}(\tilde{k}_1, \dots, \tilde{k}_m) = I_m^n \Big|_{\text{physical}}\left(\frac{k_1}{1 + \delta_a(t)}, \dots, \frac{k_m}{1 + \delta_a(t)}\right). \quad (6.38)$$

Inserting this into eq. (6.35) and performing a series expansion of δ_a in δ_L then allows us to derive the growth-only response functions $G_n^{\text{HM}}(k)$. Note that the NFW profile we assume is uniquely determined by the scale radius $r_s(M)$ for a halo of mass M , which enters the coefficients defined in eq. (6.27) in the combination $kr_s(M)$. Thus, it is easily possible to include a dependence of the scale radius $r_s(M)$, or equivalently the halo concentration, on the long-wavelength density in a similar way. We will leave this for future work.

Quantitatively, the main contribution of the rescaling eq. (6.38) is from the one-halo term $\propto I_2^n(k, k)$, i.e. the term in the last line of eq. (6.36). The rescaling of the other instances of I_m^n only changes the response at the sub-percent level and we will neglect them in the following. We then obtain for the growth-only contribution to the halo model power spectrum

$$P^{\text{HM}}(k, t | \delta_{L0}) \stackrel{\text{growth}}{=} \text{only} \left(1 + \sum_{n=1}^{\infty} g_n [\delta_{L0} \hat{D}(t)]^n \right)^2 [I_1^1(k, t)]^2 P_{\text{fid}}(k, t) + \sum_{n=0}^{\infty} \frac{1}{n!} I_2^n [A(\delta_{L0}, t) k, A(\delta_{L0}, t) k, t] [\hat{D}(t) \delta_{L0}]^n, \quad (6.39)$$

where

$$A(\delta_{L0}, t) = \left(1 + \sum_{n=1}^{\infty} e_n [\delta_{L0} \hat{D}(t)]^n \right)^{-1}. \quad (6.40)$$

6.2 Separate universe simulations

To test our semi-analytical models of the power spectrum response to the homogeneous overdensity, particularly for the growth of structure due to the change of the cosmology, we run separate universe simulations and measure the power spectrum response functions directly. In this section, we describe the details for performing the separate universe simulations. We shall first introduce the straightforward modifications, cosmological parameters and the initial conditions, and then the non-trivial choices, comoving or physical coordinates.

For usual N -body codes, one needs to specify the cosmological parameters at present time and the output time t_{out} normally specified by the scale factor. As discussed in chapter 3, in the presence of the overdensity δ_{L0} , the cosmological parameters at $\tilde{a}(\tilde{t}_0) = 1$ are modified as

$$\begin{aligned} \tilde{H}_0 &= H_0(1 + \delta_H), \quad \tilde{\Omega}_m = \Omega_m(1 + \delta_H)^{-2}, \quad \tilde{\Omega}_\Lambda = \Omega_\Lambda(1 + \delta_H)^{-2} \\ \tilde{\Omega}_K &= 1 - (1 + \delta_H)^2, \quad \delta_H = \left(1 - \frac{\tilde{K}}{H_0^2} \right)^{1/2} - 1, \quad \frac{\tilde{K}}{H_0^2} = \frac{5}{3} \frac{\Omega_m}{D(t_0)} \delta_{L0}. \end{aligned} \quad (6.41)$$

For the output time, because we want to compare the simulations at the same *physical* time, we need to determine the corresponding scale factor in the modified cosmology such

that $\tilde{a}(t_{\text{out}}) = [1 + \delta_a(t_{\text{out}})]$. We can numerically solve the ordinary differential equation of δ_a in the modified cosmologies eq. (3.18); alternatively we can numerically evaluate $\tilde{a}(t_{\text{out}})$ by

$$t_{\text{out}} = \int_0^{a(t_{\text{out}})} \frac{da}{aH(a)} = \int_0^{\tilde{a}(t_{\text{out}})} \frac{d\tilde{a}}{\tilde{a}\tilde{H}(\tilde{a})} = \int_0^{a(t_{\text{out}})[1+\delta_a(t_{\text{out}})]} \frac{d\tilde{a}}{\tilde{a}\tilde{H}(\tilde{a})}. \quad (6.42)$$

In order to generate the initial conditions for N -body simulations of the modified cosmologies, we need the linear power spectrum at the initial redshift. The initial power spectrum has to be generated for the cosmology $[\tilde{\Omega}_m, \tilde{\Omega}_\Lambda, \tilde{H}_0]$ with the same amplitude of the primordial scalar curvature perturbation \mathcal{A}_s as for the fiducial cosmology. Since the transfer function only involves the physical matter and radiation densities quantified by $\tilde{\Omega}_m \tilde{H}_0^2$ and so on, it is identical in the modified and fiducial cosmologies. Therefore, the linear power spectra differ only through the difference in the linear growth factor. We use CAMB [96, 95] to compute the power spectrum of the fiducial cosmology at $z = 0$, and rescale it by

$$\left[\tilde{D}(\tilde{a}_i) \frac{\tilde{D}(\tilde{a} = 1)}{D(a = 1)} \right]^2, \quad (6.43)$$

where \tilde{a}_i is the scale factor for which the initial conditions are generated.¹ Next, we generate a Gaussian realization of the density field following the initial power spectrum. The positions and velocities of the particles are computed by the second-order Lagrangian perturbation theory [40].

Given a fixed box size for the fiducial cosmology, there are two reasonable choices for the box sizes of the modified cosmologies. Either we match the respective comoving box sizes, i.e. the box size is $500 \tilde{h}/h$ in units of \tilde{h}^{-1} Mpc comoving, or we choose the box sizes such that their physical sizes coincide with that of the fiducial simulation at one specific output time t_{out} , i.e. $500 \tilde{h}a(t_{\text{out}})/[h\tilde{a}(t_{\text{out}})]$ in units of \tilde{h}^{-1} Mpc comoving. The former choice is adequate if we are interested in the power spectrum response functions at the same comoving wavenumber, i.e. without the ‘‘dilation’’ effect. By using the mean density of the separate universe cosmology as the reference density when computing the power spectrum, we are further removing the ‘‘reference density’’ effect and are left with the growth-only response. The results of these simulations are presented in section 6.3.1.

In order to measure the full response functions, we run simulations for which we match the physical box size. We focus on two different output times t_{out} corresponding to $z = 0$ and $z = 2$ in the fiducial cosmology. As the physical size can only be matched at one specific time, we have to run a new set of simulations for each output time. The results of these simulations are presented in section 6.3.2.

¹In order to recover the correct linear power spectrum at low redshifts, we compute the growth functions (D and \tilde{D}) without taking radiation into account. This is because N -body codes do not include the effect of cosmological radiation. In our procedure, we also neglect the effect of curvature on the transfer function at very low wavenumbers $k \sim \sqrt{|K|}$, since terms of similar order are neglected in the Poisson equation used in N -body codes. For sub-horizon box sizes these effects are completely negligible.

Finally, we summarize the common features for the separate universe simulations. All simulations are gravity-only simulations and are carried out using the Tree-PM code Gadget-2 [153]. The starting redshift is $z = 49$ ($a_i = 0.02$), and the particle load for each simulation is 512^3 . For the fiducial cosmology ($\delta_{L0} = 0$), we choose a flat Λ CDM cosmology with cosmological parameters consistent with the current observational constraints: $\Omega_m = 0.27$, $h = 0.7$, $\Omega_b h^2 = 0.023$, $n_s = 0.95$, $\sigma_8 = 0.8$, and a comoving box size of $500 h \text{ Mpc}^{-1}$.

We simulate separate universes corresponding to the linearly-evolved present-day overdensities of $\delta_{L0} = 0, \pm 0.01, \pm 0.02, \pm 0.05, \pm 0.07, \pm 0.1, \pm 0.2, \pm 0.5, \pm 0.7$, and ± 1 . Then, for the separate universes, the Hubble constant and the curvature fraction vary between \tilde{h} : 0.447 to 0.883 and $\tilde{\Omega}_K$: -2.45 to 0.372 , respectively. The physical densities $\tilde{\Omega}_m \tilde{h}^2$, $\tilde{\Omega}_\Lambda \tilde{h}^2$, and $\tilde{\Omega}_b \tilde{h}^2$ as well as n_s and the amplitude of the primordial curvature power spectrum remain the same.

6.3 Results of separate universe simulations

For the power spectrum computation, we first estimate the density contrast $\delta(\mathbf{x})$ on a 1024^3 grid using the cloud-in-cell mass assignment scheme, then apply a Fast Fourier transform, and angular average the squared amplitude $|\delta_{\mathbf{k}}|^2$. The density contrast $\delta(\mathbf{x}) = \rho(\mathbf{x})/\bar{\rho} - 1$ describes the overdensity with respect to the reference density $\bar{\rho}$. When we are interested in the growth-only response function, $\bar{\rho}$ is equal to the mean density of the separate universe. When we compute the full response function, $\bar{\rho}$ is equal to the mean density of the fiducial cosmology. Similarly, for the growth-only response, distances are measured using the comoving coordinates of the respective cosmology², whereas, for the full response, the power spectrum is always measured in comoving coordinates of the fiducial cosmology.

We only report results up to a maximum wavenumber of $2 h^{-1} \text{ Mpc}$. A convergence study with simulations with 8 times lower mass resolution shows differences in G_1 , G_2 and G_3 of only 1 (3) to 5 (10) percent at $z = 0$ ($z = 2$) up to that wavenumber, where the deviations increase from the linear response function to the higher-order response functions. The results for the full response functions R_1 , R_2 and R_3 are converged to an even better degree. We therefore expect that the simulation results presented here converge to a sub-percent to a few percent level.

In order to compute the first three response functions, we fit a polynomial in δ_L to the fractional difference in the measured power spectrum $\Delta_k(\delta_L) \equiv P(k|\delta_L)/P(k|\delta_L = 0) - 1$ for each k -bin. For the fit, we only include results from separate universe simulations with $|\delta_L(t_{\text{out}})| \leq 0.5$ and use a polynomial with degree 6 to be unbiased from higher-order response functions. As the random realization of the initial density field is the same across different δ_L values, the corresponding power spectra are strongly correlated. By considering the ratio, or the relative difference, of two power spectra a large fraction of the noise cancels. However, for the same realization, the measured fractional differences

²Note, however, that the unit of length is always $h^{-1} \text{ Mpc}$, where h corresponds to the fiducial cosmology.

$\Delta_k(\delta_L)$ are still correlated over δ_L . As the number of realizations (16) is not large enough to reliably estimate the covariance between different δ_L values, we cannot include this correlation in the polynomial fitting. Instead, we construct quasi-decorrelated samples of $\Delta_k(\delta_L)$ by randomly choosing a realization for each δ_L value. Fitting many of those subsamples allows for a robust error estimation of the derived response functions.

6.3.1 Growth-only response functions

Figure 6.2 shows the first three growth-only response functions measured from the simulations at $z = 0$ (left column) and $z = 2$ (right column). These correspond to the fully nonlinear squeezed limit bispectrum (three-point function), trispectrum (four-point function) and five-point function. The small wiggles in the growth-only response functions result from the damping of the baryon acoustic oscillations (BAO), which depends on the amplitude of density fluctuations and thus on δ_L .

Let us compare the simulation results to the theoretical predictions discussed in section 6.1. On sufficiently large scales, the perturbation theory predictions are the most accurate, as expected. At high redshift, the 1-loop predictions best describe the results overall. The 1-loop predictions also show a BAO damping effect. At $z = 0$, the growth-only response is captured best by the halofit prescription (in case of G_1) or the halo model (in case of G_2, G_3). We see that the halofit prescription describes the simulation results of the linear response well at both redshifts, but performs significantly worse for the higher-order response functions. The BAO damping effect is essentially absent in both halofit and halo model predictions. Overall, none of the models is able to accurately describe the simulation data in the nonlinear regime, with discrepancies at $z = 0$ ranging from 20% in the best case to a factor of several. These discrepancies are not surprising given that we are looking at scales beyond the validity of perturbation theory and at higher N -point functions for which the semi-analytical approaches were not tuned.

The halo model prediction does not asymptote exactly to the linear result in the $k \rightarrow 0$ limit. This is because the one-halo term asymptotes to a white noise contribution in this limit, and since the one-halo term contributes to G_n due to the dependence of the halo mass function on δ_L (section 6.1.4), this induces a correction to the linear prediction which contributes on large scales. Physically, this occurs because the halo model does not enforce momentum conservation of the matter density field. This issue can be fixed by introducing a “mass compensation scale” [116].

The halo model predictions can be tuned to better match the simulation results by allowing for a dependence of the halo profiles on the long-wavelength density, which is expected on physical grounds (see also [98]). Specifically, if the scale radius of halos at fixed mass increases in the presence of a long-wavelength density perturbation, this lowers the peak in the response and thus could lead to better agreement with the simulations results.

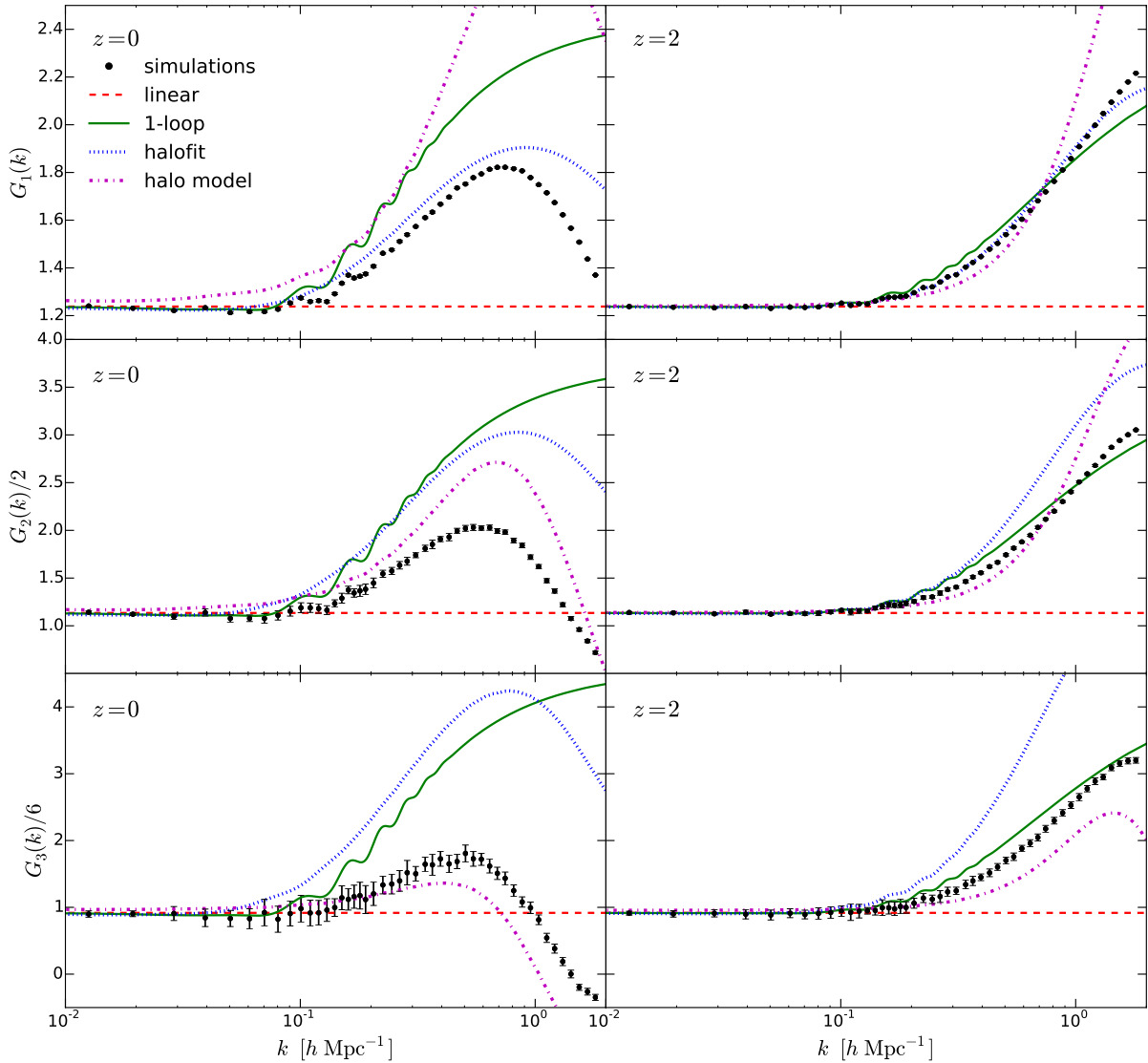


Figure 6.2: The first three growth-only response functions of the power spectrum measured from the separate universe simulations at $z = 0$ (left) and $z = 2$ (right). The error bars show the statistical error derived by random resampling of the data (see text). For data points apparently without error bars, the statistical error is smaller than the size of a dot.

6.3.2 Full response functions

We now turn to the results for the full response functions, i.e. including the “dilation” and “reference density” effects. The results of the simulations and the model predictions are shown in figure 6.3. The oscillations in the response functions can be traced back to the BAOs in the power spectrum. The BAOs propagate to the response functions primarily by

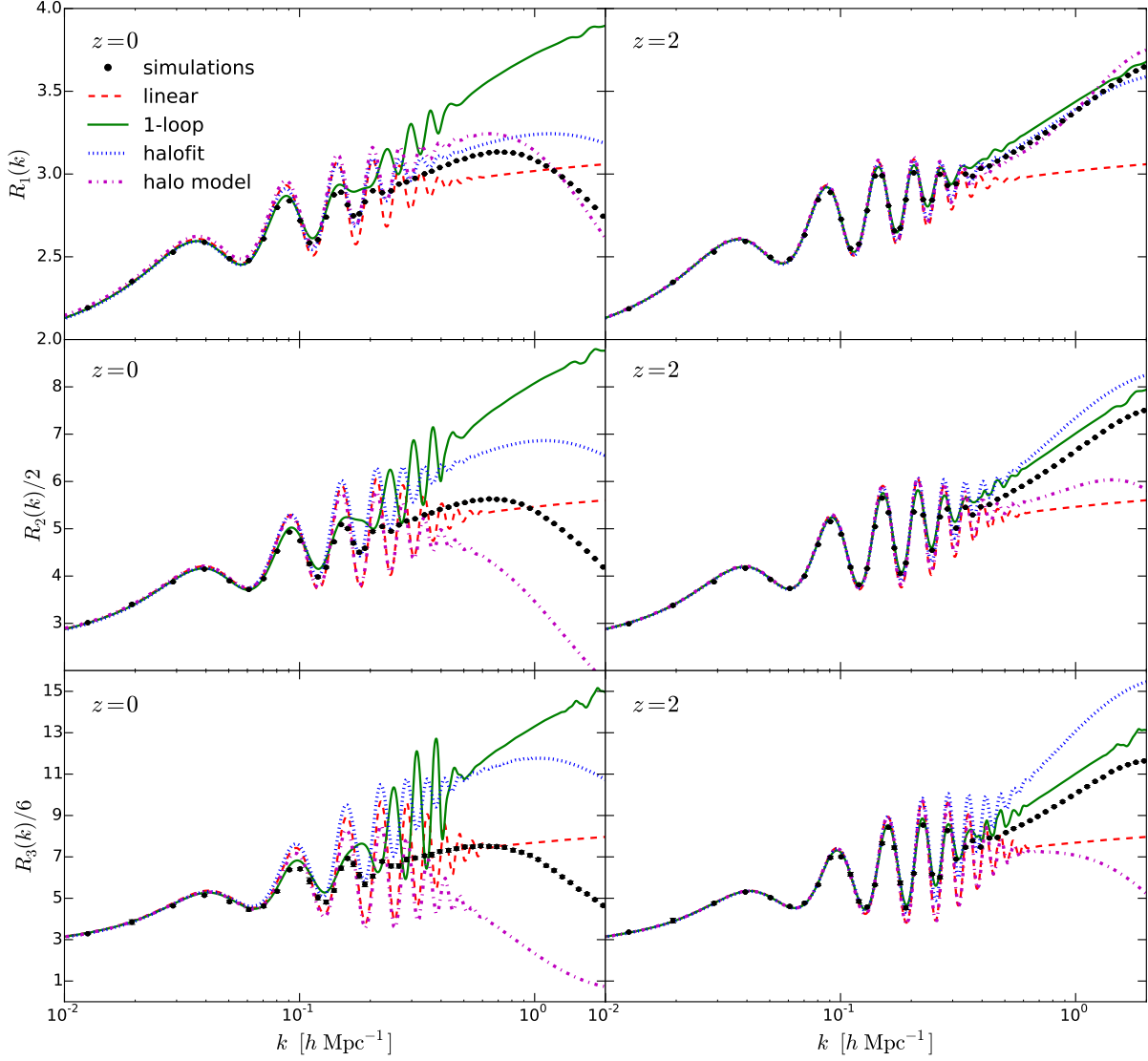


Figure 6.3: The first three full response functions of the power spectrum measured from the separate universe simulations at $z = 0$ (left) and $z = 2$ (right).

the “dilation” effect, which yields derivatives of the power spectrum with respect to k (see eqs. (6.14)–(6.16)). The 1-loop perturbation theory predictions describe the simulation results accurately up to $k \leq 0.15 h^{-1} \text{ Mpc}$ and $k \leq 0.3 h^{-1} \text{ Mpc}$ at $z = 0$ and $z = 2$, respectively. As the other theoretical models do not include the damping of the BAOs in the nonlinear power spectrum, they predict oscillations in the response functions which are too large. To improve the accuracy of those models around the BAO scale, one would need to put in the BAO damping by hand. In the nonlinear regime, none of the models is able to reproduce the simulation data. In principle, one could build a hybrid model for the

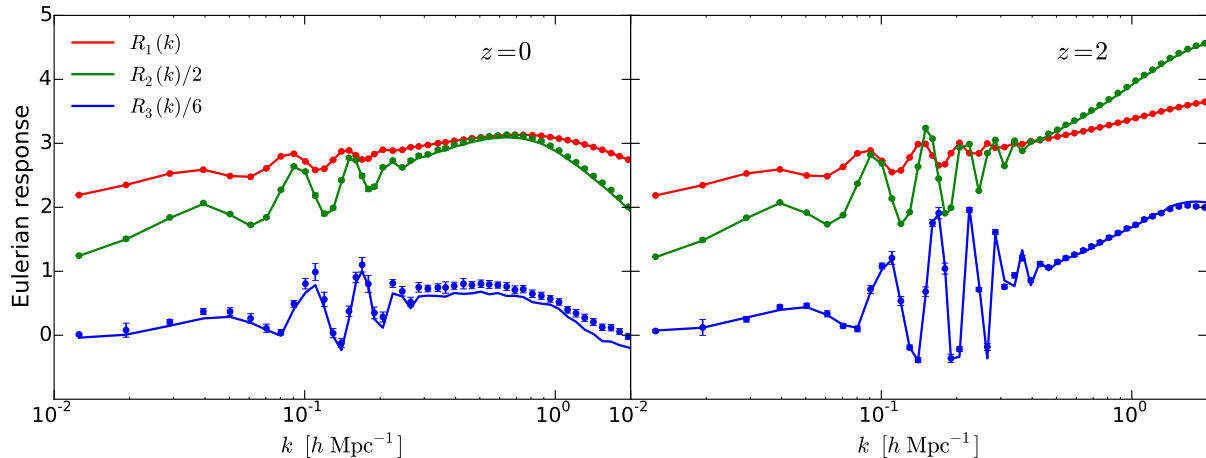


Figure 6.4: The first three Eulerian response functions of the power spectrum measured from the separate universe simulations (data points) at $z = 0$ (left) and $z = 2$ (right). The lines show the corresponding linear combinations of the Lagrangian response functions using the f_n coefficients derived for the Einstein-de Sitter universe (see eq. (6.44) and eq. (3.36)).

full response by combining an accurate prediction of the nonlinear power spectrum of the fiducial cosmology and the growth-only response functions $G_n(k)$ discussed in the previous section. However, we do not pursue this approach.

6.3.3 Eulerian response functions

So far, we have always considered the response to the linearly-extrapolated initial (Lagrangian) overdensity δ_L . We now consider the corresponding response to the *evolved nonlinear* (Eulerian) overdensity δ_ρ . Using the expansion derived for the Einstein-de Sitter universe, eq. (3.36), we find

$$\begin{aligned}
 R_1^{\text{Eulerian}}(k) &= R_1(k) , \\
 R_2^{\text{Eulerian}}(k) &= R_2(k) - 2f_2 R_1(k) , \\
 R_3^{\text{Eulerian}}(k) &= R_3(k) - 6f_2 R_2(k) + 6(2f_2^2 - f_3) R_1(k) .
 \end{aligned}
 \tag{6.44}$$

In figure 6.4, we compare the directly measured Eulerian response functions with the appropriate linear combinations of the measured Lagrangian response functions. The agreement is excellent as expected, especially at high redshift at which the Λ CDM universe is very well approximated by the Einstein-de Sitter universe.

Interestingly, the higher-order Eulerian response functions are much smaller than in the Lagrangian case. That is, the response of the nonlinear matter power spectrum to a uniform nonlinear final-time density δ_ρ is close to linear. This is most likely due to the fact

that the growth-only response functions are subdominant compared to the rescaling and reference density contributions, especially at higher order. In this case, eq. (6.10) implies a close to linear scaling with δ_ρ .

6.4 Simulations with rescaled initial amplitudes

All models for the growth-only response functions that we have presented in section 6.1 and section 6.3.1 are based on the approximation that we can trade the effect of δ_L for an appropriate change to the linear growth factor (or equivalently, the linear power spectrum). But how well does this approximation work?

To investigate how well the effect of a homogeneous overdensity on the growth of structure can be modeled by a change in the amplitude of the linear power spectrum, we additionally run a set of simulations for which we always assume the fiducial cosmology but vary the amplitude of the initial power spectrum. Specifically, for each δ_{L0} value for which we simulate a separate universe, we also simulate the fiducial cosmology with the initial power spectrum amplitude multiplied by $\tilde{D}(t_0)^2/D(t_0)^2$, where $\tilde{D}(t_0)$ is the linear growth factor in the corresponding separate universe cosmology.

Using these “rescaled-amplitude simulations”, we can explicitly test the approximation that δ_L effects the growth of structure only through the change in the linear growth factor on all scales including the nonlinear regime.

6.4.1 Comparison to separate universe simulations

In figure 6.5, we show the growth-only response functions measured from two different sets of simulations. In case of G_1 , this comparison was also shown in figure 6 of [98], and our results agree with theirs.³ The rescaled-amplitude simulations all assume the fiducial cosmology but vary the amplitude of the linear power spectrum used to initialize the simulations so as to match the linear power spectrum in the modified cosmology at the given output times [eq. (6.18) and eq. (6.24)]. On linear scales, these simulations thus agree with the separate universe simulations by construction. As the simulations share the same random realization of the initial density, the sample variance (noise in the upper panels) gets vastly reduced when considering the difference of the measured response functions, $\Delta G_n = G_n^{\text{rescaled}} - G_n^{\text{separate}}$. This is shown in the lower subpanels of figure 6.5, where we have divided ΔG_n by the corresponding linear growth-only response, i.e. the prediction in the $k \rightarrow 0$ limit.

The differences seen in figure 6.5 are caused by the different growth history, which is not captured by the rescaling of the initial amplitude. Following the discussion in section 6.1.3, the commonly used SPT approach factorizing the growth factor and scale dependence assumes at all orders that a long wavelength density perturbation enters exclusively through the modified linear growth. Thus, *even when calculated to all orders*, the best that this

³Note that the in [120] a different comparison is performed using the time derivative of the nonlinear power spectrum in simulations of the fiducial cosmology.

SPT calculation could do is to reproduce the rescaled amplitude result in figure 6.5, which deviates from the actual response at $z = 0$ by 10% at $k \simeq 0.5 h^{-1}$ Mpc and 20% at $k \simeq 1 h^{-1}$ Mpc for G_1 , and significantly worse for the higher-order response functions. At $z = 2$ on the other hand, the rescaled-amplitude G_1 matches the separate universe response to better than 10% even beyond $k = 1 h^{-1}$ Mpc, and for G_2, G_3 performs significantly better as well.

There are two possible explanations for these discrepancies in the SPT context. First, using the SPT kernels derived for an Einstein-de Sitter universe (which have time-independent coefficients), with the Λ CDM linear growth factor replacing the Einstein-de Sitter $a(t)$, could become highly inaccurate for Λ CDM at higher orders. Note that the same issue exists for a fiducial flat Einstein-de Sitter universe, since for $\delta_L \neq 0$ the quantity Ω_m/f^2 is no longer 1 ($d(\Omega_m/f^2)/d\delta_L = -5/21$ [15]; see also the discussion in [120]). There is no indication of such a strong effect at low orders in perturbation theory, where this approximation typically performs to better than a percent [17]. Furthermore, it is found in [15] that a cancellation in the curvature contribution to the growth integral suppresses this effect. Finally, it is shown in [98] that the growth-only response of the power spectrum to a change in the Hubble constant while keeping $\Omega_m h^2$ fixed follows the separate universe response very closely (figure 6 there). If the much larger discrepancies between separate universe response and rescaled amplitude response were due to the cosmology dependence of the SPT kernels, one would not expect this to be the case. Nevertheless, we do not claim to be able to rigorously exclude this possibility.

The other possibility, more likely in our opinion, is that the discrepancy between rescaled amplitude and full separate universe simulations is due to effective non-perfect fluid terms, such as pressure and anisotropic stress, in the dark matter fluid [14]. The effective fluid properties depend on highly nonlinear small scales which are not described by the Euler-Poisson system. Their value can depend on the growth history (as well as the power spectrum shape) thus leading to a discrepancy between rescaled amplitude and separate universe simulations. Assuming this interpretation is correct, figure 6.5 explicitly shows the breakdown of SPT on nonlinear scales as effective pressure, anisotropic stress and sound speed need to be included. Separate universe simulations can be used to measure the response of these effective terms to a long-wavelength overdensity, which is crucial when modeling ($N > 2$)-point functions. The results shown in figure 6.5 are analogous to what has been found for the mass function of halos which is a key ingredient in the halo model description of the nonlinear matter density field. The mass function shows departures from being a simple function of the linear matter power spectrum at the 5–10% level [163, 20].

In an Einstein-de Sitter cosmology with scale-invariant initial power spectrum $P_l(k) \propto k^n$, there is only one characteristic spatial scale at any given time, which corresponds to the scale at which the density field becomes order 1 [124]. Let us denote this wavenumber as $k_{\text{NL}}(t)$. Then, the response functions have to follow a universal function of $k/k_{\text{NL}}(t)$, i.e. $G_m(k, t) = G_m(k/k_{\text{NL}})$ (keeping the index of the initial power spectrum fixed). Thus, in this specific case, separate universe simulations and rescaled-amplitude simulations will give exactly the same result when compared at fixed k/k_{NL} . The departures shown in figure 6.5

can thus be seen as a consequence of the Λ CDM background and the departure from scale-invariance of the initial power spectrum. It would be interesting to disentangle the two effects, e.g. by performing separate universe simulations in Λ CDM with scale-invariant initial conditions. We leave this for future work, but point out that when plotting the differences shown in the lower panel of figure 6.5 as a function of k/k_{NL} , we still find a factor of several difference in the $z = 0$ and $z = 2$ results.

6.5 Discussion and conclusion

In this chapter, we described in detail the procedure for performing N -body simulations with the separate universe technique. Using the separate universe simulations, we compute the response of the nonlinear matter power spectrum to a homogeneous overdensity superimposed on a flat FLRW universe. The response functions we computed give the squeezed limits of the 3-, 4-, and 5-point functions, in which all but two wavenumbers are taken to be small and are angle-averaged. By virtue of the separate universe technique, we reach an unprecedented accuracy of these nonlinear matter N -point functions.

The response function consists of three parts: changing the reference density with respect to which the power spectrum is defined; rescaling of comoving coordinates; and the effect on the growth of structure. The former two effects can be calculated trivially, whereas the third one requires separate universe simulations. We have compared the simulation results with analytical and semi-analytical results, in particular standard perturbation theory (SPT), the empirical fitting function halofit, and the halo model, finding that SPT typically yields the best results at high redshifts. The fitting function and halo model, while qualitatively describe the trends seen in the response functions, give a poor quantitative description on nonlinear scales.

A fundamental assumption of all of the analytical and semi-analytical methods used in this chapter, including standard perturbation theory at any order, is that nonlinear matter statistics at a given time are given solely by the linear power spectrum at the same time, and do not depend on the growth history otherwise. As was done in [98] for the response function for $n = 1$, we were able to test this assumption for $n = 2$ and 3 quantitatively by comparing the separate universe simulations with simulations with a rescaled initial power spectrum amplitude. We find that this assumption fails at the level of 10% at $k \simeq 0.2 - 0.5 h^{-1}$ Mpc for 5- to 3-point functions at $z = 0$. The failure occurs at higher wavenumbers at $z = 2$. In the context of SPT, this may signal a breakdown of the perfect fluid description of the dark matter density field at and beyond these wavenumbers. In other words, even if computed to all orders, SPT (and its variants such as RPT [41]) fails to describe the nonlinear structure formation beyond these wavenumbers. Therefore, our results yields a quantitative estimate for the scales at which effective fluid corrections become important in the bispectrum and higher N -point functions, and at which one should stop trusting pure SPT calculations.

Finally, we point out that the approach presented here can be augmented to measure more general squeezed-limit N -point functions, by including the response to long-

wavelength tidal fields and by considering the response of small-scale n -point functions in addition to the small-scale power spectrum considered here.

6. The angle-averaged squeezed limit of nonlinear matter N -point functions and separate universe simulations

100

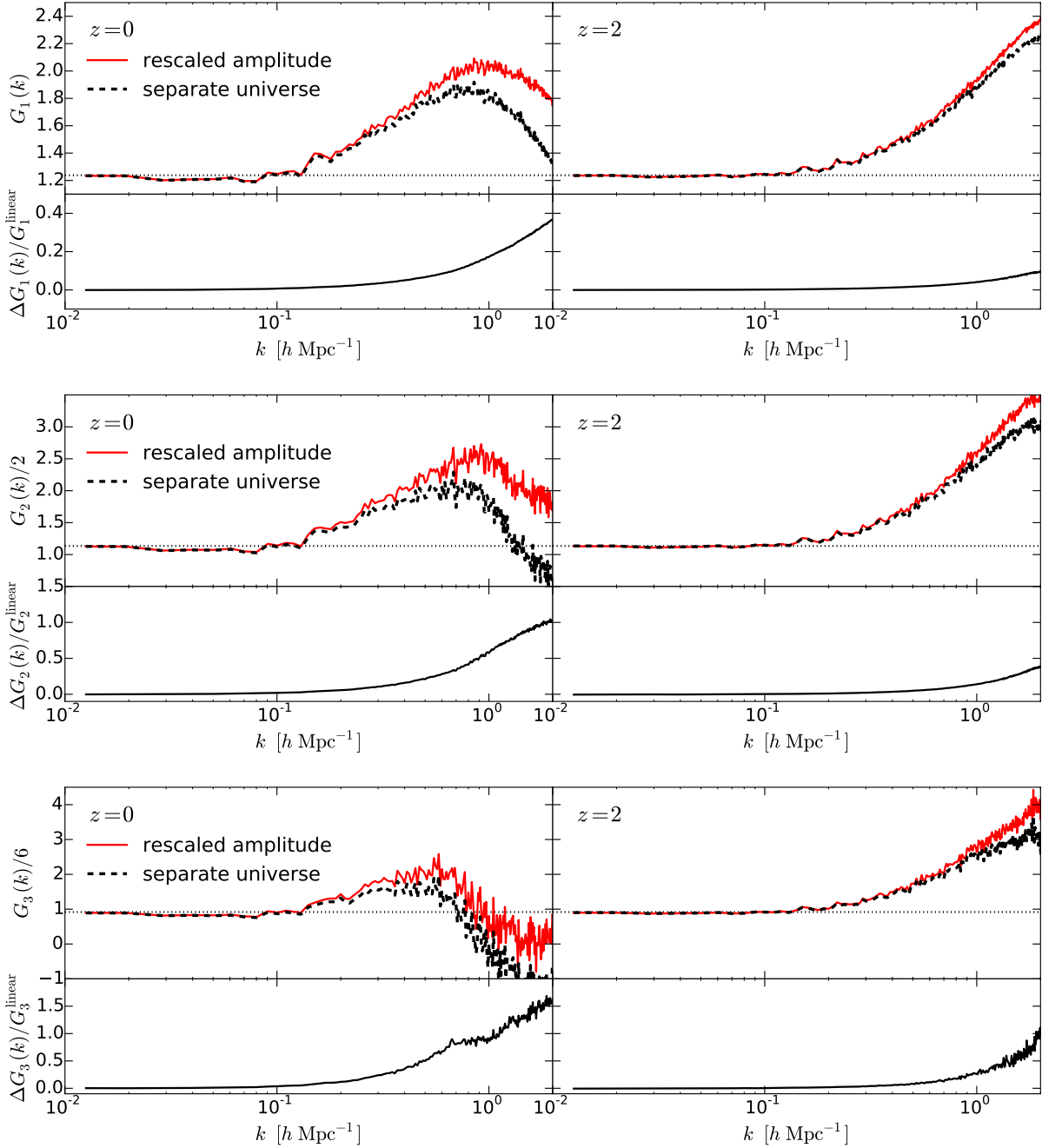


Figure 6.5: Comparison of the growth-only response functions G_1 , G_2 , G_3 (top to bottom) measured at $z = 0$ (left column) and $z = 2$ (right column) from one realization of the separate universe simulations and from the same realization simulated by varying the initial amplitude. The bottom subpanels show the difference, $\Delta G_n = G_n^{\text{rescaled}} - G_n^{\text{separate}}$, divided by the response of the linear matter power spectrum, G_n^{linear} .

Chapter 7

Summary and outlook

In this dissertation, we have proposed and developed in detail a new observable, position-dependent power spectrum, to extract the squeezed-limit bispectrum of the large-scale structure by measuring the correlation between the position-dependent two-point statistics and the mean overdensity in the subvolumes of a survey volume. Since this new technique requires essentially measurements of the two-point statistics and mean overdensity, it sidesteps the complexity of the traditional three-point function estimation.

The correlation between the position-dependent two-point statistics and the mean overdensity can be regarded as how the small-scale structure formation responds to a long-wavelength mode. In chapter 3, we have shown that the long-wavelength overdensity compared to the scale of interest can be absorbed into the background cosmology, and the small-scale structure formation evolves in the corresponding modified cosmology. This *separate universe approach* thus provides an intuitive way to model the squeezed-limit bispectrum, i.e. the response of the small-scale power spectrum to a long-wavelength mode.

In chapter 4, we have measured the position-dependent power spectrum from cosmological N -body simulations, and compared the measurements to different theoretical modeling. In particular, we have shown that it is not only straightforward to combine the separate universe approach with various power spectrum models, but the separate universe approach also describes nonlinearity in the squeezed-limit bispectrum due to gravitational evolution better than the traditional approach based on the perturbation theory. This would enable us to measure the primordial non-Gaussianity in the large-scale structure because we must distinguish the primordial signal from the contamination due to the late-time contribution that we have computed precisely in this dissertation.

In chapter 5, we have reported on the first measurement of the three-point function with the position-dependent correlation from the SDSS-III BOSS DR10 CMASS sample. Since the integrated three-point function of a given subvolume size depends on only one separation (unlike the full three-point function which depends on three separations), the covariance matrix, which is necessary for the statistical interpretation of the cosmological information, can be well estimated with 600 PTHalos mock catalogs. This allows the detection of the amplitude of the three-point function of the BOSS CMASS galaxies at 7.4σ , which can be turned into the constraint on the nonlinear bias $b_2 = 1.30 \pm 0.54$ when

combining with the anisotropic clustering and the weak lensing signal.

We have generalized the study of the response of the small-scale power spectrum to m long-wavelength overdensities in chapter 6. This response can be linked to the angle-average squeezed-limit $(m + 2)$ -point function, where two modes have wavenumbers much larger than the other ones. We have used separate universe simulations, where N -body simulations are performed in the presence of a long-wavelength overdensity by modifying the cosmological parameters, to test the separate universe approach on fully nonlinear scales to the unprecedented accuracy. We have also tested the standard perturbation theory hypothesis that the nonlinear n -point function is completely predicted by the linear power spectrum at the equal time. We have found the discrepancies of 10% at $k \simeq 0.2 - 0.5 h \text{ Mpc}^{-1}$ for five- to three-point functions at $z = 0$, suggesting that the standard perturbation theory fails to describe the correct dynamics of collisionless particles beyond these wavenumbers, even if it is calculated to all orders in perturbations.

While the topic of chapter 6 seems somewhat academic because even measuring the three-point function from galaxy surveys is already challenging at the moment, the idea of separate universe simulations can largely alleviate the computational resources for studying nonlinearities in the squeezed-limit n -point functions. That is, we do not need to perform N -body simulations with a huge volume to simulate the mode coupling between long and short wavelength modes. As nonlinearity due to gravitational evolution is the dominant contamination for extracting the primordial non-Gaussianity from the large-scale structure bispectrum, being able to accurately model the gravity induced bispectrum is currently the most important challenge in this field. We can better construct and test the models for the squeezed-limit bispectrum with separate universe simulations.

The quantum origin of all the structures we observe today is one of the most amazing ideas in history of physics. Such a bold claim requires careful investigations and validations. Upcoming galaxy surveys contain data with unprecedented amount and quality, which allow critical tests of this paradigm. The soon-to-be-public BOSS DR12 CMASS sample contains approximately 50% more observed galaxies and volume than the DR10 sample. We have used the Fisher matrix to show that the BOSS DR12 CMASS sample can potentially constrain the local-type primordial non-Gaussianity to be $\sigma(f_{\text{NL}}) \sim 17$ (95% C.L.). Thus, we plan to apply in the near future the same technique to the BOSS DR12 CMASS sample, and obtain better constraints on the nonlinear bias, as well as on the logarithmic growth rate and the primordial non-Gaussianity.

Appendix A

Tree-level redshift-space bispectrum

In this appendix, we summarize the tree-level redshift-space bispectrum following [141, 17].

A.1 Mapping between real and redshift space

In redshift space, the observed radial position of an object (galaxy) is the combination of the Hubble flow and its peculiar velocity, which is known as redshift-space distortion. The mapping between the real-space position \mathbf{x} and the redshift-space position \mathbf{s} is

$$a\mathbf{s} = a\mathbf{x} + \frac{\tilde{v}_{\parallel}(\mathbf{x})}{H}\hat{x}_{\parallel} \quad \text{or} \quad \mathbf{s} = \mathbf{x} - fu_{\parallel}(\mathbf{x})\hat{x}_{\parallel}, \quad (\text{A.1})$$

where \mathbf{x} and \mathbf{s} are in the comoving coordinates, \hat{x}_{\parallel} is the line-of-sight direction, $\tilde{v}_{\parallel} = \tilde{\mathbf{v}} \cdot \hat{x}_{\parallel}$ is the line-of-sight component of the *physical* peculiar velocity field, $\mathbf{u} = -\tilde{\mathbf{v}}/(\mathcal{H}f)$ is the *rescaled* peculiar velocity field, and $\mathcal{H} = aH = a'/a$ is the conformal Hubble parameter with prime being the derivative with respect to conformal time

$$\tau = \int_0^t \frac{dt'}{a(t')}. \quad (\text{A.2})$$

The density fluctuation in redshift space, $\delta_s(\mathbf{s})$, is related to the real-space one, $\delta(\mathbf{x})$, by mass conservation, i.e.

$$[1 + \delta_s(\mathbf{s})]d^3s = [1 + \delta(\mathbf{x})]d^3r. \quad (\text{A.3})$$

Since the Jacobian, $J(\mathbf{x}) = d^3s/d^3r$, is known exactly through eq. (A.1), the redshift-space density fluctuation can be written as

$$\delta_s(\mathbf{s}) = \frac{1 + \delta(\mathbf{x})}{J(\mathbf{x})} - 1 = \frac{\delta(\mathbf{x}) + f\nabla_{\parallel}u_{\parallel}(\mathbf{x})}{J(\mathbf{x})}, \quad (\text{A.4})$$

where $J(\mathbf{x}) = 1 - f\nabla_{\parallel}u_{\parallel}(\mathbf{x})$ and $\nabla_{\parallel} \equiv d/dr_{\parallel}$. In Fourier space, the redshift-space density fluctuation is

$$\begin{aligned}\delta_s(\mathbf{k}) &= \int d^3s \delta_s(\mathbf{s})e^{-i\mathbf{k}\cdot\mathbf{s}} = \int d^3s \frac{\delta(\mathbf{x}) + f\nabla_{\parallel}u_{\parallel}(\mathbf{x})}{J(\mathbf{x})}e^{-i\mathbf{k}\cdot[\mathbf{x}-fu_{\parallel}(\mathbf{x})\hat{x}_{\parallel}]} \\ &= \int d^3r [\delta(\mathbf{x}) + f\nabla_{\parallel}u_{\parallel}(\mathbf{x})] e^{ifk_{\parallel}u_{\parallel}(\mathbf{x})}e^{-i\mathbf{k}\cdot\mathbf{x}},\end{aligned}\quad (\text{A.5})$$

where $k_{\parallel} = \mathbf{k} \cdot \hat{x}_{\parallel}$. Note that in eq. (A.5) the only approximation is the plane-parallel approximation, and so it describes the fully nonlinear density fluctuation in redshift space. The term in the square brackets describes the so-called ‘‘squashing effect’’, i.e. the increase of the clustering amplitude due to infall into the gravitational potential [80]; the term in the exponent encodes the ‘‘Finger-of-God effect’’ which erases power due to the velocity dispersion along the line-of-sight [75].

To proceed, we define the divergence of the rescaled peculiar velocity field as $\tilde{\theta}(\mathbf{x}) \equiv \nabla \cdot \mathbf{u}(\mathbf{x})$, and so

$$\begin{aligned}\int d^3r u_{\parallel}(\mathbf{x})e^{-i\mathbf{k}\cdot\mathbf{x}} &= \frac{-i\mathbf{k} \cdot \hat{x}_{\parallel}}{k^2} \tilde{\theta}(\mathbf{k}) = \frac{-i\mu_k}{k} \tilde{\theta}(\mathbf{k}) \\ \int d^3r \nabla_{\parallel}u_{\parallel}(\mathbf{x})e^{-i\mathbf{k}\cdot\mathbf{x}} &= \left(\frac{\mathbf{k} \cdot \hat{x}_{\parallel}}{k}\right)^2 \tilde{\theta}(\mathbf{k}) = \mu_k^2 \tilde{\theta}(\mathbf{k}),\end{aligned}\quad (\text{A.6})$$

where $\mu_k \equiv \mathbf{k} \cdot \hat{x}_{\parallel}/k = k_{\parallel}/k$ is the cosine of the angle between \mathbf{k} and the line-of-sight. We then perturbatively expand $e^{ifk_{\parallel}u_{\parallel}(\mathbf{x})}$ and use eq. (A.6) to get

$$\begin{aligned}\delta_s(\mathbf{k}) &= \int d^3r e^{-i\mathbf{k}\cdot\mathbf{x}} [\delta(\mathbf{x}) + f\nabla_{\parallel}u_{\parallel}(\mathbf{x})] \left\{ \sum_{n=0}^{\infty} \frac{[ifk_{\parallel}u_{\parallel}(\mathbf{x})]^n}{n!} \right\} \\ &= \int d^3r e^{-i\mathbf{k}\cdot\mathbf{x}} \int \frac{d^3q}{(2\pi)^3} [\delta(\mathbf{q}) + f\mu_q^2 \tilde{\theta}(\mathbf{q})] e^{i\mathbf{q}\cdot\mathbf{x}} \\ &\quad \times \left[1 + \sum_{n=1}^{\infty} \frac{(if\mu_k k)^n}{(n)!} \int \frac{d^3q_1}{(2\pi)^3} \cdots \int \frac{d^3q_n}{(2\pi)^3} \right. \\ &\quad \left. \left(-i\frac{\mu_{q_1}}{q_1}\right) \tilde{\theta}(\mathbf{q}_1) \cdots \left(-i\frac{\mu_{q_n}}{q_n}\right) \tilde{\theta}(\mathbf{q}_n) e^{i(\mathbf{q}_1+\cdots+\mathbf{q}_n)\cdot\mathbf{x}} \right] \\ &= \left[\delta(\mathbf{k}) + f\mu_k^2 \tilde{\theta}(\mathbf{k}) \right] \\ &\quad + \sum_{n=2}^{\infty} \int \frac{d^3q_1}{(2\pi)^3} \cdots \int \frac{d^3q_n}{(2\pi)^3} \left[\delta(\mathbf{q}_1) + f\mu_{q_1}^2 \tilde{\theta}(\mathbf{q}_1) \right] [\delta_D]_n \\ &\quad \times \frac{(f\mu_k k)^{n-1}}{(n-1)!} \frac{\mu_{q_2}}{q_2} \tilde{\theta}(\mathbf{q}_2) \cdots \frac{\mu_{q_n}}{q_n} \tilde{\theta}(\mathbf{q}_n),\end{aligned}\quad (\text{A.7})$$

where $[\delta_D]_n \equiv (2\pi)^3 \delta_D(\mathbf{k} - \mathbf{q}_1 - \cdots - \mathbf{q}_n)$.

A.2 Redshift-space kernel

To obtain $\delta_s(\mathbf{k})$, we need to solve the velocity divergence. Since we are interested in scales smaller than the Jeans length, we shall treat dark matter and baryons as pressureless fluid. Moreover, as the peculiar velocity is much smaller than the speed of light and the scales of density fluctuations are much smaller than the horizon size, the system can be treated by Newtonian dynamics. The equations of the system are (see, e.g. [77])

$$\begin{aligned}\delta' + \nabla \cdot [(1 + \delta)\mathbf{v}] &= 0, \\ \mathbf{v}' + (\mathbf{v} \cdot \nabla)\mathbf{v} &= -\mathcal{H} - \nabla\phi, \\ \nabla^2\phi &= 4\pi G a^2 \bar{\rho}\delta,\end{aligned}\tag{A.8}$$

where $\mathbf{v} = d\mathbf{x}/d\tau = \tilde{\mathbf{v}}$ is the peculiar velocity field in the *comoving coordinate with conformal time* and is equivalent to the physical peculiar velocity field, ϕ is the peculiar gravitational potential from density fluctuations and $\bar{\rho}$ is the mean density. Combining eq. (A.8) and the Friedmann equation (i.e. $4\pi G\bar{\rho}(\tau) = \frac{3}{2}H^2\Omega_m(\tau)$), the continuity equation (the first line in eq. (A.8)) and the Euler equation (the second line in eq. (A.8)) in Fourier space can be written as

$$\begin{aligned}\delta'(\mathbf{k}, \tau) + \theta(\mathbf{k}, \tau) &= - \int \frac{d^3k_1}{(2\pi)^3} \int \frac{d^3k_2}{(2\pi)^3} [\delta_D]_2 \frac{\mathbf{k} \cdot \mathbf{k}_1}{k_1^2} \delta(\mathbf{k}_2, \tau) \theta(\mathbf{k}_1, \tau), \\ \theta'(\mathbf{k}, \tau) + \mathcal{H}\theta(\mathbf{k}, \tau) + \frac{3}{2}\mathcal{H}^2\Omega_m(\tau)\delta(\mathbf{k}, \tau) &= - \int \frac{d^3k_1}{(2\pi)^3} \int \frac{d^3k_2}{(2\pi)^3} [\delta_D]_2 \frac{k^2(\mathbf{k}_1 \cdot \mathbf{k}_2)}{2k_1^2k_2^2} \theta(\mathbf{k}_1, \tau) \theta(\mathbf{k}_2, \tau),\end{aligned}\tag{A.9}$$

where $\theta \equiv \nabla \cdot \mathbf{v}$ is the comoving velocity divergence. Note that $\theta = -aHf\tilde{\theta}$.

To proceed further, we assume that the universe is Einstein de-Sitter, i.e. $\Omega_m(\tau) = 1$ and $a(\tau) \propto \tau^2$. Then, δ and θ can be solved perturbatively as [58, 65]

$$\begin{aligned}\delta(\mathbf{k}, \tau) &= \sum_{n=1}^{\infty} a^n(\tau) \int \frac{d^3q_1}{(2\pi)^3} \cdots \int \frac{d^3q_n}{(2\pi)^3} [\delta_D]_n F_n^{\text{unsym}}(\mathbf{q}_1, \dots, \mathbf{q}_n) \delta_l(\mathbf{q}_1) \cdots \delta_l(\mathbf{q}_n), \\ \theta(\mathbf{k}, \tau) &= - \sum_{n=1}^{\infty} a'(\tau) a^{n-1}(\tau) \int \frac{d^3q_1}{(2\pi)^3} \cdots \int \frac{d^3q_n}{(2\pi)^3} [\delta_D]_n G_n^{\text{unsym}}(\mathbf{q}_1, \dots, \mathbf{q}_n) \delta_l(\mathbf{q}_1) \cdots \delta_l(\mathbf{q}_n),\end{aligned}\tag{A.10}$$

where δ_l is the linear density field, F_n^{unsym} and G_n^{unsym} are the (unsymmetrized) kernels of eq. (A.9), and the recursion relation can be found in [76, 17]. Strictly speaking, eq. (A.10) is only valid in Einstein de-Sitter universe, but a good approximation is to replace $a = D$ and $a' = D^2Hf$ (see appendix B.3 in [139]), where D is the linear growth factor and

$f = d \ln D / d \ln a$ is the logarithmic growth rate, and eq. (A.10) can be written as

$$\begin{aligned}\delta(\mathbf{k}, \tau) &= \sum_{n=1}^{\infty} D^n(\tau) \int \frac{d^3 q_1}{(2\pi)^3} \cdots \int \frac{d^3 q_n}{(2\pi)^3} [\delta_D]_n F_n^{\text{unsym}}(\mathbf{q}_1, \dots, \mathbf{q}_n) \delta_l(\mathbf{q}_1) \cdots \delta_l(\mathbf{q}_n), \\ \tilde{\theta}(\mathbf{k}, \tau) &= \sum_{n=1}^{\infty} D^n(\tau) \int \frac{d^3 q_1}{(2\pi)^3} \cdots \int \frac{d^3 q_n}{(2\pi)^3} [\delta_D]_n G_n^{\text{unsym}}(\mathbf{q}_1, \dots, \mathbf{q}_n) \delta_l(\mathbf{q}_1) \cdots \delta_l(\mathbf{q}_n).\end{aligned}\tag{A.11}$$

One can then define

$$\begin{aligned}\delta_n(\mathbf{k}, \tau) &= D^n(\tau) \int \frac{d^3 q_1}{(2\pi)^3} \cdots \int \frac{d^3 q_n}{(2\pi)^3} [\delta_D]_n F_n^{\text{unsym}}(\mathbf{q}_1, \dots, \mathbf{q}_n) \delta_l(\mathbf{q}_1) \cdots \delta_l(\mathbf{q}_n), \\ \tilde{\theta}_n(\mathbf{k}, \tau) &= D^n(\tau) \int \frac{d^3 q_1}{(2\pi)^3} \cdots \int \frac{d^3 q_n}{(2\pi)^3} [\delta_D]_n G_n^{\text{unsym}}(\mathbf{q}_1, \dots, \mathbf{q}_n) \delta_l(\mathbf{q}_1) \cdots \delta_l(\mathbf{q}_n)\end{aligned}\tag{A.12}$$

such that $\delta(\mathbf{k}, \tau) = \sum_{n=1}^{\infty} \delta_n(\mathbf{k}, \tau)$ and $\tilde{\theta}(\mathbf{k}, \tau) = \sum_{n=1}^{\infty} \tilde{\theta}_n(\mathbf{k}, \tau)$, and thus δ_n and $\tilde{\theta}_n$ are the n^{th} order in linear density field.

For observation, however, one cannot probe dark matter directly, but only the biased tracers (e.g. halos or galaxies). Let us assume that the halo (galaxy) density fluctuations can be parametrized by the local bias model as [59]

$$\delta_h(\mathbf{x}) = \sum_{n=0}^{\infty} \frac{b_n}{n!} \delta^n(\mathbf{x}),\tag{A.13}$$

where b_n are local bias parameters and b_0 assures $\langle \delta_h \rangle = 0$. On the other hand, because of the conservation of mass and momentum, we assume that the halo peculiar velocity field is identical to the underlying matter peculiar velocity field, i.e. $\tilde{\theta}_h = \tilde{\theta}$ (see e.g. [26]).¹ The redshift-space halo density fluctuations can thereby be written as

$$\begin{aligned}\delta_{h,s}(\mathbf{k}) &= \sum_{n=1}^{\infty} \int \frac{d^3 q_1}{(2\pi)^3} \int \frac{d^3 q_2}{(2\pi)^3} \cdots \int \frac{d^3 q_n}{(2\pi)^3} [\delta_D]_n [\delta_h(\mathbf{q}_1) + f \mu_{q_1}^2 \tilde{\theta}(\mathbf{q}_1)] \\ &\quad \times \frac{(f \mu_k k)^{n-1}}{(n-1)!} \frac{\mu_{q_2}}{q_2} \tilde{\theta}(\mathbf{q}_2) \cdots \frac{\mu_{q_n}}{q_n} \tilde{\theta}(\mathbf{q}_n).\end{aligned}\tag{A.14}$$

¹Note however, that using N -body simulations [8] recently shows the evidence for linear *statistical* halo velocity bias which remains constant with time, as predicted by the peak model [50, 49]. It is argued in [8, 21] that the Euler equation has to be modified to correctly describe the coevolution between dark matter and halos.

Combining eqs. (A.11)–(A.14), one can expand $\delta_{h,s}(\mathbf{k})$ as

$$\begin{aligned} \delta_{h,s}(\mathbf{k}) &= [b_1\delta_1(\mathbf{k}) + f\mu_k^2\tilde{\theta}_1(\mathbf{k})] \\ &+ \left\{ \left[b_1\delta_2(\mathbf{k}) + \frac{b_2}{2} \int \frac{d^3q}{(2\pi)^3} \delta_1(\mathbf{q})\delta_1(\mathbf{k}-\mathbf{q}) + f\mu_k^2\tilde{\theta}_2(\mathbf{k}) \right] \right. \\ &+ \left. \int \frac{d^3q_1}{(2\pi)^3} \int \frac{d^3q_2}{(2\pi)^3} [\delta_D]_2 [b_1\delta_1(\mathbf{q}_1) + f\mu_{q_1}^2\tilde{\theta}_1(\mathbf{q}_1)] (f\mu_k k) \frac{\mu_{q_2}}{q_2} \tilde{\theta}_1(\mathbf{q}_2) \right\} \\ &+ \dots, \end{aligned} \quad (\text{A.15})$$

for which we expand up to the second order of δ_l .

For simplicity, one may define the redshift-space kernel $Z_n(\mathbf{q}_1, \dots, \mathbf{q}_n)$ such that

$$\delta_{h,s}(\mathbf{k}, \tau) = \sum_{n=1}^{\infty} D^n(\tau) \int \frac{d^3q_1}{(2\pi)^3} \dots \int \frac{d^3q_n}{(2\pi)^3} [\delta_D]_n Z_n(\mathbf{q}_1, \dots, \mathbf{q}_n) \delta_l(\mathbf{q}_1) \dots \delta_l(\mathbf{q}_n) \quad (\text{A.16})$$

with

$$\begin{aligned} Z_1(\mathbf{q}_i) &= b_1 + f\mu_{q_i}^2 \\ Z_2(\mathbf{q}_1, \mathbf{q}_2) &= b_1 F_2(\mathbf{q}_1, \mathbf{q}_2) + \frac{b_2}{2} + f\tilde{\mu}^2 G_2(\mathbf{q}_1, \mathbf{q}_2) + \frac{f\tilde{\mu}\tilde{q}}{2} \left[\frac{\mu_{q_1}}{q_1} (b_1 + f\mu_{q_2}^2) + \frac{\mu_{q_2}}{q_2} (b_1 + f\mu_{q_1}^2) \right], \end{aligned} \quad (\text{A.17})$$

where $\tilde{\mu} = \tilde{\mathbf{q}} \cdot \hat{x}_{\parallel} / \tilde{q}$ with $\tilde{\mathbf{q}} = \mathbf{q}_1 + \dots + \mathbf{q}_n$ at the n^{th} order, and F_n and G_n are the symmetrized kernels and obtained by taking the mean of all possible permutations of the unsymmetrized kernels. Eqs. (A.16)–(A.17) are the main results of this appendix.

The redshift-space halo bispectrum is defined as

$$\langle \delta_{h,s}(\mathbf{k}_1) \delta_{h,s}(\mathbf{k}_2) \delta_{h,s}(\mathbf{k}_3) \rangle = (2\pi)^3 \delta_D(\mathbf{k}_1 + \mathbf{k}_2 + \mathbf{k}_3) B_{h,s}(\mathbf{k}_1, \mathbf{k}_2, \mathbf{k}_3). \quad (\text{A.18})$$

Using the redshift-space kernels, one obtains the leading order terms as

$$B_{h,s}(\mathbf{k}_1, \mathbf{k}_2, \mathbf{k}_3) = 2[Z_1(\mathbf{k}_1)Z_1(\mathbf{k}_2)Z_2(\mathbf{k}_1, \mathbf{k}_2)P_l(k_1)P_l(k_2) + 2 \text{ cyclic}], \quad (\text{A.19})$$

in which we use the fact that $Z_2(-\mathbf{k}_1, -\mathbf{k}_2) = Z_2(\mathbf{k}_1, \mathbf{k}_2)$ and δ_l is Gaussian so that $\langle \delta_l(\mathbf{k}_1) \delta_l(\mathbf{k}_2) \rangle = (2\pi)^3 \delta_D(\mathbf{k}_1 + \mathbf{k}_2) P_l(k_1)$ and $\langle \delta_l^n \rangle = 0$ for odd n .

It is useful to separate $B_{h,s}$ into four categories: the linear squashing terms (SQ1) which are proportional to $F_2(\mathbf{k}_1, \mathbf{k}_2)$; the second-order squashing terms (SQ2) which are proportional to $G_2(\mathbf{k}_1, \mathbf{k}_2)$; the nonlinear bias terms (NLB) which are related to b_2 ; the damping terms (FOG) due to the velocity dispersion which are not related to $F_2(\mathbf{k}_1, \mathbf{k}_2)$,

$G_2(\mathbf{k}_1, \mathbf{k}_2)$, and b_2 . That is, $B_{h,s} = B_{\text{SQ1}} + B_{\text{SQ2}} + B_{\text{NLB}} + B_{\text{FOG}}$ such that

$$\begin{aligned}
B_{\text{SQ1}}(\mathbf{k}_1, \mathbf{k}_2, \mathbf{k}_3) &= b_1^3 \sum_{i=1}^3 \beta^{i-1} B_{\text{SQ1},i}(\mathbf{k}_1, \mathbf{k}_2, \mathbf{k}_3) , \\
B_{\text{SQ2}}(\mathbf{k}_1, \mathbf{k}_2, \mathbf{k}_3) &= b_1^3 \beta \sum_{i=1}^3 \beta^{i-1} B_{\text{SQ2},i}(\mathbf{k}_1, \mathbf{k}_2, \mathbf{k}_3) , \\
B_{\text{NLB}}(\mathbf{k}_1, \mathbf{k}_2, \mathbf{k}_3) &= b_1^2 b_2 \sum_{i=1}^3 \beta^{i-1} B_{\text{NLB},i}(\mathbf{k}_1, \mathbf{k}_2, \mathbf{k}_3) , \\
B_{\text{FOG}}(\mathbf{k}_1, \mathbf{k}_2, \mathbf{k}_3) &= b_1^4 \beta [B_{\text{FOG},1}(\mathbf{k}_1, \mathbf{k}_2, \mathbf{k}_3) + \beta B_{\text{FOG},2}(\mathbf{k}_1, \mathbf{k}_2, \mathbf{k}_3) + \beta B_{\text{FOG},3}(\mathbf{k}_1, \mathbf{k}_2, \mathbf{k}_3) \\
&\quad + \beta^2 B_{\text{FOG},4}(\mathbf{k}_1, \mathbf{k}_2, \mathbf{k}_3) + \beta^2 B_{\text{FOG},5}(\mathbf{k}_1, \mathbf{k}_2, \mathbf{k}_3) + \beta^3 B_{\text{FOG},6}(\mathbf{k}_1, \mathbf{k}_2, \mathbf{k}_3)] , \tag{A.20}
\end{aligned}$$

where $\beta = f/b_1$. The explicit expressions are: for SQ1,

$$\begin{aligned}
B_{\text{SQ1},1}(\mathbf{k}_1, \mathbf{k}_2, \mathbf{k}_3) &= 2[F_2(\mathbf{k}_1, \mathbf{k}_2)P_l(k_1)P_l(k_2) + 2 \text{ cyclic}] , \\
B_{\text{SQ1},2}(\mathbf{k}_1, \mathbf{k}_2, \mathbf{k}_3) &= 2[(\mu_1^2 + \mu_2^2)F_2(\mathbf{k}_1, \mathbf{k}_2)P_l(k_1)P_l(k_2) + 2 \text{ cyclic}] , \\
B_{\text{SQ1},3}(\mathbf{k}_1, \mathbf{k}_2, \mathbf{k}_3) &= 2[\mu_1^2 \mu_2^2 F_2(\mathbf{k}_1, \mathbf{k}_2)P_l(k_1)P_l(k_2) + 2 \text{ cyclic}] ; \tag{A.21}
\end{aligned}$$

for SQ2,

$$\begin{aligned}
B_{\text{SQ2},1}(\mathbf{k}_1, \mathbf{k}_2, \mathbf{k}_3) &= 2[\mu^2 G_2(\mathbf{k}_1, \mathbf{k}_2)P_l(k_1)P_l(k_2) + 2 \text{ cyclic}] , \\
B_{\text{SQ2},2}(\mathbf{k}_1, \mathbf{k}_2, \mathbf{k}_3) &= 2[(\mu_1^2 + \mu_2^2)\mu^2 G_2(\mathbf{k}_1, \mathbf{k}_2)P_l(k_1)P_l(k_2) + 2 \text{ cyclic}] , \\
B_{\text{SQ2},3}(\mathbf{k}_1, \mathbf{k}_2, \mathbf{k}_3) &= 2[\mu_1^2 \mu_2^2 \mu^2 G_2(\mathbf{k}_1, \mathbf{k}_2)P_l(k_1)P_l(k_2) + 2 \text{ cyclic}] ; \tag{A.22}
\end{aligned}$$

for NLB,

$$\begin{aligned}
B_{\text{NLB},1}(\mathbf{k}_1, \mathbf{k}_2, \mathbf{k}_3) &= P_l(k_1)P_l(k_2) + 2 \text{ cyclic} , \\
B_{\text{NLB},2}(\mathbf{k}_1, \mathbf{k}_2, \mathbf{k}_3) &= (\mu_1^2 + \mu_2^2)P_l(k_1)P_l(k_2) + 2 \text{ cyclic} , \\
B_{\text{NLB},3}(\mathbf{k}_1, \mathbf{k}_2, \mathbf{k}_3) &= \mu_1^2 \mu_2^2 P_l(k_1)P_l(k_2) + 2 \text{ cyclic} ; \tag{A.23}
\end{aligned}$$

for FOG,

$$\begin{aligned}
B_{\text{FOG},1}(\mathbf{k}_1, \mathbf{k}_2, \mathbf{k}_3) &= k\mu \left(\frac{\mu_1}{k_1} + \frac{\mu_2}{k_2} \right) P_l(k_1)P_l(k_2) + 2 \text{ cyclic} , \\
B_{\text{FOG},2}(\mathbf{k}_1, \mathbf{k}_2, \mathbf{k}_3) &= 2 \left[k\mu\mu_1\mu_2 \left(\frac{\mu_2}{k_1} + \frac{\mu_1}{k_2} \right) P_l(k_1)P_l(k_2) + 2 \text{ cyclic} \right] , \\
B_{\text{FOG},3}(\mathbf{k}_1, \mathbf{k}_2, \mathbf{k}_3) &= k\mu \left(\frac{\mu_1^3}{k_1} + \frac{\mu_2^3}{k_2} \right) P_l(k_1)P_l(k_2) + 2 \text{ cyclic} , \\
B_{\text{FOG},4}(\mathbf{k}_1, \mathbf{k}_2, \mathbf{k}_3) &= 2 \left[k\mu\mu_1^2\mu_2^2 \left(\frac{\mu_1}{k_1} + \frac{\mu_2}{k_2} \right) P_l(k_1)P_l(k_2) + 2 \text{ cyclic} \right] , \\
B_{\text{FOG},5}(\mathbf{k}_1, \mathbf{k}_2, \mathbf{k}_3) &= k\mu\mu_1\mu_2 \left(\frac{\mu_2^3}{k_1} + \frac{\mu_1^3}{k_2} \right) P_l(k_1)P_l(k_2) + 2 \text{ cyclic} , \\
B_{\text{FOG},6}(\mathbf{k}_1, \mathbf{k}_2, \mathbf{k}_3) &= k\mu\mu_1^3\mu_2^3 \left(\frac{\mu_2}{k_1} + \frac{\mu_1}{k_2} \right) P_l(k_1)P_l(k_2) + 2 \text{ cyclic} . \tag{A.24}
\end{aligned}$$

Note that in eqs. (A.21)–(A.24) we shall simplify the notations $\mu_n = \mu_{k_n}$ and $\tilde{\mu} = \mu$ for clarity.

A.3 Tree-level redshift-space integrated bispectrum in the squeezed-limit

Let us define the integrated bispectrum of each component as

$$\begin{aligned}
iB_{X,i}(k) &= \frac{1}{V_L^2} \int \frac{d^2\hat{k}}{4\pi} \int \frac{d^3q_a}{(2\pi)^3} \int \frac{d^3q_b}{(2\pi)^3} B_{X,i}(\mathbf{k} - \mathbf{q}_a, -\mathbf{k} + \mathbf{q}_a + \mathbf{q}_b, -\mathbf{q}_b) \\
&\quad \times W_L(\mathbf{q}_a)W_L(-\mathbf{q}_a - \mathbf{q}_b)W_L(\mathbf{q}_b) , \tag{A.25}
\end{aligned}$$

where X refers to SQ1, SQ2, NLB, or FOG. We numerically evaluate all the components of the integrated bispectrum through eq. (A.25) and eqs. (A.21)–(A.24). Figure A.1 shows the ratios of the components at $z = 0$ with $L = 200 h^{-1}$ Mpc. The left and middle panels of figure A.1 show $iB_{X,j}(k)/iB_{X,1}(k)$ for X =SQ1, SQ2, NLB, and FOG with $j = 2$ and 3; the right panel shows $iB_{X,1}(k)/iB_{\text{SQ1},1}(k)$ for X =SQ2, NLB, and FOG. We find that the ratios become quite scale-independent for $k \gtrsim 0.5 h$ Mpc $^{-1}$, indicating that all components have very similar scale-dependencies when the squeezed limit is reached ($k \gg 1/L = 0.005 h$ Mpc $^{-1}$). Note that in principle the ratios depend on the window function and the power spectrum. Fortunately, the anisotropy of the window function can be neglected in the squeezed limit.

To understand the similar scale-dependencies for different terms of the tree-level redshift-space integrated bispectrum in the squeezed limit, let us now consider the three wavenumbers to be $\mathbf{k}_1 = \mathbf{k} - \mathbf{q}_a$, $\mathbf{k}_2 = -\mathbf{k} + \mathbf{q}_a + \mathbf{q}_b$, and $\mathbf{k}_3 = \mathbf{q}_b$ for the k -configuration of

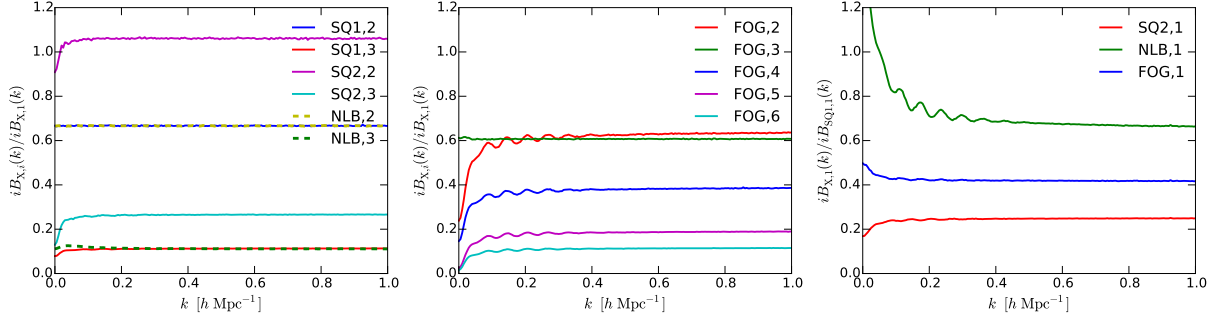


Figure A.1: Ratios of the components of the tree-level redshift-space halo bispectrum at $z = 0$ with $L = 200 h^{-1}$ Mpc, and the line-of-sight direction is \hat{z} . Left and middle panels: $iB_{X,j}(k)/iB_{X,1}(k)$ for $X=SQ1, SQ2, NLB$, and FOG , and $j = 2$ and 3 . Right panel: $iB_{X,1}(k)/iB_{SQ1,1}(k)$ for $X=SQ2, NLB$, and FOG .

the integrated bispectrum. In the squeezed limit, where $k \gg q_a, q_b$, we can expand all quantities in series of (q_a/k) and (q_b/k) , and in the leading order (up to $(q_{a,b}/k)^0$) we get

$$\begin{aligned}
k_1 &= k \left(1 - \mu_{ak} \frac{q_a}{k} \right), \quad k_2 = k \left(1 - \mu_{ak} \frac{q_a}{k} - \mu_{bk} \frac{q_b}{k} \right), \quad k_3 = q_b, \\
P_l(k_1) &= P_l(k) \left[1 - \frac{q_a \mu_{ak}}{k} \frac{d \ln P_l(k)}{d \ln k} \right], \quad P_l(k_2) = P_l(k) \left[1 - \frac{q_a \mu_{ak} + q_b \mu_{bk}}{k} \frac{d \ln P_l(k)}{d \ln k} \right], \\
P_l(k_3) &= P_l(q_b), \quad F_2(\mathbf{k}_1, \mathbf{k}_2) = 0, \quad G_2(\mathbf{k}_1, \mathbf{k}_2) = 0, \\
F_2(\mathbf{k}_1, \mathbf{k}_3) &= \frac{5}{7} - \frac{k \mu_{bk} - q_a \mu_{ab}}{2q_b} + \frac{2}{7} \mu_{bk}^2, \quad F_2(\mathbf{k}_2, \mathbf{k}_3) = \frac{3}{14} + \frac{k \mu_{bk} - q_a \mu_{ab}}{2q_b} + \frac{2}{7} \mu_{bk}^2, \\
G_2(\mathbf{k}_1, \mathbf{k}_3) &= \frac{3}{7} - \frac{k \mu_{bk} - q_a \mu_{ab}}{2q_b} + \frac{4}{7} \mu_{bk}^2, \quad G_2(\mathbf{k}_2, \mathbf{k}_3) = \frac{-1}{14} + \frac{k \mu_{bk} - q_a \mu_{ab}}{2q_b} + \frac{4}{7} \mu_{bk}^2, \\
\mu_1 &= \mu_k + \frac{q_a \mu_{ak} \mu_k - q_a \mu_a}{k}, \quad \mu_2 = -\mu_k + \frac{q_a \mu_{ak} + q_b \mu_{bk} - q_a \mu_a \mu_k - q_b \mu_b \mu_k}{k}, \quad \mu_3 = -\mu_b,
\end{aligned} \tag{A.26}$$

where $\mu_k = \hat{k} \cdot \hat{x}_{\parallel}$, $\mu_a = \hat{q}_a \cdot \hat{x}_{\parallel}$, $\mu_b = \hat{q}_b \cdot \hat{x}_{\parallel}$, $\mu_{bk} = \hat{q}_b \cdot \hat{k}$, and $\mu_{ab} = \hat{q}_a \cdot \hat{q}_b$. The redshift-space bispectrum can then be expanded in series of (q_a/k) and (q_b/k) as (at the leading order up

to $(q_{a,b}/k)^0$

$$\begin{aligned}
 B_{\text{SQ1},1,\text{sq}} &= P_l(k)P_l(q_b) \left[\frac{13}{7} + \frac{8}{7}\mu_{bk}^2 - \frac{d \ln P_l(k)}{d \ln k} \mu_{bk}^2 \right], \\
 B_{\text{SQ1},2,\text{sq}} &= P_l(k)P_l(q_b) \left[\frac{13}{7}\mu_k^2 + \frac{22}{7}\mu_{bk}^2\mu_k^2 - 2\mu_{bk}\mu_k\mu_b + \frac{13}{7}\mu_b^2 + \frac{8}{7}\mu_{bk}^2\mu_b^2 \right. \\
 &\quad \left. - \frac{d \ln P_l(k)}{d \ln k} (\mu_{bk}^2\mu_k^2 + \mu_{bk}^2\mu_b^2) \right], \\
 B_{\text{SQ1},3,\text{sq}} &= P_l(k)P_l(q_b) \left[\frac{13}{7}\mu_k^2\mu_b^2 + \frac{22}{7}\mu_{bk}^2\mu_k^2\mu_b^2 - 2\mu_{bk}\mu_k\mu_b^3 - \frac{d \ln P_l(k)}{d \ln k} \mu_{bk}^2\mu_k^2\mu_b^2 \right], \\
 B_{\text{SQ2},1,\text{sq}} &= P_l(k)P_l(q_b) \left[\frac{5}{7}\mu_k^2 + \frac{2}{7}\mu_{bk}^2\mu_k^2 + 2\mu_{bk}\mu_k\mu_b - \frac{d \ln P_l(k)}{d \ln k} \mu_{bk}^2\mu_b^2 \right], \\
 B_{\text{SQ2},2,\text{sq}} &= P_l(k)P_l(q_b) \left[\frac{5}{7}\mu_k^4 + \frac{16}{7}\mu_{bk}^2\mu_k^4 + \frac{5}{7}\mu_k^2\mu_b^2 + \frac{2}{7}\mu_{bk}^2\mu_k^2\mu_b^2 + 2\mu_{bk}\mu_k\mu_b^3 \right. \\
 &\quad \left. - \frac{d \ln P_l(k)}{d \ln k} (\mu_{bk}^2\mu_k^4 + \mu_{bk}^2\mu_k^2\mu_b^2) \right], \\
 B_{\text{SQ2},3,\text{sq}} &= P_l(k)P_l(q_b) \left[\frac{5}{7}\mu_k^4\mu_b^2 + \frac{16}{7}\mu_{bk}^2\mu_k^4\mu_b^2 - \frac{d \ln P_l(k)}{d \ln k} \mu_{bk}^2\mu_k^4\mu_b^2 \right], \\
 B_{\text{NLB},1,\text{sq}} &= P_l(k)P_l(q_b)[2], \\
 B_{\text{NLB},2,\text{sq}} &= P_l(k)P_l(q_b)[2\mu_k^2 + 2\mu_b^2], \\
 B_{\text{NLB},3,\text{sq}} &= P_l(k)P_l(q_b)[2\mu_k^2\mu_b^2], \\
 B_{\text{FOG},1,\text{sq}} &= P_l(k)P_l(q_b) \left[2\mu_k^2 + \mu_b^2 - \frac{d \ln P_l(k)}{d \ln k} \mu_{bk}\mu_k\mu_b \right], \\
 B_{\text{FOG},2,\text{sq}} &= P_l(k)P_l(q_b) \left[4\mu_{bk}\mu_k^3\mu_b + 2\mu_k^2\mu_b^2 - 2\frac{d \ln P_l(k)}{d \ln k} \mu_{bk}\mu_k^3\mu_b \right], \\
 B_{\text{FOG},3,\text{sq}} &= P_l(k)P_l(q_b) \left[2\mu_k^4 + \mu_b^4 - \frac{d \ln P_l(k)}{d \ln k} \mu_{bk}\mu_k\mu_b^3 \right], \\
 B_{\text{FOG},4,\text{sq}} &= P_l(k)P_l(q_b) \left[4\mu_k^4\mu_b^2 + 4\mu_{bk}\mu_k^3\mu_b^3 - 2\mu_k^2\mu_b^4 - 2\frac{d \ln P_l(k)}{d \ln k} \mu_{bk}\mu_k^3\mu_b^3 \right], \\
 B_{\text{FOG},5,\text{sq}} &= P_l(k)P_l(q_b) \left[4\mu_{bk}\mu_k^5\mu_b - 3\mu_k^4\mu_b^2 + 2\mu_k^2\mu_b^4 - \frac{d \ln P_l(k)}{d \ln k} \mu_{bk}\mu_k^5\mu_b \right], \\
 B_{\text{FOG},6,\text{sq}} &= P_l(k)P_l(q_b) \left[4\mu_{bk}\mu_k^5\mu_b^3 - \mu_k^4\mu_b^4 - \frac{d \ln P_l(k)}{d \ln k} \mu_{bk}\mu_k^5\mu_b^3 \right], \tag{A.27}
 \end{aligned}$$

where $\mu_k = \hat{k} \cdot \hat{x}_\parallel$. Note that eq. (A.27) is independent of \mathbf{q}_a , so we can simplify the

integrated bispectrum as

$$\begin{aligned}
iB(k) &= \frac{1}{V_L^2} \int \frac{d^2 \hat{k}}{4\pi} \int \frac{d^3 q_a}{(2\pi)^3} \int \frac{d^3 q_b}{(2\pi)^3} B(\mathbf{k} - \mathbf{q}_a, -\mathbf{k} + \mathbf{q}_a + \mathbf{q}_b, -\mathbf{q}_b) \\
&\quad \times W_L(\mathbf{q}_a) W_L(-\mathbf{q}_a - \mathbf{q}_b) W_L(\mathbf{q}_b) \\
&\stackrel{k \gg q_a, q_b}{=} \frac{1}{V_L^2} \int \frac{d^2 \hat{k}}{4\pi} \int \frac{d^3 q_b}{(2\pi)^3} B(\mathbf{k} - \mathbf{q}_a, -\mathbf{k} + \mathbf{q}_a + \mathbf{q}_b, -\mathbf{q}_b) W_L^2(\mathbf{q}_b), \tag{A.28}
\end{aligned}$$

where we use the fact that

$$\int \frac{d^3 q_a}{(2\pi)^3} W_L(\mathbf{q}_a) W_L(-\mathbf{q}_a - \mathbf{q}_b) = W_L(\mathbf{q}_b). \tag{A.29}$$

If the window function is isotropic, we can angular average both \hat{k} and \hat{q}_b over eq. (A.27) and obtain

$$\begin{aligned}
B_{\text{SQ1,1,sq}} &= P_l(k) P_l(q_b) \left[\frac{47}{21} - \frac{1}{3} \frac{d \ln P_l(k)}{d \ln k} \right], \quad B_{\text{SQ1,2,sq}} = P_l(k) P_l(q_b) \left[\frac{94}{63} - \frac{2}{9} \frac{d \ln P_l(k)}{d \ln k} \right], \\
B_{\text{SQ1,3,sq}} &= P_l(k) P_l(q_b) \left[\frac{17}{75} - \frac{11}{225} \frac{d \ln P_l(k)}{d \ln k} \right], \quad B_{\text{SQ2,1,sq}} = P_l(k) P_l(q_b) \left[\frac{31}{63} - \frac{1}{9} \frac{d \ln P_l(k)}{d \ln k} \right], \\
B_{\text{SQ2,2,sq}} &= P_l(k) P_l(q_b) \left[\frac{274}{525} - \frac{26}{225} \frac{d \ln P_l(k)}{d \ln k} \right], \\
B_{\text{SQ2,3,sq}} &= P_l(k) P_l(q_b) \left[\frac{149}{1225} - \frac{17}{525} \frac{d \ln P_l(k)}{d \ln k} \right], \quad B_{\text{NLB,1,sq}} = P_l(k) P_l(q_b) [2], \\
B_{\text{NLB,2,sq}} &= P_l(k) P_l(q_b) \left[\frac{4}{3} \right], \quad B_{\text{NLB,3,sq}} = P_l(k) P_l(q_b) \left[\frac{2}{9} \right], \\
B_{\text{FOG,1,sq}} &= P_l(k) P_l(q_b) \left[1 - \frac{1}{9} \frac{d \ln P_l(k)}{d \ln k} \right], \quad B_{\text{FOG,2,sq}} = P_l(k) P_l(q_b) \left[\frac{22}{45} - \frac{2}{15} \frac{d \ln P_l(k)}{d \ln k} \right], \\
B_{\text{FOG,3,sq}} &= P_l(k) P_l(q_b) \left[\frac{3}{5} - \frac{1}{15} \frac{d \ln P_l(k)}{d \ln k} \right], \quad B_{\text{FOG,4,sq}} = P_l(k) P_l(q_b) \left[\frac{22}{75} - \frac{2}{25} \frac{d \ln P_l(k)}{d \ln k} \right], \\
B_{\text{FOG,5,sq}} &= P_l(k) P_l(q_b) \left[\frac{13}{105} - \frac{1}{21} \frac{d \ln P_l(k)}{d \ln k} \right], \quad B_{\text{FOG,6,sq}} = P_l(k) P_l(q_b) \left[\frac{13}{175} - \frac{1}{35} \frac{d \ln P_l(k)}{d \ln k} \right]. \tag{A.30}
\end{aligned}$$

Using eq. (A.30), the integrated bispectrum can further be simplified as

$$iB(k) \stackrel{k \gg q_a, q_b}{=} P_l(k) \sigma_{i,L}^2 H_X(k), \tag{A.31}$$

where $\sigma_{i,L}^2 = \frac{1}{V_L^2} \int \frac{dq_b}{2\pi^2} q_b^2 P_l(q_b) W_L^2(q_b)$ and $H_X(k)$ corresponds to the terms of the four categories in the square brackets in eq. (A.30). For $n_s = 0.95$, in the squeezed limit $\frac{d \ln P_l(k)}{d \ln k} \sim n_s - 4 = -3.05$. Plugging in the value of $\frac{d \ln P_l(k)}{d \ln k}$, we find that the analytical (eq. (A.30)) and numerical (figure A.1) results agree well.

Appendix B

Variance of the integrated bispectrum estimator

In this section we compute the variance of the integrated bispectrum estimator. In a survey/simulation with volume V_r , we first estimate the mean overdensity and the position-dependent power spectrum in the j^{th} subvolume with volume V_L by

$$\hat{\delta}_j = \frac{1}{N_{rL}} \sum_{\mathbf{l}\Delta r \in V_{Lj}} \delta_{r,\mathbf{l}}, \quad \hat{P}_j(k) = \frac{1}{V_L N_{kL}} \sum_{|\mathbf{l}k_{FL}| \in k \pm \Delta k/2} \delta_{kj,\mathbf{l}} \delta_{kj,\mathbf{l}}^*, \quad (\text{B.1})$$

where N_{rL} is the number of meshes in V_{Lj} , $\Delta r = (V_L/N_{rL})^{1/3}$ is the mesh size, $\delta_{r,\mathbf{l}}$ is the discrete density fluctuation field at the integer vector \mathbf{l} , N_{kL} is the number of Fourier modes in $(k - \Delta k/2, k + \Delta k/2)$ of V_L , $k_{FL} = 2\pi/L$ is the fundamental frequency of V_L , and δ_{kj} is the local Fourier transformation of the density fluctuation field in the j^{th} sub-volume. The estimated integrated bispectrum is then

$$i\hat{B}_L(k) = \frac{1}{N_{\text{cut}}^3} \sum_{j=1}^{N_{\text{cut}}^3} \hat{\delta}_j \hat{P}_j(k), \quad (\text{B.2})$$

where $N_{\text{cut}}^3 = V_r/V_L$ is the number of subvolumes.

We can rewrite eq. (B.1) using the window function $W_{rj,\mathbf{l}}$ ($W_{rj,\mathbf{l}} = 1$ if $\mathbf{l}\Delta r \in V_{Lj}$ and 0 otherwise) as

$$\begin{aligned} \hat{\delta}_j &= \frac{1}{N_{rL}} \sum_{\mathbf{l}\Delta r \in V_r} \delta_{r,\mathbf{l}} W_{rj,\mathbf{l}} = \left(\frac{k_F}{2\pi}\right)^3 \frac{1}{V_L} \sum_{\mathbf{m}k_F \in V_k} \delta_{k,m}^* W_{kj,\mathbf{m}}, \\ \delta_{kj,\mathbf{l}} &= (\Delta r)^3 \sum_{\mathbf{m}\Delta r \in V_{Lj}} \delta_{r,\mathbf{m}} e^{-i(\mathbf{m}-\mathbf{n}_{sj})\cdot\mathbf{l}M_L} = \left(\frac{k_F}{2\pi}\right)^3 e^{i\mathbf{n}_{sj}\cdot\mathbf{l}M_L} \sum_{\mathbf{n}k_F \in V_k} \delta_{k,\mathbf{L}-\mathbf{n}} W_{kj,\mathbf{n}}, \end{aligned} \quad (\text{B.3})$$

where V_k is the Fourier volume of V_r with the fundamental frequency $k_F = 2\pi/V_r^{1/3} = 2\pi/L_r$, $M_r = \Delta r k_F = 2\pi/N_{rL,1}$ with $N_{rL,1} = N_{rL}^{1/3}$ being the mesh number of L_r ,

$M_L = \Delta r k_{FL} = M_r N_{\text{cut}}$, $\mathbf{L} = \mathbf{1} N_{\text{cut}}$, and exponential term of $\delta_{jk,1}$ reflects the phase of the local Fourier transform (which will then be canceled out when computing the local power spectrum $\hat{P}_j(k)$). We shall use the capital letters to denote the integer vector multiplied by N_{cut} . $W_{ki,1}$ is the window function in Fourier space, which can be written as

$$W_{ki,1} = (\Delta r)^3 \sum_{\mathbf{m} \Delta r \in V_r} W_{ri,\mathbf{m}} e^{-i\mathbf{m} \cdot \mathbf{1} M_r} = W_L(\mathbf{1} k_F) e^{-i k_F \mathbf{r}_{L_i}} , \quad (\text{B.4})$$

where $W_L(\mathbf{k}) = V_L \prod_{i=0}^2 \text{sinc}(k_i L/2)$ is the window function of V_L . Eq. (B.4) is true in the continuous limit, i.e. $k_F \rightarrow 0$. Namely, there is a slight difference between the discrete Fourier transform of the window function and $W_L(\mathbf{k})$. However we shall ignore this difference and use the continuous limit in the derivation for simplicity.

Combining the above equations, the integrated bispectrum can be estimated as

$$i\hat{B}_L(k) = \left(\frac{k_F}{2\pi}\right)^9 \frac{1}{V_L^2 N_{kL}} \sum_{|\mathbf{j}| \in k \pm \Delta k/2} \sum_{(\mathbf{l}, \mathbf{m}, \mathbf{n}) \in V_k} \delta_{k,1}^* \delta_{k,\mathbf{J}-\mathbf{m}} \delta_{k,\mathbf{J}+\mathbf{n}}^* W_L(\mathbf{l}) W_L(\mathbf{m}) W_L(\mathbf{n}) \\ \times \frac{1}{N_{\text{cut}}^3} \sum_{i=1}^{N_{\text{cut}}^3} e^{-i(1+\mathbf{m}+\mathbf{n})k_F \cdot \mathbf{r}_{L_i}} . \quad (\text{B.5})$$

Here, to simplify the notation, we drop all the fundamental units (Δr and k_F) of the integer vectors in the summation and the window function. We find that the p^{th} axis of \mathbf{r}_{L_i} (\mathbf{r}_L is the center of the i^{th} subvolume) is $r_{L_{i,p}} = (i_p + 1/2)L$ with i_p being the order of the i^{th} subvolume in the p^{th} axis, hence the last term of eq. (B.5) can be simplified as

$$\sum_{i=1}^{N_{\text{cut}}^3} e^{-i(1+\mathbf{m}+\mathbf{n})k_F \cdot \mathbf{r}_{L_i}} = \prod_{p=0}^2 (-1)^{l_p+m_p+n_p} \frac{\sin[(l_p+m_p+n_p)\pi]}{\sin[(l_p+m_p+n_p)\pi/N_{\text{cut}}]} . \quad (\text{B.6})$$

Eq. (B.6) is non-zero only if $l_p+m_p+n_p = N_{\text{cut}} s_p$ with s_p being an integer, and the value is $(-1)^{s_0+s_1+s_2} N_{\text{cut}}^3$ for even N_{cut} and N_{cut}^3 for odd N_{cut} . We shall assume odd N_{cut} for simplifying the notation, but the results (variance of the estimator) would be identical for both cases, as we will show later. We can thus rewrite eq. (B.6) as

$$N_{\text{cut}}^3 \delta_{\mathbf{1}+\mathbf{m}+\mathbf{n}, \mathbf{s} N_{\text{cut}}}^K = N_{\text{cut}}^3 \delta_{\mathbf{1}+\mathbf{m}+\mathbf{n}, \mathbf{S}}^K , \quad (\text{B.7})$$

where $\delta_{a,b}^K$ is the Kronecker delta and $\mathbf{S} \equiv \mathbf{s} N_{\text{cut}}$. Finally, the estimator of the integrated bispectrum becomes

$$i\hat{B}_L(k) = \left(\frac{k_F}{2\pi}\right)^9 \frac{1}{V_L^2 N_{kL}} \sum_{|\mathbf{j}| \in k \pm \Delta k/2} \sum_{(\mathbf{m}, \mathbf{n}) \in V_k} \sum_{\mathbf{s}=-\infty}^{\infty} \delta_{k,\mathbf{S}-\mathbf{m}-\mathbf{n}}^* \delta_{k,\mathbf{J}-\mathbf{m}} \delta_{k,\mathbf{J}+\mathbf{n}}^* \\ \times W_L(\mathbf{S}-\mathbf{m}-\mathbf{n}) W_L(\mathbf{m}) W_L(\mathbf{n}) . \quad (\text{B.8})$$

Eq. (B.8) is an unbiased estimator because

$$\begin{aligned}
\langle \hat{iB}_L(k) \rangle &= \left(\frac{k_F}{2\pi} \right)^9 \frac{1}{V_L^2 N_{kL}} \sum_{|\mathbf{j}| \in k \pm \Delta k/2} \sum_{(\mathbf{m}, \mathbf{n}) \in V_k} \sum_{\mathbf{s} = -\infty}^{\infty} \langle \delta_{k, \mathbf{S} - \mathbf{m} - \mathbf{n}}^* \delta_{k, \mathbf{J} - \mathbf{m}} \delta_{k, \mathbf{J} + \mathbf{n}}^* \rangle \\
&\quad \times W_L(\mathbf{S} - \mathbf{m} - \mathbf{n}) W_L(\mathbf{m}) W_L(\mathbf{n}) \\
&= \frac{1}{V_L^2 N_{kL}} \sum_{|\mathbf{j}| \in k \pm \Delta k/2} \int \frac{d^3 q_1}{(2\pi)^3} \int \frac{d^3 q_2}{(2\pi)^3} B(+\mathbf{q}_1 + \mathbf{q}_2, \mathbf{J}k_F - \mathbf{q}_1, -\mathbf{J}k_F - \mathbf{q}_2) \\
&\quad \times W_L(\mathbf{q}_1) W_L(\mathbf{q}_2) W_L(-\mathbf{q}_1 - \mathbf{q}_2) \\
&= \frac{1}{N_{kL}} \sum_{|\mathbf{j}| \in k \pm \Delta k/2} iB(\mathbf{J}k_F) = iB(\mathbf{k}) , \tag{B.9}
\end{aligned}$$

where we replace the discrete Fourier transform with the continuous one as $[k_F^3/(2\pi)^3] \sum_{\mathbf{m} \in V_k} \rightarrow \int d^3 q/(2\pi)^3$. Note that only $\mathbf{s} = 0$ contributes to $\langle \hat{iB}_L(k) \rangle$.

Replacing the discrete Fourier transform with the integral form, the variance of the integrated bispectrum estimator can be computed by

$$\begin{aligned}
\langle [i\hat{B}_L(k) - \langle i\hat{B}_L(k) \rangle]^2 \rangle &= \langle [i\hat{B}_L(k)]^2 \rangle - [\langle i\hat{B}_L(k) \rangle]^2 \\
&= \left(\frac{k_F}{2\pi} \right)^{18} \frac{1}{V_L^4 N_{kL}^2} \sum_{|\mathbf{j}_1, \mathbf{j}_2| \in k \pm \Delta k/2} \sum_{\mathbf{s}_1, \mathbf{s}_2 = -\infty}^{\infty} \int \frac{d^3 q_1}{(2\pi)^3} \cdots \int \frac{d^3 q_4}{(2\pi)^3} \\
&\quad \langle \delta(\mathbf{k}_1 - \mathbf{q}_1) \delta(-\mathbf{k}_1 - \mathbf{q}_2) \delta(\mathbf{q}_1 + \mathbf{q}_2 - \mathbf{g}_1) \delta(\mathbf{k}_2 - \mathbf{q}_3) \delta(-\mathbf{k}_2 - \mathbf{q}_4) \delta(\mathbf{q}_3 + \mathbf{q}_4 - \mathbf{g}_2) \rangle \\
&\quad \times W_L(\mathbf{q}_1) W_L(\mathbf{q}_2) W_L(\mathbf{g}_1 - \mathbf{q}_1 - \mathbf{q}_2) W_L(\mathbf{q}_3) W_L(\mathbf{q}_4) W_L(\mathbf{g}_2 - \mathbf{q}_3 - \mathbf{q}_4) , \tag{B.10}
\end{aligned}$$

where $\mathbf{k}_n = \mathbf{J}_n k_F$ and $\mathbf{g}_n = \mathbf{S}_n k_F$. We shall assume that the dominant component of the six-point function is the disconnected part, and thus the only non-zero component has the wavenumber combinations as¹

$$\mathbf{k}_1 - \mathbf{q}_1 - \mathbf{k}_2 - \mathbf{q}_4 = 0 , \quad -\mathbf{k}_1 - \mathbf{q}_2 + \mathbf{k}_2 - \mathbf{q}_3 = 0 , \quad \mathbf{q}_1 + \mathbf{q}_2 - \mathbf{g}_1 + \mathbf{q}_3 + \mathbf{q}_4 - \mathbf{g}_2 = 0 . \tag{B.12}$$

This gives three delta functions as

$$(2\pi)^9 \delta_D(\mathbf{k}_1 - \mathbf{k}_2 - \mathbf{q}_1 - \mathbf{q}_4) \delta_D(-\mathbf{k}_1 + \mathbf{k}_2 - \mathbf{q}_2 - \mathbf{q}_3) \delta_D(\mathbf{g}_1 + \mathbf{g}_2) . \tag{B.13}$$

The last delta function in eq. (B.13) requires $\mathbf{g}_1 = -\mathbf{g}_2$ or $\mathbf{s}_1 = -\mathbf{s}_2$. This means that even if even N_{cut} has a parity term $(-1)^s$, it would be canceled because $\mathbf{s}_1 = -\mathbf{s}_2$.

¹Note that another seemingly non-zero component has the wavenumber combinations as

$$\mathbf{k}_1 - \mathbf{q}_1 + \mathbf{k}_2 - \mathbf{q}_3 = 0 , \quad -\mathbf{k}_1 - \mathbf{q}_2 - \mathbf{k}_2 - \mathbf{q}_4 = 0 , \quad \mathbf{q}_1 + \mathbf{q}_2 - \mathbf{g}_1 + \mathbf{q}_3 + \mathbf{q}_4 - \mathbf{g}_2 = 0 . \tag{B.11}$$

However, this requires $\mathbf{k}_1 = -\mathbf{k}_2$ or $\mathbf{j}_1 = -\mathbf{j}_2$. Since we count only the independent Fourier modes, only half of the Fourier space is counted (or only the hemisphere is considered), and so it is impossible to have $\mathbf{j}_1 = -\mathbf{j}_2$.

With the above results, the variance of the integrated bispectrum estimator is given by ($\mathbf{g} = \mathbf{S}k_F = \mathbf{s}N_{\text{cut}}k_F$)

$$\begin{aligned} & \left(\frac{k_F}{2\pi}\right)^3 \frac{1}{V_L^4 N_{kL}^2} \sum_{|\mathbf{j}_1, \mathbf{j}_2| \in k \pm \Delta k/2} \sum_{\mathbf{s}=-\infty}^{\infty} \int \frac{d^3 q_1}{(2\pi)^3} \int \frac{d^3 q_2}{(2\pi)^3} P(\mathbf{k}_1 - \mathbf{q}_1) P(-\mathbf{k}_1 - \mathbf{q}_2) P(\mathbf{q}_1 + \mathbf{q}_2 - \mathbf{g}) \\ & \times W_L(\mathbf{q}_1) W_L(\mathbf{q}_2) W_L(\mathbf{g} - \mathbf{q}_1 - \mathbf{q}_2) W_L(\mathbf{k}_1 - \mathbf{k}_2 - \mathbf{q}_1) W_L(-\mathbf{k}_1 + \mathbf{k}_2 - \mathbf{q}_2) W_L(-\mathbf{g} + \mathbf{q}_1 + \mathbf{q}_2). \end{aligned} \quad (\text{B.14})$$

Note that eq. (B.14) is non-zero only if $\mathbf{k}_1 = \mathbf{k}_2$ or $\mathbf{j}_1 = \mathbf{j}_2$, so the variance of the integrated bispectrum estimator can be simplified as ($\mathbf{k} = \mathbf{J}k_F = \mathbf{j}N_{\text{cut}}k_F$)

$$\begin{aligned} & \frac{1}{V_r V_L^4 N_{kL}^2} \sum_{|\mathbf{j}| \in k \pm \Delta k/2} \sum_{\mathbf{s}=-\infty}^{\infty} \int \frac{d^3 q_1}{(2\pi)^3} \int \frac{d^3 q_2}{(2\pi)^3} P(\mathbf{k} - \mathbf{q}_1) P(-\mathbf{k} - \mathbf{q}_2) P(\mathbf{q}_1 + \mathbf{q}_2 - \mathbf{g}) \\ & \times |W_L(\mathbf{q}_1)|^2 |W_L(\mathbf{q}_2)|^2 |W_L(\mathbf{g} - \mathbf{q}_1 - \mathbf{q}_2)|^2, \end{aligned} \quad (\text{B.15})$$

where we replace $k_F^3/(2\pi)^3$ with V_r . To proceed further, let us consider the sum over \mathbf{s} . Since $\mathbf{g} = \mathbf{s}N_{\text{cut}}k_F = \mathbf{s}k_{F,L}$, we replace the discrete sum with the integral as

$$\begin{aligned} & \sum_{\mathbf{s}=-\infty}^{\infty} P(\mathbf{q} - \mathbf{g}) |W_L(\mathbf{g} - \mathbf{q})|^2 \rightarrow \left(\frac{k_{F,L}}{2\pi}\right)^{-3} \int \frac{d^3 g}{(2\pi)^3} P(\mathbf{q} - \mathbf{g}) |W_L(\mathbf{g} - \mathbf{q})|^2 \\ & = \left(\frac{k_{F,L}}{2\pi}\right)^{-3} V_L^2 \sigma_L^2 = V_L^3 \sigma_L^2, \end{aligned} \quad (\text{B.16})$$

where $\sigma_L^2 = \frac{1}{V_L^2} \int \frac{d^3 q}{(2\pi)^3} P(q) |W_L(\mathbf{q})|^2$ is the variance of the fluctuation in the volume V_L .

Finally, the variance of the integrated bispectrum estimator is simply

$$\begin{aligned} & \frac{1}{V_r V_L^4 N_{kL}^2} \sum_{|\mathbf{j}| \in k \pm \Delta k/2} V_L^3 \sigma_L^2 \left[\int \frac{d^3 q}{(2\pi)^3} P(\mathbf{k} - \mathbf{q}) |W_L(\mathbf{q})|^2 \right]^2 \\ & = \frac{V_L}{V_r N_{kL}^2} \sigma_L^2 \sum_{|\mathbf{j}| \in k \pm \Delta k/2} [P_L(\mathbf{k})]^2 = \frac{V_L}{V_r N_{kL}} \sigma_L^2 [P_L(k)]^2, \end{aligned} \quad (\text{B.17})$$

where $P_L(\mathbf{k}) = \frac{1}{V_L} \int \frac{d^3 q}{(2\pi)^3} P(\mathbf{k} - \mathbf{q}) |W_L(\mathbf{q})|^2$ is the convolved power spectrum of the subvolume V_L . Note that the previous derivation ignores the shot noise contribution. If the shot noise is Poisson like, i.e. $P_{\text{shot}} = \bar{n}^{-1}$ with \bar{n} being the number density of the discrete particles, then it is trivial to add back as

$$\frac{V_L}{V_r N_{kL}} \left[\sigma_L^2 + \frac{P_{\text{shot}}}{V_L} \right] [P_L(k) + P_{\text{shot}}]^2. \quad (\text{B.18})$$

For the normalized integrated bispectrum, we assume that the variance is dominated by the bispectrum term instead of the normalization which contains $P_L(k)$ and σ_L^2 , and so its variance is

$$\frac{V_L}{V_r N_{kL}} \frac{\left[\sigma_L^2 + \frac{P_{\text{shot}}}{V_L} \right] [P_L(k) + P_{\text{shot}}]^2}{\sigma_L^4 P_L^2(k)}. \quad (\text{B.19})$$

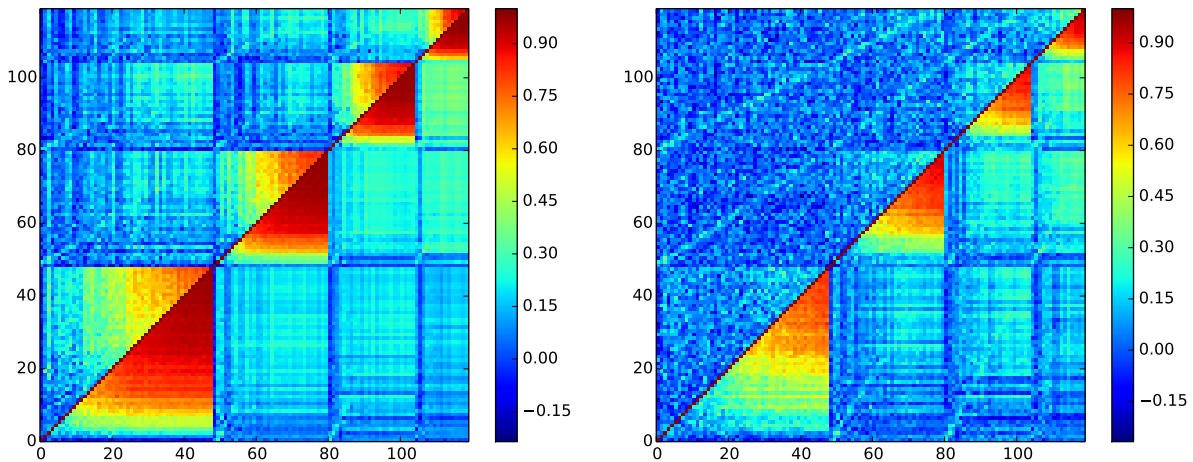


Figure B.1: Correlation matrices measured from 160 dark matter N -body simulations at $z = 0$ (left) and 2 (right) for $N_{\text{cut}} = 4$ (bin 0 to 47 in the axis labels), 6 (bin 48 to 79), 8 (bin 80 to 103), 12 (bin 104 to 119), which correspond to 600, 400, 300, and 200 h^{-1} Mpc, respectively. The bottom half and top half of the correlation matrices show the unnormalized and normalized integrated bispectrum.

Figure B.1 shows the correlation matrices measured from 160 dark matter N -body simulations at $z = 0$ and 2. The details of the simulations are given in section 4.1. There are four subvolume sizes: 600 (bin 0 to 47 in the axis labels), 400 (bin 48 to 79), 300 (bin 80 to 103), and 200 h^{-1} Mpc (bin 104 to 119). The bottom (top) half of the correlation matrices is the unnormalized (normalized) integrated bispectrum. We find that the cross-correlation between different subvolumes is much smaller than that within the same subvolumes. This is expected because different subvolumes have different long-wavelength modes, which are uncorrelated. At $z = 2$ the correlation matrices are more diagonal than at $z = 0$ because of the smaller nonlinearity. We also find that the normalization largely diagonalizes the correlation matrices, particularly at $z = 2$ where the off-diagonal components nearly vanish. Note that there are stripes, which are more obvious in the normalized integrated bispectrum at $z = 2$, across the diagonal elements of the cross covariances between different sizes of subvolumes. This is because these components have the same short-wavelength modes, i.e. the scales of the position-dependent power spectrum. Consequently, the correlation is stronger.

Figure B.2 shows the square root of the variances of the normalized integrated bispectra at $z = 0$ (left) and 2 (right). The data points are measured from simulations, and the solid lines are computed using eq. (B.19) with the linear power spectrum and zero shot noise. We find that on large scales as well as at high redshift, the agreement between simulations and analytical calculation is good. The agreement between the data points and the solid lines confirm our calculation of the variance of the integrated bispectrum estimator.

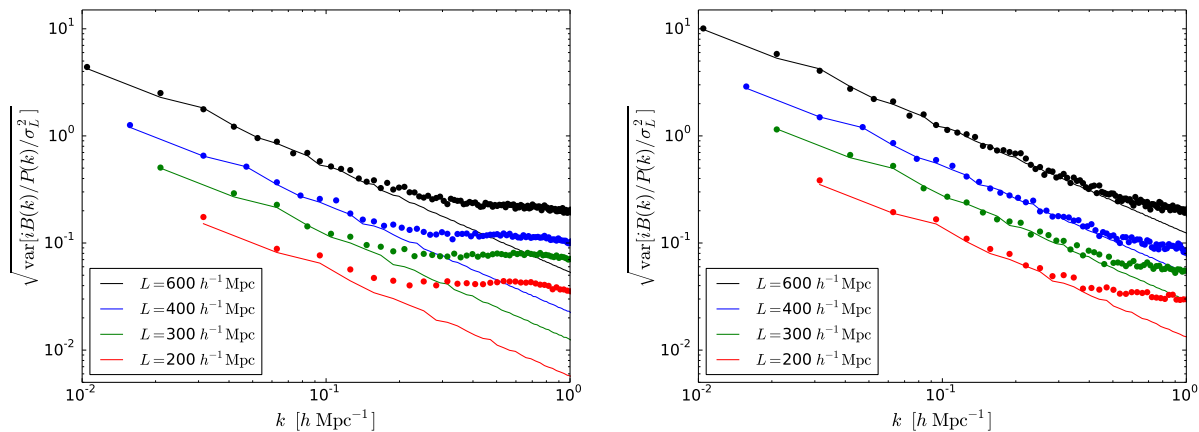


Figure B.2: Square root of the variances of the normalized integrated bispectrum at $z = 0$ (left) and 2 (right). The data points show the measurements from the simulations and the solid lines show eq. (B.19) with the linear power spectrum and zero shot noise.

Appendix C

Testing the integrated three-point function estimator with Gaussian realizations and the local bias model

We shall demonstrate that our integrated three-point function estimator is unbiased. To do this, we first generate the matter density field, $\delta_m(\mathbf{r})$, by Gaussian realizations¹ with $P_l(k)$ at $z = 0$ for the volume V_r of $1200 h^{-3} \text{ Mpc}^3$ and a mesh size of $4 h^{-1} \text{ Mpc}$. We then compute a mock “halo” density field using the local bias model via

$$\delta_h(\mathbf{r}) = b_1 \delta_m(\mathbf{r}) + \frac{b_2}{2} \left[\delta_m^2(\mathbf{r}) - \frac{\sum_{\mathbf{r} \in V_r} \delta_m^2(\mathbf{r})}{\sum_{\mathbf{r} \in V_r} 1} \right], \quad (\text{C.1})$$

where we set $b_1 = 3$ and $b_2 = 1$, and $\sum_{\mathbf{r} \in V_r}$ denotes a sum over grid cells in the entire volume. Note that $\sum_{\mathbf{r} \in V_r} \delta_h(\mathbf{r}) = 0$. We then divide the entire volume V_r into $N_s = 12^3 = 1728$ subvolumes V_L of $100 h^{-3} \text{ Mpc}^3$ and $N_s = 6^3 = 216$ subvolumes V_L of $200 h^{-3} \text{ Mpc}^3$. The two-point function in the subvolumes and the integrated three-point function are estimated by

$$\xi_h(r, \mathbf{r}_L) = \frac{\sum_{\mathbf{x}+\mathbf{r}, \mathbf{x} \in V_L} \delta_h(\mathbf{x} + \mathbf{r}) \delta_h(\mathbf{x})}{\sum_{\mathbf{x}+\mathbf{r}, \mathbf{x} \in V_L} 1}, \quad i\zeta_{L,h}(r) = \sum_{i=1}^{N_s} \xi_h(r, \mathbf{r}_L) \bar{\delta}_h(\mathbf{r}_L), \quad (\text{C.2})$$

where $\bar{\delta}_h(\mathbf{r}_L)$ is the mean halo overdensity in the subvolume centered at \mathbf{r}_L . Note that the denominator in the estimator of $\xi_h(r, \mathbf{r}_L)$ takes the boundary effect into account so $\langle \xi_h(r, \mathbf{r}_L) \rangle = \xi_h(r)$ without $f_{L,\text{bndry}}(r)$. This means that the theoretical model of the integrated three-point function computed by eq. (2.36) has to be divided by $f_{L,\text{bndry}}(r)$. Since $\delta_m(\mathbf{r})$ is Gaussian, the only contribution to the three-point function is from the nonlinear bias term, and so the estimated integrated three-point function is exactly given by $\frac{i\zeta_{L,b_2}(r)}{f_{L,\text{bndry}}(r)}$.

¹Since $\delta_m(\mathbf{r})$ follows the Gaussian statistics, it is possible that $\delta_m(\mathbf{r}) < -1$, which is unphysical. However, as we only compute the power spectrum without Poisson sampling the density field, this effect can be neglected.

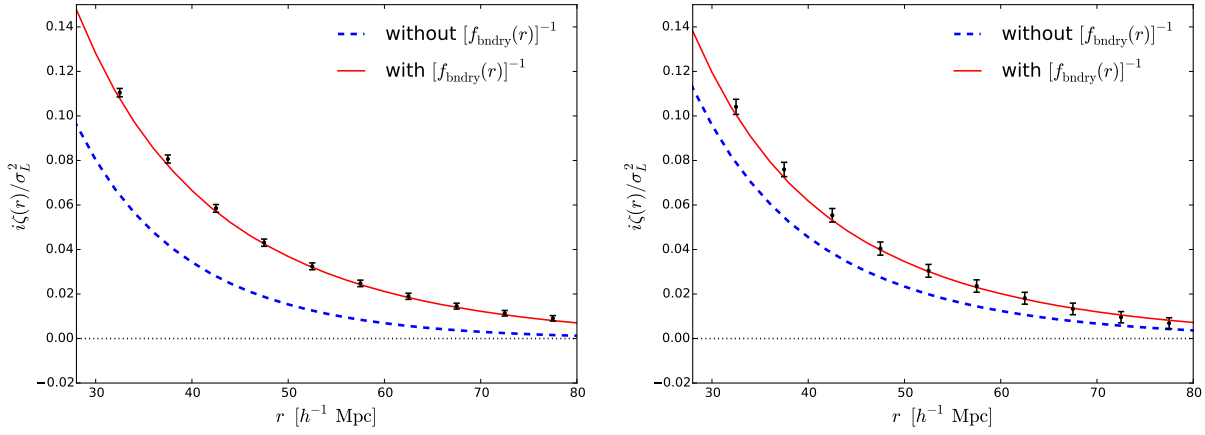


Figure C.1: The normalized integrated three-point functions of the mock halo density field with $b_1 = 3$ and $b_2 = 1$. The left and right panels are for $V_L = 100 h^{-3} \text{ Mpc}^3$ and $200 h^{-3} \text{ Mpc}^3$, respectively. The data points show the mean of 300 Gaussian realizations, and the error bars are the variances of the mean (but note that the data points are highly correlated). The blue dashed and red solid lines are the theoretical models ($i\zeta_{L,b_2}$) without and with $[f_{L,\text{bndry}}(r)]^{-1}$, respectively.

Figure C.1 shows the normalized integrated three-point functions of the mock halo density field with $b_1 = 3$ and $b_2 = 1$ from 300 Gaussian realizations. The measurements are in excellent agreement with $\frac{i\zeta_{L,b_2}(r)}{f_{L,\text{bndry}}(r)}$. This test gives us the confidence that our estimator is unbiased.

Appendix D

Effects of effective F_2 and G_2 kernels and non-local tidal bias

In this appendix, we show how the inferred value of b_2 changes when extending our baseline model for the bispectrum based on SPT at the tree level with local bias to the model used in the analysis of [62].

Their model replaces F_2 and G_2 in eq. (A.17) with “effective” kernels, F_2^{eff} [64] and G_2^{eff} [63], which are calibrated to match the nonlinear matter bispectrum in of N-body simulations. Their model also adds a non-local galaxy bias caused by tidal fields [113, 9, 148] to Z_2 , i.e.,

$$Z_2 \rightarrow Z_2 + \frac{1}{2}b_{s^2} \left[(\hat{k}_1 \cdot \hat{k}_2)^2 - \frac{1}{3} \right], \quad (\text{D.1})$$

where $b_{s^2} = -(4/7)(b_1 - 1)$. We use this model to compute the integrated three-point function, and find b_2 of the mocks in real and redshift space by performing a joint fit with the two-point function as described in section 5.1.3 and 5.1.4.

Table D.1 summarizes the results. The “baseline model” refers to the model based on SPT and local bias. The “eff kernel” refers to the model with F_2^{eff} , G_2^{eff} , and local bias. The “tidal bias” refers to the model with F_2 , G_2 , local bias, and tidal bias. Finally, “both” refers to the model with F_2^{eff} , G_2^{eff} , local bias, and tidal bias.

Both the effective kernels and the non-local tidal bias result in a larger nonlinear bias, which is in better agreement with [62]. The changes of the best-fitting nonlinear bias, however, are still within the $1 - \sigma$ uncertainties, and all the results are consistent with [62]. We also calculate the goodness of the fit for all the models in both real and redshift space by comparing the mean of the mocks and the best-fitting models, as well as the χ^2 -distribution. We find that all models perform equally well; thus, we shall primarily use the simplest model, i.e. the SPT at the tree level with local bias for modeling the three-point function, but also report the results for the extended models.

r-space	b_1	b_2	z-space	b_1	b_2
baseline	1.971 ± 0.076	0.58 ± 0.31	baseline	1.931 ± 0.077	0.54 ± 0.35
eff kernel	1.973 ± 0.076	0.62 ± 0.31	eff kernel	1.933 ± 0.077	0.65 ± 0.35
tidal bias	1.971 ± 0.076	0.64 ± 0.31	tidal bias	1.932 ± 0.077	0.60 ± 0.35
both	1.973 ± 0.076	0.68 ± 0.31	both	1.933 ± 0.077	0.71 ± 0.35

Table D.1: Best-fitting values of b_1 and b_2 and their uncertainties for mock catalogs, obtained using different models of the bispectrum in real space (left) and redshift space (right).

Appendix E

Comparison for $i\zeta(r)/\sigma_L^2$ of BOSS DR10 CMASS sample and PTHalo mock catalogs in different redshift bins

The BOSS DR10 CMASS sample and the mocks have different sets of random samples with slightly different $\bar{n}(z)$, hence the properties of the observations and the mocks may not agree well in all redshift bins. Moreover, as mentioned in [117], the CMASS sample is flux-limited, and thus the observed galaxies statistically have larger stellar masses at higher redshift (see figure 1 in [117]). This may cause redshift evolution of the bias, and so the correlation functions. We shall measure $i\zeta(r)/\sigma_L^2$ as a function of redshift to test this.

The measurements in the subvolumes are mostly the same as introduced in section 5.1.2, except that we now measure $\alpha(z_j)$ as a function of redshift bin z_j , and the average is done in the individual redshift bin. Namely,

$$\alpha(z_j) = \frac{\sum_{i \in z_j} w_{g,i}}{\sum_{i \in z_j} w_{r,i}} = \frac{w_{r,z_j}}{w_{g,z_j}}, \quad \bar{g}(z_j) = \frac{1}{w_{r,z_j}} \sum_{i \in z_j} g_i w_{r,i}. \quad (\text{E.1})$$

This assures that $\bar{\delta}(z_j) = 0$ for all redshift bins.

Figure E.1 and figure E.2 show $i\zeta(r)/\sigma_L^2$ at different redshift bins for 220 and 120 h^{-1} Mpc subvolumes, respectively. We find no clear sign that $i\zeta(r)/\sigma_L^2$ of the observations has different redshift evolution relative to the mocks. Thus, it is justified to study $i\zeta(r)/\sigma_L^2$ using one effective redshift for the BOSS DR10 CMASS sample. With the upcoming DR12 sample with a larger volume, the redshift evolution of $i\zeta(r)/\sigma_L^2$ can be better studied.

E. Comparison for $i\zeta(r)/\sigma_L^2$ of BOSS DR10 CMASS sample and PTHalo mock catalogs in different redshift bins

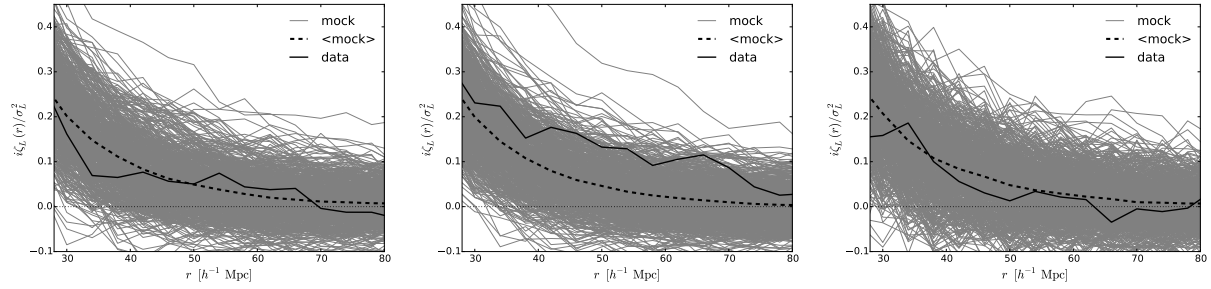


Figure E.1: $i\zeta(r)/\sigma_L^2$ of $220 h^{-1}$ Mpc subvolumes in different redshift bins. The redshift bins increase from left to right, with the redshift cuts quoted in the beginning of section 5.1 and section 5.2.

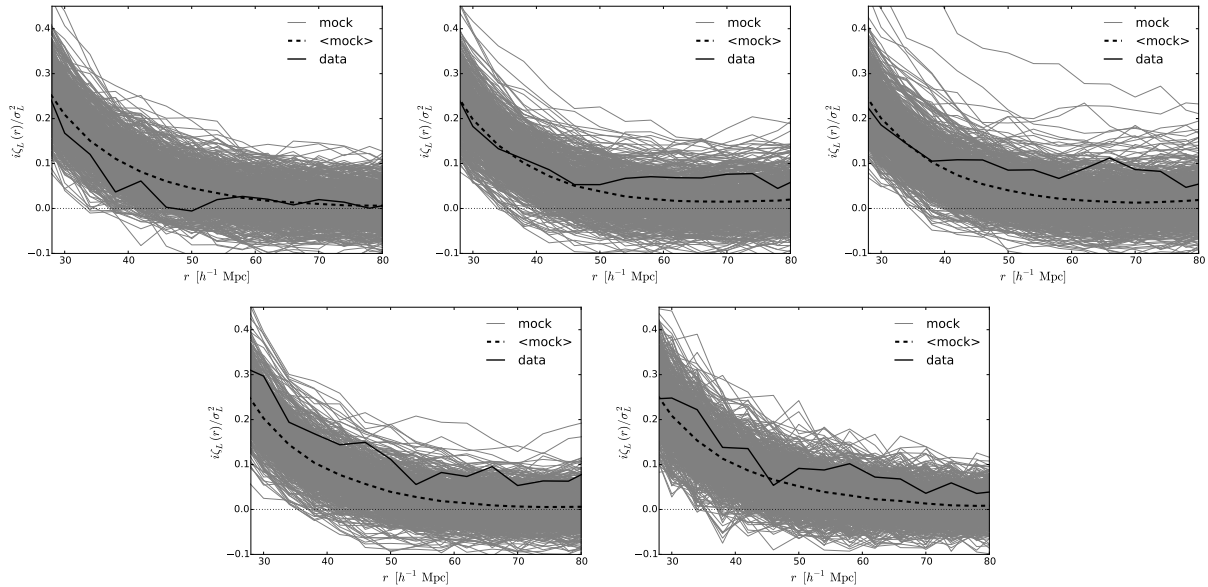


Figure E.2: Same as figure E.1, but for $120 h^{-1}$ Mpc subvolumes. The redshift bins increase from top left to bottom right.

Appendix F

Squeezed-limit N -point functions and power spectrum response

In this appendix, we prove the relation between the power spectrum response and the squeezed limit N -point functions, as discussed in chapter 6. We only consider equal-time N -point functions, to which there are no boost-type contributions from kinematic consistency relations. Further, we assume that the long-wavelength modes are well inside the horizon, removing gauge-dependent terms present for horizon-scale modes.

We first expand the power spectrum as a function of the *linearly extrapolated initial overdensity* δ_{L0} as

$$P(k, t | \delta_{L0}) = \sum_{n=0}^{\infty} \frac{1}{n!} R_n(k, t) \left[\delta_{L0} \hat{D}(t) \right]^n P(k, t) , \quad (\text{F.1})$$

where $R_n(k, t)$ are response functions with $R_0(k, t) = 1$. At the same order in derivatives, that is at the same order in k_i/k of the squeezed-limit N -point function, the power spectrum will also depend on the long-wavelength tidal field which can be parametrized through

$$K_{ij}(\mathbf{k}) \equiv \left(\frac{k_i k_j}{k^2} - \frac{1}{3} \delta_{ij} \right) \delta(\mathbf{k}) . \quad (\text{F.2})$$

As here we consider only the angle-averaged long-wavelength modes, the long-wavelength tidal field contributions drop out.

In the following, we will suppress the time argument for clarity. The definition of \mathcal{S}_n is given by

$$\mathcal{S}_n(k, k'; k_1, \dots, k_n) \equiv \int \frac{d^2 \hat{k}_1}{4\pi} \dots \int \frac{d^2 \hat{k}_n}{4\pi} \langle \delta(\mathbf{k}) \delta(\mathbf{k}') \delta(\mathbf{k}_1) \dots \delta(\mathbf{k}_n) \rangle'_c , \quad (\text{F.3})$$

where the prime denotes that the factor $(2\pi)^3 \delta_D(\mathbf{k} + \mathbf{k}' + \mathbf{k}_{1\dots n})$ is dropped and $\mathbf{k}_{1\dots n} = \sum_{i=1}^n \mathbf{k}_i$. We consider the limit

$$\lim_{k_i \rightarrow 0} \frac{\mathcal{S}_n(k, k'; k_1, \dots, k_n)}{P(k) P_l(k_1) \dots P_l(k_n)} , \quad (\text{F.4})$$

which means that *all* $|\mathbf{k}_i|$ are taken to zero. In this limit, spatial homogeneity enforces $\mathbf{k}' = -\mathbf{k} + \mathcal{O}(k_i/k)$, so that (for statistically isotropic initial conditions) the right-hand-side of eq. (F.4) only depends on k .

In order to prove $R_n(k)$ is equivalent to eq. (F.4), we first note that since we are interested in the limit $k_i \rightarrow 0$, we can replace $\delta(\mathbf{k}_i)$ in eq. (F.3) with the linear density field $\delta_L(\mathbf{k}_i)$. We further transform \mathbf{k}_i into configuration space, writing

$$\begin{aligned} \mathcal{S}_n(k; k_1, \dots, k_n) &= \int \frac{d^2 \hat{k}_1}{4\pi} \dots \int \frac{d^2 \hat{k}_n}{4\pi} \prod_{i=1}^n \int d^3 x_i e^{i\mathbf{x}_i \cdot \mathbf{k}_i} \langle \delta(\mathbf{k}) \delta(\mathbf{k}') \delta(\mathbf{x}_1) \dots \delta(\mathbf{x}_n) \rangle'_c \\ &= \prod_{i=1}^n \int d^3 x_i e^{i\mathbf{x}_i \cdot \mathbf{k}_i} \tilde{\mathcal{S}}_n(k, x_1, \dots, x_n), \end{aligned} \quad (\text{F.5})$$

where

$$\tilde{\mathcal{S}}_n(k; x_1, \dots, x_n) \equiv \int \frac{d^2 \hat{x}_1}{4\pi} \dots \int \frac{d^2 \hat{x}_n}{4\pi} \langle \delta(\mathbf{k}) \delta(\mathbf{k}') \delta(\mathbf{x}_1) \dots \delta(\mathbf{x}_n) \rangle'_c. \quad (\text{F.6})$$

Note that the angle average is a linear operation and thus commutes with the Fourier transform; in other words, the k -space angle average of the Fourier transform of a function is the Fourier transform of the x -space angle average of the same function.

Now consider the limit $k_i \rightarrow 0$, which implies that $x_i \rightarrow \infty$ in the argument of $\tilde{\mathcal{S}}_n$. Then $\tilde{\mathcal{S}}_n(k)$ describes the modulation of the small-scale power spectrum $P(k, \mathbf{0})$ measured around $\mathbf{x} = 0$ by n spherically symmetric large-scale modes (recall that $\mathbf{k}' \approx -\mathbf{k}$). This statement can be formalized by introducing an intermediate scale R_L such that $1/k \ll R_L \ll |\mathbf{x}_i| \sim 1/k_i$ and defining $\delta(\mathbf{k}) \rightarrow \delta_{R_L}(\mathbf{k})$ to be the Fourier transform within a cubic volume of size R_L around $\mathbf{x} = 0$. Then, $\delta_{R_L}(\mathbf{k}) = \delta(\mathbf{k}) + \mathcal{O}(1/(kR_L))$, while the long-wavelength modes are constant over the same volume with corrections suppressed by $k_i R_L$. The corrections we expect in the end are thus of order k_i/k . To lowest order in these corrections, $\tilde{\mathcal{S}}_n(k)$ can be written as

$$\lim_{k_i \rightarrow 0} : \tilde{\mathcal{S}}_n(k; x_1, \dots, x_n) = \int \frac{d^2 \hat{x}_1}{4\pi} \dots \int \frac{d^2 \hat{x}_n}{4\pi} \langle P(k, \mathbf{0}) \delta_L(\mathbf{x}_1) \dots \delta_L(\mathbf{x}_n) \rangle'_c. \quad (\text{F.7})$$

Inserting the expression for the local power spectrum from eq. (F.1), we obtain

$$\lim_{k_i \rightarrow 0} : \tilde{\mathcal{S}}_n(k; x_1, \dots, x_n) = \sum_{m=0}^{\infty} \frac{1}{m!} R_m(k) P(k) \int \frac{d^2 \hat{x}_1}{4\pi} \dots \int \frac{d^2 \hat{x}_n}{4\pi} \langle \delta_L^m(\mathbf{0}) \delta_L(\mathbf{x}_1) \dots \delta_L(\mathbf{x}_n) \rangle'_{i-0}. \quad (\text{F.8})$$

Here, the subscript $i-0$ indicates that only contractions between $\mathbf{0}$ and \mathbf{x}_i are to be taken, since the left-hand-side of eq. (F.8) is defined through the connected correlation function (all other contractions would contribute to the disconnected part of $\langle \delta(\mathbf{k}) \delta(\mathbf{k}') \delta(\mathbf{x}_1) \dots \delta(\mathbf{x}_n) \rangle$). Since all density fields in the correlator in eq. (F.8) are linear, limiting to the contractions

between $\mathbf{0}$ and \mathbf{x}_i then constrains $m = n$. Therefore,

$$\begin{aligned} \lim_{k_i \rightarrow 0} : \tilde{\mathcal{S}}_n(k; x_1, \dots, x_n) &= \frac{1}{n!} R_n(k) P(k) n! \prod_{i=1}^n \int \frac{d^2 \hat{x}_i}{4\pi} \xi_L(\mathbf{x}_i) \\ &= R_n(k) P(k) \prod_{i=1}^n \int \frac{d^3 k_i}{(2\pi)^3} e^{i\mathbf{x}_i \cdot \mathbf{k}_i} P_L(k_i) . \end{aligned} \quad (\text{F.9})$$

Here, ξ_L and P_L denote the linear matter correlation function and power spectrum, respectively. Going back to Fourier space then immediately yields that for $k_i \rightarrow 0$,

$$\mathcal{S}_n(k; k_1, \dots, k_n) = R_n(k) P(k) \prod_{i=1}^n P_L(k_i) + \mathcal{O}\left(\frac{k_i}{k}, \frac{k_i}{k_{\text{NL}}}\right) , \quad (\text{F.10})$$

where k_{NL} is the nonlinear scale. Finally, we can show that

$$R_n(k) = \lim_{k_i \rightarrow 0} \frac{\mathcal{S}_n(k; k_1, \dots, k_n)}{P(k) P_L(k_1) \dots P_L(k_n)} . \quad (\text{F.11})$$

This provides the connection between the response functions $R_n(k)$ and the angle-averaged matter $(n + 2)$ -point function eq. (F.3) in a certain limit squeezed limit (since $k_i \ll k$). Note that no assumption about the magnitude of k has been made, i.e. this value can be fully nonlinear. In the following, we illustrate eq. (F.11) at tree level in perturbation theory for the cases $n = 1$ (three-point function) and $n = 2$ (four-point function).

F.1 Tree-level result: $n = 1$

At tree-level for $n = 1$ we obtain

$$\lim_{k_i \rightarrow 0} \mathcal{S}_1(k; k_1) \stackrel{\text{tree-level}}{=} 2 \lim_{k_1 \rightarrow 0} \int \frac{d^2 \hat{k}_1}{4\pi} [F_2(\mathbf{k}, \mathbf{k}_1) P_l(k) + F_2(-\mathbf{k} - \mathbf{k}_1, \mathbf{k}_1) P_l(|\mathbf{k} + \mathbf{k}_1|)] P_l(k_1) . \quad (\text{F.12})$$

Eq. (F.11) then yields

$$R_1(k) \stackrel{\text{tree-level}}{=} \frac{2}{P_l(k)} \lim_{k_1 \rightarrow 0} \int \frac{d^2 \hat{k}_1}{4\pi} [F_2(\mathbf{k}, \mathbf{k}_1) P_l(k) + F_2(-\mathbf{k} - \mathbf{k}_1, \mathbf{k}_1) P_l(|\mathbf{k} + \mathbf{k}_1|)] \quad (\text{F.13})$$

with

$$F_2(\mathbf{k}_1, \mathbf{k}_2) = \frac{5}{7} + \frac{1}{2} \mu \left(\frac{k_1}{k_2} + \frac{k_2}{k_1} \right) + \frac{2}{7} \mu^2 , \quad (\text{F.14})$$

where μ is the cosine of \mathbf{k}_1 and \mathbf{k}_2 . The term $\mu/2(k/k_1)$ is problematic as we are sending $k_1 \rightarrow 0$. Using that

$$\begin{aligned} |\mathbf{k} + \mathbf{k}_1| &= k [1 + q\mu + \mathcal{O}(q^2)] , \quad q = \frac{k_1}{k} \\ P_l(|\mathbf{k} + \mathbf{k}_1|) &= P_l(k) \left[1 + \frac{d \ln P_l(k)}{d \ln k} q\mu + \mathcal{O}(q^2) \right] , \end{aligned} \quad (\text{F.15})$$

the sum of the two IR-divergent terms in eq. (F.13) becomes

$$\frac{1}{2} \left\{ \mu \frac{k}{k_1} P_l(k) + \frac{-(\mathbf{k} + \mathbf{k}_1) \cdot \mathbf{k}_1}{|\mathbf{k} + \mathbf{k}_1| k_1} P_l(|\mathbf{k} + \mathbf{k}_1|) \right\} = \frac{1}{2} P_l(k) \left[-\mu^2 \frac{d \ln P_l(k)}{d \ln k} - 1 \right] + \mathcal{O}(q) . \quad (\text{F.16})$$

As expected, the divergent pieces have canceled. We have dropped terms of order k_1/k which are irrelevant in the limit we are interested in. We finally obtain

$$\begin{aligned} R_1(k) \stackrel{\text{tree-level}}{=} & 2 \int_{-1}^1 \frac{d\mu}{2} \left[\frac{10}{7} - \frac{1}{2} \left(\mu^2 \frac{d \ln P_l(k)}{d \ln k} + 1 \right) + \frac{4}{7} \mu^2 \right] \\ & = 2 \left[\frac{10}{7} - \frac{1}{6} \frac{d \ln P_l(k)}{d \ln k} - \frac{1}{2} + \frac{4}{21} \right] = \frac{47}{21} - \frac{1}{3} \frac{d \ln P_l(k)}{d \ln k} . \end{aligned} \quad (\text{F.17})$$

Eq. (F.17) agrees with the linear prediction for R_1 shown in chapter 6, with f_1 , e_1 , and g_1 computed in chapter 3 assuming Einstein-de Sitter universe.

F.2 Tree-level result: $n = 2$

At $n = 2$, we have

$$\begin{aligned} \mathcal{S}_n(k; k_1, k_2) &= \int \frac{d^2 \hat{k}_1}{4\pi} \int \frac{d^2 \hat{k}_2}{4\pi} \langle \delta(\mathbf{k}) \delta(\mathbf{k}') \delta(\mathbf{k}_1) \delta(\mathbf{k}_2) \rangle'_c \\ & \stackrel{k_1, k_2 \rightarrow 0}{=} \int \frac{d^2 \hat{k}_1}{4\pi} \int \frac{d^2 \hat{k}_2}{4\pi} \left\{ 6 \left[F_3(\mathbf{k}, \mathbf{k}_1, \mathbf{k}_2) P_l(k) + F_3(-\mathbf{k} - \mathbf{k}_{12}, \mathbf{k}_1, \mathbf{k}_2) P_l(|\mathbf{k} + \mathbf{k}_{12}|) \right] \right. \\ & \quad + 4 \left[F_2(-\mathbf{k}_1, \mathbf{k} + \mathbf{k}_1) F_2(\mathbf{k}_2, \mathbf{k} + \mathbf{k}_1) P_l(|\mathbf{k} + \mathbf{k}_1|) \right. \\ & \quad \left. \left. + F_2(\mathbf{k}_1, \mathbf{k} + \mathbf{k}_2) F_2(-\mathbf{k}_2, \mathbf{k} + \mathbf{k}_2) P_l(|\mathbf{k} + \mathbf{k}_2|) \right] \right\} P_l(k_1) P_l(k_2) , \end{aligned} \quad (\text{F.18})$$

where F_3 is the symmetrized third-order perturbation theory kernel, and the unsymmetrized form can be found in [65]. Both F_2^2 and F_3 contain formally IR-divergent terms up to $\mathcal{O}[(q_{1,2})^2]$ where $q_{1,2} = k_{1,2}/k$ for $k_{1,2} \rightarrow 0$ which cancel in the end, so we should expand the power spectrum to $\mathcal{O}[(k_{1,2})^2]$ to obtain the consistent result at order $\mathcal{O}[(q_{1,2})^0]$.

We have

$$\begin{aligned}
P_l(|\mathbf{k} + \mathbf{k}_1|) &= P_l(k) \left[1 + \left(q_1 \mu_1 + \frac{q_1^2}{2} [1 - \mu_1^2] \right) \frac{k}{P_l(k)} \frac{dP_l(k)}{dk} + \frac{q_1^2 \mu_1^2}{2} \frac{k^2}{P_l(k)} \frac{d^2 P_l(k)}{dk^2} + \mathcal{O}(q_1^3) \right] \\
P_l(|\mathbf{k} + \mathbf{k}_1 + \mathbf{k}_2|) &= P_l(k) \left[1 + \left([q_1 \mu_1 + q_2 \mu_2] + \frac{1}{2} [q_1^2 (1 - \mu_1^2) + q_2^2 (1 - \mu_2^2) \right. \right. \\
&\quad \left. \left. + 2q_1 q_2 (\mu_{12} - \mu_1 \mu_2)] \right) \frac{k}{P_l(k)} \frac{dP_l(k)}{d \ln k} \right. \\
&\quad \left. + \frac{1}{2} (q_1^2 \mu_1^2 + q_2^2 \mu_2^2 + 2q_1 q_2 \mu_1 \mu_2) \frac{k^2}{P_l(k)} \frac{d^2 P_l(k)}{dk^2} + \mathcal{O}[(q_{1,2})^3] \right], \tag{F.19}
\end{aligned}$$

where $\mu_{1,2}$ is the cosine of \mathbf{k} and $\mathbf{k}_{1,2}$, and μ_{12} is the cosine of \mathbf{k}_1 and \mathbf{k}_2 . The leading order terms are

$$\begin{aligned}
R_2(k) \stackrel{\text{tree-level}}{=} & \int \frac{d^2 \hat{k}_1}{4\pi} \int \frac{d^2 \hat{k}_2}{4\pi} \frac{1}{147} \left[(628 + 324\mu_1^2 + 112\mu_{12}^2 - 280\mu_1\mu_2\mu_{12} \right. \\
& \quad \left. + 380\mu_2^2 + 656\mu_1^2\mu_2^2 - 56\mu_2^2\mu_{12}^2) \right. \\
& \quad \left. + (-273\mu_1^2 + 147\mu_1\mu_2\mu_{12} - 336\mu_2^2 \right. \\
& \quad \left. - 483\mu_1^2\mu_2^2 + 63\mu_2^2\mu_{12}^2) \frac{k}{P_l(k)} \frac{dP_l(k)}{dk} \right. \\
& \quad \left. + 147\mu_1^2\mu_2^2 \frac{k^2}{P_l(k)} \frac{d^2 P_l(k)}{dk^2} \right] \\
&= \frac{8420}{1323} - \frac{100}{63} \frac{k}{P_l(k)} \frac{dP_l(k)}{dk} + \frac{1}{9} \frac{k^2}{P_l(k)} \frac{d^2 P_l(k)}{dk^2}. \tag{F.20}
\end{aligned}$$

Eq. (F.20) also agrees with the linear prediction in chapter 6, with e_i, f_i, g_i ($i = 1, 2$), computed in chapter 3 assuming Einstein-de Sitter universe, are inserted.

Bibliography

- [1] S.J. Aarseth, *Monthly Notices of the RAS* **126** (1963), 223.
- [2] N. Agarwal, S. Ho and S. Shandera, *Journal of Cosmology and Astroparticle Physics* **2** (2014), 38.
- [3] C.P. Ahn, R. Alexandroff, C. Allende Prieto, F. Anders, S.F. Anderson, T. Anderton, B.H. Andrews, É. Aubourg, S. Bailey, F.A. Bastien and et al., *Astrophysical Journal, Supplement* **211** (2014), 17.
- [4] S. Alam, F.D. Albareti, C. Allende Prieto, F. Anders, S.F. Anderson, B.H. Andrews, E. Armengaud, É. Aubourg, S. Bailey, J.E. Bautista and et al., *ArXiv e-prints* (2015).
- [5] A. Albrecht and P.J. Steinhardt, *Physical Review Letters* **48** (1982), 1220.
- [6] L. Anderson, É. Aubourg, S. Bailey, F. Beutler, V. Bhardwaj, M. Blanton, A.S. Bolton, J. Brinkmann, J.R. Brownstein, A. Burden, C.H. Chuang, A.J. Cuesta, K.S. Dawson, D.J. Eisenstein, S. Escoffier, J.E. Gunn, H. Guo, S. Ho, K. Honscheid, C. Howlett, D. Kirkby, R.H. Lupton, M. Manera, C. Maraston, C.K. McBride, O. Mena, F. Montesano, R.C. Nichol, S.E. Nuza, M.D. Olmstead, N. Padmanabhan, N. Palanque-Delabrouille, J. Parejko, W.J. Percival, P. Petitjean, F. Prada, A.M. Price-Whelan, B. Reid, N.A. Roe, A.J. Ross, N.P. Ross, C.G. Sabiu, S. Saito, L. Samushia, A.G. Sánchez, D.J. Schlegel, D.P. Schneider, C.G. Scoccola, H.J. Seo, R.A. Skibba, M.A. Strauss, M.E.C. Swanson, D. Thomas, J.L. Tinker, R. Tojeiro, M.V. Magaña, L. Verde, D.A. Wake, B.A. Weaver, D.H. Weinberg, M. White, X. Xu, C. Yèche, I. Zehavi and G.B. Zhao, *Monthly Notices of the RAS* **441** (2014), 24.
- [7] L. Anderson, E. Aubourg, S. Bailey, F. Beutler, A.S. Bolton, J. Brinkmann, J.R. Brownstein, C.H. Chuang, A.J. Cuesta, K.S. Dawson, D.J. Eisenstein, S. Ho, K. Honscheid, E.A. Kazin, D. Kirkby, M. Manera, C.K. McBride, O. Mena, R.C. Nichol, M.D. Olmstead, N. Padmanabhan, N. Palanque-Delabrouille, W.J. Percival, F. Prada, A.J. Ross, N.P. Ross, A.G. Sánchez, L. Samushia, D.J. Schlegel, D.P. Schneider, H.J. Seo, M.A. Strauss, D. Thomas, J.L. Tinker, R. Tojeiro, L. Verde, D. Wake, D.H. Weinberg, X. Xu and C. Yèche, *Monthly Notices of the RAS* **439** (2014), 83.
- [8] T. Baldauf, V. Desjacques and U. Seljak, *ArXiv e-prints* (2014).

-
- [9] T. Baldauf, U. Seljak, V. Desjacques and P. McDonald, *Physical Review D* **86** (2012), 083540.
- [10] T. Baldauf, U. Seljak and L. Senatore, *Journal of Cosmology and Astroparticle Physics* **4** (2011), 6.
- [11] T. Baldauf, U. Seljak, L. Senatore and M. Zaldarriaga, *Journal of Cosmology and Astroparticle Physics* **10** (2011), 31.
- [12] J. Barriga and E. Gaztañaga, *Monthly Notices of the RAS* **333** (2002), 443.
- [13] J.D. Barrow and P. Saich, *Monthly Notices of the RAS* **262** (1993), 717.
- [14] D. Baumann, A. Nicolis, L. Senatore and M. Zaldarriaga, *Journal of Cosmology and Astroparticle Physics* **7** (2012), 51.
- [15] I. Ben-Dayan, T. Konstandin, R.A. Porto and L. Sagunski, *Journal of Cosmology and Astroparticle Physics* **2** (2015), 26.
- [16] A.A. Berlind, D.H. Weinberg, A.J. Benson, C.M. Baugh, S. Cole, R. Davé, C.S. Frenk, A. Jenkins, N. Katz and C.G. Lacey, *Astrophysical Journal* **593** (2003), 1.
- [17] F. Bernardeau, S. Colombi, E. Gaztañaga and R. Scoccimarro, *Physics Reports* **367** (2002), 1.
- [18] F. Bernardeau, M. Crocce and R. Scoccimarro, *Physical Review D* **85** (2012), 123519.
- [19] F. Beutler, S. Saito, H.J. Seo, J. Brinkmann, K.S. Dawson, D.J. Eisenstein, A. Font-Ribera, S. Ho, C.K. McBride, F. Montesano, W.J. Percival, A.J. Ross, N.P. Ross, L. Samushia, D.J. Schlegel, A.G. Sánchez, J.L. Tinker and B.A. Weaver, *Monthly Notices of the RAS* **443** (2014), 1065.
- [20] S. Bhattacharya, K. Heitmann, M. White, Z. Lukić, C. Wagner and S. Habib, *Astrophysical Journal* **732** (2011), 122.
- [21] M. Biagetti, V. Desjacques, A. Kehagias and A. Riotto, *Physical Review D* **90** (2014), 103529.
- [22] C. Blake, T. Davis, G.B. Poole, D. Parkinson, S. Brough, M. Colless, C. Contreras, W. Couch, S. Croom, M.J. Drinkwater, K. Forster, D. Gilbank, M. Gladders, K. Glazebrook, B. Jelliffe, R.J. Jurek, I.H. Li, B. Madore, D.C. Martin, K. Pimbblet, M. Pracy, R. Sharp, E. Wisnioski, D. Woods, T.K. Wyder and H.K.C. Yee, *Monthly Notices of the RAS* **415** (2011), 2892.

- [23] C. Blake, E.A. Kazin, F. Beutler, T.M. Davis, D. Parkinson, S. Brough, M. Colless, C. Contreras, W. Couch, S. Croom, D. Croton, M.J. Drinkwater, K. Forster, D. Gilbank, M. Gladders, K. Glazebrook, B. Jelliffe, R.J. Jurek, I.H. Li, B. Madore, D.C. Martin, K. Pimblet, G.B. Poole, M. Pracy, R. Sharp, E. Wisnioski, D. Woods, T.K. Wyder and H.K.C. Yee, *Monthly Notices of the RAS* **418** (2011), 1707.
- [24] J.S. Bullock, T.S. Kolatt, Y. Sigad, R.S. Somerville, A.V. Kravtsov, A.A. Klypin, J.R. Primack and A. Dekel, *Monthly Notices of the RAS* **321** (2001), 559.
- [25] J.J.M. Carrasco, M.P. Hertzberg and L. Senatore, *Journal of High Energy Physics* **9** (2012), 82.
- [26] K.C. Chan, R. Scoccimarro and R.K. Sheth, *Physical Review D* **85** (2012), 083509.
- [27] X. Chen, *Advances in Astronomy* **2010** (2010), 72.
- [28] C.T. Chiang, C. Wagner, A.G. Sánchez, F. Schmidt and E. Komatsu, *ArXiv e-prints* (2015).
- [29] C.T. Chiang, C. Wagner, F. Schmidt and E. Komatsu, *Journal of Cosmology and Astroparticle Physics* **5** (2014), 48.
- [30] C.T. Chiang, P. Wullstein, D. Jeong, E. Komatsu, G.A. Blanc, R. Ciardullo, N. Drory, M. Fabricius, S. Finkelstein, K. Gebhardt, C. Gronwall, A. Hagen, G.J. Hill, I. Jee, S. Jogee, M. Landriau, E. Mentuch Cooper, D.P. Schneider and S. Tuttle, *Journal of Cosmology and Astroparticle Physics* **12** (2013), 30.
- [31] C.H. Chuang, C. Zhao, F. Prada, E. Munari, S. Avila, A. Izard, F.S. Kitaura, M. Manera, P. Monaco, S. Murray, A. Knebe, C.G. Scoccola, G. Yepes, J. Garcia-Bellido, F.A. Marin, V. Muller, R. Skibba, M. Crocce, P. Fosalba, S. Gottlober, A.A. Klypin, C. Power, C. Tao and V. Turchaninov, *ArXiv e-prints* (2014).
- [32] S. Cole and N. Kaiser, *Monthly Notices of the RAS* **237** (1989), 1127.
- [33] S. Cole, W.J. Percival, J.A. Peacock, P. Norberg, C.M. Baugh, C.S. Frenk, I. Baldry, J. Bland-Hawthorn, T. Bridges, R. Cannon, M. Colless, C. Collins, W. Couch, N.J.G. Cross, G. Dalton, V.R. Eke, R. De Propris, S.P. Driver, G. Efstathiou, R.S. Ellis, K. Glazebrook, C. Jackson, A. Jenkins, O. Lahav, I. Lewis, S. Lumsden, S. Maddox, D. Madgwick, B.A. Peterson, W. Sutherland and K. Taylor, *Monthly Notices of the RAS* **362** (2005), 505.
- [34] M. Colless, G. Dalton, S. Maddox, W. Sutherland, P. Norberg, S. Cole, J. Bland-Hawthorn, T. Bridges, R. Cannon, C. Collins, W. Couch, N. Cross, K. Deeley, R. De Propris, S.P. Driver, G. Efstathiou, R.S. Ellis, C.S. Frenk, K. Glazebrook, C. Jackson, O. Lahav, I. Lewis, S. Lumsden, D. Madgwick, J.A. Peacock, B.A. Peterson, I. Price, M. Seaborne and K. Taylor, *Monthly Notices of the RAS* **328** (2001), 1039.

-
- [35] A. Cooray and R. Sheth, *Physics Reports* **372** (2002), 1.
- [36] P. Creminelli, G. D'Amico, J. Noreña, L. Senatore and F. Vernizzi, *Journal of Cosmology and Astroparticle Physics* **3** (2010), 27.
- [37] P. Creminelli, J. Gleyzes, L. Hui, M. Simonović and F. Vernizzi, *Journal of Cosmology and Astroparticle Physics* **6** (2014), 9.
- [38] P. Creminelli, J. Gleyzes, M. Simonović and F. Vernizzi, *Journal of Cosmology and Astroparticle Physics* **2** (2014), 51.
- [39] P. Creminelli, J. Noreña, M. Simonović and F. Vernizzi, *Journal of Cosmology and Astroparticle Physics* **12** (2013), 25.
- [40] M. Crocce, S. Pueblas and R. Scoccimarro, *Monthly Notices of the RAS* **373** (2006), 369.
- [41] M. Crocce and R. Scoccimarro, *Physical Review D* **73** (2006), 063519.
- [42] M. Crocce and R. Scoccimarro, *Physical Review D* **77** (2008), 023533.
- [43] L. Dai, E. Pajer and F. Schmidt, *ArXiv e-prints* (2015).
- [44] L. Dai, E. Pajer and F. Schmidt, *ArXiv e-prints* (2015).
- [45] N. Dalal, O. Doré, D. Huterer and A. Shirokov, *Physical Review D* **77** (2008), 123514.
- [46] M. Davis and P.J.E. Peebles, *Astrophysical Journal* **267** (1983), 465.
- [47] R. de Putter, C. Wagner, O. Mena, L. Verde and W.J. Percival, *Journal of Cosmology and Astroparticle Physics* **4** (2012), 19.
- [48] W. Dehnen and J.I. Read, *European Physical Journal Plus* **126** (2011), 55.
- [49] V. Desjacques, M. Crocce, R. Scoccimarro and R.K. Sheth, *Physical Review D* **82** (2010), 103529.
- [50] V. Desjacques and R.K. Sheth, *Physical Review D* **81** (2010), 023526.
- [51] S. Dodelson and M.D. Schneider, *Physical Review D* **88** (2013), 063537.
- [52] G. Efstathiou, N. Kaiser, W. Saunders, A. Lawrence, M. Rowan-Robinson, R.S. Ellis and C.S. Frenk, *Monthly Notices of the RAS* **247** (1990), 10P.
- [53] D.J. Eisenstein, H.J. Seo and M. White, *Astrophysical Journal* **664** (2007), 660.

- [54] D.J. Eisenstein, I. Zehavi, D.W. Hogg, R. Scoccimarro, M.R. Blanton, R.C. Nichol, R. Scranton, H.J. Seo, M. Tegmark, Z. Zheng, S.F. Anderson, J. Annis, N. Bahcall, J. Brinkmann, S. Burles, F.J. Castander, A. Connolly, I. Csabai, M. Doi, M. Fukugita, J.A. Frieman, K. Glazebrook, J.E. Gunn, J.S. Hendry, G. Hennesy, Z. Ivezić, S. Kent, G.R. Knapp, H. Lin, Y.S. Loh, R.H. Lupton, B. Margon, T.A. McKay, A. Meiksin, J.A. Munn, A. Pope, M.W. Richmond, D. Schlegel, D.P. Schneider, K. Shimasaku, C. Stoughton, M.A. Strauss, M. SubbaRao, A.S. Szalay, I. Szapudi, D.L. Tucker, B. Yanny and D.G. York, *Astrophysical Journal* **633** (2005), 560.
- [55] H.A. Feldman, J.A. Frieman, J.N. Fry and R. Scoccimarro, *Physical Review Letters* **86** (2001), 1434.
- [56] H.A. Feldman, N. Kaiser and J.A. Peacock, *Astrophysical Journal* **426** (1994), 23.
- [57] J.A. Frieman, M.S. Turner and D. Huterer, *Annual Review of Astron and Astrophys* **46** (2008), 385.
- [58] J.N. Fry, *Astrophysical Journal* **279** (1984), 499.
- [59] J.N. Fry and E. Gaztanaga, *Astrophysical Journal* **413** (1993), 447.
- [60] T. Giannantonio and W.J. Percival, *Monthly Notices of the RAS* **441** (2014), L16.
- [61] T. Giannantonio, A.J. Ross, W.J. Percival, R. Crittenden, D. Bacher, M. Kilbinger, R. Nichol and J. Weller, *Physical Review D* **89** (2014), 023511.
- [62] H. Gil-Marín, J. Noreña, L. Verde, W.J. Percival, C. Wagner, M. Manera and D.P. Schneider, *ArXiv e-prints* (2014).
- [63] H. Gil-Marín, C. Wagner, J. Noreña, L. Verde and W. Percival, *Journal of Cosmology and Astroparticle Physics* **12** (2014), 29.
- [64] H. Gil-Marín, C. Wagner, L. Verde, C. Porciani and R. Jimenez, *Journal of Cosmology and Astroparticle Physics* **11** (2012), 29.
- [65] M.H. Goroff, B. Grinstein, S.J. Rey and M.B. Wise, *Astrophysical Journal* **311** (1986), 6.
- [66] J.E. Gunn and J.R. Gott, III, *Astrophysical Journal* **176** (1972), 1.
- [67] H. Guo, Z. Zheng, Y.P. Jing, I. Zehavi, C. Li, D.H. Weinberg, R.A. Skibba, R.C. Nichol, G. Rossi, C.G. Sabiu, D.P. Schneider and C.K. McBride, *Monthly Notices of the RAS* **449** (2015), L95.
- [68] Q. Guo, S. White, R.E. Angulo, B. Henriques, G. Lemson, M. Boylan-Kolchin, P. Thomas and C. Short, *Monthly Notices of the RAS* **428** (2013), 1351.

- [69] A.H. Guth, *Physical Review D* **23** (1981), 347.
- [70] K. Heitmann, E. Lawrence, J. Kwan, S. Habib and D. Higdon, *Astrophysical Journal* **780** (2014), 111.
- [71] G.J. Hill, K. Gebhardt, E. Komatsu, N. Drory, P.J. MacQueen, J. Adams, G.A. Blanc, R. Koehler, M. Rafal, M.M. Roth, A. Kelz, C. Gronwall, R. Ciardullo and D.P. Schneider: *The Hobby-Eberly Telescope Dark Energy Experiment (HETDEX): Description and Early Pilot Survey Results*. *The Hobby-Eberly Telescope Dark Energy Experiment (HETDEX): Description and Early Pilot Survey Results*, In *Panoramic Views of Galaxy Formation and Evolution*, herausgegeben von T. Kodama, T. Yamada and K. Aoki, Band 399 von *Astronomical Society of the Pacific Conference Series*. (October 2008) Seite 115.
- [72] S. Ho, N. Agarwal, A.D. Myers, R. Lyons, A. Disbrow, H.J. Seo, A. Ross, C. Hirata, N. Padmanabhan, R. O'Connell, E. Huff, D. Schlegel, A. Slosar, D. Weinberg, M. Strauss, N.P. Ross, D.P. Schneider, N. Bahcall, J. Brinkmann, N. Palanque-Desabrouille and C. Yèche, *ArXiv e-prints* (2013).
- [73] B. Horn, L. Hui and X. Xiao, *ArXiv e-prints* (2015).
- [74] J. Huchra, M. Davis, D. Latham and J. Tonry, *Astrophysical Journal, Supplement* **52** (1983), 89.
- [75] J.C. Jackson, *Monthly Notices of the RAS* **156** (1972), 1P.
- [76] B. Jain and E. Bertschinger, *Astrophysical Journal* **431** (1994), 495.
- [77] D. Jeong and E. Komatsu, *Astrophysical Journal* **651** (2006), 619.
- [78] Y.P. Jing, *Astrophysical Journal* **620** (2005), 559.
- [79] Y.P. Jing and G. Boerner, *Astronomy and Astrophysics* **318** (1997), 667.
- [80] N. Kaiser, *Monthly Notices of the RAS* **227** (1987), 1.
- [81] G. Kauffmann, S.D.M. White and B. Guiderdoni, *Monthly Notices of the RAS* **264** (1993), 201.
- [82] I. Kayo, Y. Suto, R.C. Nichol, J. Pan, I. Szapudi, A.J. Connolly, J. Gardner, B. Jain, G. Kulkarni, T. Matsubara, R. Sheth, A.S. Szalay and J. Brinkmann, *Publications of the ASJ* **56** (2004), 415.
- [83] A. Kehagias, J. Noreña, H. Perrier and A. Riotto, *Nuclear Physics B* **883** (2014), 83.
- [84] A. Kehagias, H. Perrier and A. Riotto, *Modern Physics Letters A* **29** (2014), 50152.

-
- [85] A. Kehagias and A. Riotto, *Nuclear Physics B* **873** (2013), 514.
- [86] A. Klypin, G. Yepes, S. Gottlober, F. Prada and S. Hess, *ArXiv e-prints* (2014).
- [87] E. Komatsu, *Classical and Quantum Gravity* **27** (2010), 124010.
- [88] E. Komatsu, K.M. Smith, J. Dunkley, C.L. Bennett, B. Gold, G. Hinshaw, N. Jarosik, D. Larson, M.R.olta, L. Page, D.N. Spergel, M. Halpern, R.S. Hill, A. Kogut, M. Limon, S.S. Meyer, N. Odegard, G.S. Tucker, J.L. Weiland, E. Wollack and E.L. Wright, *Astrophysical Journal, Supplement* **192** (2011), 18.
- [89] E. Komatsu and D.N. Spergel, *Physical Review D* **63** (2001), 063002.
- [90] A.V. Kravtsov, A.A. Berlind, R.H. Wechsler, A.A. Klypin, S. Gottlöber, B. Allgood and J.R. Primack, *Astrophysical Journal* **609** (2004), 35.
- [91] S.D. Landy and A.S. Szalay, *Astrophysical Journal* **412** (1993), 64.
- [92] B. Leistedt, H.V. Peiris and N. Roth, *Physical Review Letters* **113** (2014), 221301.
- [93] G. Lemaître, *Annales de la Société Scientifique de Bruxelles* **53** (1933), 51.
- [94] J. Lesgourgues, *ArXiv e-prints* (2011).
- [95] A. Lewis and S. Bridle, *Physical Review D* **66** (2002), 103511.
- [96] A. Lewis, A. Challinor and A. Lasenby, *Astrophysical Journal* **538** (2000), 473.
- [97] Y. Li, W. Hu and M. Takada, *Physical Review D* **89** (2014), 083519.
- [98] Y. Li, W. Hu and M. Takada, *Physical Review D* **90** (2014), 103530.
- [99] A.D. Linde, *Physics Letters B* **108** (1982), 389.
- [100] LSST Dark Energy Science Collaboration, *ArXiv e-prints* (2012).
- [101] S.J. Maddox, G. Efstathiou, W.J. Sutherland and J. Loveday, *Monthly Notices of the RAS* **242** (1990), 43P.
- [102] A. Mana, T. Giannantonio, J. Weller, B. Hoyle, G. Hütsi and B. Sartoris, *Monthly Notices of the RAS* **434** (2013), 684.
- [103] M. Manera, L. Samushia, R. Tojeiro, C. Howlett, A.J. Ross, W.J. Percival, H. Gil-Marín, J.R. Brownstein, A. Burden and F. Montesano, *Monthly Notices of the RAS* **447** (2015), 437.

- [104] M. Manera, R. Scoccimarro, W.J. Percival, L. Samushia, C.K. McBride, A.J. Ross, R.K. Sheth, M. White, B.A. Reid, A.G. Sánchez, R. de Putter, X. Xu, A.A. Berlind, J. Brinkmann, C. Maraston, B. Nichol, F. Montesano, N. Padmanabhan, R.A. Skibba, R. Tojeiro and B.A. Weaver, *Monthly Notices of the RAS* **428** (2013), 1036.
- [105] F.A. Marín, C. Blake, G.B. Poole, C.K. McBride, S. Brough, M. Colless, C. Contreras, W. Couch, D.J. Croton, S. Croom, T. Davis, M.J. Drinkwater, K. Forster, D. Gilbank, M. Gladders, K. Glazebrook, B. Jelliffe, R.J. Jurek, I.h. Li, B. Madore, D.C. Martin, K. Pimblet, M. Pracy, R. Sharp, E. Wisnioski, D. Woods, T.K. Wyder and H.K.C. Yee, *Monthly Notices of the RAS* **432** (2013), 2654.
- [106] S. Matarrese and L. Verde, *Astrophysical Journal, Letters* **677** (2008), L77.
- [107] T. Matsubara, *Physical Review D* **78** (2008), 083519.
- [108] T. Matsubara, *Physical Review D* **77** (2008), 063530.
- [109] C.K. McBride, A.J. Connolly, J.P. Gardner, R. Scranton, J.A. Newman, R. Scoccimarro, I. Zehavi and D.P. Schneider, *Astrophysical Journal* **726** (2011), 13.
- [110] C.K. McBride, A.J. Connolly, J.P. Gardner, R. Scranton, R. Scoccimarro, A.A. Berlind, F. Marín and D.P. Schneider, *Astrophysical Journal* **739** (2011), 85.
- [111] N. McCullagh and D. Jeong, *in prep.* (2015).
- [112] P. McDonald, *Astrophysical Journal* **585** (2003), 34.
- [113] P. McDonald and A. Roy, *Journal of Cosmology and Astroparticle Physics* **8** (2009), 20.
- [114] H. Miyatake, S. More, R. Mandelbaum, M. Takada, D.N. Spergel, J.P. Kneib, D.P. Schneider, J. Brinkmann and J.R. Brownstein, *ArXiv e-prints* (2013).
- [115] H.J. Mo and S.D.M. White, *Monthly Notices of the RAS* **282** (1996), 347.
- [116] I. Mohammed and U. Seljak, *Monthly Notices of the RAS* **445** (2014), 3382.
- [117] S. More, H. Miyatake, R. Mandelbaum, M. Takada, D. Spergel, J. Brownstein and D.P. Schneider, *ArXiv e-prints* (2014).
- [118] J.F. Navarro, C.S. Frenk and S.D.M. White, *Astrophysical Journal* **490** (1997), 493.
- [119] T. Nishimichi, I. Kayo, C. Hikage, K. Yahata, A. Taruya, Y.P. Jing, R.K. Sheth and Y. Suto, *Publications of the ASJ* **59** (2007), 93.
- [120] T. Nishimichi and P. Valageas, *Physical Review D* **90** (2014), 023546.

- [121] T. Nishimichi and P. Valageas, *ArXiv e-prints* (2015).
- [122] T. Padmanabhan: *Structure Formation in the Universe*, May 1993.
- [123] E. Pajer, F. Schmidt and M. Zaldarriaga, *Physical Review D* **88** (2013), 083502.
- [124] E. Pajer and M. Zaldarriaga, *Journal of Cosmology and Astroparticle Physics* **8** (2013), 37.
- [125] P.J.E. Peebles, *Astrophysical Journal* **185** (1973), 413.
- [126] P.J.E. Peebles, *Astronomy and Astrophysics* **32** (1974), 391.
- [127] M. Peloso and M. Pietroni, *Journal of Cosmology and Astroparticle Physics* **5** (2013), 31.
- [128] Planck Collaboration, P.A.R. Ade, N. Aghanim, M. Arnaud, F. Arroja, M. Ashdown, J. Aumont, C. Baccigalupi, M. Ballardini, A.J. Banday and et al., *ArXiv e-prints* (2015).
- [129] B.F. Roukema, T. Buchert, J.J. Ostrowski and M.J. France, *Monthly Notices of the RAS* **448** (2015), 1660.
- [130] L. Samushia, B.A. Reid, M. White, W.J. Percival, A.J. Cuesta, G.B. Zhao, A.J. Ross, M. Manera, É. Aubourg, F. Beutler, J. Brinkmann, J.R. Brownstein, K.S. Dawson, D.J. Eisenstein, S. Ho, K. Honscheid, C. Maraston, F. Montesano, R.C. Nichol, N.A. Roe, N.P. Ross, A.G. Sánchez, D.J. Schlegel, D.P. Schneider, A. Streblyanska, D. Thomas, J.L. Tinker, D.A. Wake, B.A. Weaver and I. Zehavi, *Monthly Notices of the RAS* **439** (2014), 3504.
- [131] A.G. Sánchez, F. Montesano, E.A. Kazin, E. Aubourg, F. Beutler, J. Brinkmann, J.R. Brownstein, A.J. Cuesta, K.S. Dawson, D.J. Eisenstein, S. Ho, K. Honscheid, M. Manera, C. Maraston, C.K. McBride, W.J. Percival, A.J. Ross, L. Samushia, D.J. Schlegel, D.P. Schneider, R. Skibba, D. Thomas, J.L. Tinker, R. Tojeiro, D.A. Wake, B.A. Weaver, M. White and I. Zehavi, *Monthly Notices of the RAS* **440** (2014), 2692.
- [132] K. Sato, *Physics Letters B* **99** (1981), 66.
- [133] T. Sato, G. Hütsi, G. Nakamura and K. Yamamoto, *International Journal of Astronomy and Astrophysics* **3** (2013), 243.
- [134] T. Sato, G. Hütsi and K. Yamamoto, *Progress of Theoretical Physics* **125** (2011), 187.
- [135] W. Saunders, C. Frenk, M. Rowan-Robinson, A. Lawrence and G. Efstathiou, *Nature* **349** (1991), 32.

- [136] J. Schaye, R.A. Crain, R.G. Bower, M. Furlong, M. Schaller, T. Theuns, C. Dalla Vecchia, C.S. Frenk, I.G. McCarthy, J.C. Helly, A. Jenkins, Y.M. Rosas-Guevara, S.D.M. White, M. Baes, C.M. Booth, P. Camps, J.F. Navarro, Y. Qu, A. Rahmati, T. Sawala, P.A. Thomas and J. Trayford, *Monthly Notices of the RAS* **446** (2015), 521.
- [137] F. Schmidt, D. Jeong and V. Desjacques, *Physical Review D* **88** (2013), 023515.
- [138] F. Schmidt, M. Lima, H. Oyaizu and W. Hu, *Physical Review D* **79** (2009), 083518.
- [139] R. Scoccimarro, S. Colombi, J.N. Fry, J.A. Frieman, E. Hivon and A. Melott, *Astrophysical Journal* **496** (1998), 586.
- [140] R. Scoccimarro and H.M.P. Couchman, *Monthly Notices of the RAS* **325** (2001), 1312.
- [141] R. Scoccimarro, H.M.P. Couchman and J.A. Frieman, *Astrophysical Journal* **517** (1999), 531.
- [142] R. Scoccimarro, H.A. Feldman, J.N. Fry and J.A. Frieman, *Astrophysical Journal* **546** (2001), 652.
- [143] R. Scoccimarro and R.K. Sheth, *Monthly Notices of the RAS* **329** (2002), 629.
- [144] E. Sefusatti and E. Komatsu, *Physical Review D* **76** (2007), 083004.
- [145] U. Seljak and Z. Vlah, *ArXiv e-prints* (2015).
- [146] C.D. Shane and C.A. Wirtanen: *The distribution of galaxies*, 1967.
- [147] B.D. Sherwin and M. Zaldarriaga, *Physical Review D* **85** (2012), 103523.
- [148] R.K. Sheth, K.C. Chan and R. Scoccimarro, *Physical Review D* **87** (2013), 083002.
- [149] R.K. Sheth and G. Tormen, *Monthly Notices of the RAS* **308** (1999), 119.
- [150] E. Sirko, *Astrophysical Journal* **634** (2005), 728.
- [151] A. Slosar, C. Hirata, U. Seljak, S. Ho and N. Padmanabhan, *Journal of Cosmology and Astroparticle Physics* **8** (2008), 31.
- [152] R.E. Smith, J.A. Peacock, A. Jenkins, S.D.M. White, C.S. Frenk, F.R. Pearce, P.A. Thomas, G. Efstathiou and H.M.P. Couchman, *Monthly Notices of the RAS* **341** (2003), 1311.
- [153] V. Springel, *Monthly Notices of the RAS* **364** (2005), 1105.

- [154] V. Springel, S.D.M. White, A. Jenkins, C.S. Frenk, N. Yoshida, L. Gao, J. Navarro, R. Thacker, D. Croton, J. Helly, J.A. Peacock, S. Cole, P. Thomas, H. Couchman, A. Evrard, J. Colberg and F. Pearce, *Nature* **435** (2005), 629.
- [155] J. Stadel, D. Potter, B. Moore, J. Diemand, P. Madau, M. Zemp, M. Kuhlen and V. Quilis, *Monthly Notices of the RAS* **398** (2009), L21.
- [156] M. Takada, R.S. Ellis, M. Chiba, J.E. Greene, H. Aihara, N. Arimoto, K. Bundy, J. Cohen, O. Doré, G. Graves, J.E. Gunn, T. Heckman, C.M. Hirata, P. Ho, J.P. Kneib, O.L. Fèvre, L. Lin, S. More, H. Murayama, T. Nagao, M. Ouchi, M. Seiffert, J.D. Silverman, L. Sodr e, D.N. Spergel, M.A. Strauss, H. Sugai, Y. Suto, H. Takami and R. Wyse, *Publications of the ASJ* **66** (2014), 1.
- [157] M. Takada and W. Hu, *Physical Review D* **87** (2013), 123504.
- [158] G. Tasinato, M. Tellarini, A.J. Ross and D. Wands, *Journal of Cosmology and Astroparticle Physics* **3** (2014), 32.
- [159] S. Tassev, M. Zaldarriaga and D.J. Eisenstein, *Journal of Cosmology and Astroparticle Physics* **6** (2013), 36.
- [160] M. Tegmark, A.N. Taylor and A.F. Heavens, *Astrophysical Journal* **480** (1997), 22.
- [161] R. Teyssier, S. Pires, S. Prunet, D. Aubert, C. Pichon, A. Amara, K. Benabed, S. Colombi, A. Refregier and J.L. Starck, *Astronomy and Astrophysics* **497** (2009), 335.
- [162] The Dark Energy Survey Collaboration, *ArXiv Astrophysics e-prints* (2005).
- [163] J. Tinker, A.V. Kravtsov, A. Klypin, K. Abazajian, M. Warren, G. Yepes, S. Gottl ober and D.E. Holz, *Astrophysical Journal* **688** (2008), 709.
- [164] R. Tojeiro, A.J. Ross, A. Burden, L. Samushia, M. Manera, W.J. Percival, F. Beutler, J. Brinkmann, J.R. Brownstein, A.J. Cuesta, K. Dawson, D.J. Eisenstein, S. Ho, C. Howlett, C.K. McBride, F. Montesano, M.D. Olmstead, J.K. Parejko, B. Reid, A.G. S anchez, D.J. Schlegel, D.P. Schneider, J.L. Tinker, M.V. Maga na and M. White, *Monthly Notices of the RAS* **440** (2014), 2222.
- [165] P. Valageas, *Physical Review D* **89** (2014), 123522.
- [166] P. Valageas, *Physical Review D* **89** (2014), 083534.
- [167] L. Verde, A.F. Heavens, W.J. Percival, S. Matarrese, C.M. Baugh, J. Bland-Hawthorn, T. Bridges, R. Cannon, S. Cole, M. Colless, C. Collins, W. Couch, G. Dalton, R. De Propris, S.P. Driver, G. Efstathiou, R.S. Ellis, C.S. Frenk, K. Glazebrook, C. Jackson, O. Lahav, I. Lewis, S. Lumsden, S. Maddox, D. Madgwick, P. Norberg, J.A. Peacock, B.A. Peterson, W. Sutherland and K. Taylor, *Monthly Notices of the RAS* **335** (2002), 432.

- [168] M.S. Vogeley, C. Park, M.J. Geller and J.P. Huchra, *Astrophysical Journal, Letters* **391** (1992), L5.
- [169] M. Vogelsberger, S. Genel, V. Springel, P. Torrey, D. Sijacki, D. Xu, G. Snyder, D. Nelson and L. Hernquist, *Monthly Notices of the RAS* **444** (2014), 1518.
- [170] C. Wagner, F. Schmidt, C.T. Chiang and E. Komatsu, *Monthly Notices of the RAS* **448** (2015), L11.
- [171] C. Wagner, F. Schmidt, C.T. Chiang and E. Komatsu, *ArXiv e-prints* (2015).
- [172] D.G. York, J. Adelman, J.E. Anderson, Jr., S.F. Anderson, J. Annis, N.A. Bahcall, J.A. Bakken, R. Barkhouser, S. Bastian, E. Berman, W.N. Boroski, S. Bracker, C. Briegel, J.W. Briggs, J. Brinkmann, R. Brunner, S. Burles, L. Carey, M.A. Carr, F.J. Castander, B. Chen, P.L. Colestock, A.J. Connolly, J.H. Crocker, I. Csabai, P.C. Czarapata, J.E. Davis, M. Doi, T. Dombeck, D. Eisenstein, N. Ellman, B.R. Elms, M.L. Evans, X. Fan, G.R. Federwitz, L. Fiscelli, S. Friedman, J.A. Frieman, M. Fukugita, B. Gillespie, J.E. Gunn, V.K. Gurbani, E. de Haas, M. Halderman, F.H. Harris, J. Hayes, T.M. Heckman, G.S. Hennessy, R.B. Hindsley, S. Holm, D.J. Holmgren, C.h. Huang, C. Hull, D. Husby, S.I. Ichikawa, T. Ichikawa, Ž. Ivezić, S. Kent, R.S.J. Kim, E. Kinney, M. Klaene, A.N. Kleinman, S. Kleinman, G.R. Knapp, J. Korienek, R.G. Kron, P.Z. Kunszt, D.Q. Lamb, B. Lee, R.F. Leger, S. Limmongkol, C. Lindenmeyer, D.C. Long, C. Loomis, J. Loveday, R. Lucinio, R.H. Lupton, B. MacKinnon, E.J. Mannery, P.M. Mantsch, B. Margon, P. McGehee, T.A. McKay, A. Meiksin, A. Merelli, D.G. Monet, J.A. Munn, V.K. Narayanan, T. Nash, E. Neilsen, R. Neswold, H.J. Newberg, R.C. Nichol, T. Nicinski, M. Nonino, N. Okada, S. Okamura, J.P. Ostriker, R. Owen, A.G. Pauls, J. Peoples, R.L. Peterson, D. Petravick, J.R. Pier, A. Pope, R. Pordes, A. Protopio, R. Rechenmacher, T.R. Quinn, G.T. Richards, M.W. Richmond, C.H. Rivetta, C.M. Rockosi, K. Ruthmansdorfer, D. Sandford, D.J. Schlegel, D.P. Schneider, M. Sekiguchi, G. Sergey, K. Shimasaku, W.A. Siegmund, S. Smee, J.A. Smith, S. Snedden, R. Stone, C. Stoughton, M.A. Strauss, C. Stubbs, M. SubbaRao, A.S. Szalay, I. Szapudi, G.P. Szokoly, A.R. Thakar, C. Tremonti, D.L. Tucker, A. Uomoto, D. Vanden Berk, M.S. Vogeley, P. Waddell, S.i. Wang, M. Watanabe, D.H. Weinberg, B. Yanny, N. Yasuda and SDSS Collaboration, *Astronomical Journal* **120** (2000), 1579.
- [173] Y.B. Zel'dovich, *Astronomy and Astrophysics* **5** (1970), 84.
- [174] F. Zwicky, E. Herzog, P. Wild, M. Karpowicz and C.T. Kowal: *Catalogue of galaxies and of clusters of galaxies, Vol. I*, 1961.

Acknowledgment

First, I would like to thank my advisor, Eiichiro Komatsu, for everything he has done to me through my graduate school life, in particular for not giving me up after my qualifying exam and for taking me from Austin to Munich. Without his help, I will not be able to finish this dissertation. His broad knowledge from observational astronomy to high energy physics always amazes me, and sets a gold standard for me in my future career. Not only advising me academically, he also cares about me personally as my family, and takes me away from work when necessary. I will never ever forget the immense gratitude from him.

I would like to thank Donghui Jeong, who is essentially my second advisor and led me into the field of large-scale structure. Although we only overlapped in Austin for one year, he taught me so many things in cosmology, especially during our Friday-textbook-reading session, which were extremely useful for a beginning student. I also got tremendous amount of help from him for my first published paper [30].

I would like to thank Christian Wagner, whom I worked the most with after moving to MPA. He taught me everything about simulations, and I really enjoyed discussing with him on all topics in the large-scale structure. Thank him for his patience when I found “another” bug in my code. This dissertation is based on the work I started working with him in late 2012, and thankfully he became interested in so we could publish a series of work [29, 170, 171, 28].

Faiban Schmidt is one of the most intelligent people I know. His way of tackling problems as well as extracting the physical meaning always inspires me. Because of his physical insight, the project that I started working with Christian grew bigger and became even more interesting. I benefited a lot from working and discussing with him.

I would like to thank Ariel Sánchez and Marat Gilfanov for serving as my committee members. I got many useful from the annual committee meeting, especially their encouragement when I was still waiting for the results from my job applications. Especially, I would also like to thank Ariel, who taught me all the things about BOSS data, so I can finish the work in chapter 5.

Being able to participate in this cool project is one of the greatest experiences in my career. I would like to thank the HETDEX members, in particular Gary Hill and Karl Gebhardt, for their guide when I first joined the project and their useful comments on my sparse sampling work [30]. I would also like to thank Niv Drory, who gave me a “serious” lesson on not missing the deadline. He probably does not remember what happened, but it was a shocking experience for me so now I always be prepared beforehand.

Masatoshi Shoji and Jonathan Ganc are my best academic siblings. Sharing office RLM 16.206 is one of the best memories during my graduate school life. I miss the time when we discussed various issues in cosmology, made fun of each other, and made the most noise in the hallway. Our short-lived Monday drinking tradition and Masa's lung-exercising (smoking) time were truly memorable.

I would like to thank all the astronomy folks in Austin, especially my classmates Jacob Hummel, Taylor Chonis, Sam Harrold, Rodolfo Santana, Myoungwon Jeon, Mimi Song, Nalin Vutisalchavakul, and Alan Sluder. I still remember the time when we were working hard together for the homework problems. I am also benefited a lot from the Texas cosmology group: Hyunbae Park, Jun Zhang, Andreas Pawlik, Tanja Rindler-Daller, Jun Koda, Yi Mao, and Paul Shapiro.

I would like to thank all my friends in Austin. Without them my graduate student life would be boring. In particular, I would like to thank Ping-Chun Li and Ke-Yi Lin. They were always the people I talked to when I felt down about work or life. I still remember the times when we gathered at late night drinking and complaining the bad things in our lives, but in the next morning we still had to deal with them!

Moving to Germany is not an easy thing for me. I would like to thank Philipp Wullstein for all the help whenever I needed it, and Sonja Gründl for helping me find an apartment. Without their help I would not be able to survive in Germany. I also want to thank my landlord Herr Mooseder, who is extremely kind to me even if I do not speak German at all. (I promised to learn, but gave up because of the difficulty and time...) He lent his bike"s" to me and fixed them whenever I broke them... I genuinely appreciate what they have done for me.

For the years in MPA, I would like to thank everyone in physical cosmology group: Jaiseung Kim, Xun Shi, Inh Jee, Aniket Agrawal, Kari Helgason, Sam Ip, and Titouan Lazeyras. Having lunch with them and discussing various things are always fun. I hope they do not hate me for pushing them to read papers for the large-scale structure journal club. In particular, I would like to thank Tsz Yan Lam, who gave me many useful suggestions for job applications, and encouraged me when I was still waiting for the results. It was very thoughtful.

I would like to thank all my friends in Munich, especially Yi-Hao Chen (who also helped me a lot when I moved to Germany), Chia-Yu Hu, Chien-Hsiu Lee, Ming-Yi Lin, Li-Ting Hsu, and I-Non Chiu. Our Friday study group (which you should keep even without me) was a truly enjoyable experience, and I learned a lot about different topics in astronomy, especially observations.

Last but most importantly, I would like to thank my parents and sister for understanding me of pursuing my own dream, and supporting me endlessly. I would like to show my deepest appreciation to my beloved fiancée, Hua-Shu, for her constant encouragement and warm love, especially during the job application season. She is always the source of happiness and bliss in my life.